Lifting grains from a dust bed by interaction with optical radiation and gas at low ambient pressure.

With applications to Mars and protoplanetary disks.

Von der Fakultät für Physik der Universität Duisburg-Essen
genehmigte Dissertation von

Dipl.-Phys. Caroline de Beule

zur Erlangung des akademischen Grades

Dr. rer. nat.

1. Gutachter: Prof. Dr. Gerhard Wurm
2. Gutachter: Prof. Dr. Olivier Mousis
3. Gutachter: Prof. Dr. Axel Lorke
Disputation: 23.02.2016

UNIVERSITÄT
DUISBURG
ESSEN

Open-Minded

"Wo kämen wir hin,
wenn alle sagten, wo kämen wir hin,
und niemand ginge, um einmal zu schauen,
wohin man käme, wenn man ginge."

— *Kurt Marti, 1967*

1

Abstract

Earlier experiments have shown that dust beds efficiently eject particles under illumination at low ambient pressure. Recent experiments performed in microgravity have shown a convective flow pattern, traced by eroded particles. As thermal convection can be ruled out without residual gravity, the explanation is a gas flow not only above but also through the dust bed.
The forces acting on a surface particle of an illuminated dust bed are gravity, cohesion, photophoresis, thermophoresis and gas drag. In addition, another force based upon a pressure build-up within the dust bed is presented.
Experiments were performed to determine the magnitude of each force. Each experiment revealed new information about the acting forces and the results clearly show that the main lifting force for light-induced erosion is based on the overpressure within the dust bed and gas drag.
Porous bodies in protoplanetary disks can be efficiently eroded by the light-induced gas flow, which might be one explanation for the micron-sized dust observed over the entire lifetime of a protoplanetary disk. Another application is on Mars, where the solar insolation induces a planet wide gas pump in the regolith of the planet. Atmospheric gas is pumped into the soil at shadowed places, traverses underground and is pumped up again in illuminated regions. This also eases dust lifting.

Zusammenfassung

Experimente haben gezeigt dass die Beleuchtung von Staubbetten in einer gasarmen Umgebung zu einer effektiven Erosion von Staubpartikeln führt. Weitere Experimente unter Schwerelosigkeit zeigten dass ausgeworfene Staubartikel einem konvektiven Gasfluss folgten. Da thermische Konvektion bei der Abwesenheit von Gravitation ausgeschlossen werden kann, bleibt als Erklärung ein durch Licht induzierter Gasstrom der nicht nur oberhalb, sondern auch durch das Staubbett geht.
Die Kräfte welche auf ein Partikel an der Oberfläche eines beleuchteten Staubbetts wirken sind Gravitation, Kohäsion, Photophorese, Thermophorese und Luftreibung. Desweiteren präsentiert diese Arbeit eine Kraft die auf einem Druckaufbau innerhalb des Staubbetts basiert.
Die Größe der wirkenden Kräfte auf ein Oberflächenpartikel werden mit Hilfe von Experimenten abgeschätzt. Jedes der Experimente lieferte dabei neue Informationen von den

wirkenden Kräften und die Ergebnisse zeigen deutlich dass die treibende Kraft bei der Erosion durch einen Überdruck innerhalb des Staubbettes und Luftreibung gegeben ist. Poröse Körper in protoplanetaren Scheiben können effektiv durch licht-induzierten Gasfluss erodiert werden, was eine Erklärung für den mikrometer-großen Staub sein kann, der über die gesamte Lebenszeit einer protoplanetaren Scheibe beobachtet wird. Eine weitere Anwendung findet sich auf dem Mars, bei welchem die Sonneneinstrahlung zu einer plantengroßen Gaspumpe führt. Das Gas aus der Atmosphäre wird in schattigen Orten in das Regolith gesogen, innerhalb des Regoliths weiter transportiert und in beleuchteten Orten wieder an die Oberfläche gepumpt. Das Pumpen des Gases durch den Marsboden kann das Abheben von Staub von der Oberfläche begünstigen.

2

Publications

Articles (peer reviewed)

- C. de Beule, T. Kelling, G. Wurm, J. Teiser, and T. Jankowski. *From planetesimals to dust: Low gravity experiments on recycling solids in inner protoplanetary disks.* **The Astrophysical Journal**, 763, 2013.

- C. de Beule, G. Wurm, T. Kelling, M. Küpper, T. Jankowski, and J. Teiser *The martian soil as a planetary gas pump.* **Nature Physics**, 10, 2014.

- M. Küpper, C, Dürmann, C. de Beule, and G. Wurm. *Propulsion of porous plates in thin atmospheres by temperature fields.* **Microgravity Science and Technology**, 5, 2014.

- M. Küpper, C. de Beule, G. Wurm, L. S. Matthews, J.B. Kimery, and T. W. Hyde. *Photophoresis on polydisperse basalt microparticles under microgravity.* **Journal of Aerosol Science**, 76, 2014.

- C. de Beule, G. Wurm, T. Kelling, M. Koester, and M. Kocifaj. *An Insolation Activated Dust Layer on Mars.* **Icarus**, 260, 2015.

- L. S. Matthews, J. B. Kimery, G. Wurm, C. de Beule, M. Kuepper, and T. W. Hyde. *Photophoretic Force on Aggregate Grains* **Monthly Notices of the Royal Astronomical Society**, in review.

- C. de Beule, J. Landers, G. Wurm, H. Wende, and S. Salamon. *Planetesimal Formation in the warm inner Disk.*, submitted.

- C. de Beule, G. Wurm, G. Musiolik, *Measuring the Tensile Strength of Cohesive Granular Matter on Small Scales.*, submitted.

Proceedings

- C. de Beule, T. Kelling, G. Wurm, J. Teiser, and T. Jankowski. *Light Induced Dust Lifting on Mars: 0g Experiments.* **EPSC-DPS Joint Meeting 2011**, p. 201, 2011.

- C. de Beule, T. Kelling, G. Wurm, T. Teiser, and T. Jankowski *Light induced erosion of dusty planetesimals and mars: μg experiments.* **Journal of Physics: Conference Series**, 327, 2011.

Conference contribution

- C. de Beule, T. Kelling, G. Wurm, J. Teiser, and T. Jankowski. Planet Formation and Evolution Workshop, Göttingen, 14-16.02.2011, *Erosion of Illuminated Planetesimals: Microgravity Experiments*, Poster
- C. de Beule, T. Kelling, G. Wurm, J. Teiser, and T. Jankowski. EPSC-DPS Joint Meeting, Nantes, 02-07.10.2011, *Light Induced Lifting of Dust on Mars: μg Experiments*, Talk
- C. de Beule, C. Dürmann, M. Küpper, A. Hesse. Fly Your Thesis! 2012 Selection Workshop, Nordwijk, 07.-08.02.2011, *Moving Particles in Protoplanetary Disks by a Knudsen Compressor Effect*, Talk
- C. de Beule, T. Kelling, J. Teiser, G. Wurm, and T. Jankowski. Protostars and Planets VI, Heidelberg, 15-20.07.2013, *Erosion by photophoresis and natural Knudsen Compressors in Microgravity*, Poster
- C. de Beule, G. Wurm, T. Kelling, M. Küpper, T. Jankowski, and J. Teiser. 45th Annual Meeting of DPS (Division for Planetary Science), Denver, 6-11.10.2013, *The Martian soil: A planetary gas pump*, Talk
- C. de Beule, J. Landers, G. Wurm, H. Wende, and S. Salamon. Planet Formation and Evolution Workshop, Kiel, 8-10.09.2014, *Planetesimal Formation in the warm inner Disk*, Poster
- C. de Beule, G. Wurm, T. Kelling, M. Koester, and M. Kocifaj. Granular Matter in Low Gravity, Erlangen, 25-27.03.2015, *Gas flow through insolated granular matter in low gravity and the Blowfish effect*, Talk

Invited Talks

- ZARM Förderpreis für besondere Studienleistung auf dem Gebiet der Forschung unter Mikrogravitation, 1. Platz, ZARM Bremen, *Gravitationsabhängigkeit lichtinduzierter Stauberuptionen*, 2012
- Guest lecture, Otto-von-Guericke-Universität Magdeburg, Abteilung Nichtlineare Phänomene, *An insolation activated dust layer and gas flow through porous media*, 2015

Contents

3

Motivation

The question "Where do we come from?" is as old as mankind. This question comprises many sub-questions and in between the wide range of the big bang and human evolution, a question arises: "How did Earth form?" or, in general: "How do planets form?".

One major step in the observation of the solar system was achieved by Nicolas Kopernikus, who proposed the theory of a heliocentric system - in which the planets revolve around the sun. This theory contradicted the geocentric system, which had been widely accepted until then. Indeed, we subsequently started to learn that the Earth is not the center of everything - but a part of something larger, namely the solar system. There is more outside our atmosphere and even more outside our solar system: our galaxy.

After inventing telescopes and improving and - after space probes were sent to collect information from space, we learned more about the solar system and thus the result of planet formation. Unfortunately, the process itself remained uncertain.
The first theories for the formation of planets were based upon the only system that we knew at that time: our own solar system. How fascinating must it have been to think about a second Earth within reach?

The detection of extra-solar planets is not simple as the light from a planet is diminutive in comparison to the host star. After supposing that extra-solar planets exist, significant effort was undertaken to find them, although it took until 1992 to achieve a confirmed discovery, when Wolszczan and Frail (1992) found two planets orbiting a pulsar by pulsar timing measurements.
The following decade led to a rapid discovery of further exoplanets. Until today, 1,931 confirmed expolant candidates have been found in 1,221 planetary systems (484 of them are multiple planetary systems) (Schneider, 2015).
NASA's Kepler mission recent found an Earth-like planet (Kepler 425b) in the habitable zone around a sun-like star.

The discovery of those exoplanets provided a better insight into the diversity of planetary systems and - as a byproduct the process of planet formation. Additionally, the advent of space observatories like Spitzer and Herschel in combination with theoretical models and simulations led to great progress in this field.

However, not all questions concerning the formation of planets have been answered yet and this work is tied up to some of these questions. In the last decade, laboratory experiments have shown that the illumination of a dust bed in a gaseous environment can lead to effective ejection of dust particles from the surface (Wurm and Krauss, 2006; Wurm, 2007; Kelling et al., 2011; Kelling and Wurm, 2011; Kelling, 2012). These conditions (low pressure, insolation) can be found in protoplanetary disks, which are known to be the birthplace of planets (see Sec. 3.1). This work concentrates on the understanding of this effect and developing the model of light–induced erosion for the application in theoretical models for protoplanetary disks.

The effect of light–induced erosion is not only applicable for protoplanetary disks - but as also for our neighbor planet Mars. The dust cycle on the red planet is not fully understood, but it holds great interest concerning the climate and its evolution on Mars. This work presents experiments showing that on planet Mars - with a low atmospheric pressure - the insolation by the sun is sufficient to induce processes to reduce the force needed to lift dust from the surface.

3.1 Astrophysical background

The idea of planet formation in a nebula of gas and dust formulated by Kant (1755) and similar by his coeval Laplace (1836) is close to the findings of today: scientists are in agreement that the process of planet formation is strongly connected to the formation of stars from a collapsing molecular cloud.
Due to the conversion of angular momentum, the collapsing parts of the cloud flatten to a rotating disk, leaving a system with a developing star in the center and a disk of dust and gas surrounding it (Shu et al., 1987). Typical sizes of protoplanetary disks are a few 100 AU (with 1 AU $\approx 149.6 \cdot 10^6$ km, the distance between Earth and Sun), although they can be extended to 10^4 AU. An example of a protoplanetary disk is shown in Fig. 3.1.

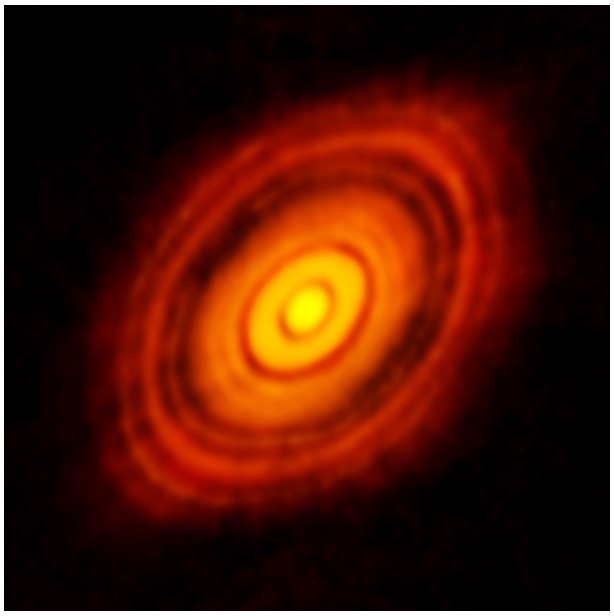

Figure 3.1: Image of the protoplanetary disc around HL Tauri taken by ALMA. Credit: ALMA (NRAO/ESO/NAOJ); C. Brogan, B. Saxton (NRAO/AUI/NSF).

Dutrey et al. (2014) find temperatures of 10^3 K close to the central star down to a few 10 K in the outer disk. The pressure inside the disk is about 10^{-7} mbar in the outer regions and up to 1 mbar in the inner regions (Wood, 2000). A sketch of the temperature and pressure distribution within a protoplanetary disk based upon the minimum mass solar nebula model by Hayashi et al. (1985) is shown in Fig.3.2.
Protoplanetary mainly comprise of molecular hydrogen and helium. However, 1 % of the mass of the disk is dust: micron-sized refractory particles (e.g. silicates) and ice (H_2O, CO_2, CO). Terrestrial planets are thought to be built from this 1% of solids. The growth from dust particles to planets can be roughly divided into two parts (Johansen et al., 2014):

- Growth from small dust particles to planetesimals. Planetesimals are pre-planetary bodies of 100 m to 1 km, which are held together by self-gravity rather than material strength.
- Growth from planetesimals to planets.

The standard scenario for the initial growth of planetary bodies in a protoplanetary disk is the coagulation model, based upon collision (Testi et al., 2014). Dust particles grow via hit and stick collisions.

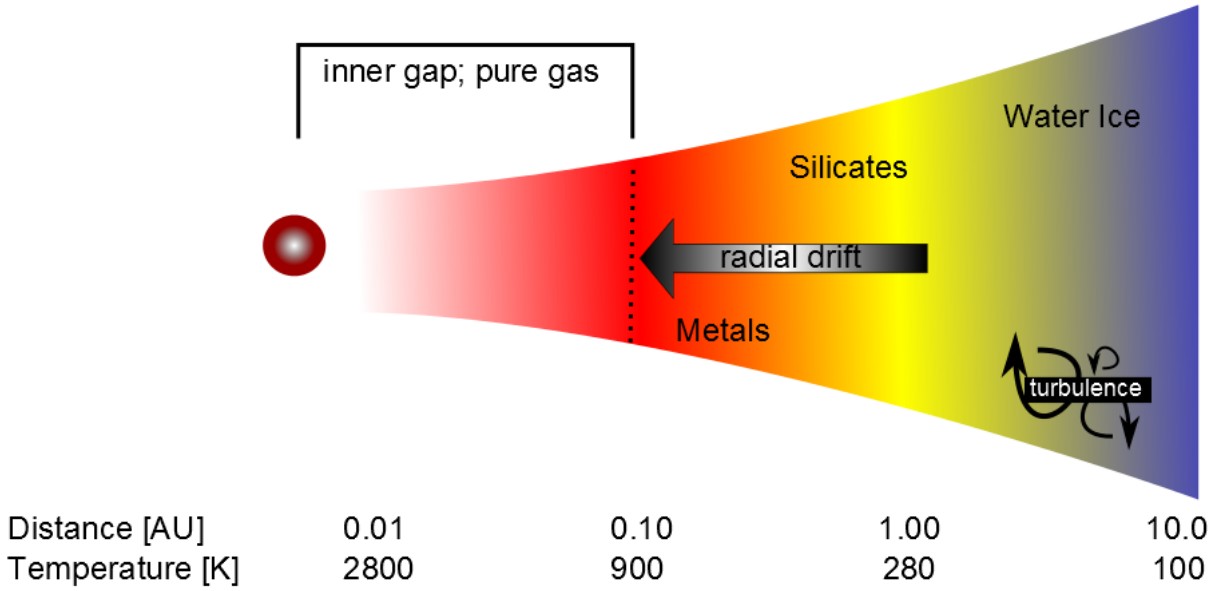

Figure 3.2: Side-view sketch of a protoplanetary disk with a temperature distribution based upon the model of minimum mass solar nebula by Hayashi et al. (1985). From de Beule et al. (2015a).

Some challenges of the coagulation model are the fragmentation barrier (Blum and Wurm, 2008) and the bouncing barrier (Zsom et al., 2011). The latter is based upon experiments showing that the sticking efficiency strongly drops for aggregates with sizes between millimeters and meters (Blum and Wurm, 2008). Attempts to cross this bouncing barrier were undertaken by Windmark et al. (2012) with the introduction of lucky larger particles that sweep-up smaller ones.
This is strongly related to fragmentation and the so–called meter-size barrier: the rapid inward drift of meter-sized bodies in combination with high relative velocities (Weidenschilling, 1977), at which collisions lead only to fragmentation or erosion (Blum and Wurm, 2008), make it generally very challenging to grow planets.
The radial drift of meter-sized bodies itself is another challenge: the typical pressure gradient inside the protoplanetary disk supports the gas against the gravitational force and effectively reduces it, causing the gas of the disk to orbit with slightly sub-keplerian velocity. Small particles (< 1 mm) couple well to the gas and rotate with it, although -

greater bodies do not couple to the gas and rotate with keplerian velocity around the central star (Testi et al., 2014; Weidenschilling, 1977). Hence, they feel the gas and smaller particles as a headwind. The rotation of bodies on the size of planetesimals or planets is not disturbed, although meter-sized bodies slow down and rapidly drift radial inwards. A meter-sized body can drift 1 AU in 100 years (Weidenschilling, 1977; Nakagawa et al., 1986).
One way of preventing the inward drift and reduce relative velocities is through trapping of pebbles inside pressure bumps (Haghighipour and Boss, 2003). Simulations by Johansen et al. (2009) show magneto-rotational instabilities as a source for these pressure bumps. Other possible sources such as turbulence or vortices are listed in Johansen et al. (2014).
This research also leads to an alternative model for planetesimal formation, which is based upon gravitational instability (Goldreich and Ward, 1973; Youdin and Chiang, 2004).

Once planetesimals have formed- by coagulation or self-gravity or a combination of both, gravity starts to dominate the further growth. In the inner disk, the collision of planetesimals leads to the formation of terrestrial planets, which are planets primarily comprising silicates or metals. In the solar system, the terrestrial planets are Mercury, Venus, Earth and Mars.
Further outward beyond the snowline of the disk - which is the line at which water condenses to ice - the planetary bodies comprise hydrogen compounds and rocky material. According to the core accretion model, if they are sufficiently large to gravitationally capture large quantities of the gas in the disk they form giant planets, sometimes called gas giants (Pollack et al., 1996; D'Angelo et al., 2014).
Alternatively, in a massive protoplanetary disk dense and cold regions might collapse and form planets directly (Boss, 2008). In the solar system the giant planets are Jupiter and Saturn.

An interesting aspect of protoplanetary disks is the observation of millimeter- and centimeter-sized grains over the lifetime of a protoplanetary disk (Haisch et al., 2001; Natta et al., 2007). Experiments and theoretical models predict a very efficient process of planet formation thus far, which is in conflict with the observations (Natta et al., 2007). Taking the fragmentation of colliding bodies into account, theoretical models cannot predict every observation of protoplanetary disks (Natta et al., 2007; Testi et al., 2014), whereby there need to be other sources for the replenishment of small dust grains over the lifetime of the disk.

At this point, this work becomes important, as the process of light-induced erosion may efficiently erode porous bodies in protoplanetary disks and provide small particles over a long timescale. This is especially valid in transitional disks, which have an optically thin (dust-free) inner part.

A protoplanetary disk with a gap in some distance to the star is called a pre-transitional disk, whereas a disk with a hole around the star is called a transitional disk (Fig.3.3). (Espaillat et al., 2014). Transitional disks were first identified by Strom et al. (1989), although opinions differ regarding the clearing of such gaps and holes: planets, grain

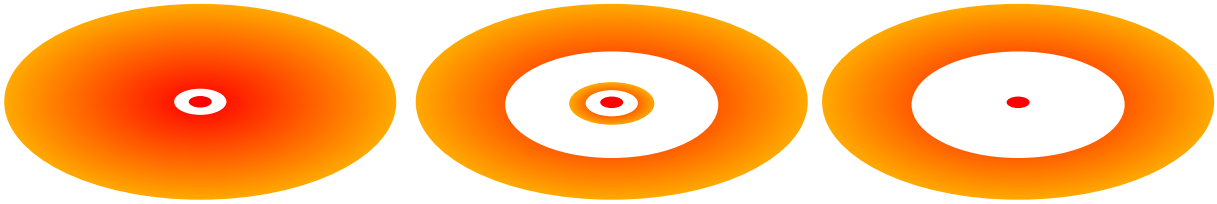

Figure 3.3: Sketch of a full (left), pre-transitional (middle) and transitional disk (right) (Espaillat et al., 2014). The gaps/holes are marked white.

growth and photo-evaporation are discussed (for details, see review in Espaillat et al. (2014)). However, the existence of those transitional disks and their structure is very interesting for the effect of light induced-erosion in this work, because the gap is optically thin, whereby the central star can easily penetrate these holes or gaps. These circumstances of high temperatures and low pressure inside the gaps are sufficient to consider light-induced erosion.
Espaillat et al. (2012) modeled some disk properties of full, pre-transitional and transitional disks around T-Tauri stars. For these examples, the inner wall of a pre-tranistional disk is about 0.1 to 0.3 AU, whereas the outer wall is around 1 to 5 AU; by contrast, the inner wall of full disks is around 0.1 AU and the wall of transitional disks is at 1 to 4 AU. For the inner wall of transitional disks and the outer wall of pre-transitional disks, they also find temperatures between 90 and 240 K.

3.2 Mars

The red planet Mars has been interesting for us since the evolution of mankind. Despite its mean distance of 55.6 million kilometers from Earth, it appears bright and clear on the night sky. Our neighbor planet is similar to Earth (Fig.3.4): it is a terrestrial planet with a thin atmosphere comprising CO_2 and landscape features like mountains, deserts and polar ice caps. The components of the martian atmosphere are listed in Tab.3.1. However, Mars in its present form is hostile to life: the average temperature on Mars

Major (by volume)	Carbon Dioxide (CO_2)	95.32%
	Nitrogen (N_2)	2.7 %
	Argon (Ar)	1.6 %
	Oxygen (O_2)	0.13 %
	Carbon Monoxide (CO)	0.08 %
Minor (ppm)	Water (H_2O)	210
	Nitrogen Oxide (NO)	100
	Neon	2.5

Table 3.1: Components of the martian atmosphere (1 ppm = 1 part per million) (Barlow, 2008).

is about 210 K, although it can drop down to 140 K in the night and can reach 300 K (Kieffer et al., 1992).
Due to its greater distance (1.5 AU) to the sun, the solar constant is only 588 W/m^2 on the surface at mean Mars distance from the sun (Kieffer et al., 1992). Mars is known to have a very low thermal inertia, which means that the martian surface can heat quickly in the sunshine, although the atmosphere is not a good storage for heat (Mellon et al., 2000). Temperature variations on Mars lead to pressure differences and wind.

There have been Mars missions since 1964, when Mariner 4 was launched and flew by Mars in 1965, taking the first closer pictures of the martian surface. Additional Flybys, Orbiter and Lander revealed a closer look to the outstanding landmarks of Mars: indeed, some of them are listed below:

1. Olympis Mons: the largest volcano in the solar system with 25 km height (3 times the Mount Everest) and 600 km width (Kieffer et al., 1992).

2. Valles Marineris: the largest canyon on Mars with a length of 4.000 km, a width of 200 km and a depth up to 7 km. It is around 3.5 billion years old.

3. Borealis Basin: A basin which makes up 40% of the martian surface. A possible origin was a single large impact (Marinova et al., 2008).

The martian atmosphere is much thinner than the atmosphere on Earth. The average atmospheric pressure is 5.6 mbar, although it varies from 14 mbar in valleys down to 1 mbar on mountains like Arsia Mons (Kieffer et al., 1992).
An unanswered question is how dust from the surface can be entrained into the atmosphere: Dust storms are ubiquitously observed on Mars and they can darken the sky for

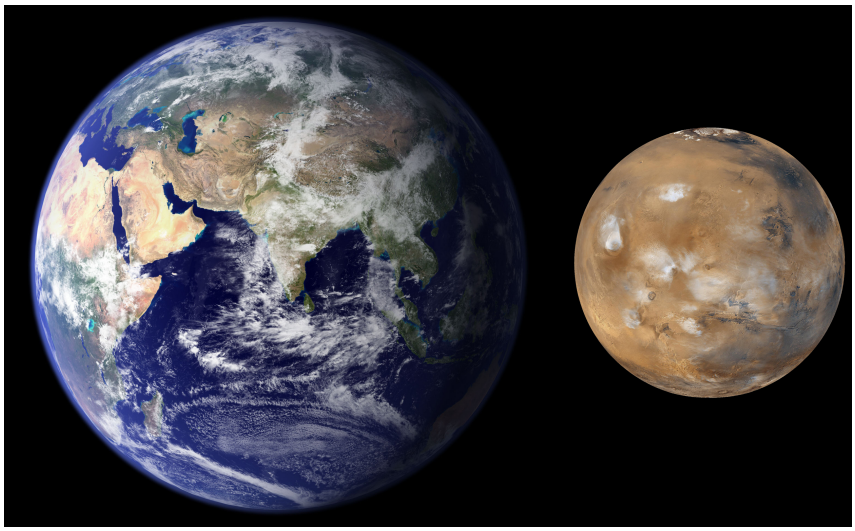

Figure 3.4: Comparison of the appearance and size between Earth and Mars. Image Credit: NASA/JPL/MSSS.

months (Kahn et al., 1992). The size of the dust particles entrained in the atmosphere is a few microns (Pollack et al., 1979; Greeley et al., 1992; Wolff and Clancy, 2003). With the low atmospheric pressure of Mars, wind tunnel experiments have shown that wind speeds of about 30 m/s are necessary to effectively lift dust from the martian surface (Greeley et al., 1992; White et al., 1997), although observed wind speeds are generally 10 m/s and can only extend to 30 m/s in isolated events (Hess et al., 1977; Haberle et al., 1999). In addition, Reiss et al. (2009) observed dust devils on Arsia Mons, where the low atmospheric pressure of 1 mbar requires even larger wind speeds.

Understanding the martian dust cycle holds great interest - as it plays a key role in the current, past and future climate on Mars (Kahn et al., 1992). However, the evolution and occurrence of dust storms is not understood in every detail. Greeley et al. (1992) suggest that it is based upon randomly occurring variations in the atmosphere/dust/polar cap system during earlier seasons.
Wind has different forms of appearance on Mars: dust devils, seasonal large-scale weather patterns and moving dust storms (Kahn et al., 1992). The details about the dynamic in the martian atmosphere is very complex and can be found in Greeley et al. (1992); Kahn et al. (1992). Beside wind stress, out-gassing of the surface, pressure differences within dust devils or meteorite impacts have been suggested as effects of dust lifting (Greeley et al., 1992).

The martian surface is one–quarter of the size of the Earth's surface and about one–fifth of it is covered with a thick mantle of dust (Schorghofer, 2013), providing particles to be entrained in the atmosphere. In addition, rocks and boulders are observed on the martian surface (Fig.3.5, right (Christensen and Moore, 1992)). The Mars Lander Curiosity took a sample of the martian regolith (Fig.3.5, left) at the Gale Crater and analyzed it. They found that the fraction of sand with sizes smaller than 150 μm mainly (55 %) comprise crystalline material (basaltic) and 45 % of amorphous (iron-rich and silicon-

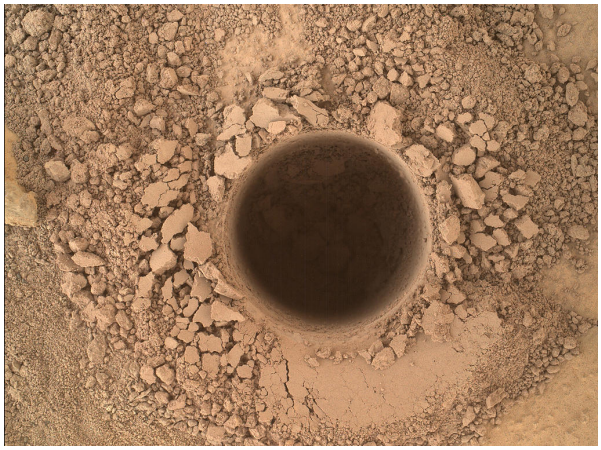

(a) Picture of a hole drilled in Mount Sharp by the NASA's rover Curiosity to collect regolith samples. The hole has a diameter of 1.6 cm. The image was taken by the Mars Hand Lens Imager (MAHLI) camera on Sept. 24, 2014. Image Credit: NASA/JPL-Caltech/MSSS.

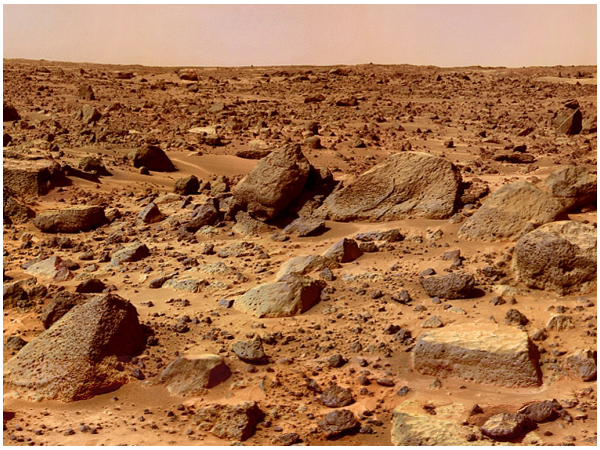

(b) Picture of rocks and boulders on Mars taken by the Mars Pathfinder on July 4, 1997. The composite picture is an overlay of seven frames taken with different color filters and the color balance was chosen to approximate the true color of Mars. Image Credit: NASA/JPL

Figure 3.5: Pictures of the martian regolith taken by Mars Landers.

poor) material (Blake et al., 2013). The amorphous part hosts volatiles such as water, oxygen and carbon dioxide (Blake et al., 2013). In addition, Blake et al. (2013) showed similarities between the soils and aeolian materials to soil analyzed at Meridiani Planum and Gusev Crater, which may imply locally-sourced, globally-similar basaltic materials.
Beneath the martian surface, a large amount of subsurface ice has been detected (e.g. Squyres et al. (1992)). This ice is shielded from sublimation by the layers of martian soil above, as it may also form into liquid by warming. Boynton et al. (2002) found large quantities of hydrogen in the near surface by gamma-ray spectroscopy. They assume that the thickness of the hydrogen layer decreases with the distance to the pole, ranging from 150 g/m^2 to 40 g/m^2, although they cannot state the chemical form in which it is present. However, Yen et al. (2005) detected high concentrations of subsurface salts (via MER spacecraft), which admits the possibility of liquid water redistributing this mineral within the regolith.

Feldman et al. (2008) used observations to constrain the ice distribution in Olympia Undae, a vast dune field within the Borealis basin. They estimate this region as having a two-layer-model, where the bottom layer has about 30 % water and the top layer has a thickness of 6 cm (at an estimated regolith-density of 1.5 g/m^2).
The rate of water vapor transported through the martian regolith determines the timescale of the existence of subsurface ice. The physical processes for ice in the sub-layer of the martian surface are vapor diffusion and deposition (Schorghofer and Forget, 2005). In the present climate of Mars, sub-surface ice exists at latitudes poleward of about 60 degrees (Schorghofer and Forget, 2005) and it may have been placed by precipitation and subsequent burial, whereas the ground ice closer to the surface comes directly from the atmospheric water vapor (Mellon and Jakosky, 1993).

As the transport of atmospheric gas and water vapor through the martian regolith plays an important role in the present and past climate on Mars, this work may benefit the understanding of these observations. A directed gas flow through the porous regolith facilitates the transport of gas and water vapor and is more effective than diffusion.

4

Theoretical background

The interplay of low ambient pressures and (visible) radiation leads to the ejection of particles from a dust bed. The background of this mechanism is based upon forces induced by temperature gradients within the dust bed. This chapter provides a general overview of the temperature distributions and resulting forces within an illuminated dust bed in a low-pressure environment.

4.1 Temperature distribution within an illuminated dust bed

Simulations

Experiments for determining the temperature distribution within a dust bed on the first few hundred micrometers suffer from the imprecision of measuring instruments. However, computer simulations have been undertaken by Kocifaj et al. (2010, 2011) where heat transfer within an illuminated dust layer was investigated. Based upon the properties of a dust bed, incoming radiation is partly reflected, absorbed and transmitted to deeper layers from the surface. In their recent simulations, Kocifaj et al. (2011) consider absorption, heat conduction and thermal radiation within the dust bed. The hypothetical setup is as follows: a dust bed comprising spherical particles with uniform sizes (e.g. 25 μm) is illuminated with 10 kW/m^2 at a wavelength of 680 nm. Temperature data was extracted from 0.05 s up to 3600 s. For the application on Mars, temperature distributions were simulated for a light intensity of 300 W/m^2 and 700 W/m^2 and an illumination time of 12.5 hours (Sec.9.2).
Details of the simulations are treated in Kocifaj et al. (2010, 2011) and Kelling (2012) and will not be elaborately discussed in this work.

Heat can be transported through a porous medium by heat conduction, heat radiation and heat transmission by the surrounding gas. Heat conduction depends on the direct contact of the particles, while heat radiation depends on the holes between the particles and heat transmission depends on the surrounding gas. The heat conduction of a porous medium is connected to the thermal conductivity, whereby the heat flux $\dot{q}$ is given by

$$\dot{q} = -\kappa \nabla T \tag{4.1}$$

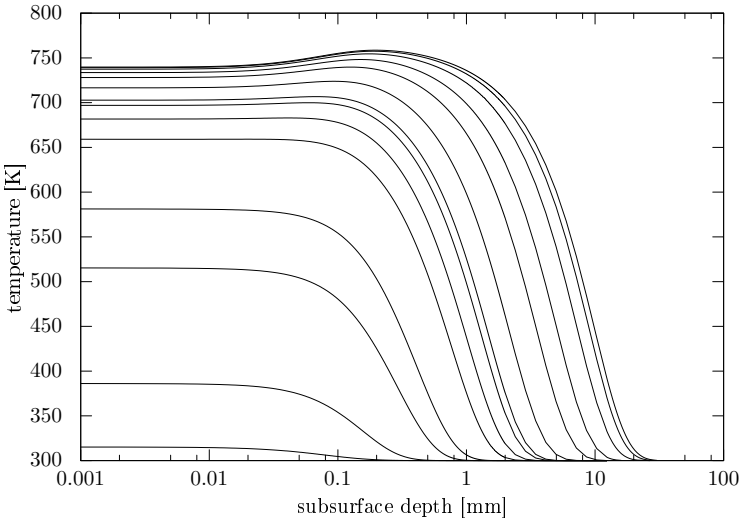

Figure 4.1: Temperature distribution within an illuminated dust bed. The illumination times are 0.1, 1, 5, 10, 30, 50, 80, 100, 200, 500, 1000, 2000, 3000, 3600 s from bottom to top. The dust bed comprises 25 μm spheres and is illuminated by 13 kW/m^2. The thermal conductivity is $\kappa = 0.01$ W/(Km). The evolution of a solid state greenhouse effect is shown in Fig.4.4.

with the heat conduction $\kappa = \kappa(p, T)$ depending on the temperature and the pressure and the temperature gradient ∇T (Meschede, 2015). Thermal conductivity is a material constant and describes how effective heat is transported through a medium. For example, metals are good heat conductors ($\kappa = 390$ W/(Km) for Copper at 330 K) and gas is a very poor heat conductor ($\kappa = 0.031$ W/(Km) for air at 273 K) (Meschede, 2015).

The thermal conductivity of a dust bed is based upon many different parameters like composition, bulk density, pressure and temperature. The bulk density is defined as the mass of the particles divided by the volume that they occupy (including holes).
Measurements for the thermal conductivity of crushed basalt (37 - 62 μm) depending on the bulk density and temperature were performed by Fountain and West (1970) in a vacuum. Their results show that the thermal conductivity of the basaltic grains increases

Table 4.1: Thermal conductivity of basaltic grains (44-104 μm) at different pressures (Presley and Christensen, 1997).

pressure [mbar]	thermal conductivity [W/(Km)]
0.013 ... 0.13	10^{-2}
1.3	$5 \cdot 10^{-2}$
13 ... 133	10^{-1}

by a factor of 3 (from $1 \cdot 10^{-4}$ W/(Km) to $3 \cdot 10^{-4}$ W/(Km)) when the bulk density differs from 800 kg/m^3 to 1500 kg/m^3. Even more interesting is the strong dependence on the pressure measured by (Presley and Christensen, 1997) shown in Tab.4.1.

Krause et al. (2011) found thermal conductivities between 0.002 to 0.02 W/(Km) for 1.5 μm sized, spherical SiO_2 particles.

Kocifaj et al. (2010, 2011) showed that the temperature distribution within an illuminated dust bed depends on the actual thermal conductivity of the granular matter. The simulations were run for three different thermal conductivities: 0.1, 0.01 and 0.001 W/(Km). Given that most of the experiments in this work were performed at an ambient pressure between 0.1 and 6 mbar, the temperature distribution of a dust bed with 0.01 W/(Km) is prominently considered. An exemplary result of the calculations by Kocifaj et al. (2010, 2011) is shown in Fig.4.1.

The distribution shows the development of temperature within a dust bed with 25 μm sized grains with time. A striking feature of this distribution is that after an illumination time of 40 s, a maximum of temperature establishes within the dust bed and not at the surface (Fig.4.4).
This phenomenon is known to be the solid–state greenhouse effect as described in the upcoming subsection. It is necessary to repeat again that these simulations were conducted for a light intensity of 13 kW/m^2. Recent computations were performed with lower light flux and show that the solid–state greenhouse effect only becomes visible for long illumination times (with 4 kW/m^2 it takes 200 s).

Further simulations were conducted for lower light fluxes, as the solar constant is lower on Mars than on Earth (Sec.3.2). Fig.4.2 in Sec.9.2 shows the temperature distribution within a dust bed illuminated at 700 W/m^2 with the minimum temperature reduced to 200 K for the application on Mars, as the average temperature on Mars is lower than on Earth. As a martian day is about 12.5 h long, the illumination times are extended to 12.5 h in Sec.9.2 (Fig.9.3).
A temperature difference within the dust bed establishes starting a few 100 μm below the surface and reaching down to a few 10 mm below the surface. It is interesting how this temperature difference within the dust bed (without solid-state greenhouse effect) develops over time.
Fig.4.3 shows the development of the temperature differences within an illuminated dust bed. At low intensities and short time scales the temperature difference ΔT is proportional to the incoming light flux.

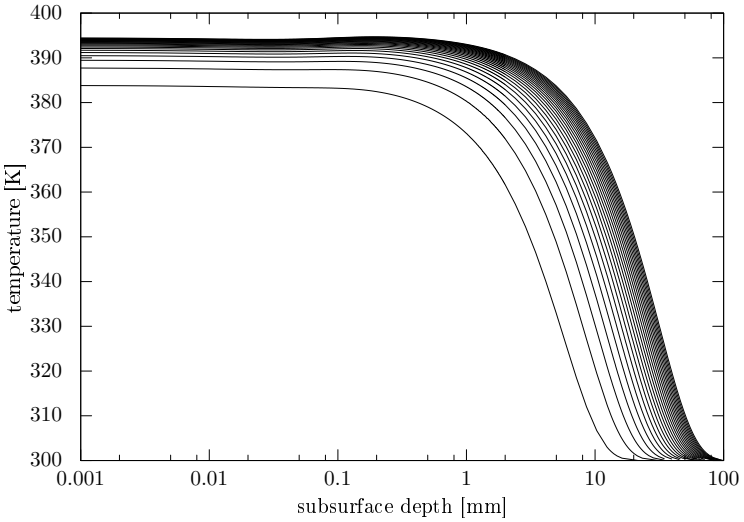

Figure 4.2: Temperature distribution within an illuminated dust bed. The illumination times are 0.1, 1, 5, 10, 30, 50, 80, 100, 200, 500, 1000, 2000, 3000, 3600 s from bottom to top. The dust bed comprises 25 μm spheres and is illuminated by 700 W/m^2. The thermal conductivity is $\kappa = 0.01$ W/(Km). A small solid state greenhouse effect becomes visible after long illumination times.

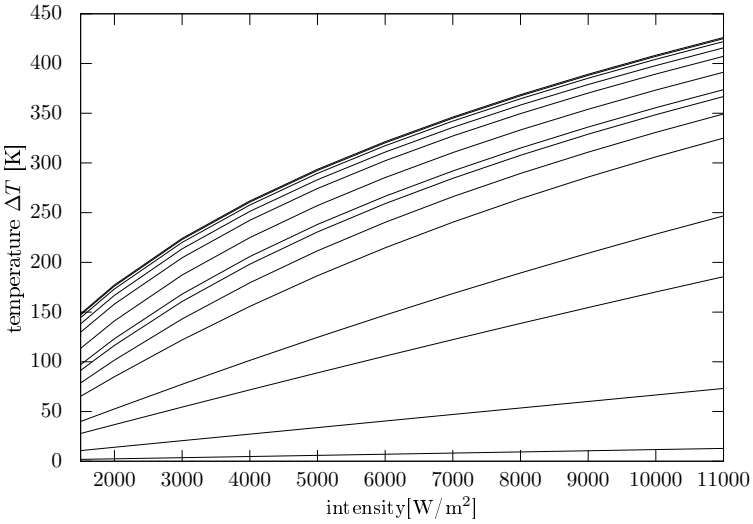

Figure 4.3: Simulation of temperature differences within an illuminated dust bed. The illumination times are 0.1, 1, 5, 10, 30, 50, 80, 100, 200, 500, 1000, 2000, 3000, 3600 s from bottom to top. At low intensities and short time scales the temperature difference ΔT is proportional to the incoming light flux. The simulations were conducted for 25 μm spherical particles with $\kappa = 0.01$ W/(Km) (Kocifaj et al., 2011).

Solid-state greenhouse effect

When visible light enters a porous body, it is absorbed either directly at the surface or inside the body (over a large distance or at dark embedded particles (Brown and Matson, 1987)). The latter is known to be the solid-state greenhouse effect (Fig.4.4 and 4.5), first experimentally affirmed by Niederdorfer (1933), who measured the temperature of insolated snow at the surface and down to a depth of 20 cm for several hours. Niederdorfer (1933) found that the snow cover established a maximum of temperature about 1 cm below the surface.

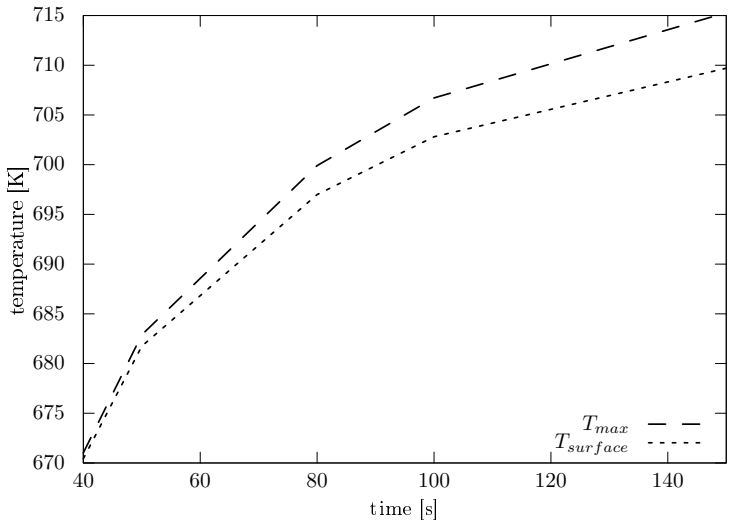

Figure 4.4: Simulation: Evolution of a solid-state greenhouse effect within the dust bed with time. The dashed line shows the temperature of the maximum within a sublayer and the dotted line shows the temperature of the surface of the dust bed. The temperatures are extracted from Fig.4.1.

This effect is similar to the greenhouse effect on Earth, where sunlight passes the atmosphere to the planetary surface, which in return emits infrared thermal radiation. However, greenhouse gases in the atmosphere absorb the thermal infrared and re-radiate a part of it back to the surface, whereby long-wavelength radiation is trapped between the surface and the atmosphere (Fourier, 1824).

In case of snow, the visible light enters the matter but cannot escape the same way, though its surface can cool by thermal radiation. Brown and Matson (1987) were the first to identify the effect of a temperature maximum at the sub-surface as the *solid-state greenhouse effect*. They showed that this phenomenon is applicable for every surface comprising particles that are optically thin in the visual and opaque in the thermal infrared. They assumed that a porous regolith can develop a higher temperature at the subsurface than at the surface due to insolation (Matson and Brown, 1989).

Kaufmann et al. (2006) performed laboratory experiments with samples mainly comprising optically transparent medi, namely glass beads and water-ice. Their measurements

revealed that a maximum of temperature is attained below the surface in case of a radiation source matching the spectrum of the Sun. In addition, they showed that the solid state greenhouse effect works at atmospheric pressure as well as under vacuum conditions. In case of the glass beads, it depends on its size.

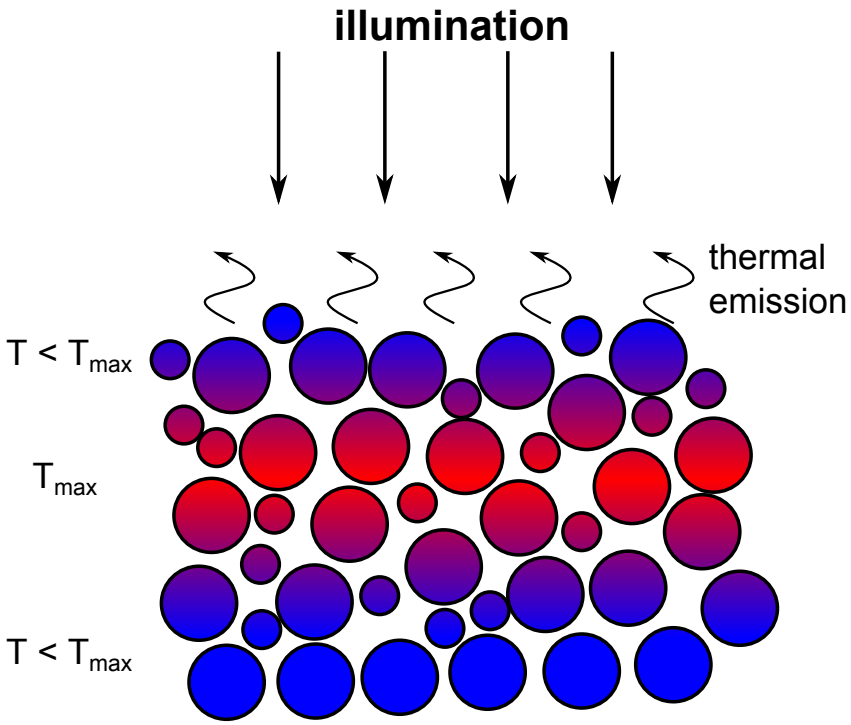

Figure 4.5: Schematic of the solid-state greenhouse effect: Incoming radiation is absorbed at some deeper layer of the sample (for example a dust bed), where the surface can cool by thermal emission. Hence, a maximum of temperature T_{max} is established below the surface.

4.2 Gas flow

A helpful parameter for the characterization of a rarefied gas flow is given by the Knudsen number Kn

$$Kn = \frac{\lambda}{L}, \tag{4.2}$$

where L is the representative length scale (e.g. the pore or grain size) and λ is the mean free path of the gas molecules

$$\lambda = \frac{k_B T}{\sqrt{2}\sigma p}, \tag{4.3}$$

with the Boltzmann-constant $k_B = 1.38 \cdot 10^{-23}$ J/K, the gas temperature T, the pressure p and the diameter of the gas molecules σ.
Based upon the Knudsen number Kn, the gas flow regime comprises three sub-regimes (Tab.4.2). For $Kn \ll 1$, the continuum flow model is used and the gas can be described by macroscopic variables like velocity and temperature. In the transition flow regime $Kn \approx 1$, the mean free path of the gas molecules is in the order of the scale length and the molecules react as frequently with the solid surface as they do with each other. When the pressure is further reduced, whereby the mean free path increases, the interaction of gas molecules with the walls dominates the processes in the free-molecule regime $Kn \gg 1$.

Table 4.2: Different flow regimes based upon the Knudsen number (Eq.4.2).

flow regimes	
continuum flow	$Kn \ll 1$
transition flow	$Kn \approx 1$
free-molecule flow	$Kn \gg 1$

Darcy's law

The flow of gas through a porous medium can be described by the Navier-Stokes equation with the conservation of momentum (Batchelor, 1865)

$$\rho \frac{Dv}{Dt} = -\nabla p + \nabla \tau + f, \tag{4.4}$$

where v is the flow velocity, ρ is the fluid density, p is the pressure, τ is the deviatoric total stress tensor and f represents the body forces acting on the fluid. In the case of gas flowing through a porous body, it is an incompressible (constant ρ) and isotropic Newtonian fluid (e.g. no accelerations due to convection), which means that the left-hand side is approximated to

$$\rho \frac{Dv}{Dt} \approx 0. \tag{4.5}$$

It only becomes important for high Reynold numbers (Reynolds, 1883); for example, at high velocity, high permeability or low viscosity. The Reynolds number is (Reynolds, 1883)

$$Re = \frac{\rho v L}{\eta}, \tag{4.6}$$

with the gas density ρ, the velocity v, the characteristic length L and the viscosity η. Without an external body force (f is considered zero), we obtain

$$0 \approx -\nabla p + \nabla \tau \tag{4.7}$$

Now, some additional assumptions are made: the length of the pores is large compared to its diameter and the stress tensor τ can be approximated by a function of the pore diameter, or more precisely by the viscosity η divided by the permeability κ. The residual Navier-Stokes equation is thus

$$0 \approx -\frac{\eta v}{\kappa} - \nabla p. \tag{4.8}$$

Solving this equation for the fluid velocity, we obtain Darcy's Law (Darcy, 1856)

$$v \approx -\frac{\kappa}{\eta} \cdot \nabla p, \tag{4.9}$$

where the fluid velocity is proportional to the pressure difference. The important application for this thesis is that a pressure difference induces a gas flow.
For example, a porous dust bed with grain sizes of about 100 micrometer and a depth of centimeters is set in a low-pressure environment of a few millibars of air. The Reynolds number is given by Eq.4.6. The gas density is calculated by

$$\rho_L = \frac{p}{R_S T}. \tag{4.10}$$

For dry air, the specific gas constant is $R_S = 287$ J/kg K and we assume a pressure of $p = 1$ mbar and a temperature of $T = 273$ K. This leads to a gas density of $\rho_L \approx 10^{-3}$ kg/m^3. The characteristic length of the dust bed is $L = 100$ μm and the dynamic viscosity of air is $\eta \approx 10^{-5}$ N/(m^{2}s). Assuming a fluid velocity of $v = 1$ cm/s, we obtain a Reynolds number (Eq.4.6) of about $Re = 0.001$, which satisfies Eq.4.5. We conclude, that at low pressures, the gas velocity through a porous body with grain (and pore) sizes in the micrometer range, can extend up to km/s before it breaks the validity of Darcy's Law.
A pressure difference between the top and the bottom of the mentioned dust bed would increase a gas flow through the porous body (Eq.4.9). With the permeability of porous dust $\kappa = 10^{-12}$ m^2 (measured, Sec.6.1), the dynamic viscosity of air $\eta \approx 10^{-5}$ N/m^{2}s [1] and a pressure difference of $\Delta p = 0.5$ mbar over a depth of 1 cm, this equation results in a gas velocity of about 1 mm/s through the dust bed. In the context of this work, gas velocities through a dust bed were measured in the order of mm/s and cm/s.

[1] Sutherland (1893) approximated the temperature dependence of the viscosity of gases. The repulsive forces between the molecules is described by a very simplified spherical-symmetrical potential $V(r) \propto -r^{-6}$ with the distance r between the molecules. The Sutherland equation is then (Sutherland, 1893) $\eta(T) = \eta_0 \frac{T_0+C}{T+C} \left(\frac{T}{T_0}\right)^{3/2}$ with the dynamic viscosity μ at temperature T, the reference temperature T_0 and the Sutherland constant C. Although it is a very simplified approximation, the error in the comparison to real viscosities is only about 10%.

Knudsen compressor

The effect of thermal creep was introduced by Maxwell (1879), Reynolds (1879) and Knudsen (1909): two gas reservoirs with different temperatures are connected by a channel, whose diameter d is small compared to the mean free path λ of the gas molecules. The pressure in the warmer reservoir will increase until a steady state is reached. The relation between pressure and temperature is described by Knudsen (1909) as

$$\frac{p_2}{p_1} = \sqrt{\frac{T_2}{T_1}}, \tag{4.11}$$

with pressure p_1, p_2 and temperature T_1, T_2 in the cold and in the warm chamber, respectively (see Fig.4.6).
The basic effect is that gas molecules creep along the walls of the channel towards the warmer direction. The gas molecules inside the channel interact more with the channel walls than with each other (because $\lambda \gg d$). The interaction with the wall is diffusive and molecules coming from the warm side have a larger momentum than those coming from the cold side. The molecules interact with the wall and leave it with the wall's temperature, which is called accommodation (Rohatschek, 1995). Therefore, the wall experiences a momentum transfer towards the cold side and due to conservation of momentum the gas will move in the direction of the warm chamber (Fig.4.6).

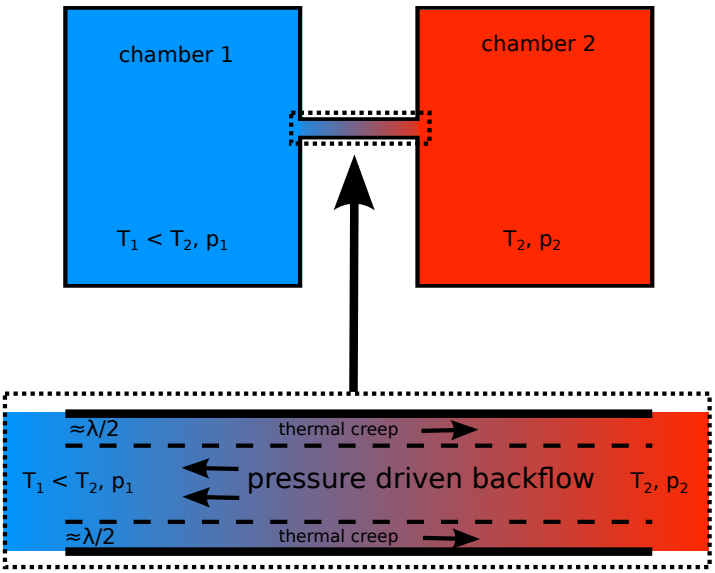

Figure 4.6: Schematic of the Knudsen compressor: two chambers with different temperatures are connected by a small tube. Thermal creep leads to a gas flow from the colder into the warm chamber, whereas the pressure-driven back-flow outbalances this creep as long as the diameter of the tube is larger than the mean free path of the gas molecules λ. Shrinking the diameter to a size comparable to λ, the thermal creep predominates the gas flow within the tube and the pressure in the warmer chamber will increase.

In a simple example described by (Knudsen, 1909) (and later by (Han, 2006)), two chambers are connected by a small aperture: one with high temperature and one with low temperature. In a low-pressure environment the number of particles crossing the aperture in a steady state is equal for both sides:

$$n_{\text{in}} \cdot v_{\text{in}} = n_{\text{out}} \cdot v_{\text{out}}, \tag{4.12}$$

with the thermal velocities v and the number of particles n. The thermal velocity v is given by Eq.4.17. The number of particles n is approximated by the model of an ideal gas $pV = nRT$ with the pressure p, the volume V and the gas constant R. Balancing both flows (steady state, no net flow), we obtain Eq.4.11.
Knudsen (1909) increased the pressure in the warm chamber by using a series of chambers and discovered a relation of $p_n/p_1 = 10$, which is nowadays known as the *Knudsen compressor*.
It took some decades before this effect became more prominent for the application in vacuum physics (Vargo and Muntz, 1999), where it is used for micro- and macro-scale vacuum pumps without moving parts or fluids. Muntz et al. (2002) showed that the ratio of pressure difference $\Delta p = |p_1 - p_2|$ to average pressure $p_{avg} = (p_1 + p_2)/2$ can be written as

$$\frac{\Delta p}{p_{avg}} = \frac{\Delta T}{T_{avg}} \frac{Q_T}{Q_P}, \tag{4.13}$$

where $\Delta T = |T_1 - T_2|$ is the temperature difference and T_{avg} is the average temperature. The coefficients Q_P and Q_T are functions depending on the Knudsen number and the dimension of the capillary and Q_T/Q_P is the ratio between the thermal creep flow and the pressure-driven back flow ((Muntz et al., 2002), Fig.4.7).
An example is a porous plate in a low-pressure environment with a temperature gradient between the top and bottom, which acts a gas pump, transferring gas from the one side to the other (Küpper et al., 2014). Expanding this idea to a porous dust bed, the pores of the dust bed can also work as capillaries and pump gas. At high temperature differences, the pumping is efficient enough to hover dust agglomerates against gravity (Kelling and Wurm, 2009).

Mass flow

The previous sub-section showed the case of the Knudsen compressor in steady state, without an active gas flow. In non-equilibrium, two gas flows develop within a channel with a temperature gradient (Sone and Itakura, 1990; Muntz et al., 2002): one is thermally-driven, leading to a flow from cold to warm along the channel walls, whereas the other one is a pressure-driven back flow (Poiseuille flow), due to the overpressure in the warm chamber. Both flows are combined in one net mass flow by Sone and Itakura (1990); Muntz et al. (2002)

$$\dot{M} = p_{avg} \frac{A}{\sqrt{2\frac{k_B}{\mu} T_{avg}}} \times \left(\frac{L_r}{L_x} \frac{\Delta T}{T_{avg}} Q_T - \frac{L_r}{L_x} \frac{\Delta p}{p_{avg}} Q_p \right), \tag{4.14}$$

with the average pressure p_{avg}, the average temperature T_{avg}, the Boltzmann-constant k_B, the molecular mass of the gas μ, the cross section A of the channel. L_r and L_x are the radius and length of the capillaries and ΔT and Δp are the temperature and pressure differences within the dust bed, respectively. The coefficients Q_P and Q_T depend on the Knudsen number and describe the pressure-driven (back) flow and the flow by thermal creep. Fig.4.7 shows the dependence of the Knudsen Coefficients Q_P and Q_T based on

Table 4.3: Extract of the values for the coefficients Q_P and Q_T based upon the Knudsen number for cylindrical tubes (Sone and Itakura, 1990; Muntz et al., 2002)

Kn	Q_T	Q_P
1128.4	0.7467	1.4996
112.84	0.7179	1.4764
56.419	0.696	1.4604
45.42	0.6867	1.454
33.85	0.6729	1.4449
28.21	0.663	1.4387
22.568	0.6495	1.4306
11.284	0.5975	1.404
5.642	0.5294	1.3187
2.257	0.4171	1.3867
1.128	0.3217	1.4584
0.5642	0.2272	1.6577
0.2257	0.1222	2.3482
0.1128	0.0686	3.5636
0.0846	0.053	4.386
0.0564	0.0363	6.0403

Tab.4.3. Q_T increases with higher Knudsen numbers, whereas Q_P is anti-proportional to the Knudsen number. Assuming a constant channel diameter, the Knudsen number is only based upon the mean free path (Eq.4.2). Hence, in the continuum flow regime the gas flow in the channel with a temperature gradient is dominated by the interaction of the gas molecules. In the transition flow regime, both, the thermal transpiration and the

Poiseuille flow occur because the gas molecules react as much with the wall of the channel as between each other. For high Knudsen numbers in the free-molecule flow regime, the gas molecules do not interact with each other, instead they interact more often with the channel walls, experiencing the temperature gradient and leading to a thermally-driven gas flow form cold to warm.

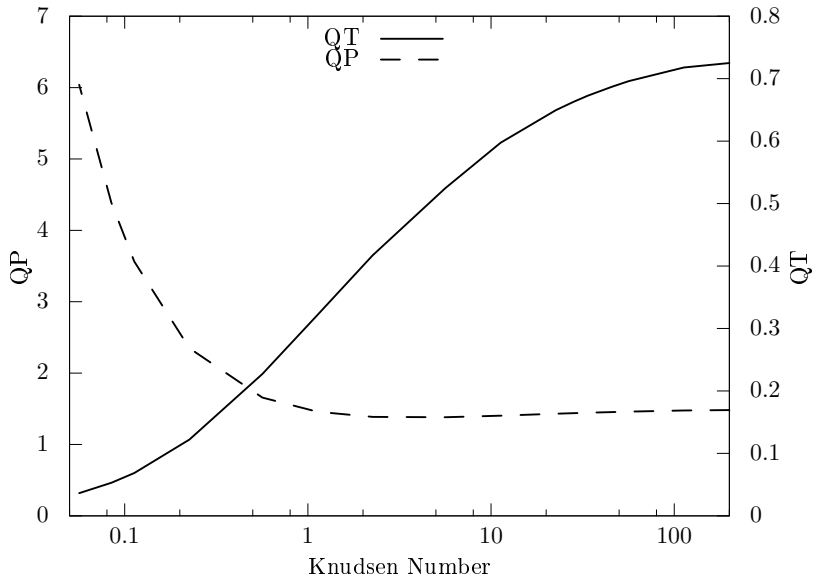

Figure 4.7: Interpolation of the Knudsen Coefficients Q_P (dashed) and Q_T (solid) (Tab.4.3).

Gas drag

Particles moving in a gas experience a drag force in the opposite direction to their relative velocity $\vec{v}_{\text{relative}} = \vec{v}_{\text{gas}} - \vec{v}_{\text{particle}}$. For a small particle in a rarefied gas (Kn $\gg 1$), this force is given by

$$F_{\text{D}} = \frac{m}{\tau_f} v_{\text{relative}}, \tag{4.15}$$

with the relative gas velocity v_{relative}, the particle mass m and the gas-grain friction time τ_f. In the Epstein gas drag regime (Epstein, 1923) (free molecular flow, $Kn \gg 1$), the gas-grain friction time is given by (Blum et al., 1996)

$$\tau_f = \epsilon \frac{m}{\sigma} \frac{1}{\rho_g v_{\text{th}}}, \tag{4.16}$$

with an empirical factor $\epsilon = 0.68$, the geometrical cross section of the particle σ, the gas density ρ_g and the mean thermal velocity of the gas molecules v_{th}. This equation is valid for single grains and dust aggregates.
The drag force decreases with particle size, whereby small particles couple better to the gas than larger particles. The thermal velocity is given by

$$v_{\text{th}} = \sqrt{\frac{8 k_B T}{\pi m_g}}, \tag{4.17}$$

with the Boltzmann constant k_B, the temperature T and the mass of one gas particle m_g.

4.3 Photophoresis

At the beginning of the 19th century, Ehrenhaft (1918) observed the motion of illuminated, suspended particles in a rarefied gas. He measured a change in the direction of motion when the particles enter and leave the light. He termed the motion of those particles within the light as *photophoresis*.
This effect is based upom either a temperature gradient over the particles surface or different accommodation coefficients $\Delta\alpha$ (Preining, 1966; Rohatschek, 1995). An illustration of both effects is shown in Fig.4.8.
In case of the ΔT photophoresis, a suspended particle in a gas has a temperature variation over its surface during direct illumination. The source of motion of the particle depends on the Knudsen number (Sec.4.2).

In the free-molecular flow regime ($Kn \gg 1$, Tab.4.2), the gas molecules accommodating the warm side of the particle leave it with a higher momentum than the particles accommodating the cold side. In the continuum regime ($Kn \ll 1$, Tab.4.2), the gas molecules creep along the particles surface from cold to warm. In both cases, there will be a net force acting on the particle and accelerating it in the direction of the cold surface. If the surface of the particle facing the light source is warmer than the surface parts averting, the particle motion away from the light source is called *positive photophoresis*. If the particle's surface facing the light source is colder, the particle will move towards the light source and it is called *negative photophoresis*. For example, the latter is possible for particles comprising different materials with different thermal conductivities.

The $\Delta\alpha$ photophoresis can be measured for particles with different accommodation coefficients over their surfaces. The accommodation coefficient is a value reflecting the ability of temperature exchange between the gas molecules and the particle.
In a simple model a spherical particle has two different accommodation coefficients on its hemispheres, whereby the hemisphere with the higher accommodation coefficient will have more contact with the gas molecules (if the surrounding gas is cooler than the particle) than the other hemisphere. Gas molecules accommodating the side of the particle with a higher accommodation coefficient will leave it with the particles surface temperature. Hence, this particle will experience a force based upon the combination of different accommodation coefficients and the temperature difference between gas and particle.

As temperature gradients within an illuminated dust bed in a rarefied gas play an important role in the context of this work, only ΔT photophoresis is considered. The approximation for the photophoretic force by Rohatschek (1995) was recently complemented by a solution in the free-molecule flow regime ($Kn \gg 1$) from Lösche (2015). The interpolation for the continuum regime is given by

$$\frac{F}{F_{\max}} = \frac{2+\delta}{\frac{p}{p_{\max}} + \delta + \frac{p_{\max}}{p}}, \tag{4.18}$$

with the maximal photohpretic force $F_{\max}$ given at pressure $p_{\max}$. p and T are average pressure and temperature and δ is a free parameter introduced by Rohatschek (1995).

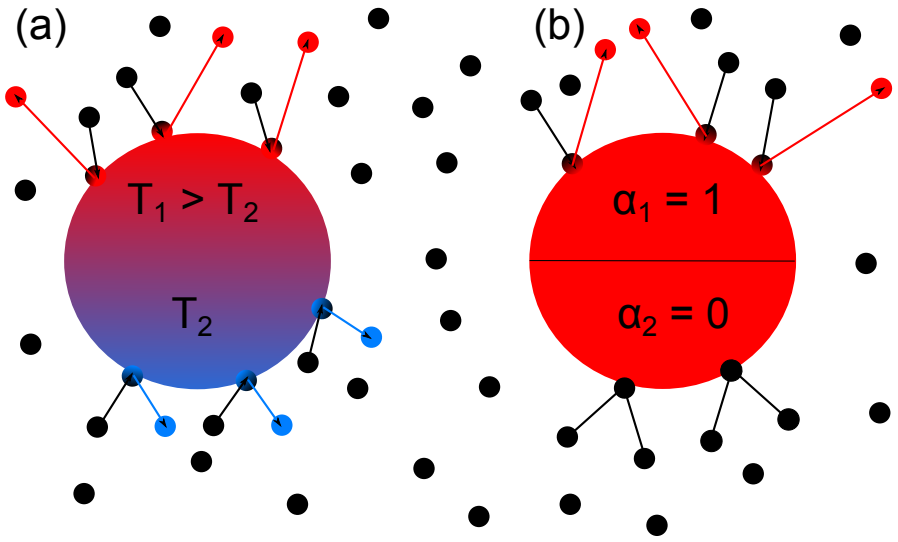

Figure 4.8: Schematic of the two photophoresis types: ΔT and $\Delta\alpha$ photophoresis on suspended particles in the free-molecular flow regime (Kn $\gg$ 1). (a) On the left side, the particle has a temperature gradient over its surface and the gas molecules accommodating the warm side of the particle leave it with a higher momentum than particles accommodating the cold side. The resulting force accelerates the particle in direction of the cold side. (b) The particle on the right side is divided into two hemispheres with different accommodation coefficients. More particles accommodate the particles hemisphere with the higher accommodation coefficient than the hemisphere with the lower coefficient. The resulting force is based upon the temperature difference between particle and gas molecules.

4.4 Thermophoresis

Ludwig (1856) found that a temperature gradient within a liquid mixture leads to a concentration gradient. This effect was later investigated by Soret (1880) in further detail. Therefore, it is known by different names, e.g. the *Soret effect*, *Ludwig-Soret effect* or *thermodiffusion*. The term *Soret effect* is most commonly used with liquid mixtures.

The related effect of particle movement within a gas with a temperature gradient is called *thermophoresis* and was first observed by Tyndall (1870), where particle-free regions around a heated wire form in dusty air. Rayleigh (1882) and Lodge and Clark (1884) additionally investigated this effect, although the experiments by Aitken (1884) were the first to discover that the dust particles close to the heated wire experience a force by the different momentum of the surrounding gas molecules.

The gas molecules coming from the hot wire transport a higher momentum to the suspended particle than the gas molecules coming from the cold, as shown in Fig.4.9. Hence, a thermophoretic net force acts on the particle and accelerates it towards the cold side. In free-molecular flow ($Kn \gg 1$, Tab.4.2), the gas accommodating from the cold side has a smaller momentum than the gas accommodating from the warm side. In the continuum flow ($Kn \gg 1$, Tab.4.2), the gas moves from cold to warm along the surface of the particle, accelerating it towards the cold gas.

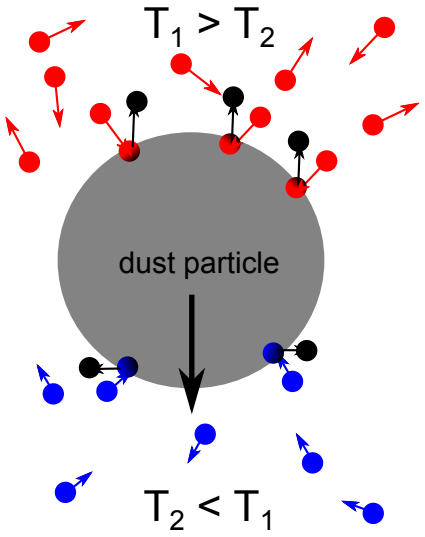

Figure 4.9: Schematic of thermophoresis: A suspended particle within a gas with a temperature gradient experiences a net force in direction of the cold gas.

The thermophoretic force on a spherical particle is given by (Zheng, 2002)

$$F_{th} = f_{th} \frac{r^2 \kappa_g}{\sqrt{2 k_B T_0 / m}} \nabla T, \tag{4.19}$$

where r is the radius of the suspended particle, κ_g is the thermal conductivity of the gas, k_B is the Boltzmann-constant, m the molecular mass of the gas, T_0 is the temperature of

the gas far away from the particle and ∇T is the temperature gradient within the gas. f_{th} is a dimension-less thermophoretic force and it defines the limits of the thermophoretic force in different Knudsen regimes. For the continuum flow regime ($Kn \ll 1$, Tab.4.2) Waldman (1959) found the dimension-less thermophoretic force to be

$$f_{th} = \frac{16\sqrt{\pi}}{15}. \tag{4.20}$$

Within the transition flow regime $Kn \approx 1$ (Tab.4.2), Brock (1962) derived

$$f_{th} = \frac{24\pi}{5} \frac{C_{tc} Kn(\kappa_r + C_t Kn)}{(1 + 3C_m Kn)(1 + 2\kappa_r + 2C_t Kn)}, \tag{4.21}$$

with the ratio of the gas to the particle thermal conductivities κ_r, the velocity slip coefficient C_m, the temperature jump coefficient C_t and the thermal creep coefficient C_{tc}. Details of these parameters can be found in Brock (1962). Within the free-molecule flow regime ($Kn \gg 1$, Tab.4.2), Yamamoto and Ishihara (1988) found

$$f_{th} = \frac{16\pi}{5} \left[A_W H_O - A_O \left(H_W + \frac{5\sqrt{\pi}}{4} \frac{Kn}{\kappa_r} \right) \right] \left(H_W + \frac{5\sqrt{\pi}}{4} \frac{Kn}{\kappa_r} \right)^{-1}, \tag{4.22}$$

with the functions A_W, A_0, H_W depending on the Knudsen numbers. A detailed list of all parameters is found in Zheng (2002).

4.5 Cohesion and tensile strength

In general, cohesion describes the attraction of the same molecules within a substance, whereas adhesion is the attraction shared between dissimilar molecules (Zimon, 1969). In the context of this work, the term cohesion is used for the attraction between dust particles and is not distinguished from adhesion.
Cohesion becomes important when particle surfaces approach into the range of molecular forces (Hinrichsen and Wolf, 2006). Hertz (1881) derived a model for the contact forces of non-cohesive particles. This model was revised by Johnson et al. (1971) (JKR) who included cohesive forces in the contact regions. According to this JKR model, the force necessary to break the contact between two smooth, elastic, spherical bodies is given by

$$F = 3\pi R_{\text{eff}}\gamma, \tag{4.23}$$

with the effective surface energy γ (with $\gamma > 0$), which quantifies the energy needed to create new surfaces. R_{eff} is the reduced radius of the two surfaces $R_{\text{eff}} = R_1 R_2/(R_1 + R_2)$ with the particle radii R_1 and R_2.
Another model was derived by Derjaguin et al. (1975) (DMT), taking non-contact forces into account. The force to separate two particles in the DMT model is given by

$$F = 4\pi R_{\text{eff}}\gamma. \tag{4.24}$$

Later studies showed that the DMT and JKR models are extreme cases of a more general model: the JKR model is favored for large and soft particles, whereas the DMT model is applicable for small, hard particles (Johnson and Greenwood, 1997).
Heim et al. (1999) measured the pull-off forces for spherical SiO_2 particles with a radius between 0.5 and 2.5 μm to $F \approx 100$ nN. They calculated the surface energy with the JKR model as $\gamma_{\text{JKR}} \approx 0.0186$ J/m^2 and with the DMT model as $\gamma_{\text{DTM}} \approx 0.0140$ J/m^2.
Tensile strength is the maximum of tensile stress that a material can take before breaking or tearing. In the context of this work, tensile strength is the maximum of stress applied to a dust bed before it breaks.
Blum et al. (2006) measured the tensile strength of a cylindrical, slightly compressed dust bed comprising micron-sized SiO_2 particles by applying a tensile stress on the bottom and top of the cylinder until failure. The measured tensile strength is in the order of a few hundred Pa.
In a more recent study, Blum et al. (2014) measured the tensile strength of millimeter-sized SiO_2 dust agglomerates (comprising micron-sized particles) by applying a gas flow through the sample, which causes a constant pressure gradient within the dust bed (Darcy, 1856). This pressure gradient was slowly increased until the sample broke. The resulting tensile strength for the millimeter-sized aggregates was measured at about 1 Pa.

4.6 Natural convection

Natural convection occurs in a gas when a temperature gradient leads to a pressure difference. The gas directly above a heated plate becomes less dense, whereas the gas away from the plate remains at its present density. Due to this pressure difference, gas starts to flow up away from the hot plate and is replaced by cooler gas from the surroundings, which

consequently heats up again and rises. As the process continues, a so-called convection roll establishes based upon the dimensions of the surrounding chamber. The driving force of natural convection is a buoyancy force and gravity is essential.
The value of the Rayleigh number R_a defines the onset of convection. It is given by

$$R_a = \frac{\Delta\rho g L^3}{D\mu} \tag{4.25}$$

with the gas density difference $\Delta\rho$, the gravitational acceleration g, the characteristic length scale L, the diffusivity D and the dynamic viscosity μ. Natural convection occurs more likely, when the absolute density difference within the gas becomes greater. Consequently natural convection vanishes to low ambient pressures when a high density difference cannot be reached by temperature gradients.

4.7 Gravity

Gravity is one of the fundamental forces and it describes the attraction of bodies. The gravitational attraction of two bodies with masses m_1 and m_2 at a distance r_d can be (non-relativistic) calculated by

$$F_G = \gamma \frac{m_1 m_2}{r_d^2}, \tag{4.26}$$

with the gravitational constant $\gamma = 6.67 \cdot 10^{-11}$ m^3/(kg s^2). Hence, the gravitational force is proportional to the mass of the two attracting bodies and decreases with growing distance by r_d^2. Assuming an object with mass m_O on the surface of a planet with radius r_P and mass m_P, the gravitational force can be written as

$$F_G = m_O\ \gamma\ \frac{m_P}{r_P^2} = m_O\ g_P, \tag{4.27}$$

with the gravitational acceleration of the planet $g_P = \gamma\ \frac{m_P}{r_P^2}$.
Every body in the universe is surrounded by a gravitational field, attracting other bodies in the surrounding. The gravitational acceleration on Earth is $g = 9.81$ m/s^2. Some gravitational accelerations are listed in Tab.4.4.

Table 4.4: Gravitational accelerations of different planetary bodies in terms of $g = 9.81$ m/s^2.

Body	grav. accel.
Earth	1 g
Earth Moon	0.16 g
Mars	0.38 g

5

Model for light-incuded erosion

5.1 Forces

The physics of granular matter is a very wide field of research and becomes very complex in detail, with many open questions left to be answered.

However, the forces in and on an illuminated dust bed in the context of this work can be roughly divided into forces that benefit lifting and those acting against lifting. An important factor for the resulting forces is the time of illumination. As shown in Sec.4.1, long illumination times lead to a solid-state greenhouse effect within the dust bed, where the maximum of temperature is not at the surface rather a few layers below. Hence, forces based upon the temperature gradients over the particles surface change their direction.

The total force acting on a particle on the surface of an illuminated dust bed is the superposition of all acting forces, given by

$$F_{\text{total}} = F_{\text{gravity}} + F_{\text{cohesion}} + F_{\text{photophoresis}} + F_{\text{thermophoresis}} + F_{\text{gas drag}} + F_{\text{Knudsen}}. \quad (5.1)$$

with the gravitational force F_{gravity}, the cohesive force F_{cohesion}, the photo- and thermophoretic forces $F_{\text{photophoresis}}$ and $F_{\text{thermophoresis}}$ and the drag force $F_{\text{gas drag}}$. F_{Knudsen} is the force induced by a Knudsen compressor leading to an overpressure within the dust bed and it will be developed in the following section.

The exact values of the single forces are not known and experiments are performed to estimate the total lifting force acting on a particle at the surface of an illuminated dust bed. These experiments are presented in Chap.7.

5.2 Overpressure by Knudsen Compressor

As shown in Sec.4.2, a temperature gradient over a tube in a rarefied gas leads to a net gas flow from cold to warm if the mean free path of the gas molecules is comparable to the diameter of the channel. Translating this to a porous body, a temperature gradient over the capillaries within the body leads to a gas flow from cold to warm.

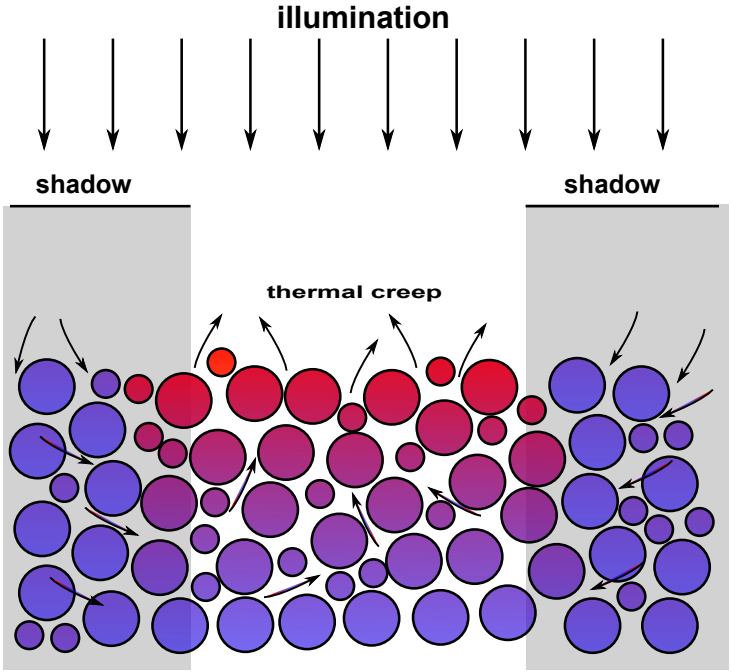

Figure 5.1: Sketch of an illuminated dust bed acting as a gas pump: the temperature gradient over the dust particles surfaces leads to a thermal creep from the cool layers up to the surface. Accordingly, this gas is soaked from shadowed places down into the dust bed. Hence, the illumination of a dust bed produces a convective gas flow above and through the dust bed.

For a simple example, we assume a porous body in air at low pressure. The mean free path of gas molecules is given by Eq.4.3 with the number of gas molecules per volume $N = p/k_B T$ (pressure p, temperature T, Boltzmann-constant k_B) for an ideal gas and $\sigma = \pi d^2$ as the effective cross sectional area provided that spherical particles are assumed. Based upon the values of Chapman and Cowling (1970), we obtain the radius of a hypothetical air gas molecule by adding the percentage molecule diameters of nitrogen (78 %) and oxygen (22 %) to

$$r_{air} = (0.78 \times 0.378 + 0.22 \times 0.3636)\,/2 \cdot 10^{-9}\mathrm{m} \tag{5.2}$$

and obtain for the effective cross sectional area

$$\sigma_{air} = \pi r_{air}^2 = 1.1 \cdot 10^{-19}\mathrm{m}, \tag{5.3}$$

which leads to a mean free path at room temperature (T = 300 K)

$$\lambda = \left(\sqrt{2}\frac{p}{k_B T}\sigma_{air}\right)^{-1} \approx \frac{2.7}{p} \cdot 10^{-4}\text{m} \cdot \text{mbar} = \frac{270\ \mu\text{m} \cdot \text{mbar}}{p}, \tag{5.4}$$

based upon the ambient pressure p in mbar. Hence, at 10 mbar, the mean free path of air molecules at room temperature is about 27 μm and thermal creep leads to a gas flow in capillaries of the same diameter with a temperature gradient. In Sec.6.1, it was shown that the effective capillary diameter is about 23 % of the grain size, whereby a mean free path of 27 μm equates to a grain diameter of $\sim$ 115 μm.

The gas mass flow rate $\dot{M}$ through channels due to thermal creep and based solely on the temperature gradient is described by Muntz et al. (2002) in Sec.4.2 with $\Delta p = 0$

$$\dot{M} = p_{avg}\frac{A}{\sqrt{2\frac{k_B}{\mu}T_{avg}}}\left(\frac{L_r}{L_x}\frac{\Delta T}{T_{avg}}Q_T\right) \tag{5.5}$$

Eq.5.5 is applicable to an illuminated dust bed under certain circumstances: the temperature gradient within the dust bed decreases from the surface to the layers below without levels of constant temperatures or temperature jumps. Gas can subsequently be continuously scooped continuously from the cold bottom to the warm top along the pore walls, because every particle with a temperature gradient transports the same amount of gas along its surface. In this case, the illumination of the dust bed can lead to ejection of particles by gas drag as loose-bound particles can be dragged along within the gas flow.

However, the numerical simulation of the temperature distribution within a dust bed showed that the first layers of an illuminated dust bed can be on the same, constant temperature when the light source is switched on and the temperature gradient starts a few layers below the surface (based upon light flux, illumination time and thermal conductivity of the dust bed). The experiment showed that ejections occur as soon as the light source is switched on.

The gas mass flow rate $\dot{M}$ through channels of constant temperature can be provided by a pressure difference (Darcy, 1856) and is described by Muntz et al. (2002) (Sec.4.2)

$$\dot{M} = -p_{avg}\frac{A}{\sqrt{2\frac{k_B}{\mu}T_{avg}}}\left(\frac{L_r}{L_x}\frac{\Delta p}{p_{avg}}Q_p\right), \tag{5.6}$$

Given that the dust layers deeper within the dust bed have a temperature gradient, gas is transported from the bottom to the beginning of the maximum of temperature of the dust bed (Fig.5.2).
The upper layer of constant temperature acts like an obstacle for the gas flow and an overpressure will build up below the layer of constant temperature. This layer will be called the *active layer* from now onwards (explained later in Sec.**??**). However, the resulting pressure difference induces another gas flow (Darcy, 1856; Sone and Itakura, 1990; Muntz et al., 2002) leading from the point of overpressure to the surface.
In addition, it leads to a pressure-driven backflow to deeper layers, pumping gas against

the thermally-driven flow (Fig.5.3). Hence, the gas flow through the dust layer with a temperature gradient is a combination of thermal creep and a pressure-driven backflow (Darcy, 1856; Sone and Itakura, 1990; Muntz et al., 2002):

$$\dot{M} = p_{avg} \frac{A}{\sqrt{2\frac{k_B}{\mu} T_{avg}}} \left(\frac{L_r}{L_x} \frac{\Delta T}{T_{avg}} Q_T - \frac{L_r}{L_x} \frac{\Delta p}{p_{avg}} Q_p \right), \tag{5.7}$$

whereas the gas flow in the top layer is still solely driven by pressure. The flow velocity of the gas is set by the thermally-driven part within the dust bed and the overpressure, which adjusts itself to also maintain that flow in the top layer. Hence, the mass flow is the same in both parts.
If the force caused by the overpressure overcomes gravity and cohesion, particles can be lifted from the surface. With respect to the different length of the capillaries L_{x1} and L_{x2}, the mass flow rate in the two parts is

$$\dot{M}_1 = p_{avg} \frac{A}{\sqrt{2\frac{k_B}{\mu} T_{avg}}} \left(\frac{L_r}{L_{x1}} \frac{\Delta T}{T_{avg}} Q_T - \frac{L_r}{L_{x1}} \frac{\Delta p_1}{p_{avg}} Q_p \right), \tag{5.8}$$

$$\dot{M}_2 = -p_{avg} \frac{A}{\sqrt{2\frac{k_B}{\mu} T_{avg}}} \left(\frac{L_r}{L_{x2}} \frac{\Delta p_2}{p_{avg}} Q_p \right), \tag{5.9}$$

with Eq.5.8 for the temperature-driven part with capillary length L_{x1} and Eq.5.9 for the pressure-driven part with capillary length L_{x2}. The overpressure Δp_1 equals Δp_2 and eventually the gas velocity is the same in both parts, as well as the mass flow (de Beule et al., 2015c). Solving the equation $\dot{M}_1 = \dot{M}_2$ for the overpressure $\Delta p = \Delta p_1 = \Delta p_2$, we obtain

$$\Delta p = \frac{L_{x2}}{L_{x1} + L_{x2}} p_{avg} \frac{\Delta T}{T} \frac{Q_T}{Q_P}. \tag{5.10}$$

The resulting pressure gradient within the activated layer is linear according to Darcy's Law (Sec.4.2); thus every particle within the activated layer experiences a pressure difference $\Delta p'$ with $\sum \Delta p' = \Delta p$ (Fig.5.3). If the pressure induced force $F_{p'}$ acting on a surface particle overcomes gravity and cohesion, the particle is lifted.

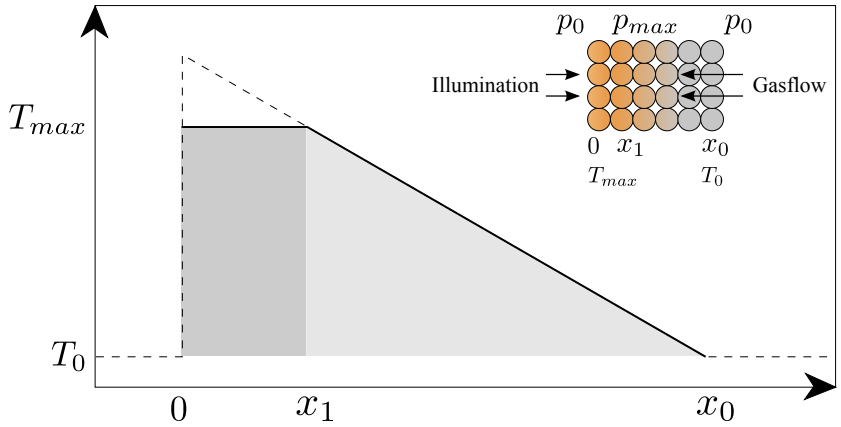

Figure 5.2: Sketch of the temperature distribution within an illuminated dust bed, where the first layer is on the same temperature and deeper layers have a temperature gradient. Gas will be pumped along the dust layers with temperature gradient to the maximum of temperature T_{max} at the layer x_0 to x_1. From de Beule et al. (2015c).

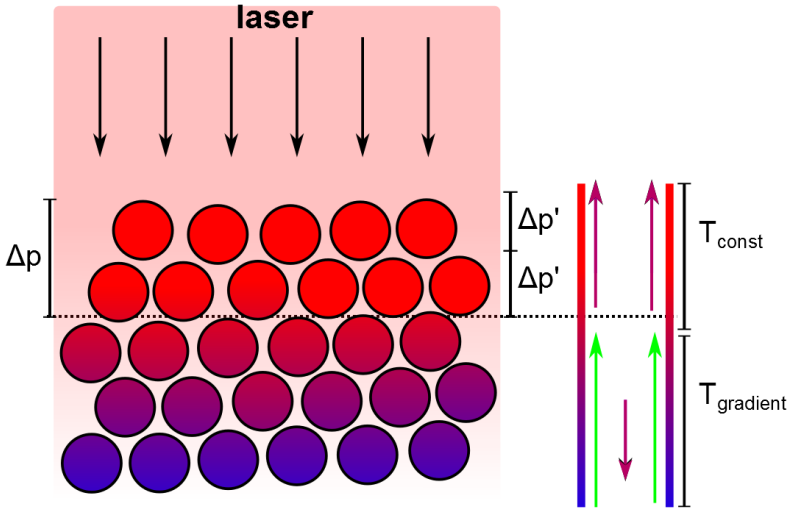

Figure 5.3: Sketch of the temperature distribution within an illuminated dust bed (left), where the first layer is on the same temperature T_{const} and deeper layers have a temperature gradient T_{gradient}. The right sketch shows an exemplary capillary within this dust bed: Purple Arrows mark the pressure-driven and green arrows the temperature-driven gas flow. Assuming a linear pressure gradient in the activated layer, every particle experiences the same pressure difference $\Delta p'$.

6

Experimental preparation

In this chapter, the experimental preparation and the basic setup of the experiments for the investigation of light-induced dust erosion are presented. The main part of every experiment is a dust bed illuminated by a laser in a low-pressure environment, which was first introduced by Wurm and Krauss (2006) and further investigated by Kelling and Wurm (2009).
In addition to the variations of the light intensity and the pressure, most of the experiments were performed in different gravitational accelerations (Parabolic Flight Campaigns and Drop Tower).

The key experiment of this work was performed in the drop tower in Bremen, where the model for light-induced erosion could be developed, as well as several experiments in low gravity on parabolic flights that clearly show the dependence of light-induced erosion on the gravitational acceleration. In addition, a laboratory experiment was performed where the combination of illumination and a tension loss led to the lifting of a dust layer from a dust bed.

- Parabolic Flight Experiments: The dependence of light-induced erosion on the gravitational acceleration.
- Drop Tower Experiment: An illuminated dust bed works as a gas pump.
- Laboratory Experiments: activated layer of a dust bed.

Table 6.1 shows the list of all experiments, sorted by the time when they were performed. However, not all experiments have been analyzed yet and not all analyzed experiments are shown in every detail in this work. For a better survey of the results, the focus of this work lies on the experiments and their results with a quintessence, leading to a better understanding of the light-induced erosion.

Sec.6.1 describes the dust samples used and the properties like, such as the size distribution and permeability. In Sec.6.2, the basic setup of all experiments is presented.

Exp.	Campaign	Note	Laser	Light	Sample
# 1	PFC 09/2012	centrifuge	655 nm	On	Basalt
# 2	JEPFF 12/2012	centrifuge	655 nm	On	Basalt, Glass beads
# 3	DT 03/2013	0g	655 nm, 955 nm	On	Basalt, Glass beads
# 4	DT 03/2014	0g	655 nm 955 nm	On/Off	Basalt, JSC Mars 1A, Glass beads
# 5	DT 07/2014	0g	435 nm 955 nm	On/Off	Basalt Glass beads
# 6	PFC 10/2012	Knudsen	655 nm	On/Off	JSC Mars 1A
# 7	Laboratory	Activated layer	655 n)	On	Basalt
# 8	DT 03/2014 Laboratory	0g Disintegration	655 nm 955 nm	On/Off	Basalt, JSC Mars 1A, Glass beads

Table 6.1: List of all experiments related to the light-induced dust eruptions. The research started with a Parabolic Flight Campaign (PFC) and was followed in the same year by a Joined European Partial-G Campaign (JEPFF). Drop Tower Campaigns (DT) were conducted in 2013 and 2014 and the last PFC was at the end of 2014. In addition to the testing of the experimental setup for the campaigns, a laboratory experiment was set up where light-induced eruptions under cohesion loss were measured (activated layer). The experiment 8 used the effect of light-induced thermal creep to measure the tensile strength between dust particles. The fifth column of the table comprises the information whether the measurements of the induced erosion was measured during light on or off.

6.1 Dust samples

This section provides the definition of the **dust bed** and **dust** used in this work.

sample	grain size
Basalt	0 - 125 μm
JSC Mars 1A	0 - 1 mm
Cospheric Beads	different sizes

Table 6.2: List of dust samples used in the experiments.

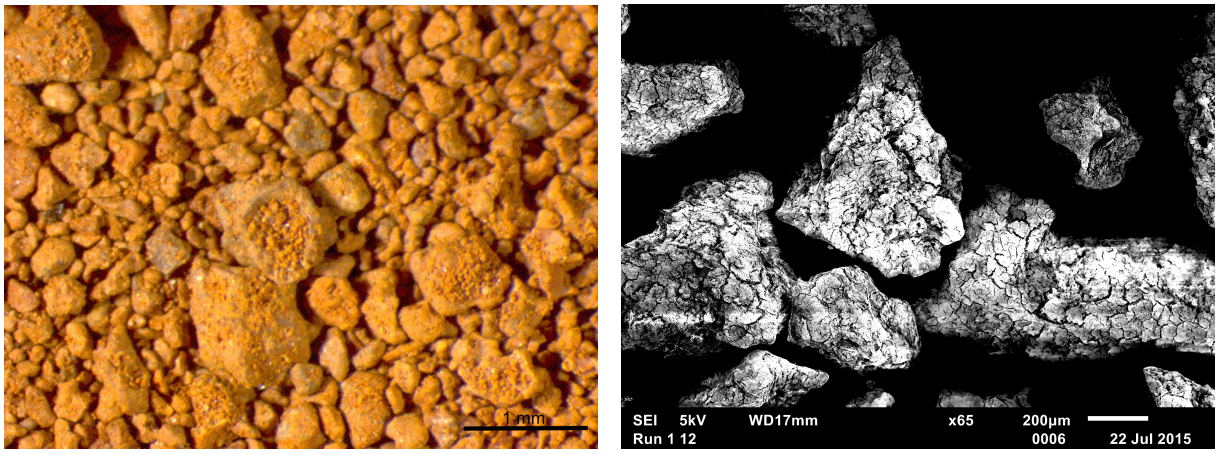

(a) Image of a JSC Mars-1A sample by an optical microscope.

(b) Image of a heated (1000 K for 1 h) JSC Mars 1A sample by a scanning electron microscope.

Figure 6.1: Close-ups of a JSC Mars-1A sample.

Samples and sizes

The term **dust** is used for dry powder, which is a fine granular material comprising discrete solid particles. According to Brown and Richards (1970) a powder is granular material with a grain size up to 100 μm and can comprise ultra fine powder (0.1 - 1 μm), super fine powder (1 - 10 μm) and granular particles (10 - 100 μm), whereas the term granular material is used for powders including granular solids, providing a range up to 3 mm grain sizes.
In the context of this work, unless otherwise noted, all dust samples cover the term granular material, comprising solid particles with grain sizes between 0 and a few 100 μm. It should be noted that the investigation of dry granular material is limited in the experiments to granular aggregates, because only in rare cases can single grains be observed. Most of the observed particles are aggregates, comprising at least two or more grains.
A few examples of dust samples are shown in Tab.6.2, with their grain sizes.

Dust bed and packing

The term **dust bed** is used for loose-strewed dust within a compartment. The granular material is filled in cylindrical containers with diameters and depth of a few centimeters, whereby the dimensions of the compartment are much larger than the single grain sizes. To obtain a homogenous surface for the experimental setup, the dust is strewed smoothly in the container with avoiding compaction or other stresses.
Given that not only the space above the surface of the dust bed is within the point of interest but also the spaces *within* the dust bed, some thoughts should be provided about how the grains are packed inside the container. Certainly, the packing of non-uniform grains with different sizes is more complex and in the context of this work the sort of packing serves as a way to describe the dimension of the capillary system, although for the experiments performed the magnitude holds more importance than the exact number. Hence, the diameter of a capillary in the dust bed can be approximated by a very simple

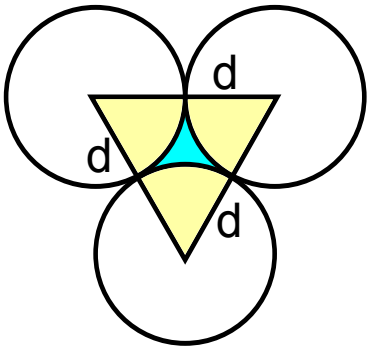

Figure 6.2: Sketch for the approximation of a pore size between closed packed of spherical particles of diameter d. The resulting capillary is shown in blue and about 23 % of the particle diameter.

model of one-sized packed spheres in a hexagonal lattice. In 1D, the area within three touching spheres (Fig.6.2) can be calculated by the difference of the triangle (each corner is the middle of a sphere) and the overlapping parts of the circles. Assuming a grain diameter d, the area of the triangle is

$$A_T = \frac{1}{2} d \sqrt{3} \frac{d}{2} = \sqrt{3} \frac{d^2}{4}. \tag{6.1}$$

Within this triangle is half the part of one circle area, which leads to a capillary area of

$$A_{capillary} = A_T - A_C = \sqrt{3} \frac{d^2}{4} - \frac{1}{2} \pi \frac{d}{2}^2 . \tag{6.2}$$

In a further approach, the effective diameter of one capillary can be approximated by equalizing this area with an area of a circle with diameter d_{eff}, which leads to

$$d_{\text{eff}} = \sqrt{\frac{\sqrt{3}}{\pi} - \frac{1}{2}} \; d \approx 0.23 \, d. \tag{6.3}$$

Particle size distribution

One of the most important properties is the particle size distribution, which was measured by the MasterSizer 3000 (Malvern Instruments) via Mie scattering. The Mie theory is the exact solution of the Maxwell equations regarding the scattering of electromagnetic waves at spherical particles of arbitrary sizes. In contrast to Rayleigh scattering, the Mie scattering (named after Gustav Mie) is not bound to a particle size and can be used to approximate the sizes of the irregular dust particles within this work. For the analysis in the MasterSizer 3000, the dust particles were dispersed in purified water to prevent aggregation of the single particles during the measurements.

Permeability

Permeability is a measure of how porous samples are able to pass through gases. The permeability of the dust samples used in the experiments holds interest regarding Darcy's Law (Darcy, 1856). Permeability for different dust samples – especially for the Mars Analog JSC-1a – are in the order of 10^{-13} m^2 at ambient pressure (1 bar) (Sizemore and Mellon, 2008). In addition, a simple setup was established to measure the permeability for basaltic dust grains in the context of this work. The volume and number distribution of the basaltic grains is shown in Fig.6.3. The setup of the permeability measurement is

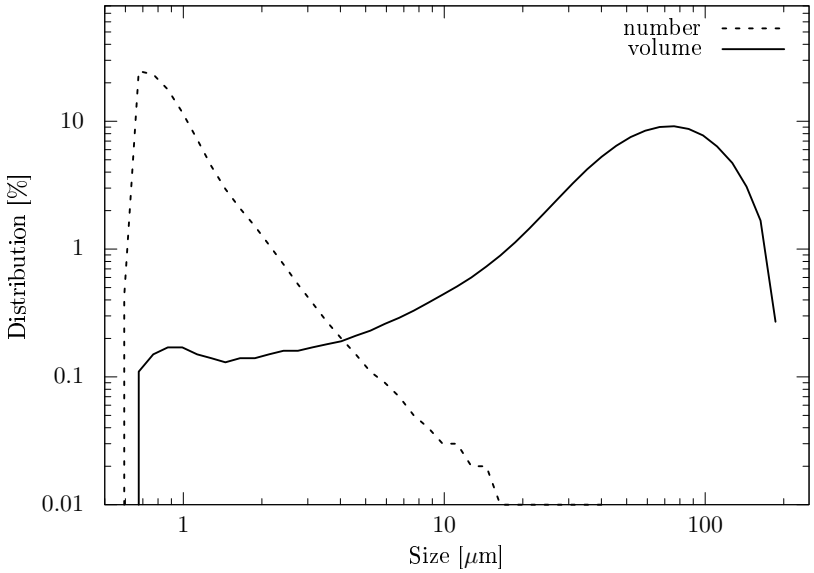

Figure 6.3: Number and volume distribution of the basalt sample used for the permeability measurement.

shown in Fig.6.4: the dust sample was filled in a tube and the ambient pressure was set to a few mbar (Tab.6.3). A vacuum pump on one side of the tube evacuated while a pressure valve on the other side of the tube vented the system. After adapting the inflow of the gas to the outflow – thus establishing a constant pressure difference – the inflow of the gas through the pressure valve was measured. Due to the constant pressure difference,

this value corresponds to the flow through the soil. The permeability can subsequently be calculated as

$$\kappa_{\text{perm}} = \frac{Q\eta L}{A\Delta P}, \tag{6.4}$$

with the flow Q at the pressure valve, the dynamic viscosity of air $\eta = 1.7\ 10^{-5}$ Ns/m^2 (Footnote 1), the length of the dust bed $L = 20$ cm, the surface area of the dust bed $A = \pi(20\text{mm})^2$ and the pressure difference ΔP. Three measurements were made, each at a different pressure difference and the results are shown in Tab.6.3. The measurements confirmed the assumption that the permeability of the dust sample is in the order of 10^{-13} m^2.

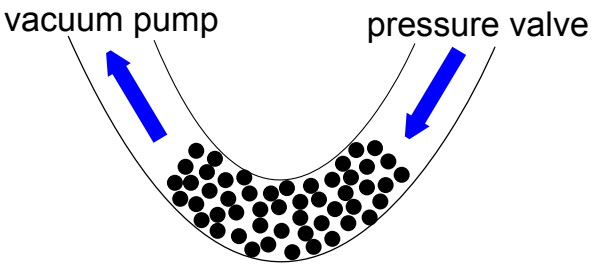

Figure 6.4: Sketch of the setup for the measurement of the permeability of basaltic dust grains.

Pressure Difference [mbar]	Gas Flow [ml/min]	Permeability [10^{-13} m^2]
2.5	3.6	6.63
3.5	10	6.58
5	14	6.45

Table 6.3: Results of the permeability measurements.

6.2 Basic setup

The basic setup for the investigation of light-induced erosion was developed by Wurm and Krauss (2006) and is shown in Fig.6.5. A dust bed comprising micron-sized (0 - 500 μm) particles is placed in a vacuum chamber, which is evacuated down to a few millibars (0.1 - 10 mbar). The surface of the dust bed is illuminated by a laser from above (red laser (655 nm), infrared laser (955 nm)) and the erosion of particles is observed by one or two cameras from the side. The diameter and depth of the dust bed is in the order of a few centimeters.
In each experiment described in this work, the laser was homogenized by coupling the light to an optical fiber and projecting the fiber outlet onto the sample (Fig.6.6). For a better overview, the upcoming sketches are depicted without the optical fiber.

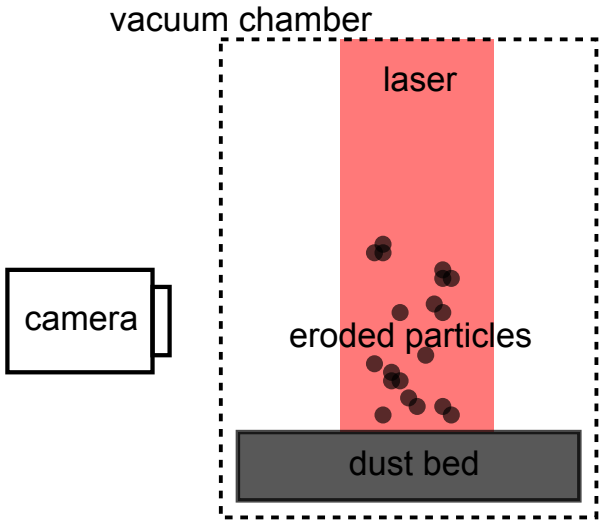

Figure 6.5: Basic Setup for the investigation of light-induced erosion. A dust bed is placed within a vacuum chamber of low ambient pressure and is illuminated by a laser from above. The eroded particles are observed by optical imaging.

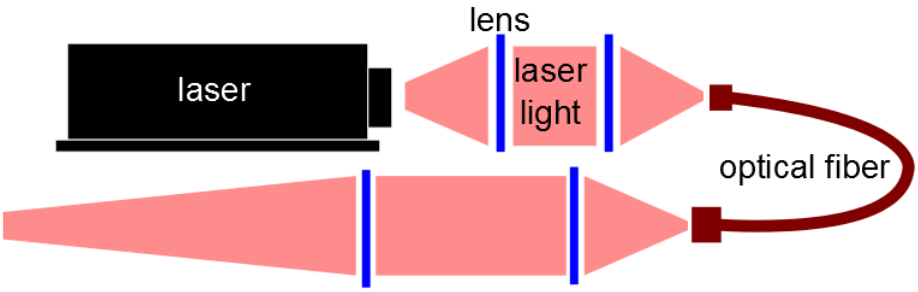

Figure 6.6: For each experiment, the light of the laser was coupled via two collector lenses into an optical fiber and the outlet of the fiber was focused via two lenses onto the sample.

6.3 Thermal convection

As shown in Sec.4.6, natural convection plays an important role concerning gas flow above heated surfaces in laboratory conditions.

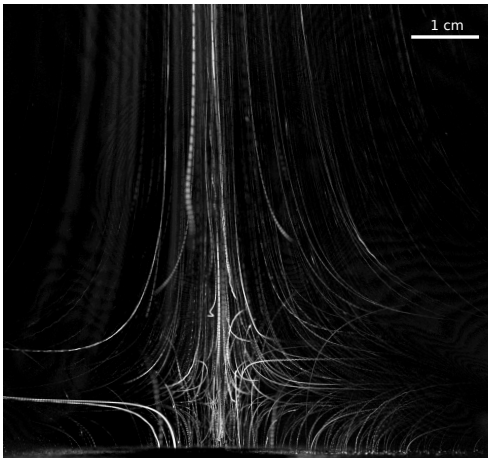

Figure 6.7: Thermal convection in low ambient pressure (24 mbar) over a heated surface (420 K). The image is an overlay of 1500 frames, with a framerate of 100 frames per second. Basaltic dust particles (< 25 μm) trace the gas flow.

To estimate the gas flow induced by thermal convection, a heater was placed into a vacuum chamber, providing a heated surface of 420 K. The ambient pressure was set to 24 mbar and tracer particles (Basalt, < 25 μm) were injected into the chamber to trace the developed gas flow due to convection.

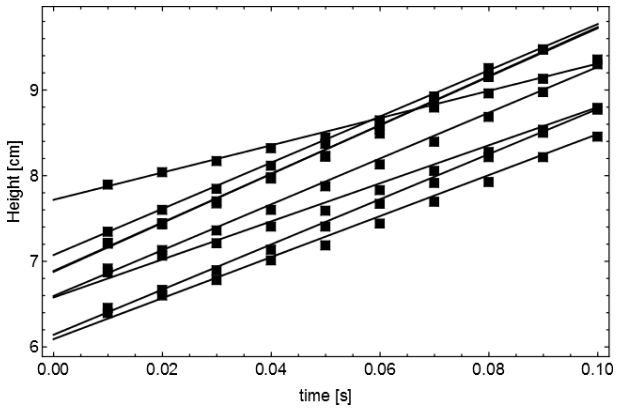

Figure 6.8: 8 Tracks of basaltic dust particles (< 25 μm) tracing the gas flow by thermal convection (Fig.6.7) over a heated surface at low ambient pressure (24 mbar). The Tracks are fitted with a function $f(x) = a \cdot x + b$ and the mean velocity is 25 m/s $\pm$ 4 m/s.

Fig.6.7 shows the traces of particles over the heated surface in an overlay of 1,500 frames. The framerate was set to 100 frames/s. Fig.6.8 shows the movement of dust particles in

vertical direction within the gas stream in the middle over the heated surface.
The mean velocitity of the eight particles tracked in Fig.6.8 is 25 m/s ± 4 m/s. In Chap.4 and 5 was shown that the illumination of a dust bed can lead to a gas flow above and through the porous bed. Fig.4.4 shows that the temperature of a dust bed's surface exceeds 400 K after an illumination time of 1 s with an intensity of 13 kW/m^2.
In a laboratory on Earth, this would lead to the thermal convection flow pattern shown in Fig.6.7. Hence, measuring a gas flow induced by temperature gradients is challenging as it is always superimposed by natural convection. Consequently, most of the experiments were performed in microgravity, where a gas flow based upon natural convection vanishes and solely the gas flow induced by temperature gradients can be observed.

7

Experiments

In this chapter the different setups of the experiments for the investigation of light-induced dust erosion are presented. Each experiment reveals new information about the acting forces within an illuminated dust bed.
Every section describes an experiment, whereby the setup and experimental procedure are presented, followed by a small resumé including the consequences for the total force acting on the dust bed.

Sec.7.1 describes the first experiment of light-induced erosion in the weightlessness of the drop tower in Bremen. The results reveal a convective flow pattern induced by temperature gradients within the illuminated dust bed. The velocity of the gas flow can be determined.
The experiment in Sec.**??** determines the photophoretic (and thermophoretic) force on single dust grains and aggregates used in the experiments. Sec.**??** describes an experiment where the depth of the active layer within an illuminated dust bed is investigated. In addition, the overpressure within the dust bed is estimated.
Sec.**??** shows that an induced gas flow can be used to measure the tensile strength (and cohesion) of dust aggregates. Sec.**??** shows experiments on a PFC where the gravitational dependency of the light-induced erosion is investigated.

The total force acting on a surface particle of an illuminated dust bed is given by

$$F_{\text{total}} = \underbrace{F_{\text{gas drag}}}_{\text{Sec.7.1}} + \underbrace{F_{\text{photophoresis}} + F_{\text{thermophoresis}}}_{\text{Sec.??}} + \underbrace{F_{\text{Knudsen}}}_{\text{Sec.??}} + \underbrace{F_{\text{cohesion}}}_{\text{Sec.?? + ??}} + \underbrace{F_{\text{gravity}}}_{\text{Sec.??}}, \qquad (7.1)$$

with the drag force $F_{\text{gas drag}}$ (Sec.4.2), the photo and thermophoretic forces $F_{\text{photophoresis}}$ and $F_{\text{thermophoresis}}$ (Sec.4.3 and 4.4), the force induced by a Knudsen compressor leading to an overpressure within the dust bed F_{Knudsen} (Chap.5), the cohesive force F_{cohesion} (Sec.4.5) and the gravitational force F_{gravity} (Sec. 4.7).

7.1 Drop tower experiments

The drop tower in Bremen is operated by the Center of Applied Technology and Microgravity (ZARM) at the University of Bremen. The drop-distance is 110 m within an evacuated (0.01 mbar) tube to circumvent air friction, providing 4.74 s of microgravity. Since 2004, it has been possible to perform experiments in catapult mode, where the duration of weightlessness could be extended to 9 s. The experimental setup is integrated into a capsule, which additionally contains a computer to store the collected data and control electronics for the catapult mode. The accuracy of weightlessness in the drop tower is 10^{-6}g. Within catapult mode, the capsule is accelerated within milliseconds and decelerated up to 40g after the flight.

Setup

The setup of the Drop Tower Experiments is shown in Fig.7.1.

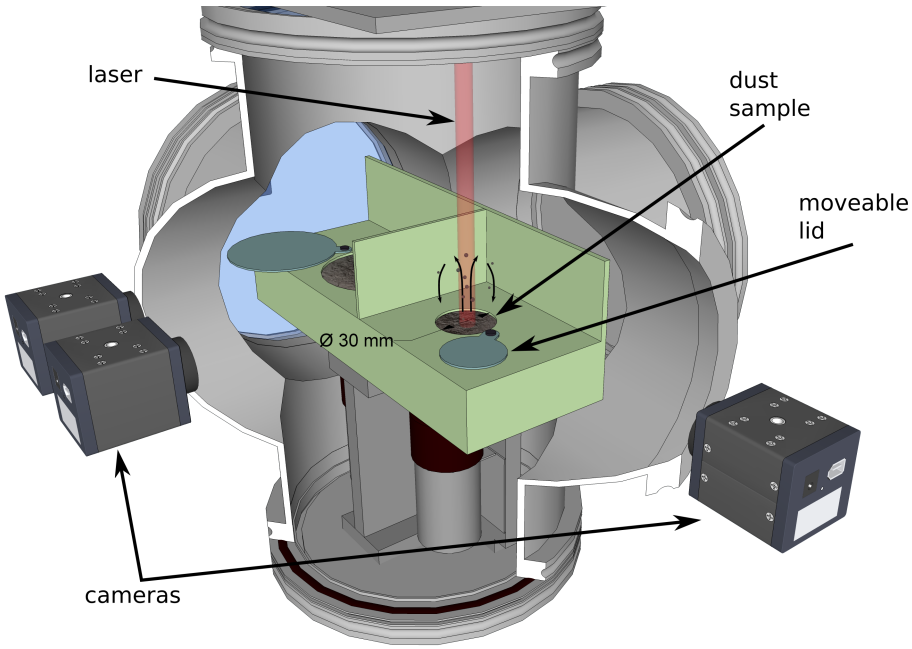

Figure 7.1: Setup of the Drop Tower experiments. From de Beule et al. (2014) and Küpper et al. (2014).

Two dust containers are placed within a vacuum chamber of low ambient pressure (between 1 and 10 mbar). The small dust container has a diameter of 3 cm and is 2 cm deep. The large container has a diameter of 7 cm and is 2 cm deep. The small container was illuminated by a red laser (655 nm) with a spot diameter of 5.5 mm and different intensities (4-13 kW/m^2). The large container was illuminated by an infrared laser (955 nm) with a spot diameter of 3.4 cm and different intensities (5-20 kW/m^2).
The setup for a drop tower experiment in catapult mode must satisfy different claims than a parabolic flight experiment. On a parabolic flight, the main problem for the dust in the container is the negative residual gravity during the micro-phase. In a drop tower

experiment, the main problem for retaining the dust inside the containers is the start and landing of the capsule. During launch, the capsule is accelerated within micro seconds and at the beginning of the zero-g phase the capsule relaxes, whereby some vibrations occur for about half a second. At the end of the free fall, the capsule is decelerated within a second in a tank with fine-grade polystyrene.
A moveable lid closes the dust containers during launch and landing to avoid particle loss, because the granular matter is very sensitive to vibration and residual gravitational acceleration.

Results

The advantage of the drop tower experiment is an unique opportunity to collect data points at 10^{-6}g (without any residual accelerations) and – importantly – without thermal convection. It was initially planned to investigate the erosion rate of the dust bed without gravity for the first time.Surprisingly, besides the effective erosion of the dust bed, some additional features could be seen in the recorded images.

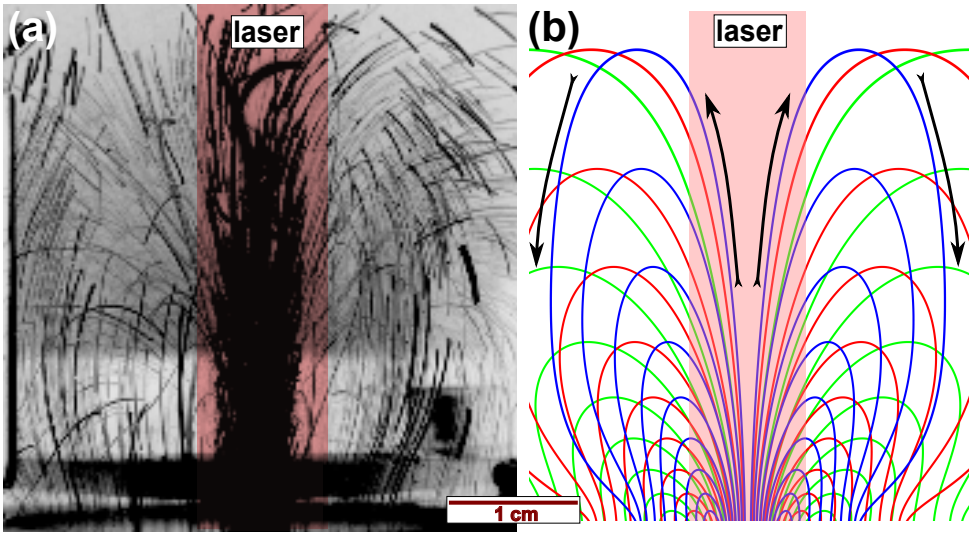

Figure 7.2: Particle trajectories above the illuminated dust bed comprising Basalt particles (> 125 μm) within the small container of the drop tower experiment. The light red bar marks the diameter (8 mm) of the laser (13 kW/m^2). The direction of the particle motion is represented by the black arrows on image (b). Due to the illumination, dust particles leave the surface within the laser beam. The lines outside the laser (red bar) mark the downwardly directed particle and gas flow outside the laser beam (de Beule et al., 2014).

The laser spot leads to an effective erosion of the dust bed and particles are ejected for entire nine seconds in catapult mode. In addition, a convective flow pattern becomes visible (Fig.7.2) when the dust bed is illuminated with a radiation flux of 13 kW/m^2. Particles leave the dust bed with a velocity of 10 m/s and move back to the dust bed with about 1 cm/s (Fig.7.3). It is even more fascinating about this feature that the gas flow is

not only above but also within the dust bed, because the gas enters the dust bed at the outer extension 1.5 cm away from the laser spot.

This was confirmed by computer simulations derived with COMSOL, where the dust sample with space above were simulated in two dimensions, shown in Fig.7.4: A body force is assumed with the width of the laserspot (7 mm), which decreases to the outer parts of the dust sample. The dust bed has 3 cm diameter and the volume above is chosen to be 4 cm high. The depth of the temperature gradient is chosen to 3 mm (Kocifaj et al., 2011), the particles are spherical with a diameter of 100 μm and the dust bed has a porosity of 0.7. The applied body force was chosen to explain the particle velocities shown in Fig.7.3 with 5 kN/m^3.

The experiments showed that the light-induced erosion is accompanied by a directed gas flow above and through the dust bed. Particles trace the streamline of the gas flow, leaving the dust bed within the laser beam and entering it outside. Some of those particles were tracked and their velocities before entering the dust bed was measured as shown in Fig.7.3.

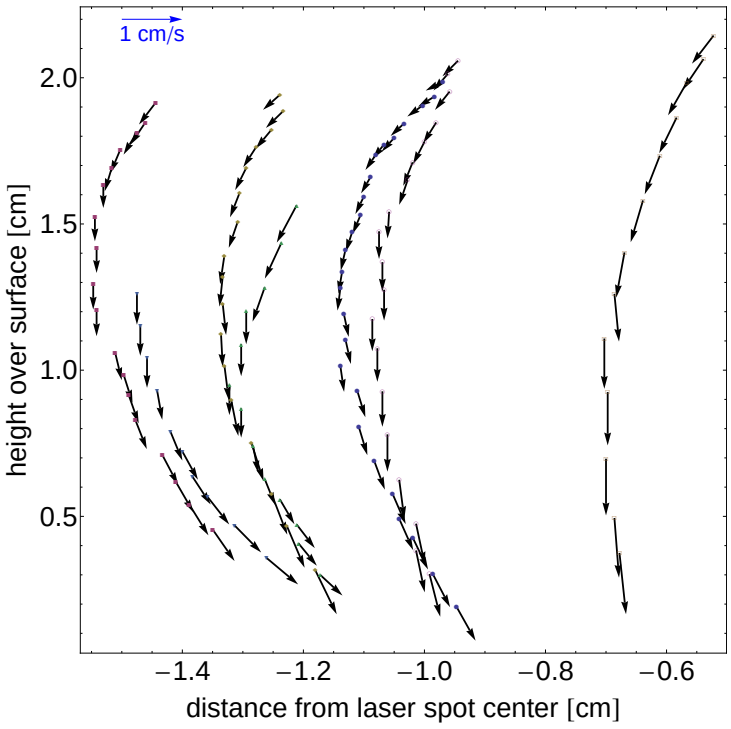

Figure 7.3: Velocities of a sample of tracer particles along their streamlines. The x axis shows the distance from the center of the laser spot and the y axis the height over the dust bed (de Beule et al., 2014).

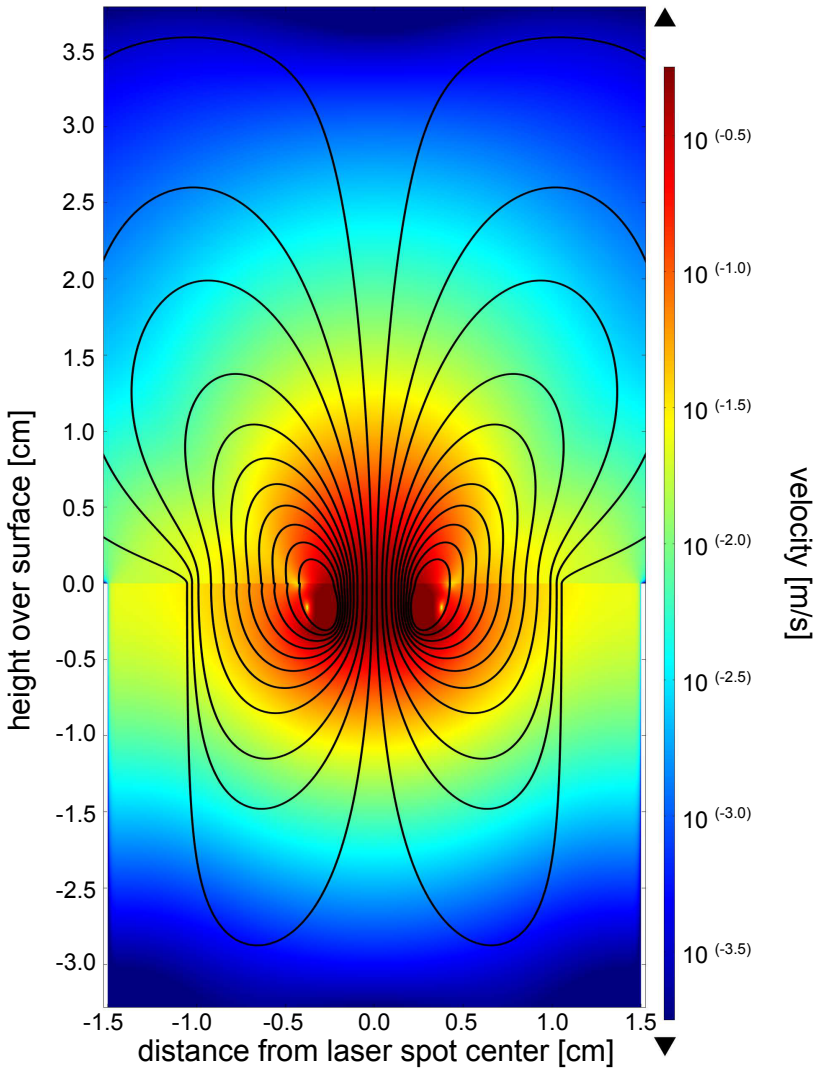

Figure 7.4: Simulation of particle velocities along their streamlines below and above the surface of the dust sample. The height 0 marks the surface of the dust bed. The colored scale provides the velocities (de Beule et al., 2014).

Forces

Besides the observation of a convective gas flow pattern above and through the dust bed, this experiment reveals information for acting forces on a surface particle of an illuminated dust bed. The measured velocities shown in Fig.7.3 are in the order of cm/s for tracer

Table 7.1: Parameters for the estimation of the gas drag acting on a spherical particle at the surface of an illuminated dust bed. The mass of a spherical particle is given by $m_P = 4/3\pi r^3 \rho_P$ with the radius r of the particle and its density ρ_P.

particle radius	r	=	25 μm
particle density	ρ_P	=	2890 kg/m^3
pressure	p	=	6 mbar
Boltzmann-constant	k_B	=	$1.38 \cdot 10^{-23}$ J/K
Avogadro constant	N_A	=	$6.022 \cdot 10^{23}$ (mol)$^{-1}$
molar mass (air)	μ	=	28.96 AMU
average temperature	T_{avg}	=	300 K

particles flowing back down to the dust bed. The simulation in Fig.7.4 is in agreement with these measurements and also shows that the gas flow within the dust bed is in the order of 1 cm/s.

The particle at the surface of the dust bed is now subject to this gas flow and experiences a force by gas drag (see Sec.4.2, Eq.4.15). The coupling time (Eq.4.16) depends on the mean thermal velocity, which is given by

$$v_{\text{th}} = \sqrt{\frac{8 k_B T}{\pi m_g}}, \tag{7.2}$$

with the mass of one gas particle m_g, which is the molecular mass of the atmospheric gas divided by the Avogadro constant. The mean thermal velocity is calculated at $v_{\text{th}} = 447$ m/s. Hence, the force acting on the particle by gas drag is $F_{\text{gas drag}} = 2 \cdot 10^{-10}$ N.

$$F_{\text{total}} = \underbrace{F_{\text{gas drag}}}_{= 2 \cdot 10^{-10}\ \text{N}} + \underbrace{F_{\text{photophoresis}} + F_{\text{thermophoresis}}}_{\text{Sec.??}} + \underbrace{F_{\text{Knudsen}}}_{\text{Sec.??}} + \underbrace{F_{\text{cohesion}}}_{\text{Sec.?? + ??}} + \underbrace{F_{\text{gravity}}}_{\text{Sec.??}}. \tag{7.3}$$

7.2 Photophoresis: A light-induced force on suspended particles.

The setup for the measurements of light-induced erosion in the drop tower was established for another investigation, involving photophoretic forces on suspended dust aggregates (Küpper et al., 2014).
The light-induced erosion produces suspended particles and when the lid is closed 1 s before the capsule decelerated, data sets are collected (Fig.**??**). No further dust particles are ejected and a cloud of particles is distributed throughout the chamber (Fig.**??**).

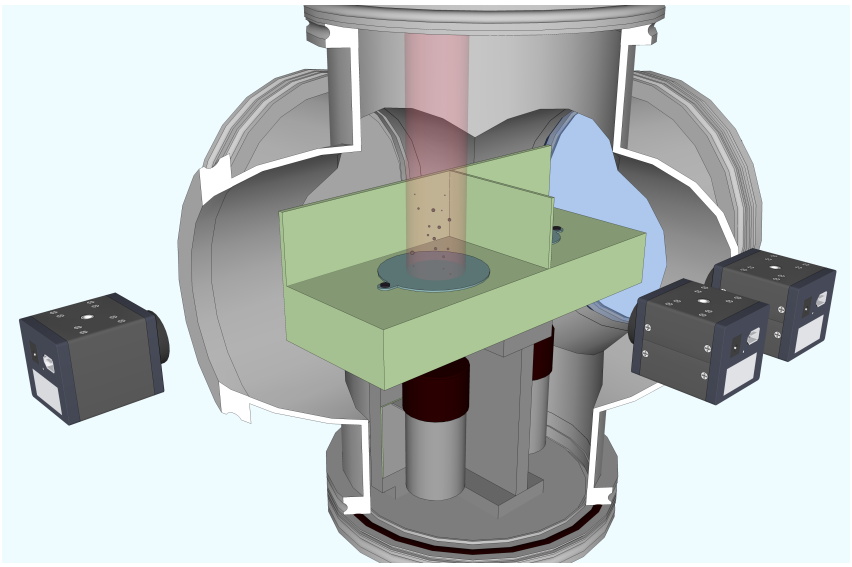

Figure 7.5: Experimental setup: a dust bed with 7 cm diameter is placed within a vacuum chamber at 4 mbar ambient pressure. An infrared laser (955 nm) with a light intensity of 20 kW/m^2 and a beam diameter of 3.4 cm is focused on the basaltic dust bed. The effect of light-induced erosion produces airborne particles and aggregates, whose movement is dominated by photophoresis after the lid is closed. Only one camera was used for this study (Küpper et al., 2014).

The illuminated airborne particles and aggregates (120 in total) are now subject to photophoretic forces undisturbed by gravity. Their movements within the laser beam are observed by a camera and tracked manually. The dust sample comprises poly-disperse Basalt with grain sizes smaller than 125 μm. The pressure within the vacuum chamber was 4 ($\pm$ 0.5) mbar and the dust particles were illuminated by an infrared laser (955 nm, 20 ($\pm$ 1) kW/m^2) with a spot diameter of 3.4 cm.
On average, the particles follow the direction of illumination, most of them away from the light source. The velocities could be measured and were in the order of a few cm/s. The suspended particles were up to mm size which implies that they are not individual grains, but also aggregates.
In addition, numerical simulations were conducted by Küpper et al. (2014) to compare the effect of the photophoretic force between irregular shaped aggregates and spheres of

the same mass.

The main result of this investigation was that the photophoresis on the studied aggregates scales with their mass and the degree of aggregation does not change the effective thermal conductivity in respect to photophoresis (Küpper et al., 2014).
In addition – and interestingly in the context of this work – Küpper et al. (2014) estimated the ratio between the photophoretic force at low pressure (in the free molecular flow regime) and the gravitational force for basaltic particles suspended in a thin atmosphere. This holds interest as in case of a solid-state greenhouse effect within an illuminated dust bed in a thin atmosphere, a photophoretic force acts on surface aggregates against gravity. Küpper et al. (2014) find the ratio

$$\frac{F_{\mathrm{Ph}}}{F_G} = \frac{Ip}{8\kappa T_\infty \rho_g g}, \tag{7.4}$$

where I is the solar insolation at pressure p. The particle density is given by ρ_p with a thermal conductivity κ. The temperature is T_∞ and g is the gravitational acceleration (9.81 m/s^2 on Earth). Applying Eq.**??** to martian conditions we choose an intensity I = 700 W/m^2, an average pressure $p = 6$ mbar, a temperature $T_\infty = 210$ K, a gravitational acceleration $g_{\mathrm{Mars}} = 0.38 \times 9.81$ m/s^2 and a particle density of $\rho_p = 3000$ kg/m^3. The thermal conductivity of the dust aggregate is not known, although Küpper et al. (2014) estimate it as $\kappa = 1$ W/(Km), which is in the order of the bulk values for siliciates. These assumptions lead to 2 % lift of a dust aggregates on the martian surface. Hence, under these circumstances, it is not possible to lift the basaltic particles against martian gravity solely by photophoresis.

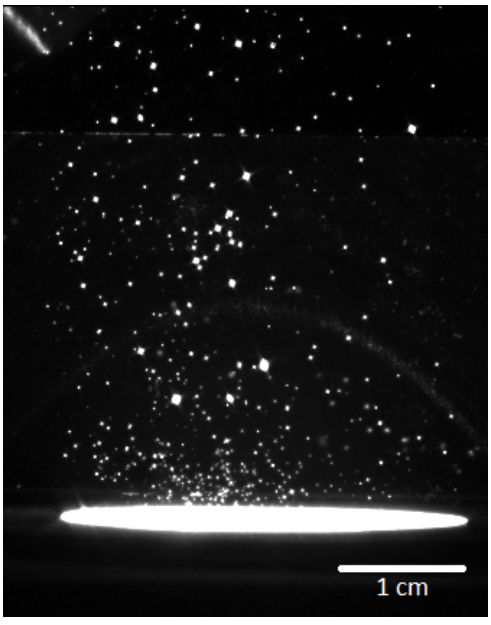

Figure 7.6: Snapshot of airborne particles and aggregates under microgravity (Küpper et al., 2014).

Forces

With Eq.**??**, it is now possible to estimate the photophoretic force on an illuminated (surface) particle. Assuming parameters listed in Tab.**??**, the photophoretic force is given by Eq.**??** multiplied by the gravitational force

$$F_{\mathrm{Ph}} = \frac{Ipm}{8\kappa T_{\mathrm{avg}} \rho_g}, \tag{7.5}$$

where I is the intensity of the light source at pressure p. The particle density is given by ρ_p with a thermal conductivity κ. The temperature is T_{avg} and m is the mass of the particle. The photophoretic force is subsequently calculated as $F_{\mathrm{Photophoresis}} = 6.5 \cdot 10^{-11}$ N. As the light heats up the dust bed, the surrounding gas also changes its temperature,

Table 7.2: Parameters for the estimation of the photophoretic and thermophoretic force acting on a spherical particle at the surface of an illuminated dust bed. The mass of a spherical particle is given by $m_P = 4/3\pi r^3 \rho_P$ with the radius r of the particle and its density ρ_P. The thermal conductivity of a single particle is from Küpper et al. (2014). The temperature gradient is estimated from Fig.**??** with $dT/dz \approx 100$ K/1 mm$= 10^5$ K/m.

particle radius	r	=	25 μm
particle density	ρ_P	=	2890 kg/m^3
pressure	p	=	6 mbar
thermal conductivity (particle)	κ	=	1 W/(K m)
thermal conductivity (gas)	κ_g	=	0.01 W/(K m)
average temperature	T_{avg}	=	300 K
intensity	I	=	4 kW/(m^2)
temperature gradient (particle)	dT/dz	=	10^5 K/m
molar mass (air)	μ	=	28.96 AMU

resulting in a temperature gradient within the gas. Hence, not only photophoresis but also thermophoresis acts on the particle. The thermophoretic force is given by (Sec.4.4)

$$F_{Th} = -f_{th} \frac{r^2 \kappa_g}{\sqrt{2 k_B T_{\mathrm{avg}}/\mu}} \frac{dT}{dz}. \tag{7.6}$$

With the dimensionless thermophoretic force $f_{th} = 0.02$ (Zheng, 2002) and the parameters found in Tab.**??**, the thermophoretic force is $F_{\mathrm{Thermophoresis}} = 2 \cdot 10^{-12}$ N.
Assuming that the duration of illumination is short and the maximum of temperature is at the surface of the dust bed, the resulting photophoretic and thermophoretic forces acting against the lifting forces and the total lifting force are given by

$$F_{\mathrm{total}} = \underbrace{F_{\mathrm{gas\ drag}}}_{=2\cdot10^{-10}\ \mathrm{N}} - \underbrace{F_{\mathrm{photophoresis}}}_{=6.5\cdot10^{-11}\ \mathrm{N}} - \underbrace{F_{\mathrm{thermophoresis}}}_{=2\cdot10^{-12}\ \mathrm{N}} + \underbrace{F_{\mathrm{Knudsen}}}_{\mathrm{Sec.??}} + \underbrace{F_{\mathrm{cohesion}}}_{\mathrm{Sec.??\ +\ ??}} + \underbrace{F_{\mathrm{gravity}}}_{\mathrm{Sec.??}}. \tag{7.7}$$

7.3 An activated dust layer

Numerical simulations of the temperature distribution within a dust bed lead to the assumption of a layer with a constant temperature below the surface in the first 30 s after the light source is turned on (Sec.4.1). Based upon the developed model (Chap.5) this layer is activated and can be lifted due to the overpressure. If the incoming light intensity is low and hence the temperature gradient does not lead to an overpressure sufficiently high to eject particles, it at least reduces the force necessary to lift particles from the dust bed. For example, an activated layer requires lower wind speeds to be lifted. In this laboratory experiment, the thickness of the activated layer was measured.

Setup

The setup of this experiment is shown in Fig **??**. Two glass plates provide a dust container with 2 mm width and 25 mm height. Basaltic dust with grain sizes between 0 and 125 μm is filled in this container and about 0.5 mm dust emerges above the glass.

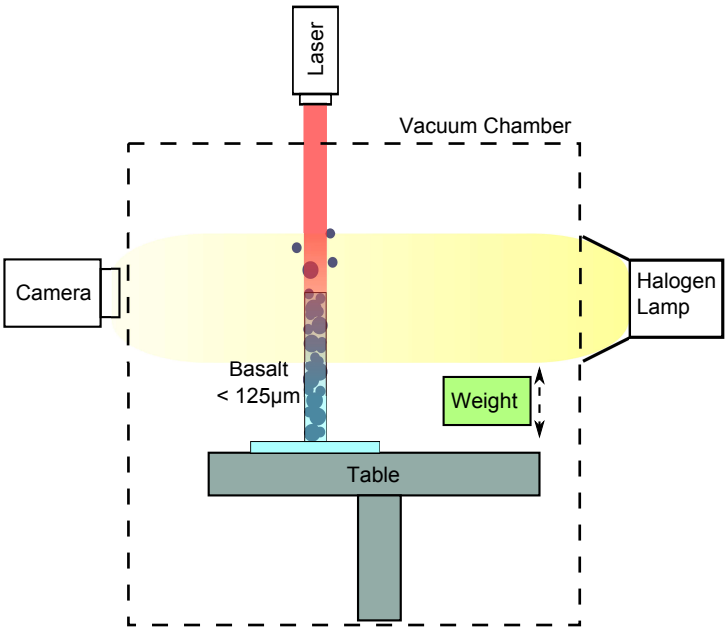

Figure 7.7: The experiment: Basaltic dust (0 - 125 μm grain sizes) is placed between two glass plates inside a vacuum chamber at low pressure. The dust is illuminated by red laser from above (4 kW/m^2) and a weight is dropped on the experimental table for each run. From de Beule et al. (2015c).

A weight of 30 g is locked 8 mm above the experimental table by an electromagnet in a distance of 3 cm to the glass container.
For each experimental run, the magnet is turned off and the weight drops, resulting in a short vibration of the dust sample and removing the cohesion between the dust particles (Fig.**??**). The entire setup is placed in a vacuum chamber with low ambient pressure. The dust bed is illuminated by a red laser (655 nm) with a spot of 8 mm diameter for

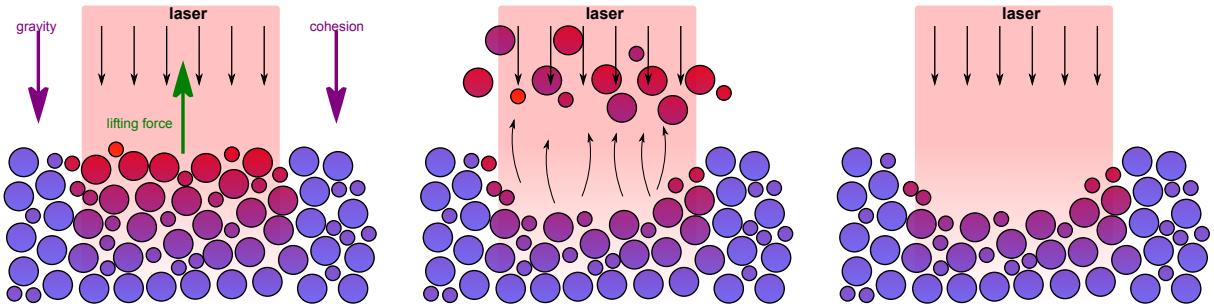

Figure 7.8: Sketch of the dust bed's surface during the experimental run. The left picture shows the illuminated surface before the drop. The picture in the middle shows the surface slightly after the drop of the weight, when the cohesion is removed between the particles and they can be lifted. The right picture shows the surface after the surface particles were lifted. The difference of the height of the surface is measured by the comparison of the left (Fig.**??** (1a)) and the right picture (Fig.**??** (1b)).

about 20 seconds, providing a flux density of 4 kW/m^2. The light-induced lifting force is too low to lift particles against gravity and cohesion, although if cohesion is removed, the lifting force exceeds gravity and particles are lifted. Experiments have been carried out at 0.1 mbar, 1 mbar and 10 mbar.
Images of the dust beds surface were taken before and after the impact, for the surface within the laser beam as well as the surface without the laser beam, as shown in Fig.**??**. The latter were taken as bright field images with transmitted light.

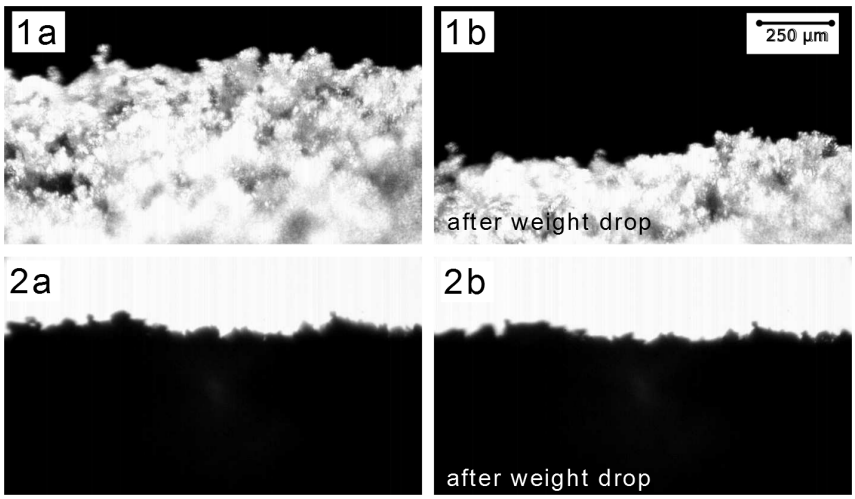

Figure 7.9: Example of the dust bed within (1a) and outside (2a) the laser beam at 1 mbar ambient pressure. The images 1b and 2b show the results after tension release. The dust bed within the laser beam (1a, 1b) was illuminated by a red laser (655 nm) with a light intensity of 4 kW/m^2 (de Beule et al., 2015c).

Results

The results of the experiment are shown in Fig.**??**. The blue bins show the probability of finding a certain depth of particle layer ejected at the three different pressures (0.1 mbar, 1 mbar and 10 mbar). The negative values are a feature of the experimental setup, because the surface of the dust bed could not be prepared perfectly smoothly and aggregates moving during the tension loss can fall onto the measured spot, where they increase the surface rather than reducing it. For comparison, the green bins show the probability of the depth to which particle loss occurs without light.

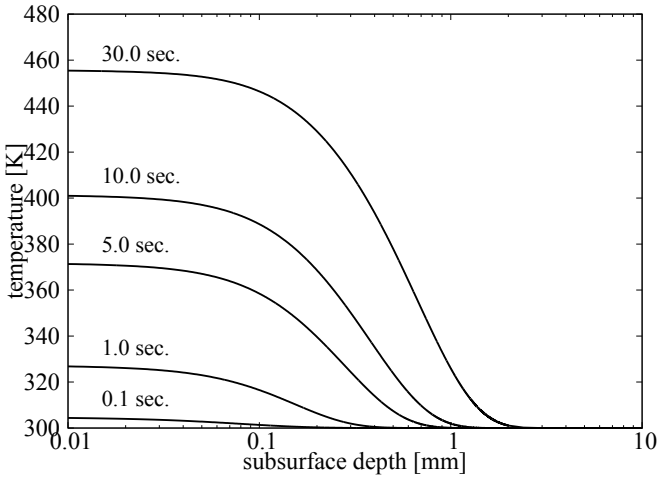

Figure 7.10: Simulation: Temperature profile in a dust bed comprising 25 μm spheres. The dust bed has a thermal conductivity of 0.01 W/(Km). The light intensity is 4 kW/m^2 and the illumination times used in the experiment are between 10 and 20 seconds (de Beule et al., 2015c).

The results show a significant difference between the depth of particle loss within and outside the laser beam. Without light the measured values are about 50 μm and within the illuminated area the measured depth ranges from 50 μm up to 500 μm for 1 mbar and 10 mbar. At 0.1 mbar the particle loss is not significantly attributed to illumination. Tab.**??** shows the average values of about 40 measurements at each pressure.

pressure	mean thickness	mean deviation
0.1 mbar	33 μm	$\pm$ 32 μm
1 mbar	166 μm	$\pm$ 57 μm
10 mbar	109 μm	$\pm$ 35 μm

Table 7.3: The mean thickness of the active dust layers for the different pressures. Each data point is based upon 40 measurements and the mean thickness was calculated after subtracting the mean offset (de Beule et al., 2015c).

Based upon the model derived in Chap.5, the results show the thickness of an activated

layer at different pressures and the existence of an overpressure within the illuminated dust bed. Fig.**??** shows the simulation of the temperature profile within an illuminated dust bed comprising 25 μm spheres. The light flux is 4 kW/m^2 and the thermal conductivity is 0.01 W/(Km) (equates to p = 10 mbar (Presley and Christensen, 1997)). The simulation shows that the temperature begins to decrease beyond 100 μm depth, which supports the results as this delivers the thickness of the activated layer.
With Eq.5.10, it is possible to estimate the overpressure within the dust bed (de Beule et al., 2015c)

$$\Delta p = \frac{L_{\text{active}}}{L_{\text{thermal}} + L_{\text{active}}} p_{avg} \frac{\Delta T}{T_{\text{avg}}} \frac{Q_T}{Q_P}, \tag{7.8}$$

with p_{avg} = 10 mbar and T_{avg} = 273 K + ΔT/2 K are the average ambient pressure and temperature, L_{thermal} = 1 mm is the capillary length with a temperature gradient (ΔT = 100 K) and L_{active} = 0.1 mm is the capillary length of constant temperature. k_B = 1.38 $\times$ 10^{-23} J/K is the Boltzmann-constant. According to Sone and Itakura (1990), the coefficients are Q_T = 0.22 and Q_P = 1.6. This results in an overpressure of Δp = 0.05

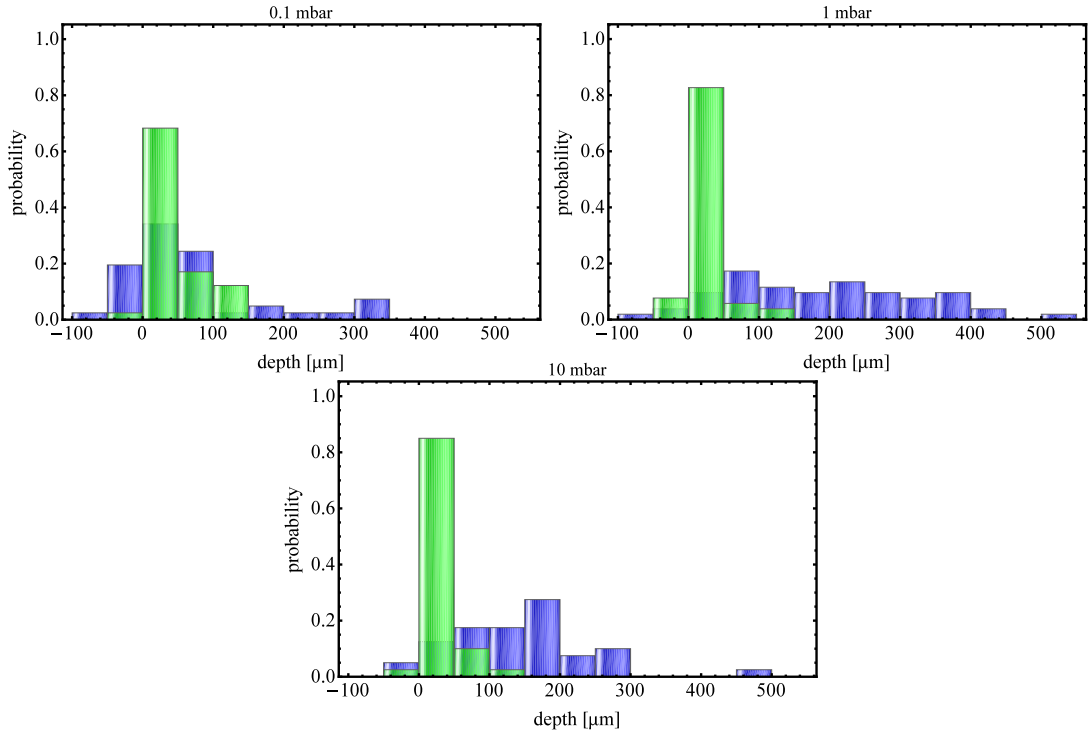

Figure 7.11: Probability of finding a certain depth of particle layer ejected at 0.1 mbar (top left), 1 mbar (top right), 10 mbar (bottom); blue bins are within the laser beam; green bins show the depth without radiation for comparison (de Beule et al., 2015c).

mbar with a mass flow through the pores of 10^{-8} kg/s. The velocity of the gas flow can subsequently be calculated by dividing the mass flow by the illuminated area and the density of the gas at the given pressure $\rho_{gas} = p\ \mu/(T_{avg} R_g)$ with the molar gas constant R_g = 8.3 J/(K mol) and the molar mass of air μ = 18.96 AMU. This leads to a gas velocity of 11 cm/s at p = 10 mbar (de Beule et al., 2015c). The velocity is on the same order

as the velocities of the tracer particles in the drop tower experiments (Sec.7.1, (de Beule et al., 2014)).

Forces

As described in this experiment, two gas flows occur within the dust bed with an active layer: one thermally and one pressure-driven gas flow. Hence, an overpressure builds up within the dust bed, beneath the active layer (Eq.**??**). The quotient Q_T/Q_P is calculated

Table 7.4: Parameters for the estimation of the force acting on a spherical particle at the surface of an illuminated dust bed by an overpressure below. The mass of a spherical particle is given by $m_P = 4/3\pi r^3 \rho_P$ with the radius r of the particle and its density ρ_P. The capillary radius is calculated by Eq.6.3 and the temperature difference is based upon Fig.**??**.

particle radius	r	=	25 μm
particle density	ρ_P	=	2890 kg/m^3
capillary radius	L_r	=	$0.23/2 \cdot r$
pressure	p	=	6 mbar
molar mass (air)	μ	=	28.96 AMU
temperature difference	ΔT	=	100 K
thermal conductivity (gas)	κ_g	=	0.01 W/(K m)
average temperature	T_{avg}	=	300 K
active layer depth	L_{active}	=	200 μm
temperature gradient depth	L_{thermal}	=	1 mm

as 0.40 (Sone and Itakura, 1990), which leads – with the given parameters – to an overpressure of 0.15 mbar. The force induced by this overpressure can be calculated for a particle column within the active layer

$$F_P = \Delta p \, \sigma. \tag{7.9}$$

With the geometrical cross section of the particle $\sigma = \pi r^2$, the force induced by overpressure is $F_{\text{Knudsen}} = 3 \cdot 10^{-8}$ N.

$$F_{\text{total}} = \underbrace{F_{\text{gas drag}}}_{=2\cdot10^{-10}\text{ N}} - \underbrace{F_{\text{photophoresis}}}_{=6.5\cdot10^{-11}\text{ N}} - \underbrace{F_{\text{thermophoresis}}}_{=2\cdot10^{-12}\text{ N}} + \underbrace{F_{\text{Knudsen}}}_{=3\cdot10^{-8}\text{ N}} + \underbrace{F_{\text{cohesion}}}_{\text{Sec.?? + ??}} + \underbrace{F_{\text{gravity}}}_{\text{Sec.??}}. \tag{7.10}$$

7.4 Disintegration of dust aggregates

Besides the effect of the light-induced gas flow, the images taken from the drop tower experiments (Fig.7.1) showed some other interesting phenomena. Aggregates lifted from the dust bed and leaving the laser beam started to disintegrate shortly after (Fig.**??**, (de Beule et al., 2015b)). An infrared laser (955 nm, 5.4 kW/m^2 and 12.7 kW/m^2) illuminated a 3.4 cm spot of a dust bed with 7 cm diameter comprising Basalt or JSC Mars-1a (palagonite). The JSC Mars-1a sample was tempered at 600°C ($\approx$ 873 K) for 1h (JSC600).

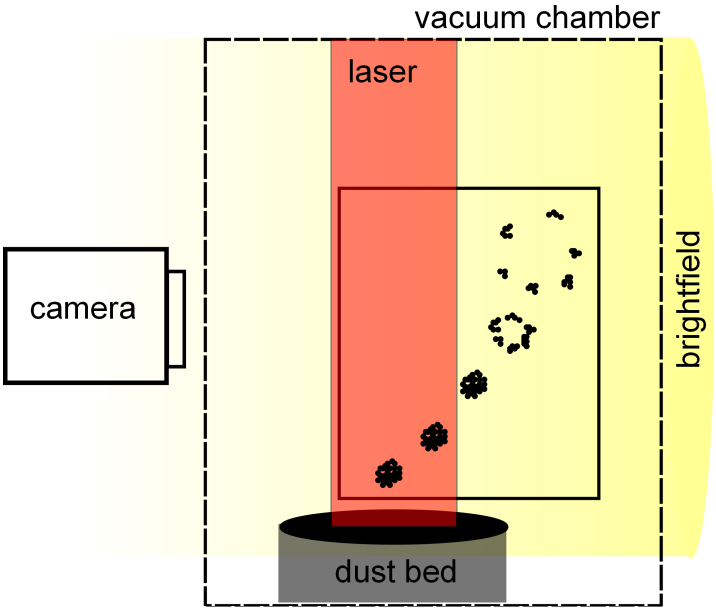

Figure 7.12: Sketch of the experimental vacuum chamber within the drop tower experiment. An aggregate is lifted from the dust bed and after leaving the illumination, it starts to disintegrate.

In addition, a red laser (655 nm, 12.6 kW/m^2) illuminated a sample of carbon spheres with a spot diameter of 8 mm. The size distribution of the dust samples are shown in Fig.**??**.The temperature of the dust bed is estimated to 420 - 650 K (Fig.4.1) (Kocifaj et al., 2011) and the sample was in a vacuum chamber with 4 mbar ambient pressure. Once the aggregates leave the surface, they are free to radiate into the surroundings and cool from the outside-in. Hence, a radial temperature gradient established within the aggregates.

As shown in Sec.4.2 and Chap.5, a temperature gradient over the surfaces of dust particles leads to thermal creep for large Knudsen numbers, $Kn \geq 1$, from cold to warm and thus in this case from the cool outer surface of the dust aggregate to the warm inside. Eventually, in small timescales, an overpressure builds up inside the aggregate, which is known as the Knudsen compressor effect (Knudsen, 1909). If the force induced by the overpressure overcomes the tensile strength of the aggregate, the aggregate disintegrates. The fragments can be described by linear motion, whereas the initial acceleration cannot

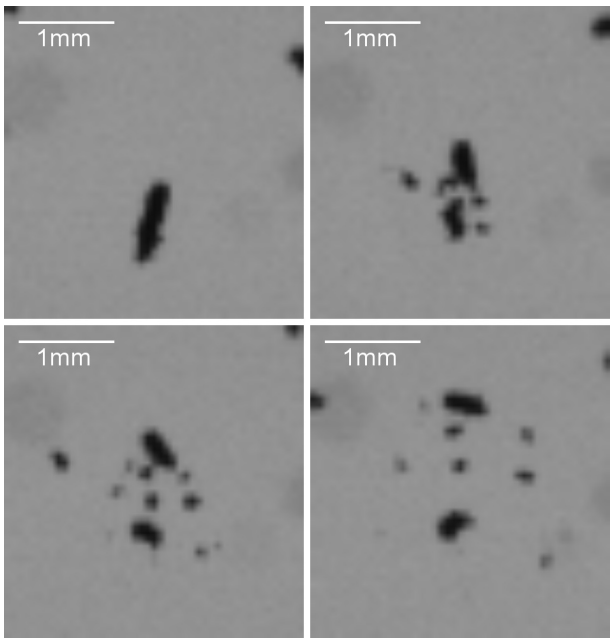

Figure 7.13: Example of a Basalt aggregate disintegrating due to an overpressure induced by thermal creep. The time steps between each image are 5 ms (de Beule et al., 2015b).

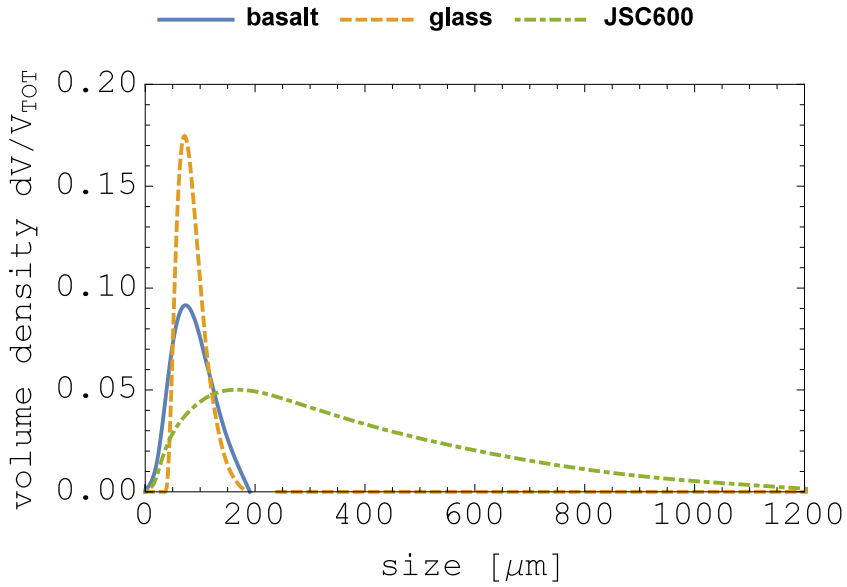

Figure 7.14: Size distributions of the dust samples analyzed in this experiment. From de Beule et al. (2015b).

be observed due to a low resolution with 1,000 fps (de Beule et al., 2015b). However, the linear motion of the fragments implies that the acceleration is restricted to a spatial extend smaller or in the order of the spatial resolution. Fig.**??** shows the data of an explosion reduced to the size and velocity of the fragments in the center of mass system.

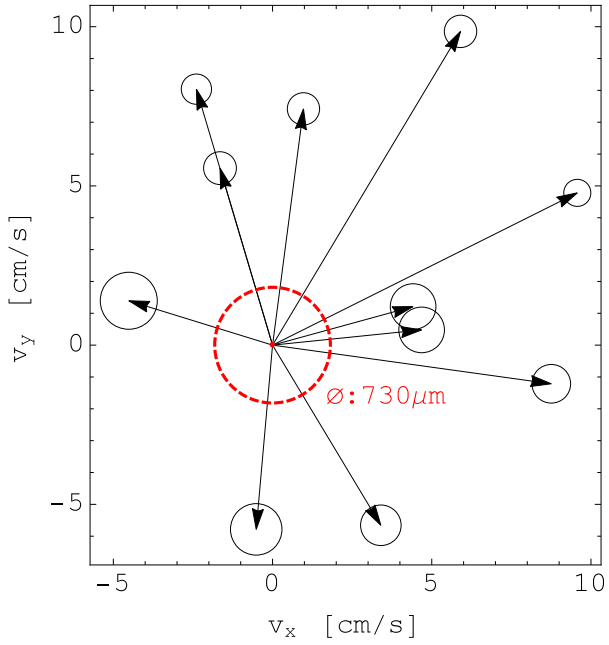

Figure 7.15: Velocities (2D projections) and sizes of the fragments in the center of mass system of a disintegrating particle (de Beule et al., 2015b).

For the model of disintegration, we approximate the aggregate as a core-mantle structure with the individual grains forming a shell surrounding a central pore (Fig.**??**). The aggregate is heated within the laser beam and when it leaves the illumination its surface cools by thermal radiation, resulting in a temperature gradient from the surface to the core of the aggregate. As shown in Sec.**??**, a temperature gradient can induce an overpressure in 100 μm depth of a dust bed. The suspended, cooling aggregate subsequently starts to soak in gas until an overpressure is reached, which breaks the contacts and smaller sub-units down to individual grains are accelerated by the pressure as long as the expansion takes.
The maximum pressure difference between outside and inside of the aggregate is given by Knudsen (1909):

$$\Delta p_{\max} = p_0 \left(\sqrt{\frac{T_i}{T_0}} - 1 \right), \tag{7.11}$$

with the ambient pressure p_0 and the ambient temperature T_0. T_i is the temperature within the pore and depends on the laser intensity and the illumination time. The time of illumination is between 1 and 5 seconds, which leads to an inner temperature between 420 K and 480 K for the 5.4 kW/m^2 laser (used for Basalt) and between 560 K and 650 K for the 12.6 kW/m^2 laser (used for glass-spheres and JSC Mars 1A) referring to Kocifaj et al. (2011). This provides the upper limits of overpressure within the aggregate: $\Delta p_{\max}$

is between 73 Pa and 105 Pa for Basalt and between 146 Pa and 189 Pa for JSC Mars 1A and the glass spheres.

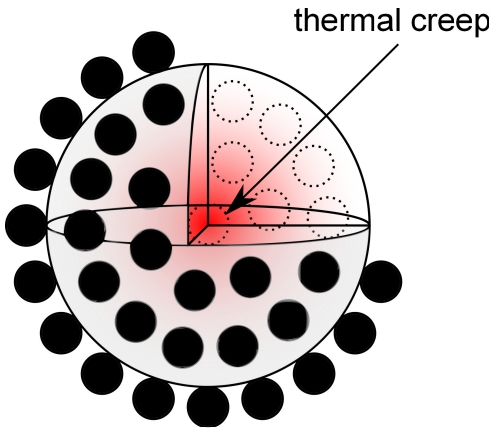

Figure 7.16: Aggregate model with a central pore surrounded by the individual grains and thin capillaries allowing thermal creep to enter the pore (de Beule et al., 2015b).

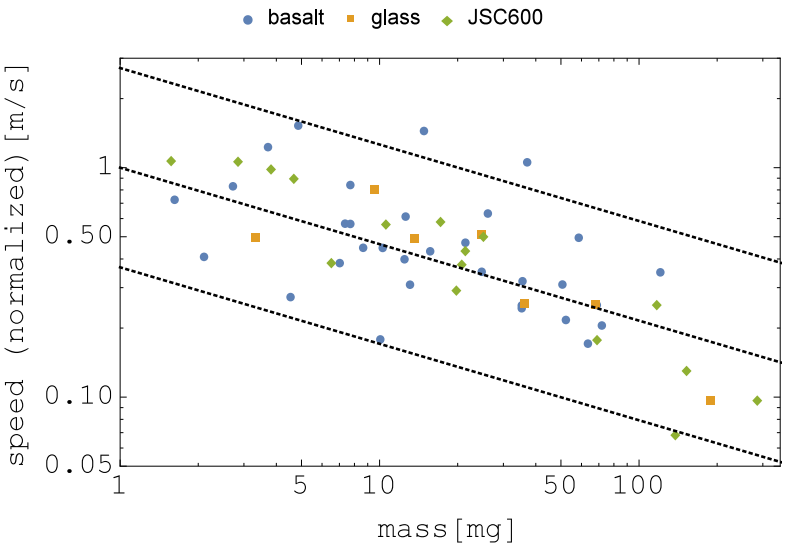

Figure 7.17: 2D velocity over mass. The velocities are normalized for different disintegrations. Overplotted are lines proportional to $1/m^{1/3}$ according to a simple explosion model. The data cover seven events (four for Basalt, two for palagonite (JSC Mars 1A) and one for carbon glass spheres) (de Beule et al., 2015b).

The kinetic energy values are based upon the 2D projections, which are systematically too low. This would shift the tensile strength to somewhat larger values. As every fragment is accelerated by the same pressure, the acceleration is proportional to $1/r$ with a fragment size r. As all fragments are accelerated over the same time, the final (measured) velocities also depend on $1/r$ or $1/m^{1/3}$. The mass dependence of the ejecta velocity seen in Fig.**??**

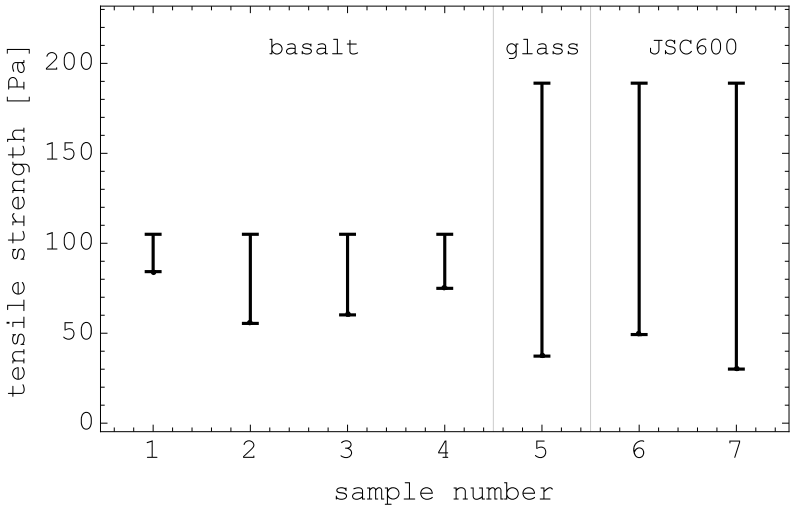

Figure 7.18: Tensile strength for different aggregates. The upper limits are the maximum pressure differences from Eq.**??** (de Beule et al., 2015b).

supports this model. Due to the low resolution of the images, it is not possible to measure the pressure changes during the expansion and hence, the acceleration of the fragments cannot be measured. However, the lower limit (due to 2D projections) of the total kinetic energy in the center of mass system can be calculated by

$$\Delta E_{\text{kin}} = \sum_i \frac{m_i}{2} v_i^2 \tag{7.12}$$

to about 0.1 nJ.
The pressure release energy is given by

$$E_{\text{pres}} = \int (p_i - p_o) dV. \tag{7.13}$$

Assuming that the shell of the aggregate expands by a distance of spatial resolution adiabatically or with a constant $b = p_i V^\kappa$ with the isentropic exponent κ, we obtain

$$E_{\text{pres}} = \int_{V_I}^{V_E} \left(\frac{b}{V^\kappa} - p_0 \right) dV = \frac{b \left(V_E^{1-\kappa} - V_I^{1-\kappa} \right)}{1-\kappa} + p_0 (V_I - V_E), \tag{7.14}$$

with the initial volume of the pore V_I and the volume of the pore after the expansion V_E. The constant b is given by $b = (p_0 + \Delta p) V_I^\kappa$. Thus, we obtain

$$\Delta p = \frac{\left[E_{\text{pres}} - p_0 (V_I - V_E) \right] (1-\kappa)}{V_I^\kappa \left(V_E^{1-\kappa} - V_I^{1-\kappa} \right)} - p_0 \tag{7.15}$$

in total. As the fragmentation occurs in a dry air environment, $\kappa = 1.4$ (Kouremenos and Antonopoulus, 1987). Assuming an initial pore size between $0.3 R_A$ and $0.8 R_A$ with the radius of the aggregate R_A, this allows estimating V_I. To calculate V_E, radii between $R_A +$ 17 μm and $R_A + 188$ μm are considered, which is an estimation resulting from the limited temporal resolution of the data. Finally, Eq.**??** allows calculating the tensile strength as $E_{\text{pres}} = \Delta E_{\text{kin}}$. The results are shown in Fig.**??**.

Forces

This experiment showed how to measure the tensile strength of dust aggregates. Assuming now that a dust particle at the surface of dust bed experiences the same magnitude of cohesive forces as a particle within a suspended aggregate as described in the experiment, the cohesive force acting on this particle can be calculated.

Fig.**??** shows the tensile strength of the different dust samples and based upon which a valuable measure for the overpressure needed to break the contacts of a particle within this aggregate is about 100 Pa. In a rough estimation, this overpressure applied on the cross section of a (spherical) particle provides it cohesion,

$$F_{\text{Cohesion}} = p_{\text{tensile}} \pi r^2. \tag{7.16}$$

With the parameters in Tab.**??**, the cohesion force is $F_{\text{Cohesion}} = 1.9 \cdot 10^{-7}$ N. It is

Table 7.5: Parameters for the estimation of the cohesive force acting on a spherical particle at the surface of an illuminated dust bed. The mass of a spherical particle is given by $m_P = 4/3\pi r^3 \rho_P$ with the radius r of the particle and its density ρ_P. The effective surface energy is from Heim et al. (1999).

particle radius	r	=	25 μm
particle density	ρ_P	=	2890 kg/m^3
tensile strength	p_{tensile}	=	1 mbar
effective surface energy	γ	=	0.02 J/m^2

important to note is that this is only an upper estimation of the cohesive force, because the measured tensile strength is in the order to breaking an entire aggregate and not separating only one particle from it.
In Sec.4.5, it was shown that the cohesive force can be calculated by Eq.4.23, assuming an effective radius R_{eff}. With the given parameters in Tab.**??**, the effective radius can be calculated as

$$R_{\text{eff}} = \frac{F_{\text{Cohesion}}}{3\pi\gamma} = 1\ \mu\text{m}. \tag{7.17}$$

Although the calculations are based upon rough assumptions, the general statement is clear: the cohesive force of a particle bound to a dust bed is dominated by the small particles within the dust bed that are in contact with this particle.

$$\begin{aligned} F_{\text{total}} = & \underbrace{F_{\text{gas drag}}}_{=2\cdot10^{-10}\text{ N}} - \underbrace{F_{\text{photophoresis}}}_{=6.5\cdot10^{-11}\text{ N}} - \underbrace{F_{\text{thermophoresis}}}_{=2\cdot10^{-12}\text{ N}} \\ & + \underbrace{F_{\text{Knudsen}}}_{=3\cdot10^{-8}\text{ N}} + \underbrace{F_{\text{cohesion}}}_{=10^{-9}\text{ N}\ldots10^{-7}\text{ N}} + \underbrace{F_{\text{gravity}}}_{\text{Sec.??}}. \end{aligned} \tag{7.18}$$

7.5 Parabolic flight experiments

The advantage of a parabolic flight is to collect data in reduced gravitational acceleration. A PFC comprises three flight days, with 31 parabolas each day. There are two different kinds of PFCs: μ-g and partial-g campaigns (g = 9.81 m/s^2). On a μ-g PFC, the low-g phase of the parabola is 0 g $\pm$ 0.05 g. On a partial-g campaign, a flight day comprises 13 parabolas at Mars-g, 12 parabolas at Moon-g and 6 parabolas at μ-g as on the μ-g PFC.

A parabola begins with a 20 s Hyper-g phase (1.7 g), followed by the 20 s low-g phase (μ-g, Mars-g, Moon-g) and ends with a 20 s Hyper-g phase. Between the parabolas are breaks of 1 to 8 minutes to prepare the experiment for the next parabola.

Experiment 1: Glass Cylinder

The first setup for light-induced erosion in microgravity is shown in Fig.**??** and published in de Beule et al. (2013). Four chambers filled with basaltic dust samples (different sizes < 125 μm) are enclosed by a rotatable glass cylinder in a vacuum chamber with 6 $\pm$ 0.9 mbar. A laser (655 nm) is focused on the dust bed with a diameter of about 6 mm, providing an intensity of 12 $\pm$ 2 kW/m^2. The ejection of particles is tracked by optical imaging and the gravity acting on the experiment is measured by an accelerometer.
The glass cylinder and the chambers were independently rotatable by a rotational feedtrough from the outside. After each parabola and before the next, the inner wall of the glass cylinder is cleaned by a small strip of foam to ensure that the laser and the camera view were not affected by dust.

The vacuum chamber is part of an experimental setup installed in a rack, which is the term for a construction satisfying the conditions of a parabolic flight, such as being robust and incombustible. In addition, working with a laser requires a doubled compartment to be light-proofed. The rack of this experiment included a membrane pump for adjusting the pressure within the chamber during flight, a pressure sensor, a camera, a laser and a laptop for the recorded data. Further details about this experimental setup are published in de Beule (2011).

A main problem of this experiment regarding μ-g PFCs was the residual gravity during the low-g phase and especially in the transition regime between the Hyper-g and the μ-g phase. The rapid change of gravitational acceleration between Hyper-g and low-g led to a relaxation within the dust bed and in most of the parabolas the beginning of the μ-g phase begins with negative residual gravity down to -0.01g, which leads to a fountain of dust within the vacuum chamber because the small dust particles are very sensitive to changes in gravitational acceleration.

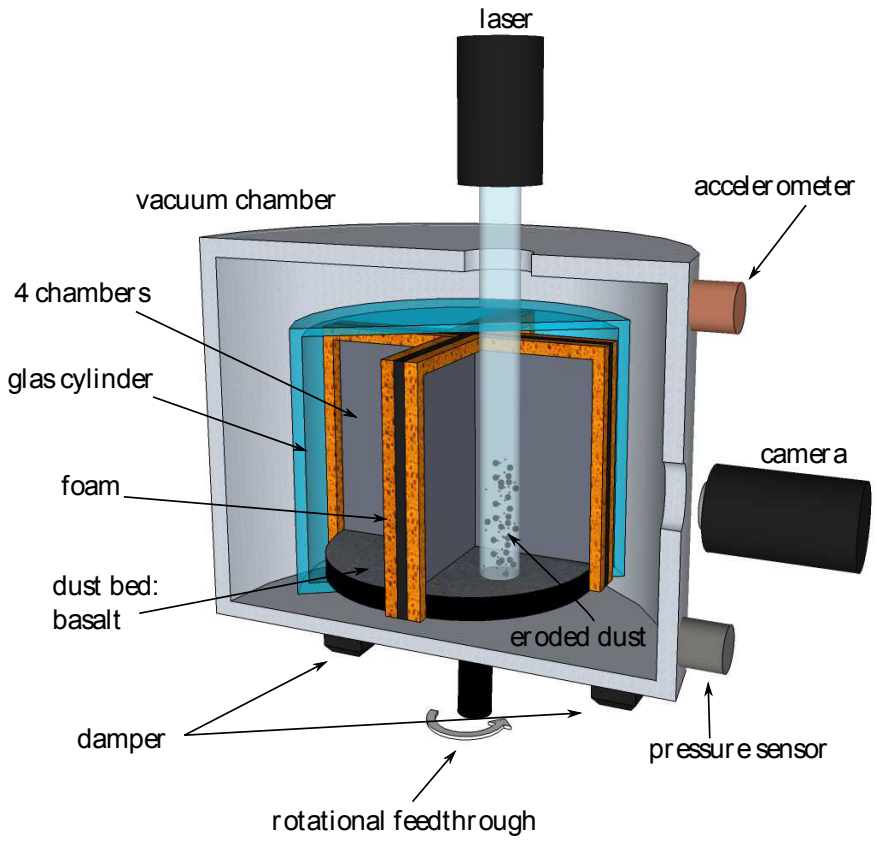

Figure 7.19: Setup of the first parabolic flight experiment where the gravity dependence of light induced erosion was investigated (de Beule et al., 2013).

Experiment 2: Centrifuge

After investigating the erosion of particles with the setup described before, it was improved regarding the handling of the residual gravity on a microgravity flight. Avoiding negative values in the residual gravity, the vacuum chamber was now placed on a centrifuge, which rotates at low speed.

The platform starts to rotate during the Hyper-g-phase, whereby the accurate speed for a particular gravity on the dust bed is reached before the microgravity phase. The gravity on the dust bed can be set between 0.1 g and 0.5 g. In rare cases, when the parabola sufficiently smooth, lower gravity down to 0.05 g can be reached. A shutter is used to close the dust bed and prevent dust loss during the transition between the Hyper-g and low-g phase. The shutter does not open before the residual gravity of the experiment is sufficiently low and closes once a critical value of gravity is exceeded or after a time of 20 seconds.

The camera is used to measure the eroded particles. LED lights are necessary to track particles after the laser is turned off.

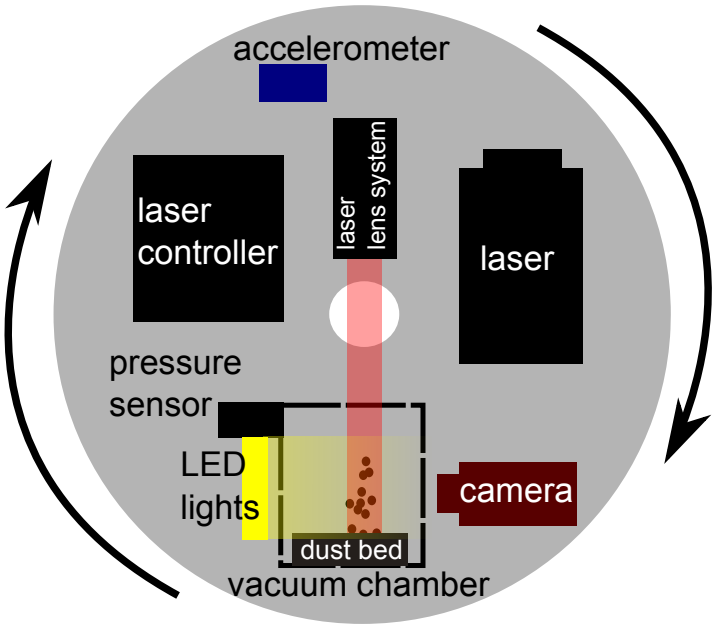

Figure 7.20: Top view of the centrifuge of the second parabolic flight experiment. The vacuum chamber, camera and laser are mounted on a rotating platform, which rotates with less than 1 Hz. A shutter in the vacuum chamber (not seen in the sketch) closes the dust container for the Hyper-g phase and in case of exzessive residual gravity. The gravity within the vacuum chamber can be calculated with the rotating speed or measured with an accelerometer.

Results

In the first experiments on a PFC, the main focus was on the gravity dependence of the light-induced erosion. The most reliable data were taken on the Joint European Partial-G Parabolic Flight campaign, where four different g-phases were achieved: 0.16 g (Moon), 0.38 g (Mars), 1.7 g (Hyper-g) and 1 g (Earth).

Released particles are observed by a camera with 60 frames per second. The gray scale value of each image is taken as a measure for the number of eroded particles. Fig.**??** shows an overlay of 100 images at different gravitational accelerations from the glass cylinder experiment.

Although a parabolic flight has the advantage that different levels of gravity can be tested, the effects of the transitions between the different g-levels have to be filtered out: Fig.**??** shows the raw acceleration data of one parabola during a Moon parabola. The gray peaks show the erosion rate of the dust bed, which clearly increases between the Hyper-g and the Moon-g phase. After this transition regime, the erosion of particles occurs continuously for about 10 s. 12 parabolas in total (6 Moon and 6 Mars) are analyzed and the ejection rates depending on gravity are measured.

The observation of light-induced erosion showed that the lifting force applied to the parti-

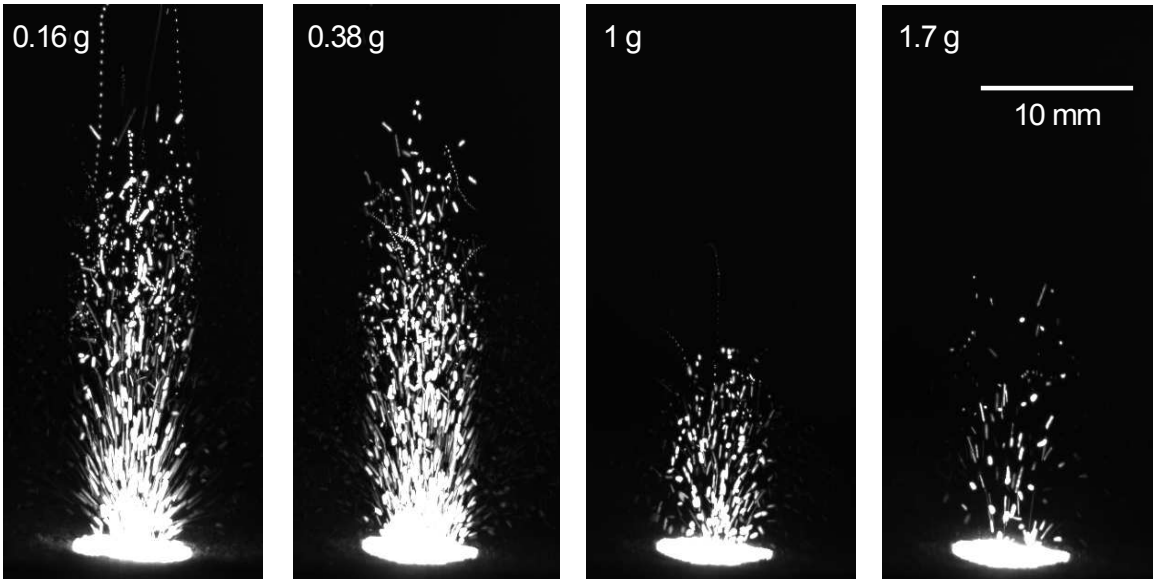

Figure 7.21: Overlay of 100 images taken at different gravitational accelerations during the Joint European Partial-G PFC with the glass cylinder. The light intensity is 12 kW/m^2, the ambient pressure 6 mbar and the dust sample comprises basaltic grains ($<$ 125 μm) (de Beule et al., 2013).

cles is time dependent. Particles are ejected after a certain time span Δt (de Beule et al., 2014). Hence, in a simple assumption, the lifting force is assumed to be proportional to this time span with

$$F_{\text{lift}} = \omega \cdot \Delta t \tag{7.19}$$

and needs to be at least in the order of cohesion and gravity

$$F_{\text{lift}} = \omega \cdot \Delta t = \Delta m \cdot g + F_{\text{C}}, \tag{7.20}$$

with the ejected mass Δm and the cohesion force F_{C}. The ejection rate (ejected mass per time span) based upon gravity can thus be described by (de Beule et al., 2013)

$$N(g) = \frac{\Delta m}{\Delta t} = \frac{\omega}{g + \frac{F_{\text{C}}}{\Delta m}} \tag{7.21}$$

This fit for the experimental data shown in Fig.**??** provides the parameters $\omega_3 = 1.6$ m/s^3 and $F_{\text{C}}/\Delta m = 6.1 \pm 1.2$ m/s^2. $F_{\text{C}}/\Delta m$ contains the information at which cohesive force an ejected aggregate was bound to the dust bed. The ejection rate is strongly connected to the cohesive forces within the dust bed, as this force sets the limit for erosion at one gravity level.

After the experiments on the Joint European Partial-g Parabolic Flight Campaign, additional data were collected for Basalt ($<$ 125 μm) with the centrifuge on a Zero-G PFC. The ejection rate at three additional gravity levels could be measured: 0.1g, 0.2g and 0.3g. This opportunity was used to explore the lower g-levels and the increase from 0.3g to 0.1g.

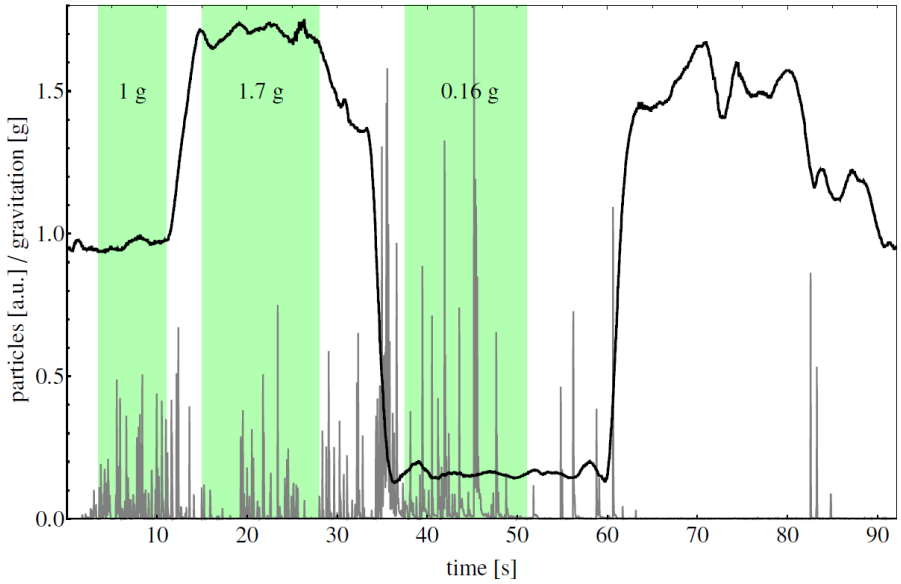

Figure 7.22: Example of raw acceleration data from one Moon parabola. The black line shows the gravitational acceleration in units of Earth gravity $g = 9.81$ m/s^2. The gray peaks indicate the erosion rate of the dust bed in arbitrary units. The green bars show which part of the different g-phases for the analysis are taken (de Beule et al., 2013).

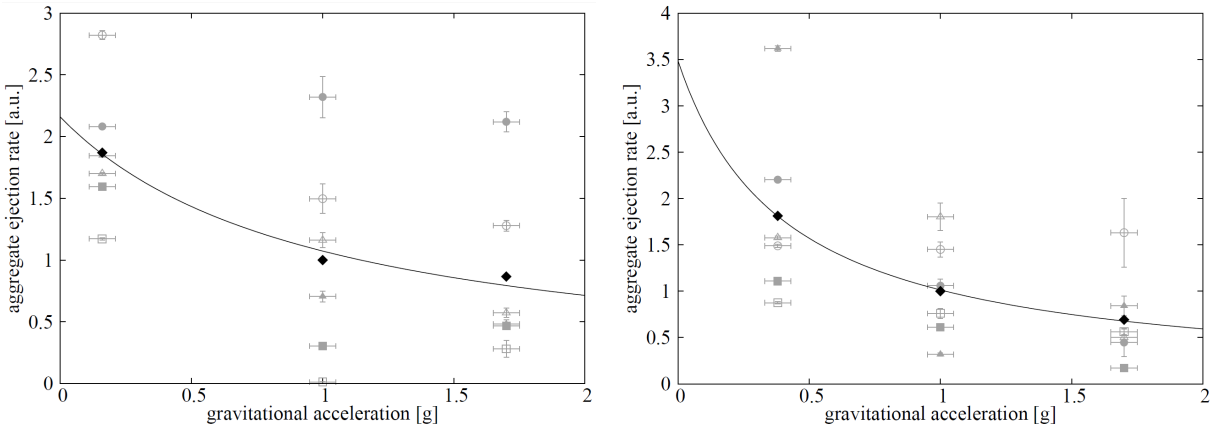

(a) Data set for the 6 Moon parabolas.

(b) Data set for the 6 Mars parabolas.

Figure 7.23: Data set for the 12 parabolas (de Beule et al., 2013). The averaged particle erosion rate is set to 1 at 1g. The results from the experiments are presented in gray, the average value in black and the black line shows the trend for the averaged data according to the model (Eq.**??**).

Fig.**??** shows the collected raw data from the first and second day of the parabolic flight. Because there were already data for Moon and Mars gravity, most of the parabolas were used for data points at 0.1g. The analysis of the data was the same as for the JEPPF campaign: The transition regime was identified, filtered out (Fig.**??**) and the gray scale value of the images were taken as a measure for the erosion rate. Some parabolas are not

shown in the plots because no data could be collected there, e.g. due to excessive residual gravitational accelerations. Whereas the black data points in Fig.?? represent reliable raw data sets, the red dots represent data where a crater within the dust bed could be seen. Given that the dust bed could not be renewed during the flight, the laserspot burrowed into the dust bed and formed a crater.

This crater prevents further release of particles, as small and loose particles are already ejected by the laser and more cohesive particles remain within the crater. This effect occurs when a small laser spot is focused on the dust bed. Hence, enlarging the laser spot on the surface of the dust bed would prevent the crater, although it was not conducted for this experiment (de Beule, 2011).
The new collected raw data in Fig.?? show no significant increase to lower g-levels.

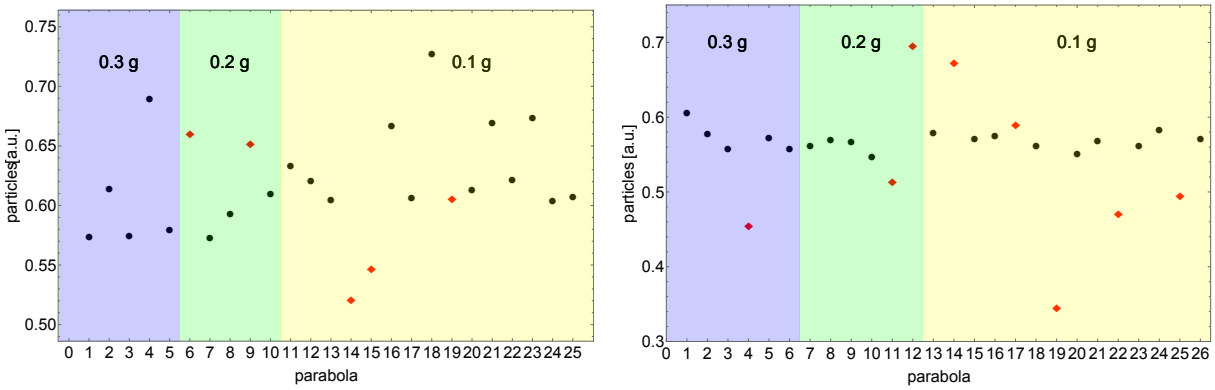

(a) Data set for the 1st day.

(b) Data set for the 2nd day.

Figure 7.24: Raw data set of the first and second day of the PFC with the centrifuge. Data were collected for the three different g-levels: 0.1g, 0.2g, 0.3g. The black dots represent reliable data without any abnormalities. The red dots represent data where a visible crater can be identified.

Fig.?? shows the general dependence of the ejection rate on the gravitational acceleration for different factors of $F_C/\Delta m$.
The plot shows that a reduction of this quotient effectively increases the ejection rate to lower g-levels (g $<$ 1). Whereas the increase from Earth-g to Moon or Mars-g is by a factor of 2 (Fig.??), there is no increase between lower g-levels (0.1g, 0.2g and 0.3g) in Fig.??. The data points are so alike that one might suggest that the plateau of a maximum erosion rate was reached during those parabolic flights.
Consequently, Fig.?? was complemented by a data point at 0.1 g with the same value as for Moon-g (Fig.??). This is a valuable assumption as Fig.?? shows no significant difference between 0.1g, 0.2g and 0.3g. This does not change the general statement of the gravity dependence of the erosion rate: the erosion rate increases by a factor of 2 from Earth-g to Moon-g, although it reaches a plateau and no further increase is visible.

The simple model used for this data does not consider the self-shielding effect of the dust bed by ejected aggregates. When dust is lifted over the dust bed, it shields the dust

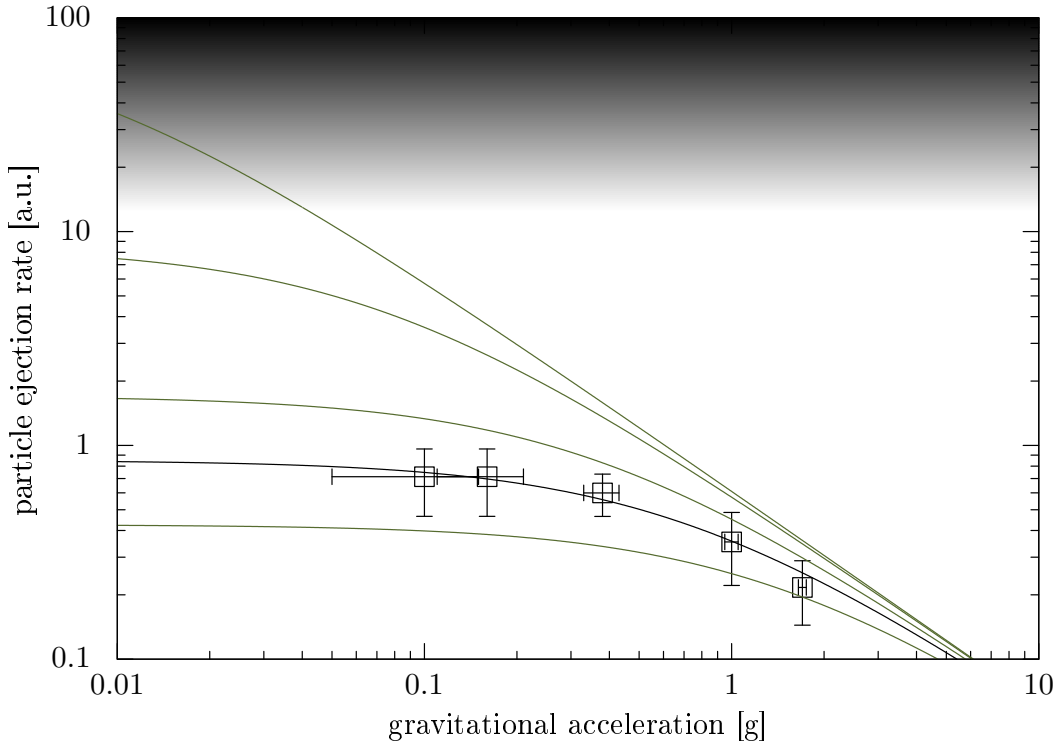

Figure 7.25: Gravity dependence of the erosion rate based upon the experimental values using Eq.**??**. The experimental value (squares) for $F_C/\Delta m$ is varied by a factor f with f = 2,1,0.5,0.1,0.001 (bottom to top). The color gradient at the top of the plot shows the shielding of the dust bed by ejected particles (de Beule et al., 2013).

bed from the light and hence the erosion rate would decrease as the temperature gradient decreases within the dust bed. de Beule et al. (2013) argued with a rough estimation that an increase of the erosion rate by a factor of 10 likely does not affect the erosion rate. This provides an upper limit for the erosion rate, although it is not further discussed here. In Fig.**??**, the color gradient indicates this self-shielding effect, which becomes important for very low $F_C/\Delta m$ coefficients.

Forces

The gravitational force acting on a single grain at the surface of the dust bed can be calculated by (Eq.4.27)

$$F_{\text{gravity}} = m_P \cdot g. \tag{7.22}$$

With the parameters in Tab.**??**, the gravitational force is $F_{\text{gravity}} = 2 \cdot 10^{-9}$ N on Earth. The experimental outcome (Fig.**??**) showed that cohesion dominates the retaining forces

Table 7.6: Parameters for the estimation of the cohesive and gravitational force acting on a spherical particle at the surface of an illuminated dust bed. The mass of a spherical particle is given by $m_P = 4/3\pi r^3 \rho_P$ with the radius r of the particle and its density ρ_P.

particle radius	r	=	25 μm
particle density	ρ_P	=	2890 kg/m^3

for g-levels smaller than 1 g, whereas cohesion becomes negligible for higher g-levels. With the results of the previous Sec.**??**, it was possible to provide an upper estimation of the cohesive forces. The results of this section show that the cohesive force is at least in the order of the gravitational forces.

$$\begin{aligned} F_{\text{total}} = & \underbrace{F_{\text{gas drag}}}_{=2\cdot10^{-10}\text{ N}} - \underbrace{F_{\text{photophoresis}}}_{=6.5\cdot10^{-11}\text{ N}} - \underbrace{F_{\text{thermophoresis}}}_{=2\cdot10^{-12}\text{ N}} \\ & + \underbrace{F_{\text{Knudsen}}}_{=3\cdot10^{-8}\text{ N}} + \underbrace{F_{\text{cohesion}}}_{=10^{-9}\text{ N}\ldots10^{-7}\text{ N}} + \underbrace{F_{\text{gravity}}}_{=2\cdot10^{-9}\text{ N}} . \end{aligned} \tag{7.23}$$

8

Conclusion

In Chap.4, all forces acting on/in an illuminated dust bed in a gaesous environment were presented. In Chap.5, a theoretical model for the light-induced erosion was derived, assuming that the dominating lifting force is based upon an overpressure within the dust bed.
Chap.6 introduced the dust samples and the basic setup for all experiments. Chap.7 showed the experiments performed to determine the value of all forces acting on/in an illuminated dust bed. Each experiment revealed new information for the total lifting (or retaining) force. In conclusion, the total force acting on a surface particle of an illuminated dust bed is given by

$$\begin{aligned} F_{\text{total}} = & \underbrace{F_{\text{gas drag}}}_{=2\cdot10^{-10}\text{ N}} - \underbrace{F_{\text{photophoresis}}}_{=6.5\cdot10^{-11}\text{ N}} - \underbrace{F_{\text{thermophoresis}}}_{=2\cdot10^{-12}\text{ N}} \\ & + \underbrace{F_{\text{Knudsen}}}_{=3\cdot10^{-8}\text{ N}} + \underbrace{F_{\text{cohesion}}}_{=10^{-9}\text{ N}\ldots10^{-7}\text{ N}} + \underbrace{F_{\text{gravity}}}_{=2\cdot10^{-9}\text{ N}}, \end{aligned} \tag{8.1}$$

based upon the parameters listed in Tab.8.1. Details of the calculations can be found in the previous Chap.7.
As the calculations (Eq.8.1) were conducted for this special case of one particle at the surface of an illuminated dust bed with the parameters listed in Tab.8.1, the parameters must be adapted to other circumstances when another case (dust sample, size, gas, temperature...) is treated.

Especially the direction of some forces is based upon the temperature distribution within the dust bed. In Sec.4.1, it was shown that one or two temperature gradients can develop based on the duration of illumination. On small time scales and with low light intensity (e.g. experiment of Sec.**??**), the illumination of the dust bed leads to an active layer with a temperature gradient below. In this case, the photo and thermophoretic forces are retaining forces for the particles within the temperature gradient.

On larger time scales ($>$ 1 min) and high light intensity ($>$ 10 kW/m^2), a solid-state greenhouse effect establishes inside the illuminated dust bed with two temperature gradients (Sec.4.1). The maximum of temperature is in the subsurface of the dust bed, whereby the surface particles are cool on the top and warm at the bottom. Hence, the photo and thermophoretic force act as lifting forces in this case.

However, the calculation clearly shows that the total retaining force acting on the particle is dominated by cohesion and gravity, whereas the lifting force is dominated by the temperature-driven gas flow (overpressure and gas drag).

Table 8.1: Summary of the parameters for the estimation of the lifting force acting on a spherical particle at the surface of an illuminated dust bed. The mass of a spherical particle is given by $m_P = 4/3\pi r^3 \rho_P$ with the radius r of the particle and its density ρ_P.

particle radius	r	=	25 μm
particle density	ρ_P	=	2890 kg/m^3
capillary radius	L_r	=	$0.23/2 \cdot r$
pressure	p	=	6 mbar
Boltzmann-constant	k_B	=	$1.38 \cdot 10^{-23}$ J/K
Avogadro constant	N_A	=	$6.022 \cdot 10^{23}$ (mol)$^{-1}$
molar mass (air)	μ	=	28.96 AMU
average temperature	T_{avg}	=	300 K
thermal conductivity (particle)	κ	=	1 W/(K m)
thermal conductivity (dust bed)	κ_g	=	0.01 W/(K m)
average temperature	T_{avg}	=	300 K
intensity	I	=	4 kW/(m^2)
temperature gradient (particle)	dT/dz	=	10^5 K/m
molar mass (air)	μ	=	28.96 AMU
temperature difference	ΔT	=	100 K
thermal conductivity (gas)	κ_g	=	0.01 W/(K m)
average temperature	T_{avg}	=	300 K
active layer depth	L_{active}	=	200 μm
temperature gradient depth	L_{thermal}	=	1 mm
tensile strength	p_{tensile}	=	1 mbar
effective surface energy	γ	=	0.02 J/m^2

9

Application

9.1 Transitional disk

The effect of light-induced dust ejections can be a key process of recycling dust during the formation of planets in protoplanetary disks. Planetesimals or smaller dusty bodies at the inner edge can be partly eroded (Wurm, 2007; Kelling and Wurm, 2011).

The position of the edge in a number of transition, pre-transition and full disks has been modeled by Espaillat et al. (2012). As described in Sec.3.1, pre-transition disks are disks with an optically thin inner wall at the dust sublimation radius and a second outer wall. In Tab.9.1, modeled radii from Espaillat et al. (2012) of the disks and the luminosities of the host stars are shown.
In Chap.5,it was shown that based upon the new model, the lifting force on the particles is proportional to the overpressure established by the temperature difference ΔT (Eq.5.10)

$$F \propto \Delta p \propto p \Delta T \tag{9.1}$$

The simulations of Kocifaj et al. (2011) show that the temperature difference ΔT is approximately proportional to the incoming light flux, as shown in Fig.4.3. The experiments in Sec.**??** have shown that particle eruptions continuously occur at all gravity levels at the light intensity $I \geq 12$ kW m^{-2}, pressure $p = 6$ mbar and temperature T of about 300 K.

Object	L_{star} (L_{sun})	W_i (AU)	W_e (AU)	W_o (AU)
FM 515	2.5	0.12	0.63	45
FM 618	2.2	0.22	0.59	11
LRLL 21	3.8	0.13	0.80	9
LRLL 31	5.0	0.32	0.89	14
LRLL 37	1.3	0.17	0.46	5

Table 9.1: Pre-transitional Disks Modeled by Espaillat et al. (2012). L_{star} is the star's luminosity, W_i the inner wall, W_e the erosion dividing line and W_o the outer wall. The erosion limit distance is the distance up to which disassembly of larger dusty bodies would be possible (de Beule et al., 2014).

The threshold conditions for the erosion were not measured in this experiment, although Wurm (2007) found $I = 50$ kW m^{-2} at 1 mbar and 300 K at Earth gravity. Hence, light induced erosion can be expected as long as $Ip/T > 15$ kW m^{-2} Pa K^{-1} (Wurm, 2007). In addition, Wurm (2007) found that this condition is reached at a distance of 0.4 AU in a minimum mass solar nebula (Hayashi et al., 1985).

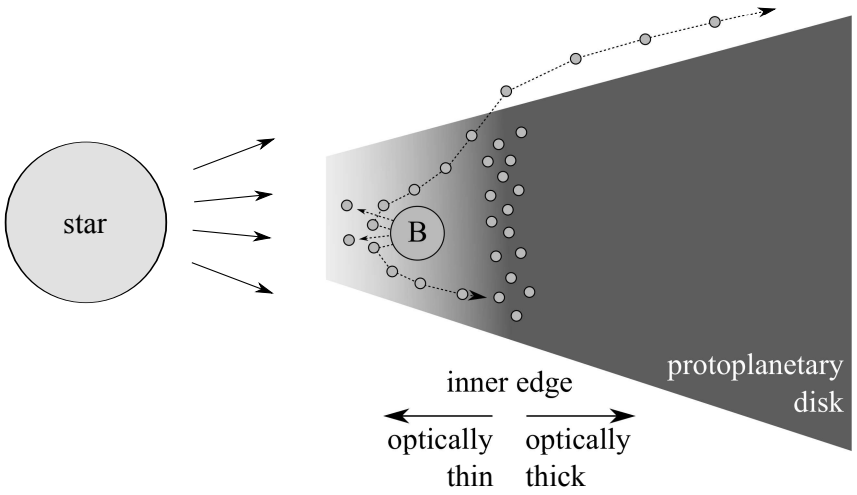

Figure 9.1: In the optically thin part of a protoplanetary disk, an inward drifting porous body (B) can be eroded by light induced erosion. The eroded mass can be transported outwards again by e.g. photophoresis (de Beule et al., 2014).

Unfortunately, the pressure and temperature at the mid -planes of pre-transitional disks are not known for certain, although the luminosities are (Espaillat et al., 2014). Hence, the dividing line between erosion and stability for the different objects in Tab.9.1 is assumed to be where the light flux of the host star equals that of a solar-type star in a minimum mass solar nebula or 0.4 AU $\times\sqrt{L/L_{\rm sun}}$ (Tab.9.1), which implies that the temperature and pressure at this distance are the same as in the minimum mass solar nebula at 0.4 AU.
For the temperature, this is a consistent assumption as the blackbody radiation temperature that defines the temperature of the disk in the minimum-mass solar nebula would be the same at the same incoming light flux.The pressure is less certain but one might argue that more luminous stars have denser disks. Therefore, it is assumed that the pressure is equal to that in a minimum mass solar nebula at the dividing line.

Tab.9.1 shows that the erosion dividing line is within the gap of the pre-transitional disk in all cases. In general, erosion is possible where the disk is optical thin, whereby light can easily reach the orbiting bodies. In full disks this is even possible at the inner edge, where the temperature is so high that melting or sintering may be an issue.

The erosion of planetary bodies in pre-transitional disks might be a mechanism to provide the small dust over the lifetime of the disk (Sec.3.1). Eroded particles within the inner gap of a pre-transitional disk can drift to the outer wall by photophoresis and increase the particle density locally (Krauss and Wurm, 2005; Haack and Wurm, 2007), which leads to enhanced growth of dust aggregates.

The holes of transitional disks are all larger than the erosion limit distance. Given that they have a largely reduced density the extent to which erosion will work here is unclear, although even small erosion zones can recycle parts of traversing bodies. Therefore, at early full disk times erosion will influence the particle recycling at the inner edge. In later pre-transitional and transitional evolution times of the clearing phase, the light-induced erosion will be an important factor in shaping the size distribution or even triggering later formation of larger bodies at the outward moving edge.

9.2 Mars

As outlined in Sec.3.2, the martian surface provides the perfect conditions for a light-induced gas flow through its regolith: if the martian soil is heated by solar insolation, gas will be pumped from colder soil layers beneath the heated layers towards the surface.
At shadowed places on the surface, gas will be efficiently soaked down into the soil, traverse the underground and pumped up again to the illuminated (heated) surface, as shown in Fig.9.2.

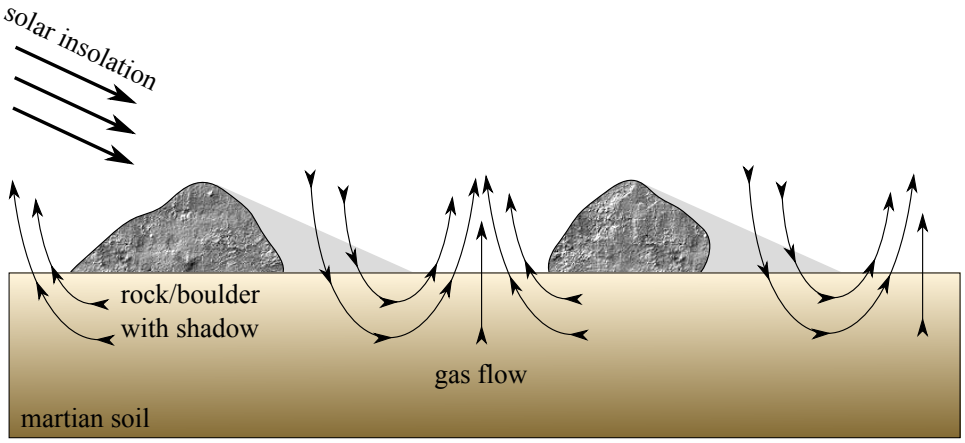

Figure 9.2: Schematic of the martian soil acting as a natural pump. The solar insolation on Mars leads to a gas flow from the colder deeper layers within the soil to the heated surface above due to thermal creep. The resulting pressure difference inside the regolith soaks up atmospheric gas from shadowed places into the soil and pumps it underneath towards the illuminated surface (de Beule et al., 2014).

In regions of Mars where dust particles and sizes exist in the micrometer range, the pores within the soil act as micro-channels, which is sufficient for the low atmospheric pressure on Mars to provide the regolith with the ability to pump gas. In addition, the experiment in Sec.**??** showed that a constant temperature beneath the surface of Mars can effectively reduce the threshold for lifting forces.
The overpressure within the soil can be calculated by (Sec.**??**)

$$\Delta p = \frac{L_{x2}}{L_{x1} + L_{x2}} p_{avg} \frac{\Delta T}{T} \frac{Q_T}{Q_P}. \tag{9.2}$$

As the atmospheric gas and solar insolation (temperature) are different from Earth, the results from the experiment must be extrapolated to martian conditions. Computations for the temperature distribution were conducted for an intensity of 700 W/m^2, as shown in Fig.9.3.

According to these simulations, an expected temperature difference of $\Delta T = 150$ K for a length $L_{x1} = 50$ mm and constant temperature (activated layer) at a length of $L_{x2} = 1$ mm can be assumed. Using CO_2 rather than air with a molecular mass of $m_{CO_2} = 44$ AMU, the geometric diameter of 4.63×10^{-10} m (Chapman and Cowling, 1970) results in a cross section $\sigma_{CO_2} = 1.6 \times 10^{-19}$ m^2. At p = 6 mbar with a particle density

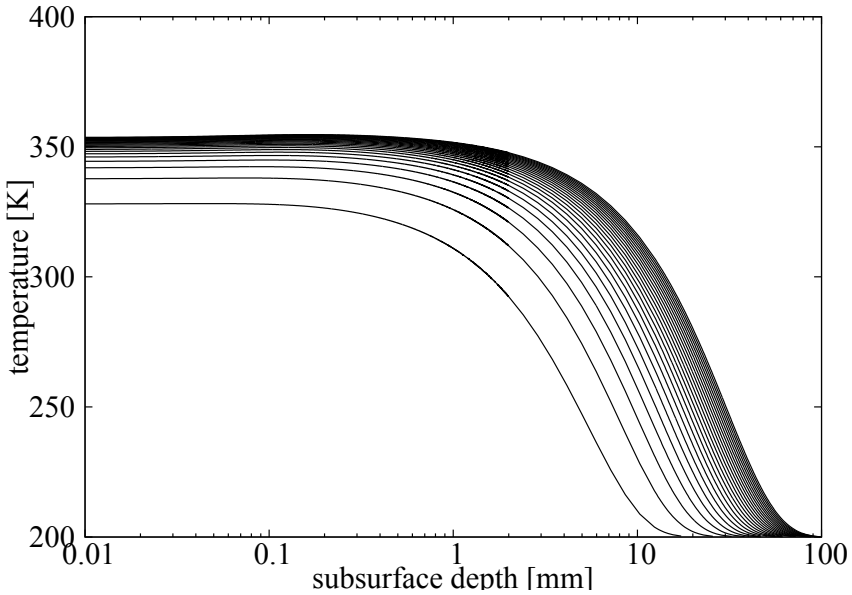

Figure 9.3: Simulation of the temperature profile within a dust bed comprising 25 μm spheres at an average temperature of 200 K. The dust bed has a thermal conductivity of 0.01 W/(Km). The light flux is 700 W/m^2 and illumination times are 0.5 h, 1 h, 1.5 h..., 12.5 h from bottom to top. Due to the simplification of the model, the maximum temperatures are larger than on Mars. (de Beule et al., 2015c).

$n = p/(k_B T)$ (T = 200 K) the mean free path of CO_2 is $\lambda = (\sqrt{2} n \sigma_{CO_2})^{-1} = 19$ μm. Hence, the ratio between Q_T and Q_P is 1.68 (Sone and Itakura (1990)). At an average temperature of $T = 200$ K, Eq.9.2 provides an overpressure of $\Delta p = 0.01$ mbar. The pressure induced force can be calculated via $F = \Delta p \sigma$ and with a particle cross section $\sigma = \pi r^2$ (r = 25 μm) the resulting force is F = $1.8 \cdot 10^{-9}$ N. With the density $\rho = 2890$ kg/m^3 (e.g. Basalt) and $m = 4/3 \pi r^3 \rho$, the gravitational force on the same particle on Mars is $F_G = (0.38g) m L_{x_2}/(2r) = 1.4 \cdot 10^{-8}$ N. Hence, the activation of a layer with 1 mm thickness reduces the needed lifting force of 13% against gravity (Küpper et al., 2014).

The gas flow through the martian regolith is a directed gas flow: vertical into the soil and horizontal within the soil. The experiments showed that gas velocities of cm/s are possible suitable conditions.

The water cycle on Mars describes exchange of water between a number of reservoirs on various timescales. These reservoirs are the atmosphere, the polar caps and the martian regolith. The interaction between the atmosphere and the porous regolith is through adsorption, condensation/sublimation, convective transport or diffusion (Smith, 2002; Hudson and Aharonson, 2008; Schorghofer and Forget, 2005).
The rate of water vapor transport through the martian regolith determines the removal and replenishment of subsurface ice. The results of this work show that the insolation of the martian regolith has a non-negligible influence on the rate of gas transported through the porous medium. Not only does it exceed the gas transport by thermal creep diffusion; moreover, but it is also a directed flow: soaking gas and water vapor in shadowed places into the regolith and pumping it upwards again in insolated places.

10

Outlook

The investigation of light-induced erosion showed a fascinating new aspect, namely a directed gas flow not only above but also *through* the dust bed.

The developed model showed that a temperature gradient within the dust bed suffices to induce a directed gas flow in a low-pressure environment. Hence, it could explain why erosion occurs right after the light source is switched on. While the gas flow can drag along loose dust particles from the surface, a layer of constant temperature at the surface can lead to an overpressure within the dust, catapulting dust particles from the surface. The solid-state greenhouse effect and photophoresis also affect light-induced erosion, albeit as a minor part.

The understanding and systematic investigation of the gas flow within the dust bed remains in fledgling stages; for instance, the observation of a strong increase of the ejection rate after the light source is turned off needs to be analyzed and interpreted in further detail. In addition, the question of how cracks and holes within a dust bed would influence the gas flow should be answered in the future concerning the application for Mars.

Although simulations thus far are in good agreement with the observed gas flow, the simulations of martian conditions can be improved within the computations for the temperature distribution of an illuminated dust bed, the particle form and sizes should become closer to reality, as well as the ambient temperature and insolation on Mars.

Another very interesting aspect of a light (temperature) induced gas flow is the choice of the sample: porous bodies can experience a rocket drive by the gas flow, accelerating them towards or away from a light source. Experimental setups are already in the planning stage: A porous body consisting of black glass spheres is placed on a sensitive scales measuring the difference in weight when illuminated from the bottom or top. The establishing gas flow reduces or increases the weight on the scales. Another planned setup is visualizing and measuring the gas flow within a non-uniform porous body (with cracks and wholes) in microgravity.

The gas flow can as well be used as a measurement for the tensile strength of a dust bed or suspended aggregates. The experiment of disintegrating aggregates in Sec.**??** showed

how a heated aggregate disintegrates due to an overpressure within. This experiment can be improved regarding the analysis of the initial acceleration right after the aggregate disintegrates. New experiments in the laboratory showed that it is possible to heat aggregates and drop them, so that they disintegrates in free-fall. With a high-speed camera it was possible to resolve the initial acceleration at 25.000 frames per second. The final analysis of these data needs to be done, as well as the use of different samples.

In addition, the observation of light induced erosion becomes interesting as well when the light source is turned off. The preliminary results show a strong increase of particle ejection right after turning of the illumination and this increase lasts for up to 10 s. This data, taken in low gravity, need to be interpreted in the near future and will complete the model of light induced erosion.

Bibliography

Aitken, J. (1884). On the formation of small clear spaces in dusty air. *Transactions of the Royal Society of Edinburgh Earth Sciences*, 32(17):239–272.

Barlow, N. (2008). *Mars: An Introduction to its Interior, Surface and Atmosphere*. Cambridge University Press (Cambridge).

Batchelor, G. K. (1865). *An Introduction to Fluid Dynamics*. Cambridge University Press (Cambridge).

Blake, D. F., Morris, R. V., Kocurek, G., Morrison, S. M., Downs, R. T., Bish, D., Ming, D. W., Edgett, K. S., Rubin, D., Goetz, W., Madsen, M. B., Sullivan, R., Gellert, R., Campbell, I., Treiman, a. H., McLennan, S. M., Yen, a. S., Grotzinger, J., Vaniman, D. T., Chipera, S. J., Achilles, C. N., Rampe, E. B., Sumner, D., Meslin, P.-Y., Maurice, S., Forni, O., Gasnault, O., Fisk, M., Schmidt, M., Mahaffy, P., Leshin, L. a., Glavin, D., Steele, a., Freissinet, C., Navarro-González, R., Yingst, R. a., Kah, L. C., Bridges, N., Lewis, K. W., Bristow, T. F., Farmer, J. D., Crisp, J. a., Stolper, E. M., Des Marais, D. J., and Sarrazin, P. (2013). Curiosity at Gale crater, Mars: characterization and analysis of the Rocknest sand shadow. *Science (New York, N.Y.)*, 341(6153):1239505.

Blum, J., Gundlach, B., Mühle, S., and Trigo-Rodriguez, J. M. (2014). Comets formed in solar-nebula instabilities! - An experimental and modeling attempt to relate the activity of comets to their formation process. *Icarus*, 235:156–169.

Blum, J., Schräpler, R., Davidsson, B. J. R., and Trigo-Rodriguez, J. M. (2006). The physics of protoplanetesimal dust agglomerates. I. Mechanical properties and relations to primitive bodies in the solar system. *The Astrophysical Journal*, 652:1768–1781.

Blum, J. and Wurm, G. (2008). The Growth Mechanisms of Macroscopic Bodies in Protoplanetary Disks. *Annual Review of Astronomy and Astrophysics*, 46(1):21–56.

Blum, J., Wurm, G., Kempf, S., and Henning, T. (1996). The Brownian motion of dust particles in the solar nebula: an experimental approach to the problem of pre-planetary dust aggregation. *Icarus*, 451:441–451.

Boss, a. P. (2008). Rapid formation of gas giants, ice giants and super-Earths. *Physica Scripta*, T130:14020–14027.

Boynton, W. V., Feldman, W. C., Squyres, S. W., Prettyman, T. H., Bruckner, J., Evans, L. G., Reedy, R. C., Starr, R., Arnold, J. R., Drake, D. M., Englert, P. a. J., Metzger, a. E., Mitrofanov, I., Trombka, J. I., D'Uston, C., Wanke, H., Gasnault, O., Hamara,

D. K., Janes, D. M., Marcialis, R. L., Maurice, S., Mikheeva, I., Taylor, G. J., Tokar, R., and Shinohara, C. (2002). Distribution of hydrogen in the near surface of Mars: evidence for subsurface ice deposits. *Science (New York, N.Y.)*, 297(5578):81–85.

Brock, J. (1962). On the theory of thermal forces acting on aerosol particles. *Journal of colloid and interface science*, 17:768–780.

Brown, R. H. and Matson, D. L. (1987). Thermal effects of insolation propagation into the regoliths of airless bodies. *Icarus*, 72(1):84–94.

Brown, R. L. and Richards, J. C. (1970). *Essays on the Packing and Flow of Powders and Bulk Solids*. Pergamon Press Ltd. (Oxford).

Chapman, S. and Cowling, T. G. (1970). *The Mathematical Theory of Non-uniform Gases*. Cambridge University Press (Cambridge).

Christensen, P. R. and Moore, H. J. (1992). The Martian surface layer. In Kieffer, H. H., Jakosky, B. M., Snyder, C. W., and Matthews, M. S., editors, *Mars*, pages 686–729. University of Arizona press (Tucson).

D'Angelo, G., Weidenschilling, S. J., Lissauer, J. J., and Bodenheimer, P. (2014). Growth of Jupiter: Enhancement of core accretion by a voluminous low-mass envelope. *Icarus*, 241:298–312.

Darcy, H. (1856). *Exposition et application des principes à suivre et des formules à employer dans les questions de distribution d'eau.* Libraire des corps imperiaux des ponts et chaussees et des nines, Quat des Augustins, Paris.

de Beule, C. (2011). Gravitationsabhängigkeit lichtinduzierter Stauberuptionen. diploma thesis, University Duisburg-Essen.

de Beule, C., Kelling, T., Wurm, G., Teiser, J., and Jankowski, T. (2013). From Planetesimals To Dust: Low-Gravity Experiments on Recycling Solids At the Inner Edges of Protoplanetary Disks. *The Astrophysical Journal*, 763:11.

de Beule, C., Landers, J., Salamon, S., Wende, H., and Wurm, G. (2015a). Planetesimal Formation in the Warm, Inner Disk: Experiments with Tempered Dust. *submitted*.

de Beule, C., Musiolik, G., and Wurm, G. (2015b). Measuring the Tensile Strength of Cohesive Granular Matter on Small Scales. *submitted*.

de Beule, C., Wurm, G., Kelling, T., Koester, M., and Kocifaj, M. (2015c). An Insolation Activated Dust Layer on Mars. *Icarus*, 260:23–28.

de Beule, C., Wurm, G., Kelling, T., Kuepper, M., Jankowski, T., and Teiser, J. (2014). The martian soil as a planetary gas pump. *Nature Physics*, 10:17–20.

Derjaguin, B. V., Muller, V. M., and Toporov, Y. P. (1975). Effect of contact deformations on the adhesion of particles. *Journal of Colloid Interface Science*, 53:314.

Dutrey, A., Semenov, D., Chapillon, E., Gorti, U., Guilloteau, S., Hersant, F., Hogerheijde, M., Hughes, M., Meeus, G., Nomura, H., Piétu, V., Qi, C., and Wakelam, V. (2014). Physical and chemical structure of planet-forming disks probed by millimeter observations and modeling. In *Protostars and Planets VI*. The University of Arizona Press (Tucson).

Ehrenhaft, F. (1918). Die photophorese. *Annalen der Physik*.

Epstein, P. S. (1923). in Their Motion Through Gases. *Physical Review*, 23(July):710–733.

Espaillat, C., Ingleby, L., Hernández, J., Furlan, E., D'Alessio, P., Calvet, N., Andrews, S., Muzerolle, J., Qi, C., and Wilner, D. (2012). on the Transitional Disk Class: Linking Observations of T Tauri Stars and Physical Disk Models. *The Astrophysical Journal*, 747(2):103.

Espaillat, C., Muzerolle, J., Najita, J., Andrews, S., Zhu, Z., Calvet, N., Kraus, S., Hashimoto, J., Kraus, A., and D'Alessio, P. (2014). An Observational Perspective of Transitional Disks. In *Protostars and Planets VI*, page 24. The University of Arizona Press (Tucson).

Feldman, W. C., Bourke, M. C., Elphic, R. C., Maurice, S., Bandfield, J., Prettyman, T. H., Diez, B., and Lawrence, D. J. (2008). Hydrogen content of sand dunes within Olympia Undae. *Icarus*, 196(2):422–432.

Fountain, J. A. and West, E. A. (1970). Thermal conductivity of particulate basalt as a function of density in simulated lunar and Martian environments. *Journal of Geophysical Research*, 75:4063–4069.

Fourier, J. (1824). Remarques générales sur les Temperatures du globe terrestre et des espaces planétaires. *Annales de Chimie et de Physique*, 27:163–167.

Goldreich, P. and Ward, W. R. (1973). The formation of planetesimals. *The Astrophysical Journal*, 183:1051–1061.

Greeley, R., Lancaster, N., Lee, S., and Thomas, P. (1992). Martian aeolian processes, sediments, and features. In Kieffer, H. H., Jakosky, B. M., Snyder, C. W., and Matthews, M. S., editors, *Mars*, pages 730–766. University of Arizona press (Tucson).

Haack, H. and Wurm, G. (2007). Life on the Edge - Formation of CAIs and Chondrules at the Inner Edge of the Dust Disk. *Meteoritics and Planetary Science Supplement*, 42:5157.

Haberle, R. M., Joshi, M. M., Murphy, J. R., Barnes, J. R., Schofield, J. T., Wilson, G., Lopez-Valverde, M., Hollingsworth, J. L., Bridger, A. F. C., and Schaeffer, J. (1999). General circulation model simulations of the Mars Pathfinder atmospheric structure investigation/meteorology data. *J. Geophys. Res.*, 104:8957–8974.

Haghighipour, N. and Boss, A. P. (2003). On Gas-Drag Induced Rapid Migration of Solids in a Non-Uniform Solar Nebula. *The Astrophysical Journal*, 598(2):1301–1311.

Haisch, K. E., Lada, E. a., and Lada, C. J. (2001). Disk Frequencies and Lifetimes in Young Clusters. *The Astrophysical Journal*, 553:153–156.

Han, Y. (2006). *Investigation of Micro/Meso-Scale Knudsen Compressors at Low Pressures*. PhD thesis, University of Southern California.

Hayashi, C., Nakazawa, K., and Nakagawa, Y. (1985). Formation of the solar system. In Black, D. C. and Matthews, M. S., editors, *Protostars and Planets II*, pages 1100–1153.

Heim, L., Blum, J., Preuss, M., and Butt, H. (1999). Adhesion and friction forces between spherical micrometer-sized particles. *Physical Review Letters*, pages 16–19.

Hertz, H. (1881). Über die Berührung fester elastischer Körper. *Journal für die reine und angewandte Mathematik*, pages 156–171.

Hess, S. L., Henry, R. M., Leovy, C. B., Tillman, J. E., and Ryan, J. A. (1977). Meteorological results from the surface of Mars - Viking 1 and 2. *J. Geophys. Res.*, 82:4559–4574.

Hinrichsen, H. and Wolf, E. D. (2006). *Adhesion of Contacting Particles*. WILE-VCH Verlag GmbH & Co.KGaA (Weinheim).

Hudson, T. L. and Aharonson, O. (2008). Diffusion barriers at Mars surface conditions: Salt crusts, particle size mixtures, and dust. *Journal of Geophysical Research E: Planets*, 113(9):1–17.

Johansen, A., Blum, J., Tanaka, H., Ormel, C., Bizzarro, M., and Rickman, H. (2014). The Multifaceted Planetesimal Formation Process. In *Protostars and Planets VI*, pages 547–550. The University of Arizona Press (Tucson).

Johansen, A., Youdin, A., and Klahr, H. (2009). Zonal Flows and Long-Lived Axisymmetric Pressure Bumps in Magnetorotational Turbulence. *The Astrophysical Journal*, 697(2):1269–1289.

Johnson, K. L. and Greenwood, J. A. (1997). An Adhesion Map for the Contact of Elastic Spheres. *Journal of Colloid and Interface Science*, 192:326–333.

Johnson, K. L., Kendall, K., and Roberts, A. D. (1971). Surface Energy and the Contact of Elastic Solids. *Royal Society of London Proceedings Series A*, 324:301–313.

Kahn, R. A., Martin, T. Z., Zurek, R. W., and Lee, S. W. (1992). The Martian dust cycle. In Kieffer, H. H., Jakosky, B. M., Snyder, C. W., and Matthews, M. S., editors, *Mars*, pages 1017–1053. University of Arizona press (Tucson).

Kant, I. (1755). *Allgemeine Naturgeschichte and Theorie des Himmels*. Johann Friederich Petersen, Königsberg und Leipzig, 1 edition.

Kaufmann, E., Komle, N., and Kargl, G. (2006). Laboratory simulation experiments on the solid-state greenhouse effect in planetary ices. *Icarus*, 185(1):274–286.

Kelling, T. (2012). *Licht-Induzierte Kräfte auf Staubaggregate und deren Anwendung auf Planetare und Protoplanetare Oberflächen*. PhD thesis, University Duisburg-Essen.

Kelling, T. and Wurm, G. (2009). Self-Sustained Levitation of Dust Aggregate Ensembles by Temperature-Gradient-Induced Overpressures. *Physical Review Letters*, 103(21):215502.

Kelling, T. and Wurm, G. (2011). a Mechanism To Produce the Small Dust Observed in Protoplanetary Disks. *The Astrophysical Journal*, 733(2):120.

Kelling, T., Wurm, G., Kocifaj, M., Klačka, J., and Reiss, D. (2011). Dust ejection from planetary bodies by temperature gradients: Laboratory experiments. *Icarus*, 212(2):935–940.

Kieffer, H. H., Jakosky, B. M., and Snyder, C. W. (1992). The planet Mars - From antiquity to the present. In Kieffer, H. H., Jakosky, B. M., Snyder, C. W., and Matthews, M. S., editors, *Mars*, pages 1–33. University of Arizona press (Tucson).

Knudsen, M. (1909). Eine Revision der Gleichgewichtsbedingung der Gase. Thermische Molekularströmung. *Annalen der Physik*, 336(1):205–229.

Kocifaj, M., Klačka, J., Kelling, T., and Wurm, G. (2011). Radiative cooling within illuminated layers of dust on (pre)-planetary surfaces and its effect on dust ejection. *Icarus*, 211:832–838.

Kocifaj, M., Klačka, J., Wurm, G., Kelling, T., and Kohút, I. (2010). Dust ejection from (pre-)planetary bodies by temperature gradients: radiative and heat transfer. *Monthly Notices of the Royal Astronomical Society*, 1518:1512–1518.

Kouremenos, D. and Antonopoulus, K. (1987). Sound Velocity and Isentropic Exponents for Gases with Different Acentric Factors by Using the Redlich-Kwong-Soave Equation of State. *Acta Mechanica*, 66:177–189.

Krause, M., Blum, J., Skorov, Y. V., and Trieloff, M. (2011). Thermal conductivity measurements of porous dust aggregates: I. Technique, model and first results. *Icarus*, 214(1):286–296.

Krauss, O. and Wurm, G. (2005). Photophoresis as the Driving Force for the Formation of Circumstellar Dust Rings and (Exo-)Kuiper Belts. In *Protostars and Planets V Posters*, page 8332.

Küpper, M., Dürmann, C., Beule, C., and Wurm, G. (2014). Propulsion of Porous Plates in Thin Atmospheres by Temperature Fields. *Microgravity Science and Technology*, 25(5):311–318.

Laplace, P. (1836). *Exposition du systeme du monde*. Courcier, Paris, 1 edition.

Lodge, O. and Clark, J. (1884). On the phenomena exhibited by dusty air in the neighbourhood of strongly illuminated bodies. *Phil. Mag. Ser.*, 5(17):214–239.

Lösche, C. (2015). *Photophoresis*. PhD thesis, University Duisburg-Essen.

Ludwig, C. (1856). Diffusion Zwischen Ungleich Erwaermten Orten Gleich Zusammengestzter Loesungen. *Akademie der Wissenschaften in Wien*, 20(1):539.

Marinova, M. M., Aharonson, O., and Asphaug, E. (2008). Mega-impact formation of the Mars hemispheric dichotomy. *Nature*, 453(7199):1216–1219.

Matson, D. and Brown, R. (1989). Solid-state greenhouse and their implications for icy satellites. *Icarus*, 81:67–81.

Maxwell, J. C. (1879). On stresses in rarified gases arising from inequalities of temperature. *Philosophical Transactions of the Royal Society of London*, 170:231–256.

Mellon, M., Jackosky, B. M., Kieffer, H. H., and Christensen, P. R. (2000). High-Resolution Thermal Inertia Mapping from the Mars Global Surveyor Thermal Emission Spectrometer. *Icarus*, 148(2):437–455.

Mellon, M. T. and Jakosky, B. M. (1993). Geographic variations in the thermal and diffusive stability of ground ice on Mars. *J. Geophys. Res.*, 98:3345–3364.

Meschede, D., editor (2015). *Gerthsen Physik*. Springer Spektrum, Berlin, 25 edition.

Muntz, E. P., Sone, Y., Aoki, K., Vargo, S., and Young, M. (2002). Performance analysis and optimization considerations for a Knudsen compressor in transitional flow. *Journal of Vacuum Science & Technology A: Vacuum, Surfaces, and Films*, 20(1):214.

Nakagawa, Y., Sekiya, M., and Hayashi, C. (1986). Settling and growth of dust particles in a laminar phase of a low-mass solar nebula. *Icarus*, 67:375–390.

Natta, a., Testi, L., Calvet, N., Henning, T., Waters, R., and Wilner, D. (2007). Dust in Proto-Planetary Disks: Properties and Evolution. In *Protostars and Planets V*, pages 767–781. The University of Arizona Press (Tucson).

Niederdorfer, E. (1933). Messungen des Wärmeumsatzes über schneebedecktem Boden. *Meteorologische Zeitschrift*, 50(6):201–208.

Pollack, J. B., Colburn, D. S., Flasar, F. M., Kahn, R., Carlston, C. E., and Pidek, D. G. (1979). Properties and effects of dust particles suspended in the Martian atmosphere. *Journal of Geophysical Research*, 84:2929–2945.

Pollack, J. B., Hubickyj, O., Bodenheimer, P. H., Lissauer, J. J., Podolak, M., and Greenzweig, Y. (1996). Formation of the Giant Planets by Concurrent Accretion of Solids and Gas. *Icarus*, 124:62–85.

Preining, O. (1966). Photophoresis. *Aerosol Science*, 2:111.

Presley, M. and Christensen, P. (1997). Thermal conductivity measurements of particulate materials 1. A review. *Journal of Geophysical Research*, pages 6535–6549.

Rayleigh, F. (1882). On the dark plane which is formed over a heated wire in dusty air. *Proceedings of the Royal Society*, 34:414–418.

Reiss, M. D., Kelling, T., Lüsebrink, D., Hiesinger, H., Wurm, G., Teiser, J., and Planetologie, I. (2009). Observation of dust devily in very low-pressure environments on Arsia Mons, Mars. *Workshop on the Microstructure of the Martian Surface*, pages 15–16.

Reynolds, O. (1879). On certain dimensional properties of matter in the gaseous state. *Philosophical Magazine of the Royal Society of London*, 170:727–845.

Reynolds, O. (1883). An experimental investigation of the circumstances which determine whether the motion of water shall be direct or sinuous, and of the law of resistance in parallel. *Proceedings of the royal society*, 174(1883):935–982.

Rohatschek, H. (1995). Semi-empirical model of photophoretic forces for the entire range of pressures. *Journal of Aerosol Science*, 26:717–734.

Schneider, J. (2015). The extrasolar planets encyclopedia catalog (called on 06.07.2015). http://exoplanet.eu/.

Schorghofer, N. (2013). Subsurface air flow on Mars. *Nature Physics*, 10(December):14–15.

Schorghofer, N. and Forget, F. (2005). History and anatomy of subsurface ice on Mars. *Icarus*, 220(2):1112–1120.

Shu, F. H., Adams, F. C., and Lizano, S. (1987). Star Formation in Molecular Clouds: Observation and Theory. *Annual Review of Astronomy and Astrophysics*, 25(1):23–81.

Sizemore, H. G. and Mellon, M. T. (2008). Laboratory characterization of the structural properties controlling dynamical gas transport in Mars-analog soils. *Icarus*, 197(2):606–620.

Smith, M. D. (2002). The annual cycle of water vapor on Mars as observed by the Thermal Emission Spectrometer. *Journal of Geophysical Research*, 107(E11):1–19.

Sone, Y. and Itakura, E. (1990). Analysis of Poiseuille and thermal transpiration flows for arbitrary Knudsen numbers by a modified Knudsen number expansion method and their database. *Journal of the Vacuum Society of Japan*, 33:92–94.

Soret, C. (1880). Influence de la temperature sur la distribution des sels dans leurs solutions. *Academie des Sciences, Paris, C.R.*, 91(5):189–291.

Squyres, S. W., Clifford, S. M., Kuz'min, R. O., Zimbelman, J. R., and Costard, F. M. (1992). Ice in the Martian regolith. In Kieffer, H. H., Jakosky, B. M., Snyder, C. W., and Matthews, M. S., editors, *Mars*, pages 523–554. University of Arizona press (Tucson).

Strom, K. M., Strom, S. E., Edwards, S., Cabrit, S., and Skrutskie, M. F. (1989). Circumstellar material associated with solar-type pre-main-sequence stars - A possible constraint on the timescale for planet building. *The Astrophysical Journal*, 97(5):1451–1470.

Sutherland, W. (1893). LII. The viscosity of gases and molecular force. *Philosophical Magazine Series 5*, 36(223):507–531.

Testi, L., Birnstiel, T., Ricci, L., Andrews, S., Blum, J., Carpenter, J. M., Dominik, C., Isella, A., Natta, A., Williams, J. P., and Wilner, D. J. (2014). Dust evolution in protoplanetary disks. In *Protostars and Planets VI*, pages 339–361. The University of Arizona Press (Tucson).

Tyndall, J. (1870). On dust and disease. *Proc. R. Inst.*, 6:1–14.

Vargo, S. and Muntz, E. (1999). Knudsen compressor as a micro-and macroscale vacuum pump without moving parts or fluids. *Journal of Vacuum Sciences*, pages 2308–2313.

Waldman, L. (1959). Über die Kraft eines inhomogenen Gases auf kleine suspendierte Kugeln. *Zeitschrift Fur Naturforschung*, 14A:589–599.

Weidenschilling, S. (1977). Aerodynamics of solid bodies in the solar nebula. *Monthly Notices of the Royal Astronomical Society*, 180:57–70.

White, B. R., Lacchia, B. M., Greeley, R., and Leach, R. N. (1997). Aeolian behavior of dust in a simulated Martian environment. *Journal of Geophysical Research*, 102:25629–25640.

Windmark, F., Birnstiel, T., Ormel, C. W., and Dullemond, C. P. (2012). Breaking through: The effects of a velocity distribution on barriers to dust growth. *Astronomy & Astrophysics*, 544:4.

Wolff, M. J. and Clancy, R. T. (2003). Constraints on the size of Martian aerosols from Thermal Emission Spectrometer observations. *Journal of Geophysical Research (Planets)*, 108:5097.

Wolszczan, a. and Frail, D. a. (1992). A planetary system around the millisecond pulsar PSR1257 + 12. *Nature*, 355(6356):145–147.

Wood, J. A. (2000). Pressure and Temperature Profiles in the Solar Nebula. *Space Sci. Rev.*, 92:87–93.

Wurm, G. (2007). Light induced disassembly of dusty bodies in inner protoplanetary discs: implications for the formation of planets. *Monthly Notices of the Royal Astronomical Society*, pages 1–14.

Wurm, G. and Krauss, O. (2006). Dust eruptions by photophoresis and solid state greenhouse effects. *Physical review letters*, 134301:1–4.

Yamamoto, K. and Ishihara, Y. (1988). Thermophoresis of a spherical particle in a rarefied gas of a transition regime. *Physics of Fluids*, 31(12):3618.

Yen, A. S., Gellert, R., Schröder, C., Morris, R. V., Bell, J. F., Knudson, A. T., Clark, B. C., Ming, D. W., Crisp, J. a., Arvidson, R. E., Blaney, D., Brückner, J., Christensen, P. R., DesMarais, D. J., de Souza, P. a., Economou, T. E., Ghosh, A., Hahn, B. C., Herkenhoff, K. E., Haskin, L. a., Hurowitz, J. a., Joliff, B. L., Johnson, J. R., Klingelhöfer, G., Madsen, M. B., McLennan, S. M., McSween, H. Y., Richter, L., Rieder, R., Rodionov, D., Soderblom, L., Squyres, S. W., Tosca, N. J., Wang, A., Wyatt, M., and Zipfel, J. (2005). An integrated view of the chemistry and mineralogy of martian soils. *Nature*, 436(7047):49–54.

Youdin, A. N. and Chiang, E. I. (2004). Particle Pile-ups and Planetesimal Formation. *The Astrophysical Journal*, 601(2):1109–1119.

Zheng, F. (2002). Thermophoresis of spherical and non-spherical particles: a review of theories and experiments. *Advances in Colloid and Interface Science*, 97:255–278.

Zimon, A. D. (1969). *Adhesion of Dust and Powder*. Plenum Press (New York).

Zsom, a., Ormel, C. W., Dullemond, C. P., and Henning, T. (2011). The outcome of protoplanetary dust growth: pebbles, boulders, or planetesimals? III. Sedimentation driven coagulation inside the snow-line. *Astronomy & Astrophysics*, 513:1–22.

11

Acknowledgements

First of all, special thanks to my advisor **Prof. Dr. Gerhard Wurm** for the continuous support of my research during the last years. Many thanks for his patience and motivation, for the freedom and guidance during my Ph.D. study.

Many thanks for the financial support by the **DLR Space Management** with funds provided by the **Federal Ministry of Economics and Technology** (BMWi) under grand number DLR 50 WM 1242.

Thank you, **Dr. Miroslav Kocifaj**, for the support of my research with the numerical simulations.

In addition, many thanks to **Tim Jankowski** and **Thorben Kelling** for lots of fruitful discussions regarding the research of light induced erosion.

Thanks to **Jens Teiser** and **Manfred Aderholz** for the support regarding the construction of experimental setups for the microgravity campaigns.

Many thanks to the **Center of Applied Technology and Microgravity** (ZARM), the **European Space Agency** (ESA) and **Novespace**.

Thanks to all the members of our group who made the working atmosphere as comfortable as it was: **Rosa Esteban**, **Christoph Lösche**, **Johannes Deckers**, **Marc Köster**, **Mathias Schywek**, **Markus Küpper**, **Gregor Musiolik** and **Tobias Steinpilz**.

I'm grateful to my **family**. **Mom** and **Dad**, thank you so much for your motivation and guidance. And last but not least: Thank you, **Johannes**, for all the hugs at the right time.

12

Selbstständigkeitserklärung

Die vorliegende Dissertation wurde von mir selbständig verfasst. Bei der Abfassung der Dissertation wurden nur die angegebenen Hilfsmittel benutzt und alle wörtlich oder inhaltlich übernommenen Stellen sind als solche gekennzeichnet. Die Dissertation ist nur in diesem Promotionsverfahren eingereicht und es wird der Doktorgrad Dr. rer. nat. angestrebt.

_____

(Ort, Datum, Unterschrift)

"Ever tried? Ever failed?
No matter.
Try again. Fail again. Fail better."

— *Samuel Beckett, 1983*

The Astrophysical Journal, 763:11 (8pp), 2013 January 20 doi:10.1088/0004-637X/763/1/11

FROM PLANETESIMALS TO DUST: LOW-GRAVITY EXPERIMENTS ON RECYCLING SOLIDS AT THE INNER EDGES OF PROTOPLANETARY DISKS

Caroline de Beule, Thorben Kelling, Gerhard Wurm, Jens Teiser, and Tim Jankowski
Universität Duisburg-Essen, Fakultät für Physik, Lotharstraße 1, D-47057 Duisburg, Germany; caroline.de-beule@uni-due.de
Received 2012 May 25; accepted 2012 November 14; published 2012 December 27

ABSTRACT

Transporting solids of different sizes is an essential process in the evolution of protoplanetary disks and planet formation. Large solids are supposed to drift inward; high-temperature minerals found in comets are assumed to have been transported outward. From low-gravity experiments on parabolic flights, we studied the light-induced erosion of dusty bodies caused by a solid-state greenhouse effect and photophoresis within a dust bed's upper layers. The gravity levels studied were $0.16g$, $0.38g$, $1g$, and $1.7g$. The light flux during the experiments was $12 \pm 2\,\mathrm{kW\,m^{-2}}$ and the ambient pressure was 6 ± 0.9 mbar. Light-induced erosion is strongly gravity dependent, which is in agreement with a developed model. In particular for small dusty bodies ((sub)-planetesimals), efficient erosion is possible at the optically thin inner edges of protoplanetary disks. Light-induced erosion prevents significant parts of a larger body from moving too close to the host star and being subsequently accreted. The small dust produced continues to be subject to photophoresis and is partially transported upward and outward over the surface of the disk; the resulting small dust particles are observed over the disk's lifetime. The fraction of eroded dust participates in subsequent cycles of growth during planetesimal formation. Another fraction of dust might be collected by a body of planetary size if this body is already present close to the disk edge. Either way, light-induced erosion is an efficient recycling process in protoplanetary disks.

Key words: methods: laboratory – planets and satellites: formation – protoplanetary disks

Online-only material: color figures

1. INTRODUCTION

The formation of planets in protoplanetary disks is strongly tied to the existence of dust which makes up about 1% of the total mass of the disk (Natta et al. 2007). The basic collisional growth model assumes that, as a first step toward planet formation, kilometer-size planetesimals are formed by sticking collisions of dust particles which are only held together by surface forces (Blum & Wurm 2008; Weidenschilling & Cuzzi 1993; Windmark et al. 2012). There are some issues in planetesimal formation which are not yet understood. Somewhat problematic is inward drift, especially of meter-size bodies. In a standard disk the pressure is supposed to decrease with distance from the star (Hayashi et al. 1985). The gas is therefore supported by a pressure gradient and rotates with sub-Keplerian velocity. Small solids couple to the gas and thus also rotate more slowly than Keplerian. However, solid bodies are not supported by the pressure gradient. This leads to an inward drift of the solid bodies which—for a meter-size body in a minimum-mass nebula—can be as large as 1 AU in 100 years (Weidenschilling 1977). Such an inward mass transport of solids leads to a redistribution of matter: the outer part of the disk becomes depleted in solids, while the inner part becomes enriched. The physics of the inner 1 AU of protoplanetary disks strongly depends on the fate of this incoming matter: it might contribute to the local planet formation process and add mass to forming planetary bodies, it might evaporate and be accreted by the star, or it might be recycled in some more complex way. As the physics in the inner part of the disk is complex, the evolution of solid bodies is still an open question. To address this problem, we started to investigate a mechanism of particle recycling which is especially active in this inner region of a protoplanetary disk and, more specifically, close to the inner edge of a disk within the inner 1 AU. There is a growing number of observations which show that, in some phases, protoplanetary disks contain inner gaps which are optically thin but still contain gas, while the outer part is still dense and optically thick (D'Alessio et al. 2005; Calvet et al. 2002; Currie & Sicilia-Aguilar 2011; Sicilia-Aguilar et al. 2008). In other words, solids at the inner edge of a disk are embedded in a gaseous environment and are illuminated by the star.

Wurm & Krauss (2006) first described a mechanism that significantly erodes dusty bodies to small particles under very general conditions, e.g., by mere illumination and at low gas pressure (kW $\mathrm{m^{-2}}$ of intensity and mbar gas pressure). Wurm (2007) showed that this erosion process also works under the conditions of transitional disks. There will most likely be a small shell at the inner edge of a disk where the conditions for particle erosion are met (Wurm 2007). Every dusty body which enters this zone and which is too small to hold its dust by gravity (sub-planetesimal) is subject to erosion by this process. Different scenarios are possible as to how this contributes to the evolution of the disk. The dust might, for example, be transported upward and outward over the disk by photophoresis. Such a model has been suggested by Wurm & Haack (2009). At later times or throughout the optically thin inner parts the dust might also be transported by photophoresis in the midplane (Wurm 2007; Takeuchi & Lin 2003; Herrmann & Krivov 2007; Moudens et al. 2011; Mousis et al. 2007). Kelling & Wurm (2011) showed that the erosion process is a suitable mechanism to explain the existence of small dust particles which are observed in protoplanetary disks over their entire lifetime. The dust might also be recycled locally and added—probably more efficiently than by the original larger bodies—to existing large planetesimals or protoplanetary bodies to boost their growth. These aspects are speculative and not the main focus of this paper, which reports on experiments that analyze the gravity dependence of the light-induced erosion mechanism, providing basic input for future modeling.

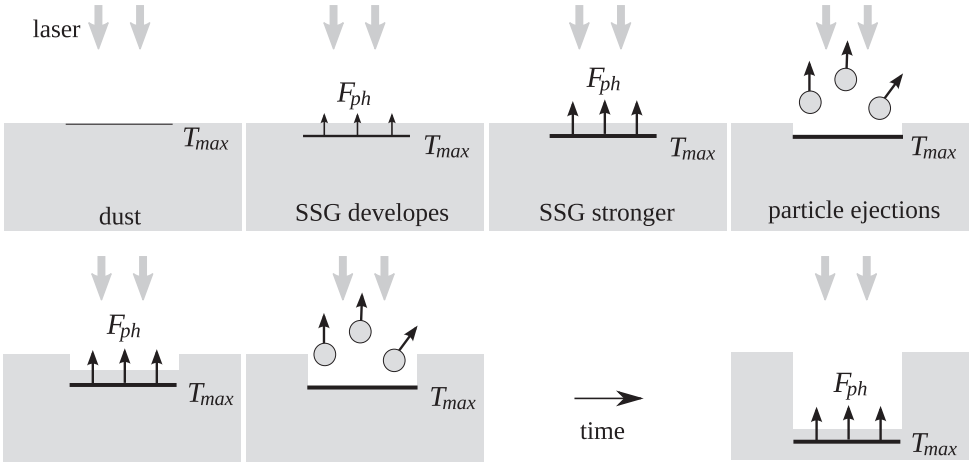

Figure 1. Visible radiation (laser) enters the dust bed and leads to a solid-state greenhouse (SSG) effect, with a maximum temperature below the surface (indicated by the black line; larger temperatures are represented by thicker lines). Photophoresis F_{ph} acts on the surface particles. When this force overcomes gravity and cohesion, the surface particles are lifted. A crater is formed where again temperature gradients develop. If the illuminated spot is limited in size, the developing crater might prevent further release of particles.

A sketch of the light-induced erosion mechanism is shown in Figure 1: the illumination of a dusty surface first leads to a solid-state greenhouse (SSG) effect. This effect is known to exist for ice and comets (Niederdorfer 1933; Davidsson & Skorov 2002; Kaufmann et al. 2002). It means that visible light enters a porous body and is absorbed over some depth, but as the body is opaque to infrared radiation only the top surface can cool by thermal emission. Therefore, the maximum temperature is below the surface. In recent years it was shown that this is also true for purely dusty surfaces (Kocifaj et al. 2010, 2011; Kelling et al. 2011; Kelling & Wurm 2011). If temperature gradients across a particle exist as in the case of an SSG profile, and if the particle is embedded in a gaseous environment, a photophoretic force acts on the particle from the warm to the cold side. Hence, the surface particles of an illuminated dust bed are subject to a lifting force. If this force is stronger than gravity and cohesion, aggregates are ejected. The SSG effect and photophoresis are the basis for light-induced erosion of dusty bodies. The physics behind this has been studied in a number of works (Wurm & Krauss 2006; Wurm 2007; Kelling & Wurm 2009, 2011; Kelling et al. 2011).

In protoplanetary disks, dust particles on dusty sub-planetesimals are bound by cohesion and gravity. However, the gravitational force is small due to the small mass of the objects. Therefore, photophoretic forces acting on the particles have to overcome less gravity and the effect of dust erosion induced by illumination is more intense compared to larger bodies or laboratory experiments. In the first microgravity experiments Wurm et al. (2008) showed that the threshold light flux for particle erosion indeed depends on the gravity level. At low-gravity, cohesion eventually becomes the dominant opposing force. The erosion rate was not measured in the experiments of Wurm et al. (2008); however, this is important in determining how rapidly a body can be eroded or what mass flux it might provide in small particles if it crosses the erosion zone in a protoplanetary disk.

To quantify the effect of light-induced erosion for application to (sub)-planetesimal recycling, we carried out low-gravity experiments and determined the gravity dependence of the erosion rate. The experiments were carried out during the first *Joint European Partial-G Parabolic Flight* campaign. On this campaign, over 3 days, 13 parabolas at $0.16g$, 12 parabolas at $0.38g$, and 6 parabolas at $0g$ ($g = 9.81\,\mathrm{m\,s^{-2}}$) were provided. We also developed a preliminary model which agrees well with the experimental results.

2. EXPERIMENT

A sketch of the experimental setup is shown in Figure 2. Four separate chambers are placed in one vacuum chamber. Each chamber contains a dust sample with a depth of 2 cm covering a total area of 6 $\mathrm{cm^2}$. For the campaign reported here the chambers were filled with basalt powder with a broad size distribution between 0 and 125 μm. We consider this dust particle size range suitable to simulate the dust in protoplanetary disks. They include micron-size particles, discussed by Brearley (1999) with reference to the matrix in chondrites (typically a few microns but occasionally up to about 20 μm). The constituents in interplanetary dust particles or cometary material are smaller, on the order of 0.1 μm (Wozniakiewicz et al. 2012) which might not be adequately represented in our experiment sample. On the other hand, chondrites largely consist of chondrules of submillimeter size, so the larger grain fraction in our sample might correlate with these dimensions. Certainly, the size dependence of the erosion mechanism should be considered in more detail in the future.

The dust samples were dried at about 500 K for 24 hr and were stored in a desiccator until they were placed in the vacuum chamber just before the experiments. The ambient pressure of air in the vacuum chamber was then set to $p = 6 \pm 0.9$ mbar for all experiments.

During each experimental run one sample was illuminated by a diode laser of 2 W optical output at 655 ± 10 nm. The laser profile was homogenized by coupling the laser to an optical fiber and projecting the fiber outlet onto the sample surface with a size of 25 ± 4 $\mathrm{mm^2}$. The average intensity was $12\,\mathrm{kW\,m^{-2}}$ which varied by 17% within the spot. This corresponds to the inner regions of a protoplanetary disk <0.4 AU where the light flux for a star similar to the sun is $I > 10\,\mathrm{kW\,m^{-2}}$. An accelerometer was used to measure the residual gravity acting on the experiment. The experimental chamber was supported by vibrational attenuators to prevent any influence of airplane vibrations, which might reduce the cohesion between the dust particles. Released aggregates were observed from the side by a camera at 60 images per second.

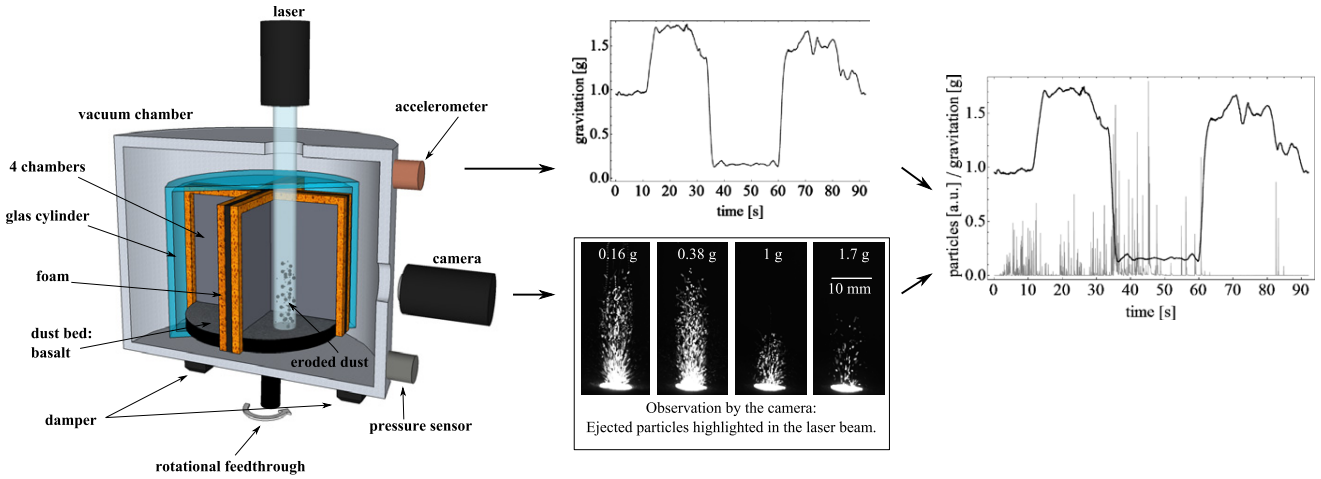

Figure 2. Experimental setup: four chambers filled with dust samples are enclosed by a rotatable glass cylinder in a vacuum chamber. A homogeneous laser spot of 25 ± 4 mm^2 size illuminates the dust bed with an intensity of 12 ± 2 kW m^{-2}. The particles being ejected at different g-levels are observed by a side-view camera. (A color version of this figure is available in the online journal.)

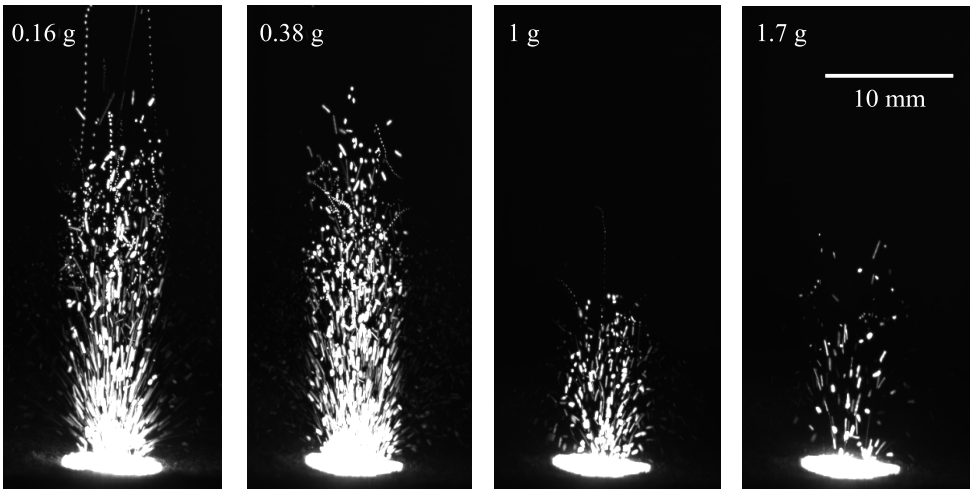

Figure 3. Dust erosion of basalt powder at 6 mbar ambient pressure and a light intensity of 12 kW m^{-2} at four different gravitational accelerations. Each figure is an overlay of 100 images to emphasize the increase of particle release with lower accelerations.

Measurements (images) were taken for 1g, the acceleration phase at 1.7g and the low-gravity phase at 0.16g (Moon level) or 0.38g (Mars level). To confine the dust within the individual chambers, they were enclosed in a glass cylinder. This cylinder and the chambers were independently rotatable by a rotational feedthrough from the outside. After each parabola, and hence before every new experiment, the inside of the rotating glass cylinder was cleaned by a small strip of foam. This ensured that the laser and the camera view were not affected by dust. Rotating the inner, dust-containing part of the chambers ensured that for every new experiment a fresh spot of the dust surface was illuminated. This prevented selection effects, e.g., that all ejectable particles (e.g., of a certain size fraction) were already released. After removing the background noise of the camera images the average gray scale value was taken as a relative measurement for the ejected mass or particle number. This assumed that the ejected particle distribution stays constant with time, that averaging is done over a significantly large number of particles and that the image is not saturated with particles. As we provide new spots for each experiment, observe well separated aggregates and take an average over a large number of aggregates in typically 900 images for a given g-phase (Figure 3), we consider the gray value as a suitable measure. Figure 3 shows an overlay of 100 images of the ejected aggregates at different g-levels. The number of ejected aggregates clearly increases with lower gravitational acceleration.

A parabolic flight has the advantage that different gravity levels can be tested with the same dust sample in a short period of time. However, the effects of the transitions between the different g-levels have to be filtered out. They induce a higher erosion rate during the transitions from high-g to low-g. This is due to the release of gravitational and photophoretic tension from the dust bed, as higher gravity levels require a steeper temperature gradient for erosion. It takes a certain time before the new equilibrium temperature profile is established at which aggregates are ejected regularly. Figure 4 shows which data were selected to determine the number of ejected aggregates in the different phases. In the 1g-phase of every parabola the laser and camera were turned on. First erosions occur after 2–3 s. During the transition from 1.7g to lower g-levels, massive particle releases appear (peaks in Figure 3). These releases are an artifact of the tension release as previously mentioned and are not used to

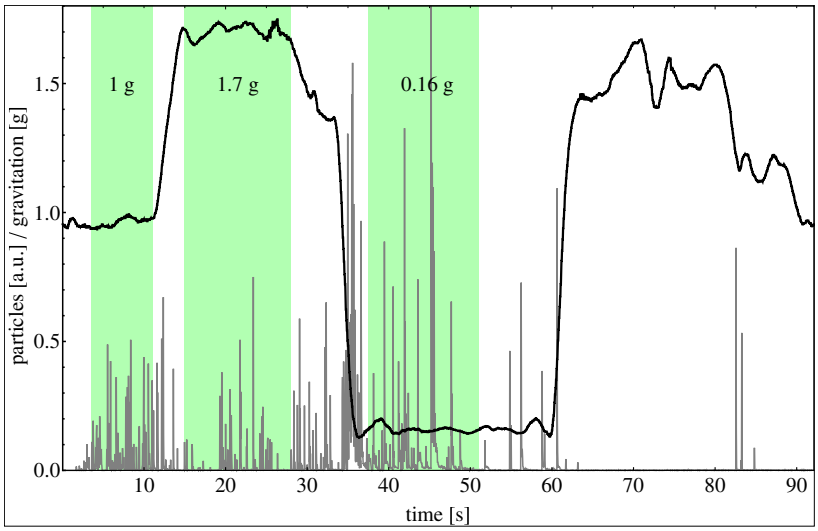

Figure 4. Example of the collected raw data of a Moon parabola. The black line shows the gravitational acceleration in units of $g = 9.81\,\mathrm{m\,s^{-2}}$. The gray peaks indicate the eroded mass in arbitrary units. For the analysis, only the data in the green boxes were taken where the release of aggregates is continuous.
(A color version of this figure is available in the online journal.)

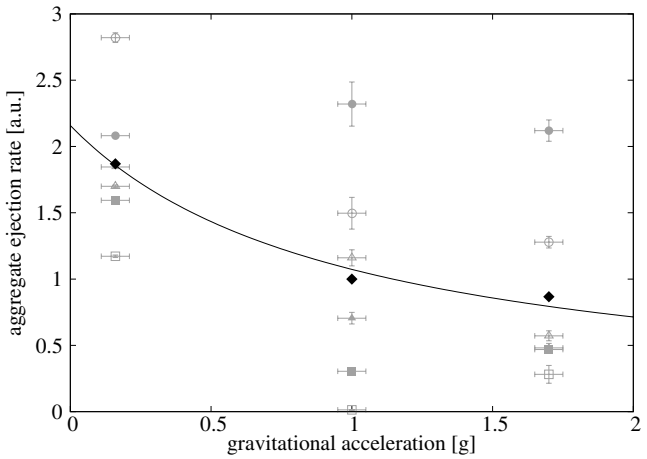

Figure 5. Data set for the 6 Moon parabolas. The particle erosion rate is set to 1 at 1g. The results from the experiments are presented in gray, the average value in black, and the black line shows the trend for the averaged data according to the model developed in Section 3.

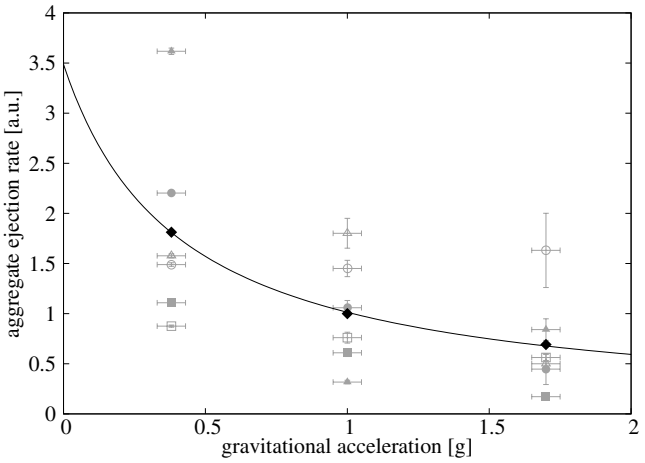

Figure 6. Data set for the 6 Mars parabolas. The particle erosion rate is set to 1 at 1g. The results from the experiments are presented in gray, the average value in black, and the black line shows the trend for the averaged data according to the model developed in Section 3.

determine the erosion rate. After the transition particle releases occur continuously at lower g-levels for about 10 s. The dust bed surface changes as the laser spot removes particles and creates an erosion crater (see also Figure 1). The presence of a crater rim induces edge effects, which efficiently reduce the erosion rate, especially in the low-gravity phase with high erosion rates. Therefore, we do not include the later times for averaging. After the data reduction, a measure of the erosion rate is given as the average brightness of all images within a single g-phase. As the brightness is an arbitrary measure of the erosion rate, the different g-phases of one parabola are scaled to a value of 1 at 1g.

The parabolic flight provided results for 12 parabolas: 6 Moon and 6 Mars parabolas. Figures 5 and 6 show the data sets for the Moon and Mars parabolas.

We further average over all parabolas (6 data points for 0.16g and 0.38g and 12 data points for 1g and 1.7g) and obtain the average ejected mass rate over gravity. In Figure 8, all (averaged) experimental data are presented in the context of the model developed below.

3. THE MODEL

The continuous aggregate ejections from the dust bed are caused by an inverse temperature gradient below the dust bed's surface and a photophoretic force F_{ph} (Wurm & Krauss 2006; Kelling et al. 2011; Kelling & Wurm 2011). In detail, the idea behind the light-induced aggregate ejections is the following: Kocifaj et al. (2010, 2011) showed that, if a dust bed is illuminated from the top, the maximum temperature T_{max} is up to some 100 μm below the surface—this is called an SSG effect. Hence, there is a temperature gradient $\partial T/\partial z$ pointing from T_{max} toward the cooler surface (inverse temperature gradient; z as depth within the dust bed). Typical thermal conductivities κ_d of the dust bed are on the order of $\kappa_d \sim 10^{-2}\,\mathrm{W\,m^{-1}\,K^{-1}}$ (Krause et al. 2011). The inverse temperature gradient then takes values

of $\partial T/\partial z \sim 10^5$ K m^{-1} at 10 kW m^{-2} illumination (Kocifaj et al. 2011).

The uppermost aggregates have a temperature gradient along their surface. Small particles with a temperature gradient in a gaseous environment are affected by a photophoretic force which can be written for spherical particles as (Rohatschek 1995)

$$F_{\rm ph} = \frac{2F_{\rm max}}{\frac{p}{p_{\rm max}} + \frac{p_{\rm max}}{p}} \quad (1)$$

$$F_{\rm max} = D\sqrt{\frac{\alpha}{2}}a^2\frac{\partial T}{\partial z} \quad (2)$$

$$F_{\rm ph} = \omega_1\frac{\partial T}{\partial z} \quad (3)$$

where p is gas pressure. $F_{\rm max}$ and $p_{\rm max}$ are particle- and gas-dependent parameters determining the pressure $p_{\rm max}$ at which the photophoretic force $F_{\rm max}$ is a maximum. D is a gas-dependent parameter, $\alpha = 1$ is the accommodation coefficient, a is the particle radius and $\partial T/\partial z$ is the temperature gradient over the particle's surface. Particles in the μm regime are most strongly affected by photophoresis at mbar pressure.

Photophoresis acts on the uppermost aggregates in illuminated dust beds. The threshold for particle ejection can be written as follows (Wurm et al. 2008):

$$F_{\rm ph_{th}} = \Delta m \cdot g_{\rm env} + F_C, \quad (4)$$

with gravity $F_G = \Delta m \cdot g_{\rm env}$, where $g_{\rm env}$ is the environmental gravitational acceleration, Δm is the ejected mass, and F_C is the cohesion force. If this force $F_{\rm ph}$ overcomes gravity and cohesion, aggregates are released from the dust bed's surface. The mass ejection rate $N = \Delta m/\Delta t$ with Δt as time interval depends on the time scale at which the threshold temperature gradient (see, e.g., Equation (2)) within the illuminated dust bed is reset after an ejection. The temperature evolution toward equilibrium within the dust bed follows an exponential dependence (Kocifaj et al. 2011). If the threshold gradient to induce particle release is reached after a time span Δt much smaller than the exponential timescale (large light flux) the temperature gradient can be approximated by a linear increase with time

$$\frac{\partial T}{\partial z}(t) = \omega_2 t. \quad (5)$$

Therefore, the threshold temperature gradient after a time span Δt can be written as

$$\frac{\partial T}{\partial z_{\rm th}} = \frac{\partial T}{\partial z}(\Delta t) = \omega_2 \Delta t. \quad (6)$$

With Equation (6) the photophoretic force (Equation (3)) can be written as

$$F_{\rm ph_{th}} = \omega_3 \Delta t \quad (7)$$

with $\omega_3 = \omega_1\omega_2$. Hence, after the time interval Δt the threshold photophoretic force ($F_{\rm ph_{th}}$, Equation (4)) is reached:

$$F_{\rm ph_{th}} = \omega_3 \Delta t = \Delta m \cdot g_{\rm env} + F_C, \quad (8)$$

and aggregates are released in steps always after an average time

$$\Delta t = \frac{\Delta m \cdot g_{\rm env} + F_C}{\omega_3}. \quad (9)$$

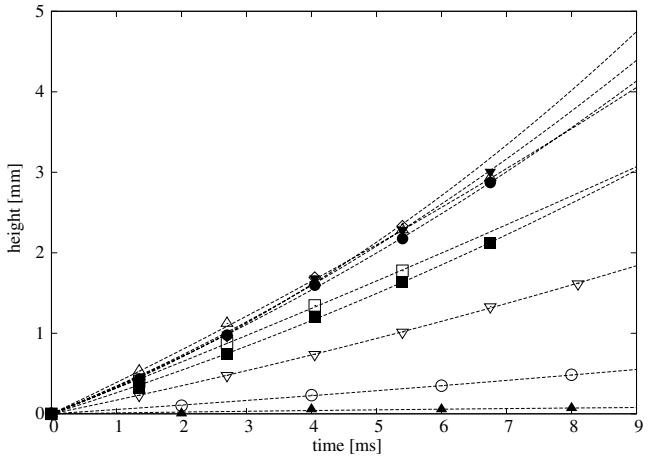

Figure 7. Trajectories of dust aggregates leaving the surface of an illuminated dust bed (basalt, 0–125 μm). The experiment was carried out on the ground at 6 mbar ambient pressure and at an intensity of 12 kW m^{-2}.

The mass ejection rate therefore is

$$N(g_{\rm env}) = \frac{\Delta m}{\Delta t} = \frac{\omega_3}{g_{\rm env.} + \frac{F_C}{\Delta m}}. \quad (10)$$

Equation (10) was used to fit the experimental data, and gives $\omega_3 = 1.6$ m s^{-3} and $F_C/\Delta m = 6.1 \pm 1.2$ m s^{-2}. ω_3 is scalable arbitrarily as it accounts for the nature of the brightness measurement as the relative measurement for one part. However, $F_C/\Delta m$ contains information on the cohesive force by which an ejected mass fraction is bound to the dust bed.

Due to the low resolution of the analyzed images we cannot give an accurate assumption for the eroded particle mass Δm. Hence, we cannot estimate the exact value of F_C from our experiments.

The acceleration $F_C/\Delta m$ from the model fits the accelerations measured in the first follow-up laboratory experiments, shown in Figure 7: basalt powder with a broad size distribution between 0 and 125 μm was placed in a vacuum chamber with 6 ± 0.9 mbar ambient pressure. It was then illuminated by a laser with 12 ± 1 kW m^{-2} and a spot size of 5 ± 0.5 mm radius. The resulting ejection of dust aggregates was measured with a camera at 500 images per second, so the accelerated aggregates could be tracked. We measured accelerations of 14.4 ± 4.9 m s^{-2}, averaged over nine ejected aggregates, which is only twice as high as the acceleration measured on the parabolic flight. This factor two can be explained by the fact that we could not use exactly the same dust sample that we had on board for the parabolic flight.

To visualize the influence of the cohesion we plot the ejection rate of Equation (10) divided by the factor $\omega_3/(F_C/\Delta m)$ for the experimental data (average values of the g-phases) which effectively normalizes the experimental data to 1 at $0g$. In Figure 8, the value $F_C/\Delta m$ is then varied by a factor f to show the general dependence on $F_C/\Delta m$. There is a prominent increase in the ejection rate toward smaller $F_C/\Delta m$ where it becomes more and more dominant at $g_{\rm env} < 1g$ while cohesion is negligible for $g_{\rm env} > 1g$.

This simple model neglects self-shielding of the dust bed by ejected aggregates. The more dust that is ejected, the more light is shielded from reaching the surface. Depending on the relation between the ejection rate and the rate at which aggregates are transported away from the ejection location, e.g., by gas drag

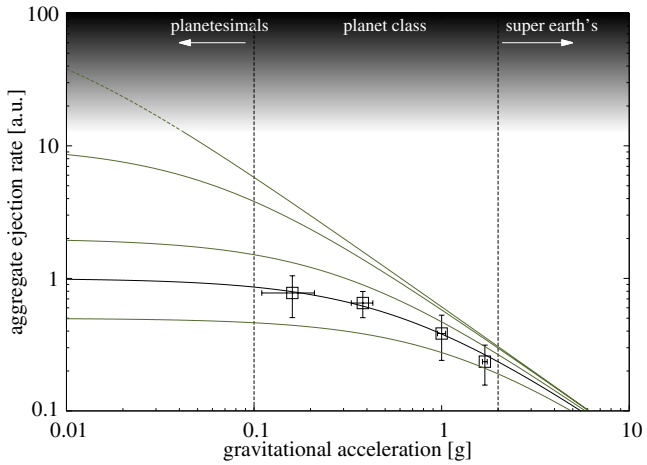

Figure 8. Ejection rate normalized to 1 at 0g for the experimental values using Equation 10. The experimental value (squares) for $F_C/\Delta m$ is varied by a factor f with $f = 2, 1, 0.5, 0.1, 0.01$ (bottom to top). The color gradient indicates that the more aggregates that are ejected, the more light is shielded from reaching the dust bed's surface. From the experiments, we estimate that an increase of the rate up to factor of 10 might be realistic for low cohesive powders.

(A color version of this figure is available in the online journal.)

in protoplanetary disks, the optical thickness of the layer above the dust bed's surface will increase. From the experiments, and based on the assumption that the light flux might be reduced to less than $1/e$ of its intensity, ejection rates that are increased by a factor 10 likely still do not affect the ejection rate. This might set an upper limit to the ejection rate but it is only a rough estimate here, which has to be quantified in the future. For planetary bodies the effect might lead to a size sorting over time where large particles fall back down while small grains get entrained into the atmosphere.

4. APPLICATIONS AND CONCLUSION

The effect of light-induced dust ejections can be a key process of recycling dust during the formation of planets in protoplanetary disks. Planetesimals or smaller dusty bodies at the inner edge can be partly eroded (Wurm 2007).

The position of the edge in a number of transition, pre-transition and full disks has been modeled by Espaillat et al. (2012). Here, pre-transition disks relate to a disk with substantial matter within the gap modeled by an optically thin inner wall at the dust sublimation radius and a second outer wall. In Table 1, we extract their modeled radii of the disks and the luminosities of the host stars. Based on photophoresis the lift force on the particles depends on the environmental parameters light flux I, gas pressure p, and gas temperature T. In the free molecular flow regime (low pressure) Equation (1) simplifies and connects these three parameters to

$$F = b\frac{Ip}{T} \tag{11}$$

(Wurm 2007), with a parameter b dependent on the dust bed.

Our experiments show that particle eruptions continuously occur at all gravity levels at the used light flux $I = 12\,\mathrm{kW\,m^{-2}}$, pressure $p = 6\,\mathrm{mbar}$ and temperature T of about 300 K. We did not probe the threshold condition where no dust is lifted but our values are consistent with threshold conditions measured for eruptions at 1g by Wurm (2007). He found $I = 50\,\mathrm{kW\,m^{-2}}$ at 1 mbar and 300 K. Therefore, we expect that light-induced erosion occurs as long as $Ip/T > 15\,\mathrm{kW\,m^{-2}\,Pa\,K^{-1}}$ (Wurm 2007).

Table 1
Pre-transitional Disks Modeled by Espaillat et al. (2012)

Object	Star's Luminosity (L_{sun})	Inner Wall (AU)	Erosion Dividing Line (AU)	Outer Wall (AU)
FM 515	2.5	0.12	0.63	45
FM 618	2.2	0.22	0.59	11
LRLL 21	3.8	0.13	0.80	9
LRLL 31	5.0	0.32	0.89	14
LRLL 37	1.3	0.17	0.46	5

Note. The erosion limit distance is the distance up to which disassembly of larger dusty bodies would be possible.

In a minimum-mass solar nebula (Hayashi et al. 1985) with given pressure, temperature, and luminosity dependence this condition is reached at a distance of about 0.4 AU, or Mercury's orbit (Wurm 2007).

For observed extrasolar systems we only know the luminosities for certain, not the pressure or temperature at the mid-planes. To determine the distance of the dividing line between erosion and stability for the different objects, we assume that the dividing line is where the light flux of the host star equals that of a solar-type star in a minimum-mass solar nebula or $0.4\,\mathrm{AU} \times \sqrt{L/L_{\mathrm{sun}}}$ (Table 1). The implicit assumptions in this equation are that the gas pressure at this distance and the temperature are the same as in the minimum-mass solar nebula at 0.4 AU.

For the temperature this is a consistent assumption as the blackbody radiation temperature which defines the temperature of the disk in the minimum-mass solar nebula would be the same at the same incoming light flux. The pressure is less certain but one might argue that more luminous stars have denser disks. We therefore assume the pressure to be equal to that in a minimum-mass solar nebula at the dividing line. However, more complex models would not change the following general statement.

We always find the erosion limit within the gap of the pre-transitional disks. In general, erosion is possible at the inner edges of full disks, although melting or sintering of particle ensembles might be an issue which has to be studied in further detail. For full disks and pre-transitional disks erosion might clearly provide the small dust observed over the lifetime of the disk. As the erosion limit distance is closer to the star than the outer wall in pre-transitional disks, particles released by the erosion mechanism can drift outward to this second wall by photophoresis and enhance the particle density locally (Krauss & Wurm 2005; Haack & Wurm 2007). This will induce an enhanced growth of dust aggregates. At the outer wall the growing bodies are safe from destruction unless they are scattered or drift inward again to the inner erosion zone during further evolution and recycling.

The holes of transitional disks are all larger than the erosion limit distance. As they have a largely reduced density it is unclear to what extent erosion will work here. The erosion limit distance would shift inward significantly. Earlier calculations by Wurm (2007) showed that, for example, in the case of TW Hya erosion close to the star would still be possible but this strongly depends on the gas content. The erosion zone likely decreases in thickness with time. However, even if it were only a very thin zone, dusty bodies traversing it might be significantly eroded. In the optically thin but still slightly gaseous hole, the dust would

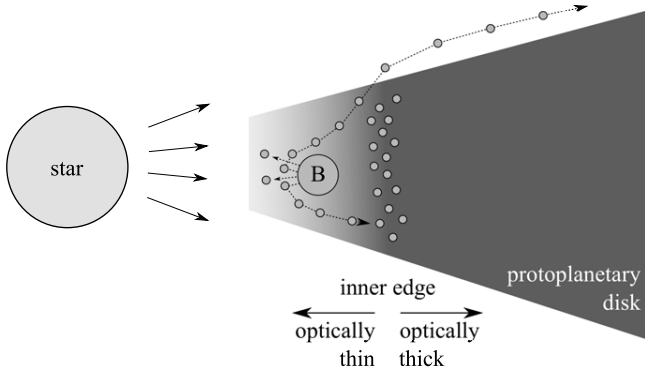

Figure 9. An inward drifting dusty body (B) can be eroded in the optically thin part of a protoplanetary disk by the effect of light-induced ejection. The planetesimal loses mass which can be transported outward again by, e.g., photophoresis.

be transported by photophoresis and locally increase the particle density again.

Therefore, at early full disk times erosion will influence the particle recycling at the inner edge. In later pre-transitional and transitional evolution times of the clearing phase, the light-induced erosion will be an important factor in shaping the size distribution or even triggering later formation of larger bodies at the outward moving edge.

The experiments reported here show that the number of ejected particles increases strongly with decreasing g-levels. The experiments performed on a parabolic flight display an inverse dependence on gravity and specific cohesion. The ejection rate is higher by a factor two in $0.16g$ than in $1g$ for the basalt sample used. The importance of gravity deduced from these data can more clearly be seen in the model. If cohesion is reduced the ejection rate might be up to one or two orders of magnitude more efficient at low-g. Lower cohesion does not change the ejection rate strongly at high g-levels.

As a consequence of microgravity on small planetesimals or sub-planetesimals, the effect is more intense than observed from ground-based experiments so far. Kelling et al. (2011) estimated from $1g$ experiments a mass-loss rate of $10^{-5}\,\mathrm{kg\,s^{-1}\,m^{-2}}$ or about $10^3\,\mathrm{kg\,year^{-1}}$ for an area 1 $\mathrm{m^2}$ in size. Low-gravity conditions would boost this value by a factor of a few. This compares well to the mass of a porous dusty body of meter size with a density of $1\,\mathrm{g\,cm^{-3}}$. The total mass is some 10^3 kg. It is therefore possible to erode, in less than one year, a significant part of such a body if it consists of loosely bound dust close to the disk edge. As the erosion zone is a fraction of an AU (Wurm 2007) the experiments show that an object that passes the edge will efficiently lose mass (Figure 9). Even for objects that lose mass but are not completely destroyed the effect is important as it provides a non-gravitational force on the body and will change the orbital parameters; the details, however, are beyond the scope of this paper.

The mechanism is more efficient in an atmosphere consisting of hydrogen instead of air. Equation (2) by Rohatschek (1995) for the photophoretic force shows a dependence on different parameters. The maximum force is proportional to a gas-dependent parameter

$$D = \frac{\pi}{2}\sqrt{\frac{\pi}{3}\kappa}\frac{c\eta}{T}. \quad (12)$$

This parameter contains the dynamic viscosity of the gas η and the average thermal velocity c, which is proportional to the square root of $1/\mu$, the inverse molar mass. Assuming $\eta_{\mathrm{air}} = 17.1$ μPa·s and $\eta_{H_2} = 8.4$ μPa·s, as well as $\mu_{\mathrm{air}} = 29\,\mathrm{g\,mol^{-1}}$ and $\mu_{\mathrm{proto}} = 2.31\,\mathrm{g\,mol^{-1}}$, we get $D_{\mathrm{proto}} = 1.75 \times D_{\mathrm{air}}$. The maximum force is therefore 1.75 times higher in a protoplanetary disk than on Earth.

In principle the erosion mechanism might compete with regrowth as a body moves through the disk and collects dust particles. This is an interesting aspect as it changes the surface morphology and the susceptibility to re-erosion. To what degree this process is important depends on the position of the dividing line with respect to the inner edge of the optically thick disk. If erosion only occurs in the transitional zone far away from the edge then this whole zone is optically thin by definition and regrowth is not important. This might be explained as follows. Assuming all dust particles to be spherical with a radius of 5 μm, the particle cross section is 78.5×10^{-12} $\mathrm{m^2}$. The disk would be optically thick if its cross section were completely covered with dust particles. At typical distances of 0.5 AU and with a scale height of 0.1 AU this would be 7×10^{21} $\mathrm{m^2}$. Dividing by the particle cross section, this gives 9×10^{31} particles. Spread out over an estimated 0.5 AU in distance the particle density would be $n = 0.17$ particles $\mathrm{m^{-3}}$. The largest drift velocities considered in disk models are on the order of $50\,\mathrm{m\,s^{-1}}$. If a body of 1 m radius collected dust at these speeds the growth rate would be 26.7 particles per second, or with a particle density of $2000\,\mathrm{kg\,m^{-3}}$ it would be $3 \times 10^{-11}\,\mathrm{kg\,s^{-1}}$. Compared to the erosion rate this worst case estimate shows that regrowth is negligible.

This changes at the edge. If the transition zone is only, for example, 100,000 km thick the particle density would be 127.3 particles $\mathrm{m^{-3}}$ and the mass growth $2 \times 10^{-8}\,\mathrm{kg\,s^{-1}}$. This is a factor of 500 less than the erosion rate under perfect conditions, but for non-perfect conditions, e.g., further toward the dark side of the edge, growth and erosion might be comparable.

Another application of the effect at low gravity is found on Mars. By adjusting the conditions (light flux, and temperature) to Mars, dust entrainment in the atmosphere might be explained (Wurm et al. 2008). The low-gravity experiments suggest higher erosion rates on Mars.

Most dust samples that absorb visible radiation show light-induced ejection. We have quantified the gravity effect for a single sample so far. We have experimental evidence that cohesion in the context of this ejection mechanism can vary strongly for different dust samples, but quantification is subject to future research. Overall, erosion of a dusty body at the low-gravity conditions of small bodies at the inner edges of protoplanetary disks is a major recycling process of dust, and is important in the context of planet formation.

This work was supported by the Deutsches Zentrum für Luft- und Raumfahrt (DLR), the Federal Ministry of Economics and Technology Germany (BMWi), the European Space Agency (ESA), and the Deutsche Forschungsgemeinschaft (DFG). We thank the anonymous reviewer for valuable comments.

REFERENCES

Blum, J., & Wurm, G. 2008, ARA&A, 46, 21
Brearley, A. J. 1999, Sci, 285, 1380
Calvet, N., D'Alessio, P., Hartmann, L., Wilner, D., Walsh, A., & Sitko, M. 2002, ApJ, 568, 1008
Currie, T., & Sicilia-Aguilar, A. 2011, ApJ, 732, 24
D'Alessio, P., Calvet, N., & Woolum, D. S. 2005, ApJ, 621, 461

Davidsson, B. J. R., & Skorov, Y. V. 2002, Icar, 156, 223
Espaillat, C., Ingleby, L., Hernández, J., et al. 2012, ApJ, 747, 103
Haack, H., & Wurm, G. 2007, M&PSA, 42, 5157
Hayashi, C., Nakazawa, K., & Nakagawa, Y. 1985, Protostars and Planets II, ed. D. C. Black & M. S. Matthews (Tucson, AZ: Univ. Arizona Press), 1100
Herrmann, F., & Krivov, A. V. 2007, A&A, 476, 829
Kaufmann, E., Kömle, N. I., & Kargl, G. 2002, in Proc. of the First European Workshop on Exo-Astrobiology, ed. H. Lacoste (ESA SP-518; Noordwijk: ESA), 87
Kelling, T., & Wurm, G. 2009, PhRvL, 103, 215502
Kelling, T., & Wurm, G. 2011, ApJ, 733, 120
Kelling, T., Wurm, G., Kocifaj, M., Klačka, J., & Reiss, D. 2011, Icar, 212, 935
Kocifaj, M., Klačka, J., Kelling, T., & Wurm, G. 2011, Icar, 212, 935
Kocifaj, M., Klačka, J., Wurm, G., Kelling, T., & Kohút, I. 2010, MNRAS, 404, 1512
Krause, M., Blum, J., Skorov, Y. V., & Trieloff, M. 2011, Icar, 214, 286
Krauss, O., & Wurm, G. 2005, ApJ, 630, 1088
Moudens, A., Mousis, O., Petit, J.-M., Wurm, G., Cordier, D., & Charnoz, S. 2011, A&A, 531, A106
Mousis, O., Petit, J.-M., Wurm, G., Krauss, O., Alibert, Y., & Horner, J. 2007, A&A, 466, L9
Natta, A., Testi, L., Calvet, N., et al. 2007, in Protostars and Planets V, ed. B. Reipurth, D. Jewitt, & K. Keil (Tucson, AZ: Univ. Arizona Press), 767
Niederdorfer, E. 1933, MetZe, 50, 201
Rohatschek, H. 1995, JAerS, 26, 717
Sicilia-Aguilar, A., Henning, T., Juhász, A., et al. 2008, ApJ, 687, 1145
Takeuchi, T., & Lin, D. N. C. 2003, ApJ, 593, 524
Weidenschilling, S. J. 1977, MNRAS, 180, 57
Weidenschilling, S. J., & Cuzzi, J. N. 1993, in Protostars and Planets III, 1031
Windmark, F., Birnstiel, T., Güttler, C., Blum, J., Dullemond, C. P., & Henning, T. 2012, A&A, 540, A73
Wozniakiewicz, P. J., Ishii, H. A., Bradley, J. P., et al. 2012, in Lunar and Planetary Institute Science Conference Abstracts, Vol., 43, 2392
Wurm, G. 2007, MNRAS, 380, 683
Wurm, G., & Haack, H. 2009, in ASP Conf. Ser. 414, Cosmic Dust - Near and Far, ed. T. Henning, E. Grün, & J. Steinacker (San Francisco, CA: ASP), 414, 509
Wurm, G., & Krauss, O. 2006, PhRvL, 96, 134301
Wurm, G., Teiser, J., & Reiss, D. 2008, GeoRL, 35, 10201

nature physics

LETTERS

PUBLISHED ONLINE: 1 DECEMBER 2013 | DOI: 10.1038/NPHYS2821

The martian soil as a planetary gas pump

Caroline de Beule*, Gerhard Wurm, Thorben Kelling, Markus Küpper, Tim Jankowski and Jens Teiser

Mars has an active surface, with omnipresent small dust particles and larger debris. With an ambient pressure below 10 mbar, which is less than 1% of the surface pressure on Earth, its CO_2 atmosphere is rather tenuous. Aeolian processes on the surface such as drifting dunes, dust storms and dust devils are nevertheless still active[1–3]. The transport of volatiles below the surface, that is, through the porous soil, is unseen but needs to be known for balancing mass flows[4,5]. Here, we describe a mechanism of forced convection within porous soils. At an average ambient gas pressure of 6 mbar, gas flow through the porous ground of Mars by thermal creep is possible and the soil acts as a (Knudsen) pump. Temperature gradients provided by local and temporal variations in solar insolation lead to systematic gas flows. Our measurements show that the flow rates can outnumber diffusion rates. Mars is the only body in the Solar System on which this can occur naturally. Our laboratory experiments reveal that the surface of Mars is efficient in cycling gas through layers at least centimetres above and below the soil with a turnover time of only seconds to minutes.

As a terrestrial planet, Mars shares many geological and physical processes with Earth[6]. However, the martian environment is unique with respect to at least one point. It is the only Solar System body with an atmosphere of significant but low surface pressure of on average 6 mbar. Consisting mostly of CO_2, this surface pressure corresponds to a mean free path of the gas molecules of 10 μm at a temperature of 218 K. Of central importance is that this mean free path is comparable to the size of the dust particles and to the pore size within the martian soil[7]. A concept from the early days of rarefied gas physics is that under these conditions—mean free path comparable to or larger than the size of a structure—a pore can act as an efficient pump, purely by applying a temperature difference to its ends[8]. In other words, if one side of a thin channel is warmer than the other side, this channel transports gas from the cold to the warm side along its walls[8–10]. This effect is called thermal creep, which can be understood as follows. Let there be a closed reservoir of gas at a temperature T. If a small hole is provided, the gas flow rate (number of particles per time and area) through this opening is proportional to the thermal velocity of the gas molecules multiplied with the density ($v_{\mathrm{therm}} \times n$). Assuming an ideal gas, this is proportional to the pressure over the square root of the temperature $p/\sqrt{\mathrm{T}}$. The lower the temperature at a given pressure, the higher the gas flow. If two reservoirs of the same pressure but at different temperatures are now connected, a net flow from the cold to the warm reservoir results. This argument applies only if the connection between the two reservoirs is smaller or comparable to the mean free path of the molecules and no interaction between gas molecules occurs within. On the basis of this effect, in 1909 Knudsen[8] measured a compression ratio in gas pressure of about a factor of 10 between the two ends of a series of small channels with a diameter of 0.6 mm at sub-millibar pressure. If the pore or the channel is too large compared with the mean free path, a backflow of gas in the centre of the channel inhibits the efficient transport along the channel[9,11]. Therefore, for a dusty soil with micrometre particles, this effect is seen only at millibar pressure. This enables thermal creep through the porous soil of Mars with its low-pressure atmosphere to act as an efficient pump if temperature gradients are present. Thermal creep is similar to, but not to be confused with thermophoresis of gas molecules in a temperature gradient. This has also been considered for transport in soil as thermodiffusion, but has been estimated to be very inefficient on Mars[12]. Gas flow in martian soil also occurs owing to the expansion and contraction during diurnal temperature variation. This also occurs between the two reservoirs at two different temperatures as considered above, but these are one-time equilibrations. In contrast, thermal creep occurs continuously along a temperature gradient. It should be noted that pumping on Mars usually refers to net vertical transport of H_2O in diurnal temperature cycles[13]. The thermal creep soil pump considered here has to be distinguished from this.

The gas mass flow rate M through channels due to thermal creep has been quantitatively described as[11]

$$M = p_{\mathrm{avg}} \sqrt{\frac{m}{2\,k_{\mathrm{B}} T_{\mathrm{avg}}}}\,\pi \frac{r^3}{l} \frac{\Delta T}{T_{\mathrm{avg}}} Q \qquad (1)$$

where p_{avg} and T_{avg} are the average ambient pressure and temperature, r is the channel radius and l is its length. ΔT is the temperature difference between the channel ends, k_{B} is the Boltzmann constant and m is the mean molecular mass of the ambient gas. Q is a factor depending on the Knudsen number. It specifies the balance between thermal creep and pressure-induced backflow. It is $Q \sim 0$ at high pressure where the mean free path is much smaller than the pore size as, for example, on Earth.

Under gravity the dominant gas flow above an illuminated and hence heated dust bed is the thermal convection. This motion is restricted to the space above the soil. A component due to gas flow through the soil by means of thermal creep is not easily discerned under gravity in the face of thermal convection. We therefore carried out experiments with an illuminated dust bed at the drop tower in Bremen (Germany) where residual gravity is below 10^{-6} g for approximately 9 s (Methods). We used basalt with a broad size distribution up to 125 μm and a gas atmosphere with a 4 mbar ambient air pressure. In the work reported here we analyse the gas flow by observing the motion of tracer dust particles. We use particle eruptions similar to those discussed in refs 14 and 15 to generate tracer particles to study the gas flow through the porous dust bed on illumination.

Without gravity thermal convection does not exist and gas flow due to thermal creep can be observed unbiasedly. An absence of convective eddies can be demonstrated in the experiments for an illuminated solid surface. The tracer particles move only within the illuminated spot owing to photophoresis—a particle motion by light-induced temperature differences over the dust particles. No motion is visible for dust particles if not illuminated directly. This translates to no significant gas flow being present.

This changes once the basaltic dust bed is exposed to the light source. A convective flow pattern becomes visible (Fig. 1a). We note again that the experiments are carried out without gravity and the

Faculty of Physics, University of Duisburg-Essen, Lotharstraße 1, D-47048 Duisburg, Germany. *e-mail: caroline.de-beule@uni-due.de

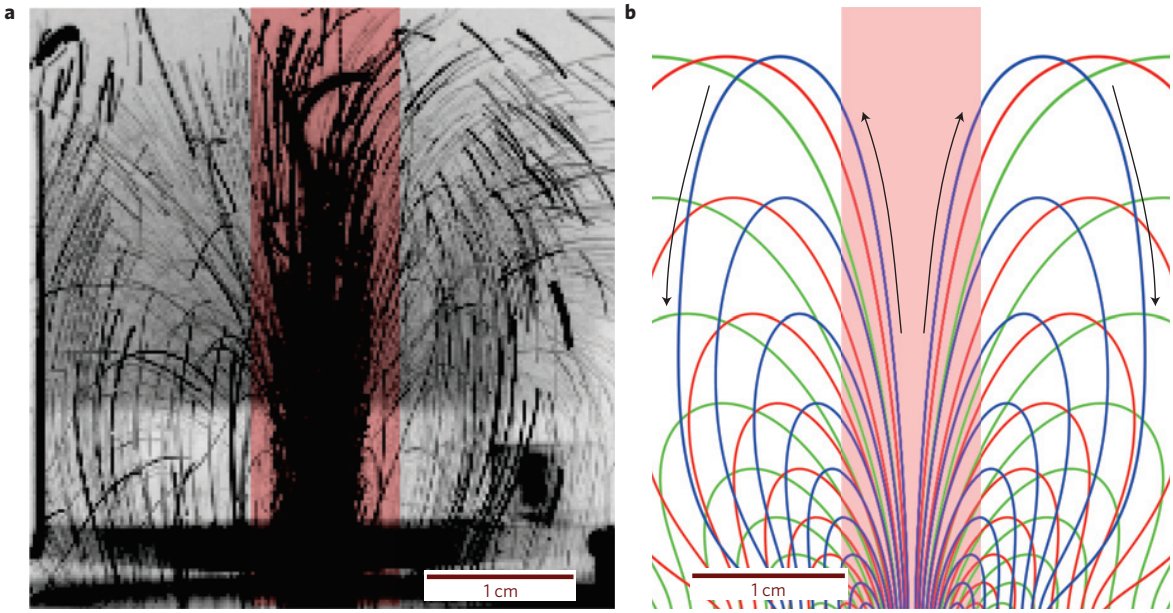

Figure 1 | Particle trajectories above an illuminated dust bed consisting of basalt particles. a,**b**, The trajectories seen in the experiments (**a**) are consistent with a simulation of the gas flow (**b**) assuming a volume force in the dust bed due to thermal creep. The light red bar marks the diameter (8 mm) of the light source (laser, 655 nm, 13 kW m^{-2}). The direction of the particle motion is represented by the black arrows on image **b**. Owing to the illumination, dust particles leave the surface within the laser beam. The lines outside the laser (red bar) mark the downwardly directed particle and gas flow. These particles are not illuminated and trace only the streamlines. Streamlines enter the dust bed's surface outside the illuminated area. The illumination of the dust bed leads to a convective flow through the soil.

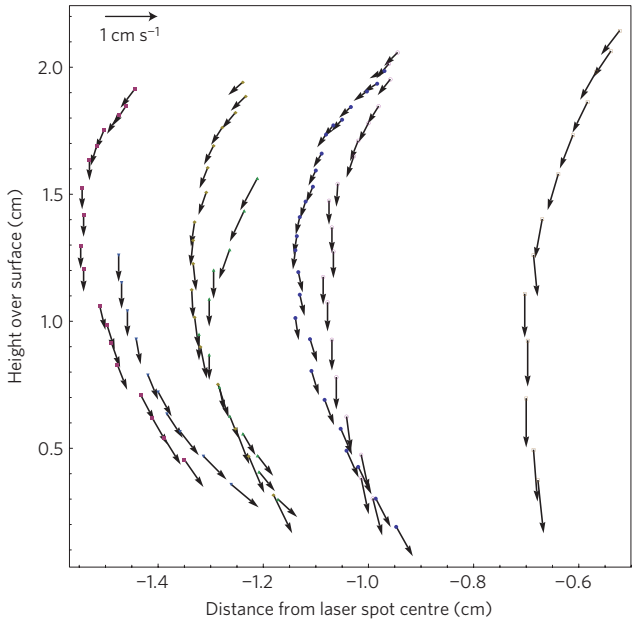

Figure 2 | Velocities of a sample of tracer particles along their streamlines. The *x* axis shows the distance from the centre of the laser spot and the *y* axis the height over the dust bed.

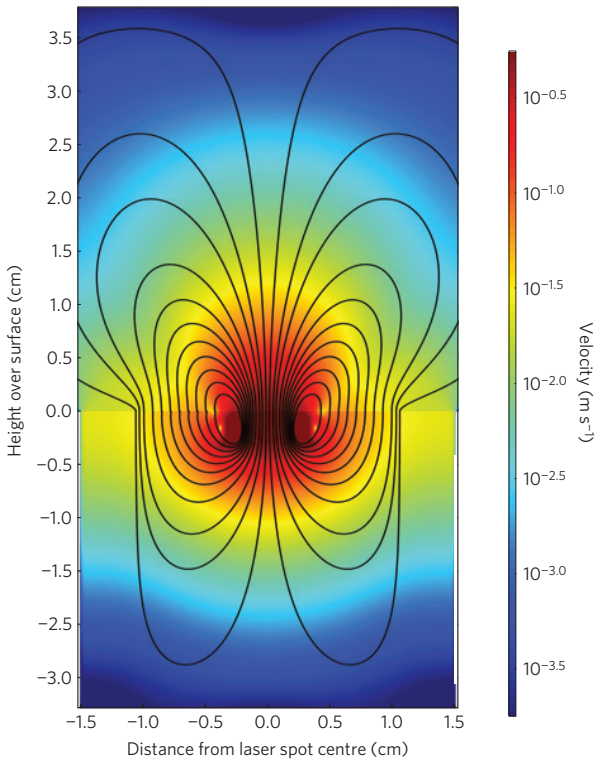

Figure 3 | Simulation of particle velocities along their streamlines below and above the surface of the dust sample. The height 0 marks the surface of the dust bed. The coloured scale gives the velocities, ranging from $10^{-0.0687}$ to $10^{-11.237}$ ms^{-1}.

convection is not a thermal convection. The tracer particles follow the gas streamlines and enter the dust bed in the non-illuminated part tracing a gas flow into the soil (Fig. 1).

At a radiation flux of 13 kW m^{-2} the upward velocity is about 10 cm s^{-1} within the illuminated spot and downward velocities outside the illuminated spot are about 1 cm s^{-1} (Fig. 2). The inflow of gas extends to the outer end of the dust bed. The fact that gas also enters the soil at the outer extension 1.5 cm away from the spot indicates that the flow within the soil is reaching down to the bottom of the dust bed 2 cm below the surface. This is consistent with a model of forced flow through the porous medium as seen in Figs 1b and 3.

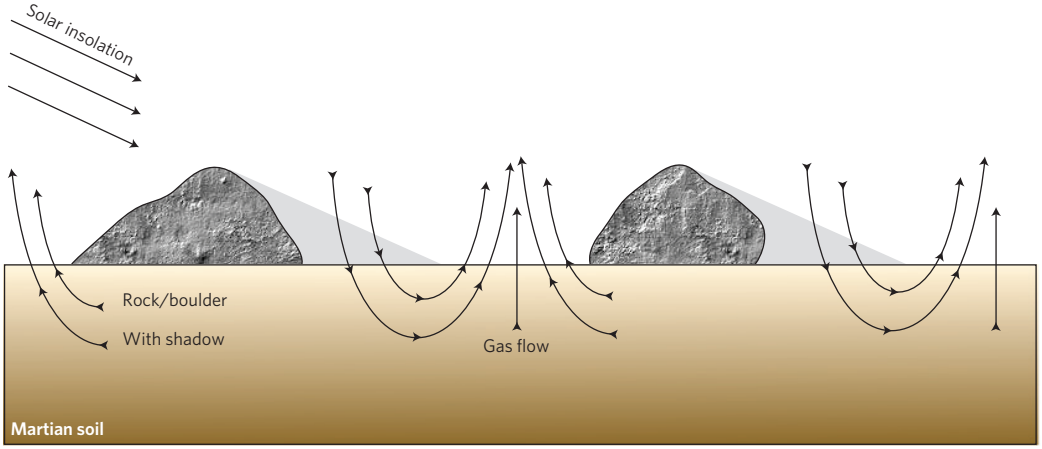

Figure 4 | The natural soil pump on Mars. Owing to solar insolation thermal creep leads to a gas flow from the cool deeper layers up to the surface. The resulting pressure difference in the dust bed soaks up atmospheric gas from shadowed surfaces into the soil and pumps it underneath the surface towards insolated (heated) surface regions.

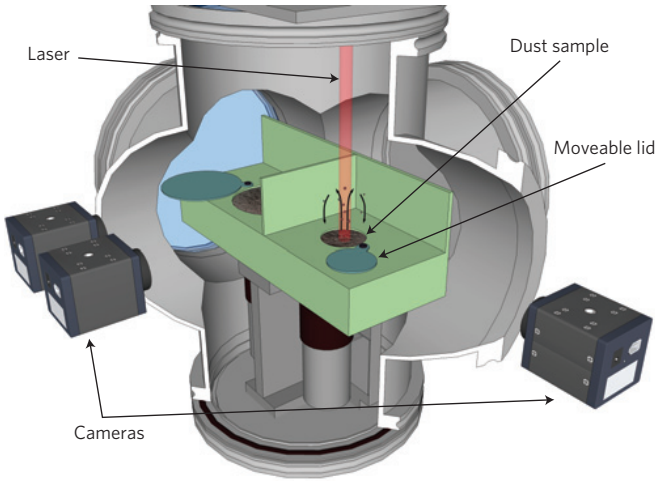

Figure 5 | Schematic diagram of the drop tower experiment. The small container for basalt powder has a diameter of 3 cm and is 2 cm deep. A red laser with 655 nm is focused on a spot diameter of 8 mm on the dust bed. Two cameras observe the movement of the dust particles at an angle of 90°.

As the experimental conditions compare well to the martian environment (detailed below), the results can readily be applied to Mars and reveal the following picture: if the martian soil is heated by solar insolation, gas will be pumped from the colder soil layers beneath the heated layers towards the surface.

At shadowed places on the surface, gas will efficiently be soaked up into the soil, traverse the underground and will be pumped up again to the heated (insolated) surface as shown in Fig. 4. Therefore, the resulting gas flow below the surface is a mixture of a vertical and a horizontal flow. In this simple picture, shadowed regions are needed as a continuous (atmospheric) reservoir of gas. As pores in soil act like micro-channels and as dust particles and pores exist in the micrometre range, the low atmospheric pressure on Mars is ideally suited to provide its soil with the ability for natural thermal creep pumping. The capability of gas flowing through heated or insolated dust layers can also lead to a significant pressure increase. It can even be sufficient to levitate large dust aggregates or to eruptively eject particles from the surface, which has been shown in ground-based laboratory experiments[10,14–17].

To evaluate the gas mass flow in the drop tower experiments we use equation (1), with $p_{avg} = 4$ mbar and $T_{avg} = 300$ K. For a length of $l = 2$ cm (depth of the dust bed) and basaltic powder with a thermal conductivity of $0.01\,W\,K^{-1}\,m^{-1}$ (ref. 18), we get $\Delta T = 300$ K (ref. 15). In a simple model of hexagonally packed spheres, the radius of a capillary is about 20% of the sphere radius; therefore, we assume $r = 0.2 r_{particle}$ with $r_{particle} = 50\,\mu m$. The molecular mass of the air is $m = 28.96$ AMU and $k_B = 1.37 \times 10^{-23}\,J\,K^{-1}$. The mean free path of air in the experiments is $\lambda = 17.5\,\mu m$. This results in a Knudsen number $Kn = (\lambda/2r) = 0.875$. For this Knudsen number, we take the Q-value from ref. 11 of $Q = 0.36$. This leads to a gas mass flow of $10^{-14}\,kg\,s^{-1}$. Divided by the cross-section of one capillary $A = 10^{-10}\,m^2$ and the density of air at 4 mbar ambient pressure $\rho = 4.8 \times 10^{-3}\,kg\,m^{-3}$, we get a mean gas velocity of 9 cm s^{-1}, which is consistent with the velocities measured in the experiment.

Scaling this to martian conditions we have to consider CO_2 instead of air, which has a molecular mass of $m_{CO_2} = 44$ AMU. With a geometric radius of 4.63×10^{-10} m (ref. 19) the molecule has a cross-section of $\sigma = 1.6 \times 10^{-19}\,m^2$. At $p = 6$ mbar, $T = 218$ K and a particle density $n = p/k_B T$, the mean free path of CO_2 is $\lambda = (1/\sqrt{2}n\sigma) = 21\,\mu m$. According to this mean free path, the Knudsen number is 1.05 and hence $Q = 0.31$ (ref. 11). Owing to the lower insolation of about $700\,W\,m^{-2}$, a smaller temperature difference than in the experiment is obtained. As a first estimate, we assume the typical diurnal surface temperature variation as $\Delta T = 50$ K. Assuming the same thermal conductivity of $0.01\,W\,K^{-1}\,m^{-1}$, a length of 2 cm and an average particle radius of 50 µm, the CO_2 gas mass flow is the same as the air mass flow in the experiments with $10^{-14}\,kg\,s^{-1}$. Divided by the cross-section $A \sim 10^{-10}\,m^2$ and the density of CO_2 at 6 mbar ambient pressure $\rho = 14.6 \times 10^{-3}\,kg\,m^{-3}$, the result is a mean gas velocity of 1.6 cm s^{-1} on Mars.

The details of the martian gas pump will depend on the local light flux, which varies with daytime and shadow-casting landmarks. It also depends on the detailed soil characteristics such as pore size, albedo and thermal inertia.

Mars is known to have buried ice within its subsurface[20] and water vapour can be transported by diffusion to the surface[12]. Ref. 21 estimated the diffusion constant of water vapour in a martian simulant (JSC Mars-1 Dust) at 6 mbar ambient pressure to 1.5 $cm^2\,s^{-1}$. Diffusive flow might roughly be estimated to 0.3 cm s^{-1} for a 5 cm layer then. This is below the pump velocity found in the experiments scaled to martian conditions. The thermal creep gas flow hitherto unconsidered might therefore be a dominant transport mechanism for water vapour in large parts of the martian soil as it is dragged along with the CO_2.

Basalt dust beds were studied here, which we regard as a suitable analogue to martian dust[22]. However, essentially all light-absorbing

dust samples show effects of thermal creep in ground-based laboratory experiments on illumination (Methods).

The natural soil pump on Mars is probably leaky, acting locally in many different ways. This natural, potentially planet-wide pump is tied to the ambient pressure and has no analogue on Earth or any other planet known in the Solar System. It certainly has an influence on the gas cycle and the soil atmosphere interaction on Mars. As the directed CO_2 gas flow carries along the other gas species as well, it also has to be considered for water transport through the soil.

Methods

The experiment. The experiments were carried out at the drop tower in Bremen (Germany) in a catapult mode. A sketch of the experiment is shown in Fig. 5.

A basaltic dust sample is placed inside a vacuum chamber. This chamber is evacuated after preparation to a preset value of 4 mbar.

During the launch the dust bed is covered by a lid to prevent particle loss during tension release. After 300 ms in microgravity the lid is opened. The dust sample is illuminated by means of a red laser (655 nm) with a spot diameter of 8 mm. The light flux is varied between 13, 9 and 6 kW m^{-2}. The laser is turned on 4 s before the launch. The light flux is chosen as high so that once the lid is opened, particle eruptions due to a solid-state greenhouse effect and photophoresis occur[10,14,16]: the solid-state greenhouse effect is mostly known for transparent bodies such as dirty ice[23]. Visible radiation enters the medium and the absorption heats it within. As thermal radiation cannot escape because ice is opaque at this wavelength, the ice heats up below and is cooler at the surface (greenhouse effect). The same can occur for dust samples as visible light enters through the pores or forward scattering and thermal radiation cannot leave the same way[17,24]. In this study, this is a minute detail, as it influences only the top dust layer of about 100 µm and does not change the coarser temperature structure of the sample. However, the temperature gradient is sufficient to lead to an upward-directed photophoretic force on particles in the top layer that can eject particles from the surface at high light flux[24].

At 4 mbar, a 50 µm size particle couples to the gas flow on a timescale of 50 ms. Therefore, in accordance with the observations, they rapidly slow down and then essentially trace the gas flow. A photophoretic motion is superimposed on the particle motion. This is visible when the dust bed is closed again by the lid 1 s before hitting the ground and returning to laboratory gravity. Particle motion by photophoresis can be stronger than the gas flow. Such particles are, for example, seen moving towards the dust bed rapidly within the laser beam. In any case, particles outside the direct light beam are not subject to photophoresis but are visible within the stray light. They move along with the gas and trace the streamlines.

The sample. We used three different dust bed samples: black spherical particles (150–250 µm in size), basalt with a broad size distribution up to 125 µm and a mixture of basalt and transparent glass spheres of 150–250 µm size. All basalt samples were heated for 48 h at 200 °C to remove any water. Neither sublimation nor expansion led to an inflow of gas into the dust bed and to a directed convection through free-floating aggregates (also observed but not shown here). Earlier levitation experiments with basalt and other samples showed that gas flow and compression are not tied to water[10,25]. In fact, the earlier levitation experiments with basalt were carried out on a 500 °C hot surface and we rule out that water plays a role here. Most experiments were carried out with pure basalt but the other samples showed the same gas flow patterns.

Model of dust bed gas flow. To support the measurements we carried out a numerical calculation according to the experimental setting. For this we simulated a gas flow within the experiments.

The problem was solved using COMSOL to simulate the flow within the dust bed and in the space above. To drive the gas flow, we placed a volume force within which the light beam enters the dust bed and it was adjusted to obtain the measured mass flow rates. Everything else, that is, the convective pattern and the depth of the gas flow, is then determined self-consistently. The simulation is carried out to compare the general circulation to the experiments and to see the part below the surface not accessible by the observations. The simulated flow matches the general flow pattern as well as the measured inflow velocities. The simulations show that gas flow at least down to 1 cm is still larger than 1 mm s^{-1} but this strongly depends on the spatial extent of the dust bed and illumination. A spatially scaled up version of the simulation shows that also the depth of the gas flow increases. Therefore, gas flow for the illuminated surface of Mars might reach larger depths.

Received 12 June 2013; accepted 25 October 2013; published online 1 December 2013

References

1. Greeley, R., Lancaster, N., Lee, S. & Thomas, P. *Mars* 730–766 (Univ. Arizona Press, 1992).
2. Bridges, N. *et al.* Earthlike sand fluxes on Mars. *Nature* **485,** 339–342 (2012).
3. Reiss, D., Zanetti, M. & Neukum, G. Multitemporal observations of identical active dust devils on Mars with the high resolution stereo camera (HRSC) and Mars orbiter camera (MOC). *Icarus* **215,** 358–369 (2011).
4. Sizemore, H. G. & Mellon, M. T. Laboratory characterization of the structural properties controlling dynamical gas transport in Mars-analog soils. *Icarus* **197,** 606–620 (2008).
5. Bryson, K. L., Chevrier, V., Sears, D. W. G. & Ulrich, R. Stability of ice on Mars and the water vapor diurnal cycle: Experimental study of the sublimation of ice through a fine-grained basaltic regolith. *Icarus* **196,** 446–458 (2008).
6. Kieffer, H. H., Jakosky, B. M. & Snyder, C. W. *Mars* 1–33 (Univ. Arizona Press, 1992).
7. Dollfus, A. & Deschamps, M. Grain size determination at the surface of Mars. *Icarus* **67,** 37–50 (1986).
8. Knudsen, M. Eine Revision der Gleichgewichtsbedingung der Gase. Thermische Molekularströmung. *Ann. Phys.* **336,** 205–229 (1909).
9. Muntz, E. P., Sone, Y., Aoki, K., Vargo, S. & Young, M. Performance analysis and optimization considerations for a Knudsen compressor in transitional flow. *J. Vac. Sci. Technol.* **20,** 214–224 (2002).
10. Kelling, T. & Wurm, G. Self-sustained levitation of dust aggregate ensembles by temperature-gradient-induced overpressures. *Phys. Rev. Lett.* **103,** 215502 (2009).
11. Han, Y. L. *Investigation of Micro/Meso-scale Knudsen Compressors at Low Pressures* (ProQuest Information and Learning Company, 2006).
12. Hudson, T. L. *et al.* Water vapor diffusion in Mars subsurface environments. *J. Geophys. Res.* **112,** E05016 (2007).
13. Mellon, M. & Jakosky, B. Geographic variations in the thermal and diffusive stability of ground ice on Mars. *J. Geophys. Res.* **98,** 3345–3364 (1993).
14. Wurm, G. & Krauss, O. Dust eruptions by photophoresis and solid state greenhouse effects. *Phys. Rev. Lett.* **96,** 134301 (2006).
15. Kelling, T. & Wurm, G. A mechanism to produce the small dust observed in protoplanetary disks. *Astrophys. J.* **733,** 120–124 (2011).
16. de Beule, C., Kelling, T., Wurm, G., Teiser, J. & Jankowski, T. From planetesimals to dust: Low-gravity experiments on recycling solids at the inner edges of protoplanetary disks. *Astrophys. J.* **763,** 11 (2013).
17. Kocifaj, M., Klačka, J., Kelling, T. & Wurm, G. Radiative cooling within illuminated layers of dust on (pre)-planetary surfaces and its effect on dust ejection. *Icarus* **211,** 832–838 (2011).
18. Presley, M. A. & Christensen, P. R. Thermal conductivity measurements of particulate materials. *J. Geophys. Res.* **102,** 6535–6549 (1997).
19. Chapman, S. & Cowling, T. in *The Mathematical Theory of Non-Uniform Gases* 3 edn 288 (Cambridge Univ. Press, 1970).
20. Squyres, S. W., Clifford, S. M., Kuzmin, R. O., Zimbelman, J. R. & Costard, F. M. *Mars* 523–554 (Univ. Arizona Press, 1992).
21. Hudson, T. L. & Aharonson, O. Diffusion barriers at Mars surface conditions: Salt crusts, particle size mixtures, and dust. *J. Geophys. Res.* **113,** E09008 (2008).
22. McSween, H. Y. Jr & Keil, K. Mixing relationships in the Martian regolith and the composition of globally homogeneous dust. *Geochim. Cosmochim. Acta* **64,** 2155–2166 (2000).
23. Krömle, N. I., Dettleff, G. & Dankert, C. Thermal behavior of pure and dusty ices on comets and icy satellites. *Astron. Astrophys.* **227,** 246–254 (1990).
24. Wurm, G. Light-induced disassembly of dusty bodies in inner protoplanetary discs: Implications for the formation of planets. *Mon. Not. R. Astronom. Soc.* **380,** 683–690 (2007).
25. Jankowski, T. *et al.* Crossing barriers in planetesimal formation: The growth of mm-dust aggregates with large constituent grains. *Astron. Astrophys.* **542,** A80 (2012).

Acknowledgements

This project is supported by DLR Space Management with funds provided by the Federal Ministry of Economics and Technology (BMWi) under grant number DLR 50 WM 1242. T.J. and M.K. are supported by the DFG. Access to earlier microgravity experiments on parabolic flights leading to the development of the experiment was granted by DLR and ESA.

Author contributions

C.d.B. and J.T. designed the experiment. C.d.B. performed the experiment with help from G.W., T.K., M.K., T.J. and J.T. M.K. simulated the gas flow with help from G.W. C.d.B. and G.W. wrote the paper with input from T.K., M.K., T.J. and J.T.

Additional information

Reprints and permissions information is available online at www.nature.com/reprints. Correspondence and requests for materials should be addressed to C.d.B.

Competing financial interests

The authors declare no competing financial interests.

Microgravity Sci. Technol.
DOI 10.1007/s12217-014-9357-1

ORIGINAL ARTICLE

Propulsion of Porous Plates in Thin Atmospheres by Temperature Fields

Experiments on Parabolic Flights

M. Küpper · C. Dürmann · C. de Beule · G. Wurm

Received: 15 March 2013 / Accepted: 30 December 2013

Abstract In low pressure environments macroscopic bodies can be subject to photo- and thermophoretic motion if temperature gradients are present. Porosity can increase the efficiency of this propulsion. We developed a setup to generate a temperature field and measure phoretic accelerations in a parabolic flight. In a first campaign we studied the pressure dependence of the acceleration for thin plates (1.7 mm thickness, 2.2 and 3.5 cm diameter) consisting of sintered glass spheres of a size range of 150 to 250 μm and 40 to 70 μm. We find evidence for two characteristic propulsion maxima at pressures related to the overall size of the plate as well as the bead (pore) size. The increase of the magnitude of acceleration due to the porosity is on the order of 10^{-2} g for the specific samples. This force is comparable to the phoretic force attributed to the overall size of the plate.

Keywords Radiometer · Thermal creep · Photophoresis · Thermophoresis · Protoplanetary disk

Introduction

The motion of macroscopic objects in low pressure environments induced by temperature gradients (photo- and thermophoresis) has been subject to research since the 19th century (eg. Crookes (1874) and Ehrenhaft et al. (1931)). It is still ongoing and a review with focus on the motion of plates has recently been published by Ketsdever et al. (2012).

M. Küpper (✉) · C. Dürmann · C. de Beule · G. Wurm
Faculty of Physics, University of Duisburg-Essen, Lotharstr. 1, 47048 Duisburg, Germany
e-mail: markus.kuepper@stud.uni-due.de

Early work referred to forces on vanes by illumination or temperature gradients as *radiometric* forces. More recently, a motion induced by temperature gradients *within the gas* is usually named *thermophoresis*. Equations for simple particle shapes e.g. spherical particles exist for all gas pressures (Zheng 2002). If light induces a temperature gradient *across the particle* due to non-uniform illumination or different absorption, the effect is called *photophoresis*. For simple shaped particles – i.e. spheres – this force can also be specified for the whole pressure range (Rohatschek 1995).

The motivation behind our work in this field is to gain a better understanding of particle propulsion in protoplanetary disks, low gravity environments, where photophoretic and thermophoretic forces might be the strongest non gravitational force. Photophoresis has been introduced to this field by Krauss and Wurm in (2005, 2006). Particles in protoplanetary disks span the size range from sub-micron dust to planets. Larger bodies are formed by aggregation and are partially highly porous (Blum and Wurm 2008; Meisner et al. 2012).

Some numerical work on small arrays of neighboring plates shows that the phoretic force increases by the proximity of plates (Gimelshein et al. 2011). This suggests that holes in an individual plate should influence photophoretic effects and porosity, in a wider sense a collection of holes, should influence the phoretic forces as well. However, it is currently unknown how a small scale porosity influences the forces experienced by a particle in a temperature field, as the reduction of surface area and the holes have competing effects.

Describing these forces over the whole pressure range is – in general – not a trivial task, as the basic mechanisms responsible for the phoretic forces vary with pressure. The mean free path of the gas molecules λ compared to the

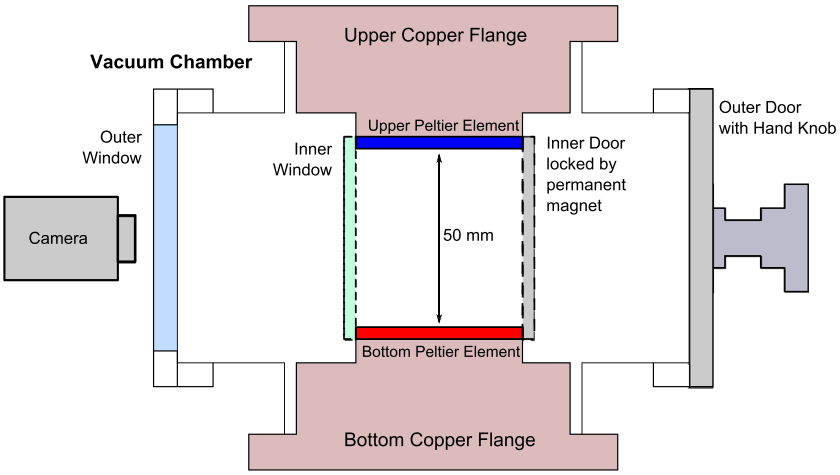

Fig. 1 Experimental setup: Inside a vacuum chamber two peltier elements generate a temperature gradient. Under microgravity conditions the movement of a sample is observed at low pressure by a camera

characteristic particle size r is the crucial parameter. It is called Knudsen number and defined as

$$\mathrm{Kn} = \frac{\lambda}{r}. \tag{1}$$

In the free molecular flow regime (at high Knudsen numbers), interaction with individual gas molecules is dominating. In the hydrodynamic regime (at high pressure) collective effects are important and the phoretic motion is initiated by gas flow from the cold to the warm particle side along a thin surface layer of the accelerated object. This is also called thermal transpiration or thermal creep. Due to conservation of momentum, the particle has to balance the gas flow and move from warm to cold as observed. Ketsdever et al. (2012) show that in the hydrodynamic flow regime the force is induced by a pressure increase on the warm particle side due to thermal creep. Because of a pressure built-up the force can be much stronger than reacting to the gas flow alone. Indeed, a pressure increase in a warm gas reservoir as a result from thermal creep through a small channel connecting to a cold reservoir has been demonstrated in 1909 by Knudsen (1909). Pumps only based on temperature gradients are therefore generally known as Knudsen compressors. Modern aspects of this include the idea of an efficient transport of gas in small structures or providing roughing pumps for applications on Mars (Lilly et al. 2007; Alexeenko et al. 2006; Vargo et al. 1999; Muntz et al. 2002; de Beule et al. 2014)). In planetary science the Knudsen compressor and internal phoretic forces are means to disassemble larger dust aggregates (Wurm and Krauss 2006; Kocifaj et al. 2011; Kelling et al. 2011; de Beule et al. 2013).

The effects of a temperature gradient driven gas flow and a phoretic motion are largest at pressures exactly between free molecular flow and hydrodynamic flow regime, i.e. if the mean free path of the gas molecules is comparable to the typical effective sizes. Therefore, the efficiency of pumps based on porous media depends on the size and structure of the pores (Lilly et al. 2007). While the maximum compression ratio is one aspect, the phoretic force on a free porous particle is another. For a porous plate of given thickness there are 3 parameters that should influence the phoretic forces: the overall size (diameter) of the plate, the size of the capillaries through this plate and the spatial density of the capillaries, i.e. the spacing between pores. Due to distinct characteristic sizes the effects should be visible in different pressure ranges. This has been seen in experiments with plates with channels of a distinct size that have been carried out by Dürmann et al. (2013). They did not measure the force on porous plates though. Also convection influences the absolute force measurements in ground based experiments.

Here we present first parabolic flight measurements on the phoretic acceleration due to temperature fields. In our setup small forces can be studied, as the gravitational driven convection is suppressed. Convection due to thermal gradients becomes important here and can not be suppressed, therefore our setup is still influenced by thermal convection.

Microgravity Experiments

Experiments are carried out in a vacuum chamber as shown in Figs. 1 and 2. Two peltier elements of 55 × 55 mm in size are placed inside the chamber separated by 50 mm. They are enclosed by a small box with a window on one side. The peltiers are in contact to copper flanges for sufficient heat transfer. The pressure in the vacuum chamber can be adjusted by a membrane and turbo molecular pump system. Throughout the different parabolas for one parabolic flight day it was varied by 4 orders of magnitude between 10^{-3} mbar and 10 mbar.

The samples used in the experiment are small plates of sintered glass beads. In Table 1 the characteristics of the 3

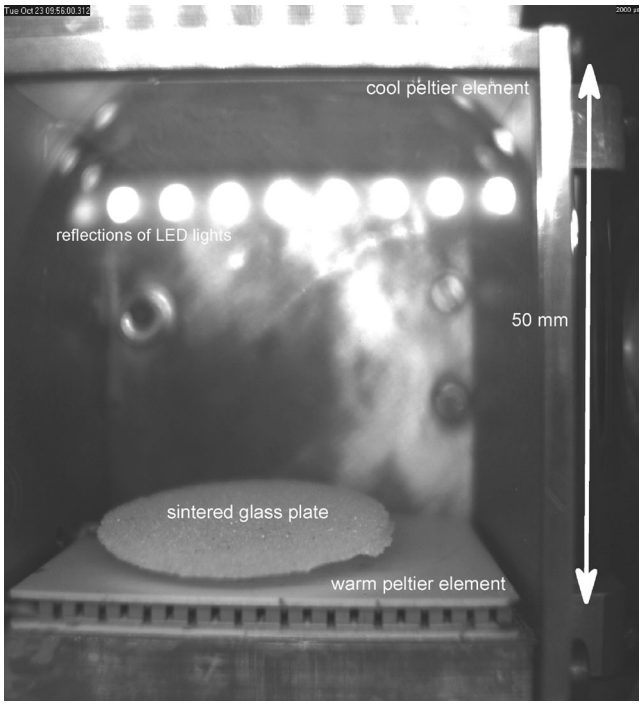

Fig. 2 Example of a sintered glass plate; sample #1 during the flight

plates used on the 3 flight days are summarized. The porosity was calculated using the thickness and radius of the plate and assuming the glass bulk density (2520 kg/m^3). One plate was used per flight day. Each parabola the sample is initially located on the bottom of the box while the peltier elements are generating the temperature field.

Due to the temperature difference, gas flows through the pores of the sample and induces a force on the glass plate. During a parabola gravity decreases and varies around 0 g. At the time the residual downward gravity matches the phoretic upward force on the sample it starts to lift from the peltier element and floats freely to the upper side due to the propulsion.

A camera is placed in front of the window of the vacuum chamber, observing the movements of the sample inside the chamber with 60 frames per second. The residual gravity level is recorded with 100 samples per second. The correlation of the observed moment of sample lift-off to the measured gravity level gives a value for the propulsion induced by the temperature gradient along the sample. We only consider the cases of free motion toward the other side here as the Knudsen compressor effect can cause the plate to hover already at normal gravity, given enough temperature gradient (Kelling and Wurm 2009).

Table 1 Plate parameters on different flight days, all three plates had the same thickness of 1.7 mm

Sample #	1	2	3
Sample ø [cm]	3.5	2.2	2.2
Sintered at [°C]	700 °C	650 °C	650 °C
for [h]	3.5h	3.5h	3h
Bead ø [µm]	150–250	150–250	40–70
Mass [g]	2.29	0.72	0.66
Porosity [%]	44.4	55.8	59.5

Experimental Procedure

The peltier elements are powered with their constant maximum safe voltage to create the biggest possible temperature gradient. Due to lack of regulation the temperature difference is not perfectly stable, but changes with the set pressure (Fig. 3). This change was attributed mainly to thermal conduction of the gas. The temperature was nearly stable (less than 1 °C change) during the parabolas. We started to measure from the lowest pressure to the highest pressure and repeated the procedure once, this leads to the two independent tracks seen in Fig. 3 for each day (During the second day we reversed the gradient temporarily, but this did not work well - therefore the track is interrupted). The data for the temperature, pressure and z-component of acceleration is shown as an example in Fig. 4. On the top peltier one can see slight warming, this results from the copper flange with the cooling unit heating up slowly to some degrees above room temperature. The bottom peltier element shows clearly that it changes with the pressure. At higher pressures the temperature drops quickly at the moment of pressure change, but stays reasonable stable during the parabolas, so that the change of temperatures during the measurements is less than one degree. The pressure values in Fig. 4 show the steps in which we wanted to measure. Beside the temperature and the pressure, Fig. 4 shows the gravitational acceleration.

As the plate was tumbling, when it was free floating it was impossible to observe the acceleration during the free floating phase precisely. Without 3D information it was not possible to determine the center of mass. The temperature gradient over the plate can not be determined well because the plate rotated. Therefore we focused on the moment of detachment, where residual gravitation and acceleration are equal. The situation is better defined there, but other effects due to the proximity of the bottom and walls have to be considered.

Due to thermal creep along the chamber walls, there is a fountain type gas flow, which has a velocity of approx. 160 mm/s in the middle of the chamber (at 1 mbar and 100 K temperature difference over the 5 cm height) (Papadopoulos and Rosner 1995). This leads to an acceleration of 2×10^{-3} g as a maximum when the sample is in the middle and

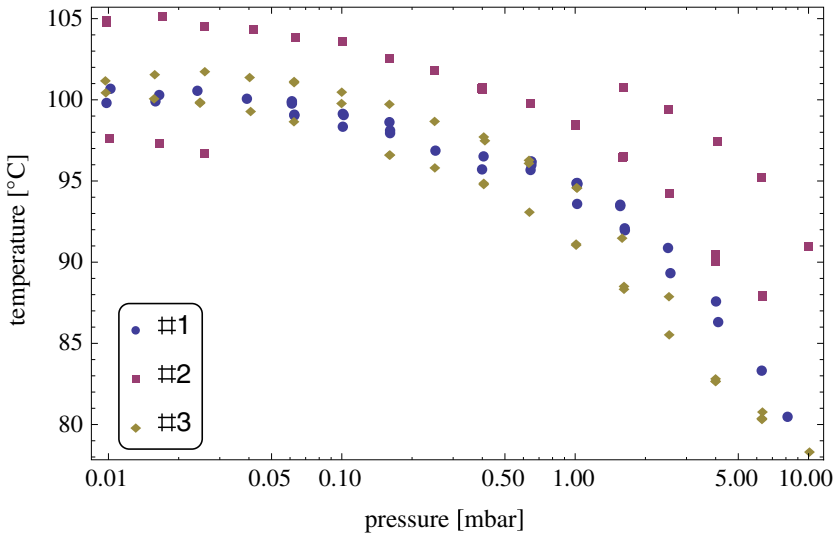

Fig. 3 Temperature difference versus pressure at the observed detachment points. It can be seen that at higher pressure the temperature difference becomes smaller

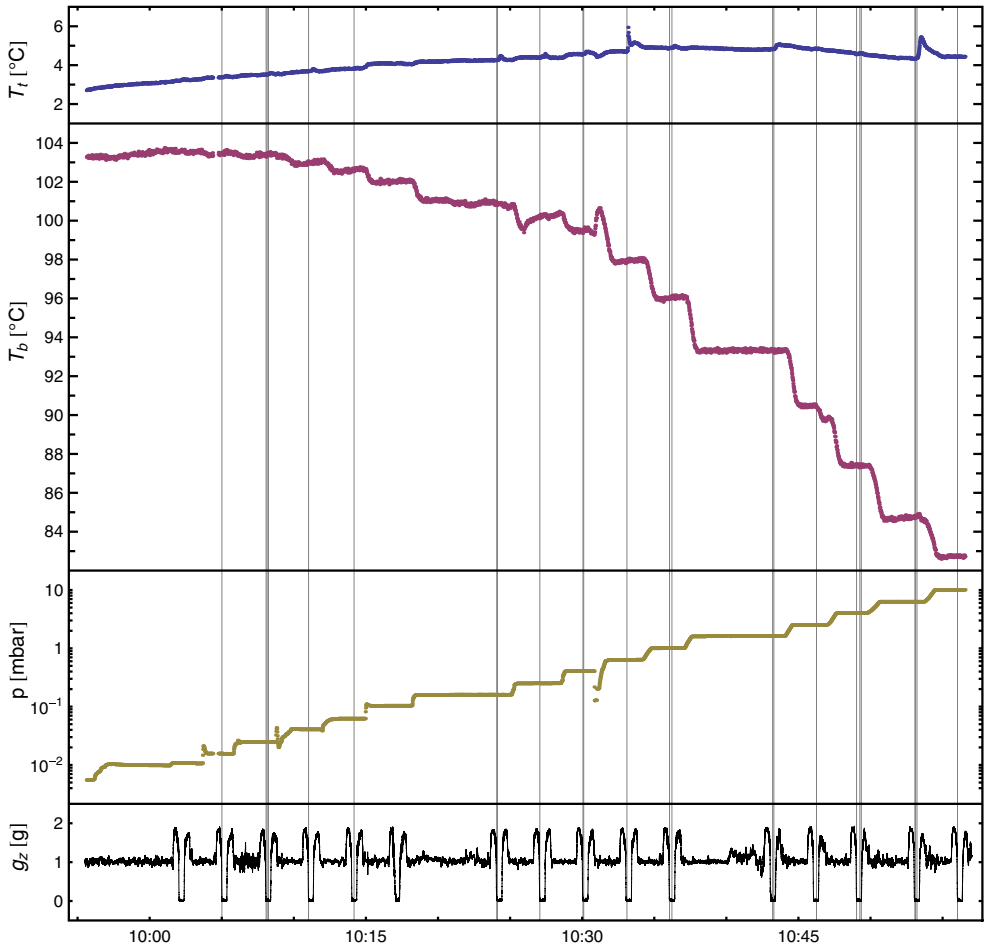

Fig. 4 Example of the recorded data (first half of the flight on the 3rd day) over time. From Top to bottom: the temperature of the upper peltier element in *blue*, of the lower peltier element in *red*, pressure on logarithmic scale in *yellow* and acceleration on z-Axis in *black*. The *vertical lines* mark the moments where the plate detached

Table 2 Fit parameters obtained for sample shown in Fig. 8

$g_{max,1}$	0.057 g	± 0.007 g
$p_{opt,1}$	0.025 mbar	± 0.006 mbar
$g_{max,2}$	0.040 g	± 0.005 g
$p_{opt,2}$	4.0 mbar	± 1.0 mbar

suffers the full (Epstein) gas drag. The effect is of minor importance, as at the moment of measurement the plate is at the bottom where the flow is perpendicular and slower diminishing the drag force further.

More important are the effects due to the proximity of the bottom. As the gas is pumped to the bottom by the thermal gradient of the plate and can not easily escape from there, an overpressure builds up, which may cause the plate to hover over the surface. This effect is further reinforced if the plate is hotter in the middle. As this effect declines steeply with the distance to the wall, the main effect is that the plate hovers over the hot surface before taking off. This may induce a slight systematical shift in the data as the plate lifts up too early and all forces are estimated to be bigger than they are. It was not observed that a sample was hopping over the surface, so this error has to be small: when the plate lifts it does not come back because the additional force is removed. If the plate showed a lot of movement in the transition between hovering and lifting, we did not do a measurement, because it could not clearly be seen how the plate moved in 3D, for example a hovering backwards movement could be mistaken for a lift off.

When the plate lifts off from the surface, the time and with it the residual gravity, the temperatures and pressure were noted. This was one individual data point. The plates moves several times from bottom to top and back. The number of measurements per parabola varies. The pressure could be set well, so we took the measurements from each pressure and calculated the mean value and the variation (where possible) of the residual gravitation at the point of detachment. Determined values for the resulting accelerations vary on a level of 0.01 g. This variation mostly results from the uncertainty in the correlation between residual gravity and time of lift-off and currently sets the limit of the measurements. We corrected the measured data by a factor accounting for the varying temperature difference for different pressure (due to the thermal conductivity of the gas the temperature difference changes). Assuming the force to be linear with temperature, we chose 100K/ΔT for an appropriate factor (see photophoresis formula (Rohatschek 1995)), so that all forces are related to the same temperature difference of 100 K between the peltier elements.

Results

Figure 8 shows the results for the sample with the strongest propulsion. It consists of 150 to 250 μm beads and has a total diameter of 2.2 cm. The measured accelerations are a few times larger than the uncertainties and allow an analysis of the pressure dependence.

The outcome is in agreement with general expectations. The two different peaks roughly differ by a factor of 100 in pressure. This corresponds to the factor 100 between total radius (10 mm) and bead radius (0.1 mm), as the photophoretic forces are strongest around $Kn = 1$. Obviously, the total size or bead (pore) size are important in different pressure ranges. We fitted the data by the sum of two pressure depending photophoretic forces according to Rohatschek (1995):

$$g = \frac{2g_{max,1}}{\frac{p_{opt,1}}{p} + \frac{p}{p_{opt,1}}} + \frac{2g_{max,2}}{\frac{p_{opt,2}}{p} + \frac{p}{p_{opt,2}}}. \quad (2)$$

This function fits the data quite well and yields the values shown in Table 2.

The other two samples show no significant pressure dependence. Data of a sample larger in total size is seen in Fig. 6. The size of the sample is close to the total extend of the experiment chamber and proximity effects of the side

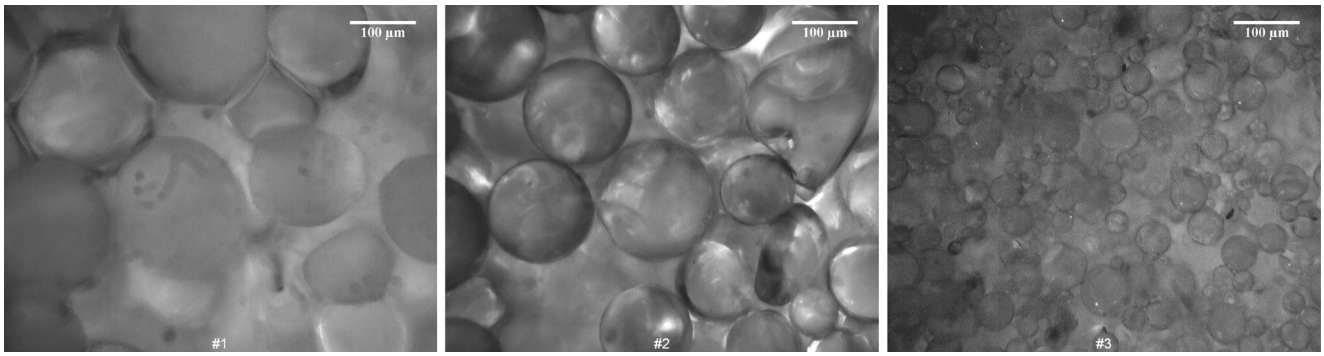

Fig. 5 Microscopic pictures of flight samples. In the first sample the interfaces between the spheres are large. The sintering on the other samples produced much less visible interfaces, retaining the pore space

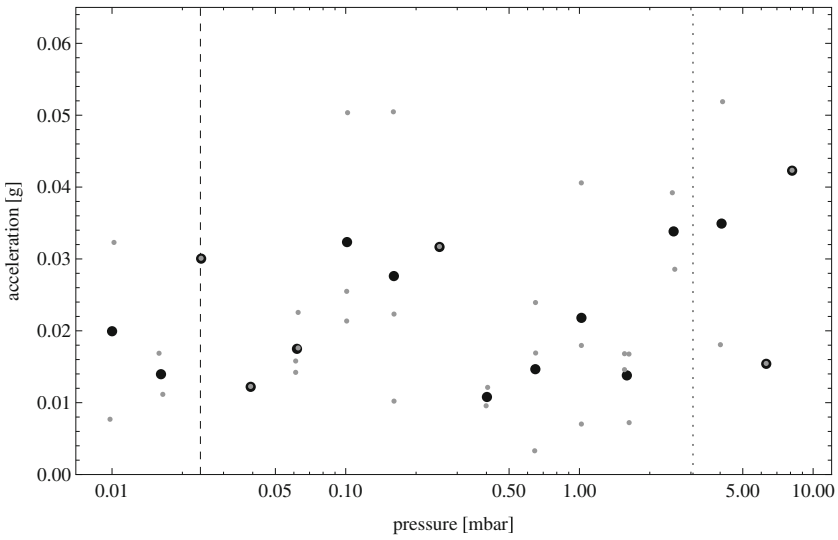

Fig. 6 Residual gravity at the time of detachment for sample #1. Uncertainties are 0.01 g. The individual measurements are marked as grey dots, the black dots represent the mean value. Additionally, the pressure where the Knudsen number reaches unity is displayed as a dashed line for the sample itself (characteristic dimension calculated according to Dürmann et al. (2013)) and as a dotted line for the pores (taken 20 % of the spheres radius as the dimension of the pores)

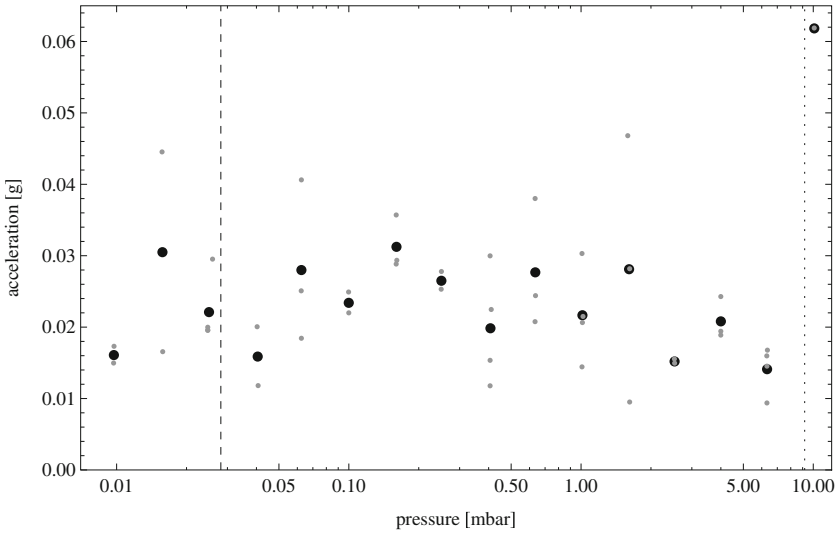

Fig. 7 Same as Fig. 6 for sample #3

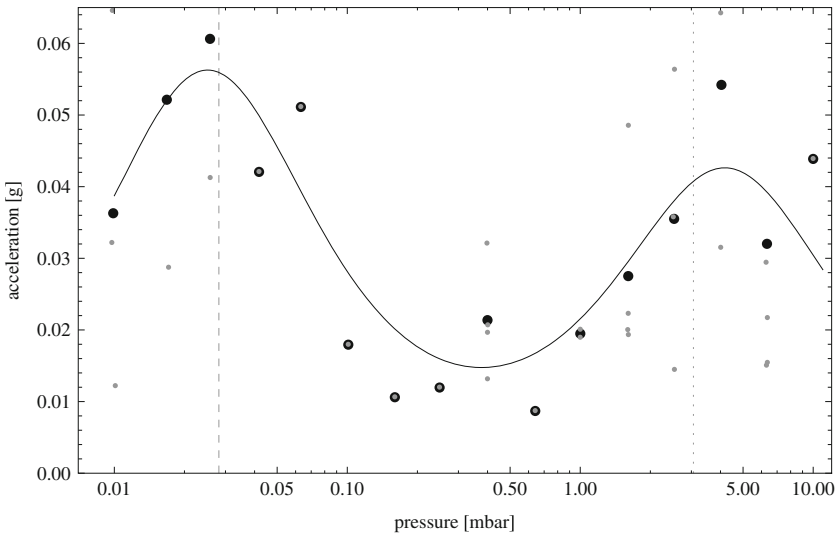

Fig. 8 Same as Fig. 6 for sample #2. The *solid line* is a fit of the sum of two photophoretic forces

walls are present, because the sample was often in contact with the wall, i.e. leaning inclined to it. In addition the sample was sintered at higher temperatures to warrant stability. We verified afterwards that the high temperature destroyed most of the pore structure by too efficient sintering (see Fig. 5). Due to these large contacts the thermal conductivity increased as well which decreases the temperature difference between both sides of the plate. As the signal to noise ratio in general is low, these differences in sample and preparation cause the absence of any pressure maxima (Figs. 6 and 8).

The third sample consisted of constituents with smaller size. The data show no significant pressure dependence (Fig. 7). The flight conditions were not as good as on the other days, as the flight was more turbulent - but this can not be seen on the g-data characteristics and has to be of minor importance for the experiment.

The absence of a maximum for the plate total size is unexpected, because the maximum is clearly observed for the sample of same total size (Fig. 8). Because of the smaller constituents the maximum at high pressures (where the pores Knudsen number reaches unity) would be expected at the edge of the measured pressure range, therefore we could have missed it - or the single last measurement indicates a sharp maximum. In addition the reduced particle size and pore size might change the flow rate and potentially decrease the phoretic force of the pores. The thermal conductivity might also be higher here, as the sintering enlarged the contact area between the spheres more, and there were more contacts and the contact surface to sphere radius ratio was higher.

Conclusions

The experiments reported here show the capability of quantifying the propulsion of cm-size porous plates on parabolic flights if the absolute acceleration is larger than 10^{-2} g. Earth bound experiments with e.g. torsion balances are possible (i.e. Ketsdever et al. (2012) and Dürmann et al. (2013)), but they are influenced by gravitational convection especially at the higher pressure end. The basic dependencies of photophoretic / thermophoretic propulsion like the influence of the ambient pressure as parameter can be deduced from such measurements. The influence of further parameter variations (i.e. pore size, thermal conductivity of the plate, material, thickness, ...) is subject to future experiments based on the same concept. Smaller force variations can be measured if the correlation between microgravity data and particle lift-off is improved during data acquisition and continuous monitoring of the plates movement is possible.

The absolute accelerations measured for the test sample of a 2.2 cm diameter and 1.7 mm thick porous plate, consisting of sintered spherical glass beads in a size range of 150 to 250 μm, are several times 0.01 g if a temperature gradient of 2000 K m^{-1} is applied over the plate.

Applied to protoplanetary disks this work implies that porous dust aggregates can experience a significant acceleration compared to stellar gravity. A more detailed treatment requires a larger parameter study. However, the data clearly show that the porosity is important increasing the efficiency of a phoretic force in a certain pressure range by a large factor.

Acknowledgments This work is based on experiments on parabolic flights carried out within the "Fly Your Thesis Campaign 2012" by ESA Eduaction. C. de Beule is supported by DLR Space Management with funds provided by the Federal Ministry of Economics and Technology (BMWi) under grant number DLR 50 WM 1242 and we also thank the DLR for supporting earlier parabolic flights related to the broader topic. M. Küpper is funded by the DFG.

References

Alexeenko, A.A., Gimelshein, S.F., Muntz, E.P., Ketsdever, A.D.: Kinetic modeling of temperature driven flows in short microchannels. Int. J. Therm. Sci. **45**(11), 1045–1051 (2006)

Blum, J., Wurm, G.: The growth mechanisms of macroscopic bodies in protoplanetary disks. Annu. Rev. Astron. Astrophys. **46**(1), 21–56 (2008)

Crookes, W.: On attraction and repulsion accompanying radiation. Philos. Mag. Ser. 4 **48**(316), 81–95 (1874)

de Beule, C., Kelling, T., Wurm, G., Teiser, J., Jankowski, T.: From planetesimals to dust: low-gravity experiments on recycling solids at the inner edges of protoplanetary disks. Astrophy. J. **763**, 11 (2013)

de Beule, C., Wurm, G., Kelling, T., Küpper, M., Jankowski, T., Teiser, J.: The martian soil: a planetary gas pump. Nat. Phys. **10**, 17–20 (2014)

Dürmann, C., Wurm, G., Küpper, M.: Radiative forces on macroscopic porous bodies in protoplanetary disks: laboratory experiments. Astron. Astrophy. **558**, A70 (2013)

Ehrenhaft, F., Reiss, M., Wasser, E.: Zur deutung der elektrophotophorese und magnetophotophorese. Zeitschrift für Physik **67**, 519–522 (1931)

Gimelshein, S.F., Gimelshein, N., Ketsdever, A.D., Selden, N.: Analysis and applications of radiometeric forces in rarefied gas flows. In: Mareschal, M., Santos A. (eds.) American Institute of Physics Conference Series, American Institute of Physics Conference Series, vol. 1501, pp. 1522–1528 (2011)

Kelling, T., Wurm, G.: Self-sustained levitation of dust aggregate ensembles by temperature-gradient-induced overpressures. Phys. Rev. Lett. **103**(215), 502 (2009)

Kelling, T., Wurm, G., Kocifaj, M., Klačka, J., Reiss, D.: Dust ejection from planetary bodies by temperature gradients: Laboratory experiments. Icarus **212**, 935–940 (2011)

Ketsdever, A., Gimelshein, N., Gimelshein, S., Selden, N.: Radiometric phenomena: From the 19th to the 21st century. Vacuum **86**, 1644–1662 (2012)

Knudsen, M.: Thermischer Molekulardruck der Gase in Röhren and porösen Körpern. Annalen der Physik **336**, 633–640 (1909)

Kocifaj, M., Klačka, J., Kelling, T., Wurm, G.: Radiative cooling within illuminated layers of dust on (pre)-planetary surfaces and its effect on dust ejection. Icarus **211**, 832–838 (2011)

Krauss, O., Wurm, G.: Photophoresis and the Pile-up of Dust in Young Circumstellar Disks. Astrophys. J. **630**, 1088–1092 (2005)

Lilly, T.C., Duncan, J.A., Nothnagel, S.L., Gimelshein, S.F., Gimelshein, N.E., Ketsdever, A.D., Wysong, I.J.: Numerical and experimental investigation of microchannel flows with rough surfaces. Physics of Fluids **19**(10), 106,101 (2007)

Meisner, T., Wurm, G., Teiser, J.: Experiments on centimeter-sized dust aggregates and their implications for planetesimal formation. Astron. Astrophys. **544**, A138 (2012)

Muntz, E.P., Sone, Y., Aoki, K., Vargo, S., Young, M.: Performance analysis and optimization considerations for a Knudsen compressor in transitional flow. J. Vac. Sci. Techn. **20**, 214–224 (2002)

Papadopoulos, D.H., Rosner, D.E.: Enclosure gas flows driven by non-isothermal walls. Phys. Fluids **7**, 2535–2537 (1995)

Rohatschek, H.: Semi-empirical model of photophoretic forces for the entire range of pressures. J. Aerosol Sci. **26**(5), 717–734 (1995)

Vargo, S.E., Muntz, E.P., Shiflett, G.R., Tang, W.C.: Knudsen compressor as a micro- and macroscale vacuum pump without moving parts or fluids. J. Vac. Sci. Techn. **17**, 2308–2313 (1999)

Wurm, G., Krauss, O.: Concentration and sorting of chondrules and CAIs in the late Solar Nebula. Icarus **180**, 487–495 (2006)

Zheng, F.: Thermophoresis of spherical and non-spherical particles: a review of theories and experiments. Adv. Colloid Interf. Sci. **97**(1–3), 255–278 (2002)

Journal of Aerosol Science 76 (2014) 126–137

Contents lists available at ScienceDirect

Journal of Aerosol Science

journal homepage: www.elsevier.com/locate/jaerosci

Photophoresis on polydisperse basalt microparticles under microgravity

Markus Küpper [a,*], Caroline de Beule [a], Gerhard Wurm [a], Lorin S. Matthews [b], Jesse B. Kimery [b], Truell W. Hyde [b]

[a] Fakultät für Physik, Universität Duisburg-Essen, Lotharstr. 1, 47048 Duisburg, Germany
[b] CASPER, Department of Physics, Baylor University, One Bear Place 97316, Waco, TX 76798-7316, United States

ARTICLE INFO

Article history:
Received 29 April 2014
Received in revised form
20 June 2014
Accepted 20 June 2014
Available online 30 June 2014

Keywords:
Photophoresis
Planetary atmospheres
Drop tower experiments
Numerical simulations
ΔT−photophoresis
$\Delta\alpha$−photophoresis

ABSTRACT

Photophoresis is a force which can dominate the motion of illuminated aerosols in low pressure environments of laboratory experiments, planetary atmospheres or protoplanetary disks. In drop tower experiments we quantified the photophoretic force on a sample of micrometer-sized basalt grains and aggregates thereof. The particle motions are systematic (linear, helical, in one direction), with most particles moving along the direction of light. Our results are consistent with analytical estimates and numerical simulations of photophoretic forces for small dust aggregates. It implies that the forces are dominated by ΔT−photophoresis with little evidence for $\Delta\alpha$−photophoresis in the micrometer size range.

1. Introduction

Over the last several decades, photophoretic forces on aerosols have been studied with respect to applications in the middle and the upper atmosphere (Beresnev et al., 2003; Cheremisin et al., 2005, 2011; Hidy & Brock, 1967; Pueschel et al., 2000; Rohatschek, 1956; Wurm & Krauss, 2008). For mesospheric or stratospheric aerosols, photophoresis can be stronger than Earth's gravity and lift particles upwards, possibly acting to concentrate them in certain layers (Beresnev et al., 2003; Cheremisin et al., 2011).

Photophoresis occurs when particles are illuminated by visible or infrared radiation and the resulting surface temperature differs from the surrounding gas temperature. Efficient momentum transfer can occur between the gas and the particle, subjecting the particle to a net force. The effect is strongly pressure dependent and is maximized if the mean free path of the gas molecules, λ, is comparable to the particle size, d, or Knudsen number $\mathrm{Kn}=1$, where

$$\mathrm{Kn}=\frac{\lambda}{d}. \tag{1}$$

Two extremes of photophoretic forces are discussed in the literature: $\Delta\alpha$ and ΔT forces (Cheremisin et al., 2005).

$\Delta\alpha$ refers to differences in the thermal accommodation coefficient α along a particle surface. The accommodation coefficient quantifies the fraction of gas molecules which are diffusely reflected from a particle surface. Upon re-emission

* Corresponding author.
E-mail address: markus.kuepper.86@uni-due.de (M. Küpper).

http://dx.doi.org/10.1016/j.jaerosci.2014.06.008
0021-8502/

from the surface this fraction of gas molecules takes a momentum determined by the local surface temperature of the particle. The remaining fraction of molecules is reflected specularly with no change in the absolute value of momentum. The accommodation coefficient likely changes over a particle surface, one extreme example being two half spheres with two values of α. In this case a $\Delta\alpha$ force results when the particle has a temperature different from that of the gas as a simple momentum balance implies. As this force only depends on the fact that the particle temperature is different from the gas temperature and as the αs are fixed to the particle, the induced motion is not related to the direction of illumination. $\Delta\alpha$ photophoresis can be viewed as an engine which is fixed to the particle and has a direction only depending on the orientation of the particle. Without alignment, a sample of random particles would set off moving in random directions upon illumination. Small micron sized particles would move on chaotic orbits due to Brownian rotation leading to constant reorientation.

$\Delta\alpha$ photophoresis can be aligned to a certain direction if the particle has a preferred orientation. This is possible in combination with other forces (or torques), such as gravity and gas drag or magnetic torques. If such alignment directs the $\Delta\alpha$ engine upwards and if the photophoretic force is greater in magnitude than gravity, an upward motion can result which has been termed gravitophotophoresis (Cheremisin et al., 2005; Rohatschek, 1996; Rohatschek & Horvath, 2010).

The strength of $\Delta\alpha$ photophoresis is given by (Cheremisin et al., 2005)

$$F_{f\alpha} = \frac{pS\Delta T_S}{4T_\infty}\Delta\alpha \mathbf{e}_{f\alpha}, \tag{2}$$

with p being the gas pressure, T_∞ the undisturbed gas temperature far from the particle, $\Delta T_S = \overline{T} - T_\infty$ the temperature difference between the particle mean temperature $\overline{T}$ and the gas, S the particle surface area and $\mathbf{e}_{f\alpha}$ the unit vector in the direction of the force. $\Delta\alpha$ is calculated as

$$\Delta\alpha = \frac{1}{S}\left|\int_S \alpha \, \mathrm{dS}\right|. \tag{3}$$

Upward motion of particles illuminated from the side has been observed in laboratory experiments (Rohatschek, 1956). As the direction of illumination is different from the direction of lift, it is tempting to assume that $\Delta\alpha$ forces have to act in general on gravitationally aligned particles to explain lifting forces in planetary atmospheres.

However, it is an open question if ΔT forces could not provide a "lift" perpendicular to the direction of illumination as well. In this extreme, the accommodation coefficient is considered to be constant over the particle surface. $\Delta T-$forces relate to photophoresis based on temperature *gradients* along the particle surface. The temperature difference leads to a difference in momentum transferred to accommodated gas molecules. Usually, a particle which is illuminated is heated on the illuminated side; this force is then related to the direction of illumination. The strength of $\Delta T-$photophoresis for a spherical grain is (Rohatschek, 1995)

$$F_{fT} = \frac{1}{2}D\sqrt{\frac{\overline{\alpha}}{2}}r\Delta T_P \frac{2}{\frac{p}{p_{opt}} + \frac{p_{opt}}{p}}, \tag{4}$$

with $\overline{\alpha}$ being the mean accommodation coefficient, ΔT_P the maximum temperature difference over the particle, and $p_{opt} = \sqrt{(2/\overline{\alpha})}(3/\pi)D(T_\infty/r)$. D is a constant determined by the state of the gas defined as a function of the thermal creep coefficient $\kappa = 1.14$, the dynamic viscosity η and the mean thermal velocity v_g

$$D = \frac{\pi}{2}\sqrt{\frac{\pi}{3}}\kappa\frac{v_g\eta}{T_\infty}. \tag{5}$$

For non-spherical, non-homogeneous particles $\Delta T-$forces are not necessarily perfectly aligned to the direction of illumination, but depend on the way the radiation heats the particle. For mm-particles Loesche et al. (2013) showed that the force can be misaligned by several degrees due to shape and compositional effects. If particles in some cases are heated at the back side negative photophoresis is even possible, where particles seem to be attracted by the light source. The situation is more complex if aggregates of particles are concerned, as gas molecules may have a complex collisional behaviour within the boundaries of the aggregate.

One way to shed light on the different potential photophoretic behaviours of natural particles is to carry out experiments under microgravity, where gravity plays no role in alignment and where slow, convection free motions can be measured. This has e.g. been carried out by Wurm et al. (2010), von Borstel & Blum (2012) or Watanabe et al. (2011). The sample in Wurm et al. (2010) consisted of mm sized particles whereas we focus on aggregates here. Watanabe et al. (2011) used smoke particles which essentially all exhibit negative photophoresis and so their focus was on the linearity of the force with illuminating flux. No detailed description of the extreme of negative photophoresis was given. von Borstel & Blum (2012) used aggregates of spherical or irregular micrometer sized particles with aggregate sizes up to 200 µm. This is strongly related to the work presented here but no quantification for the direction of the photophoretic force was presented though these details are likely present in their data. $\Delta\alpha$ forces were also not discussed.

Remaining unknowns are how aggregation changes the direction and strength of the photophoretic force. Particles of a different mineral composition are also of importance. The goal of this work is to quantify photophoretic forces on micrometer basalt particles and aggregates under microgravity. In contrast to the earlier work, these experiments focus on

determining the direction of the force with respect to illumination, as this might be a key to distinguish between $\Delta\alpha$ and ΔT forces. We further present a numerical model to explain the observed variations.

2. Drop tower experiments

A sketch of the experimental setup is shown in Fig. 1. A vacuum chamber is placed in a drop tower capsule providing 9 s of microgravity with a residual gravity below 10^{-6} g at the drop tower in Bremen. A dust bed is placed within the vacuum chamber consisting of basalt with grain sizes below 125 μm. The pressure is preset to a value of $4(\pm 0.5)$ mbar. During launch and the final phase of microgravity the sample is covered by a lid to prevent particle loss while the capsule is accelerated and decelerated. 500 ms after onset of microgravity the lid is opened and the dust bed is illuminated by an infrared laser (955 nm) with 20 ($\pm$ 1) kW/m^2 and a spot diameter of 3.4 cm. The light flux is chosen to allow a combination of different low pressure phenomena (photophoresis, Knudsen compressor, and thermal creep gas flow) to eject particles from the dust bed (de Beule et al., 2013, 2014; Kelling & Wurm, 2009; Wurm & Krauss, 2006). The directed near-infrared radiation enters the dust bed and is absorbed down to a certain depth, heating the top layers. Some heat is conducted downwards, but in addition, the surface can cool by thermal radiation. Therefore, the temperature gradient within the top dust layers differs from the gradient below which generates overpressures and particle ejections (de Beule et al., 2013; Kocifaj et al., 2011).

The collection of data begins when the lid is closed 1 s before the capsule is decelerated. No more dust particles are ejected and a cloud of particles is distributed throughout the chamber (Fig. 2). The airborne particles within the laser beam are subject to photophoretic forces undisturbed by gravity or particle eruptions. The trajectories of the particles within the laser beam are observed with a camera and tracked manually.

2.1. Dust sample

To place photophoretic forces in perspective to our earlier work on light–dust interactions we use the same natural polydisperse basalt sample here. Work on aggregates of monodisperse samples as e.g. used in ground based experiments by Haisch et al. (2008) are also necessary but are only planned for the future. The basalt powder used is commercially available (Kremer Pigmente). No further chemical analysis has been carried out on the sample. The powder is grey in the visual. The sample was sieved before the experiments to obtain only particles smaller than 125 μm. From ground based experiments by Kelling et al. (2011b) it is known that basalt dust sample ejecta have a size distribution as shown in Fig. 3. We assume that the particle size distribution in the experiment is comparable to the measured size distribution function, with an analytical fit given by

$$p_r = \frac{a}{b + \frac{r^2}{[m^2]}} \tag{6}$$

where $a = 1.37(\pm 0.07) \times 10^{-9}$ and $b = 2.7(\pm 0.2) \times 10^{-11}$.

2.2. Data analysis

As the movement of the lid stirred the gas in the chamber we started tracking grains 0.16 s later, when the gas movement had mostly ceased and the dominating force expected to be acting on the particles was photophoresis. 120 individual

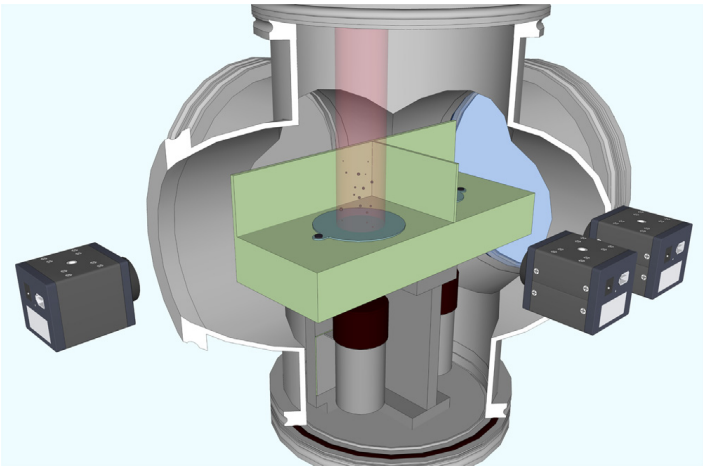

Fig. 1. Experimental setup: a dust bed with 7 cm diameter is placed in a vacuum chamber at 4 mbar ambient pressure. An infrared laser (1064 nm) with a power density of 20 kW/m^2 within a beam diameter of 3.4 cm is focussed on the basaltic dust, which is ejected. After the lid is closed the movement of airborne particles is dominated by photophoresis. Only one camera was used for the current study.

Fig. 2. Snapshot of airborne particles under microgravity.

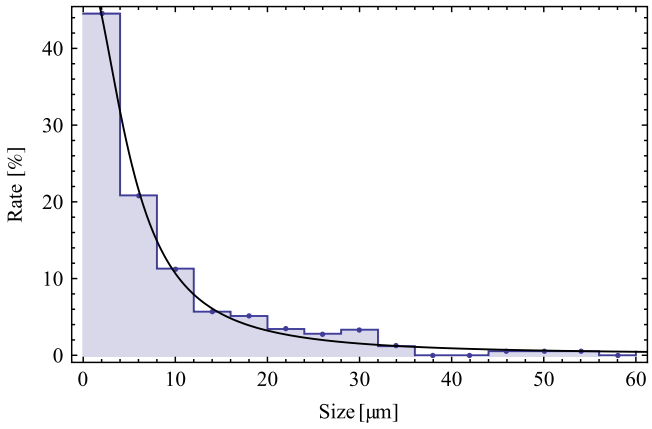

Fig. 3. Size distribution of ejected basalt (from Kelling et al., 2011b); depicted are the equivalent radii of the ejected particles. The bin width is 4 μm and the resolution limit is about 2 μm. Superimposed is a simple analytic function (see text).

particles were tracked, with trajectories classified in a small number of different types of motion, examples of which are shown in Fig. 4. The particles follow one direction on average, towards or away from the direction of illumination (see Table 1).

Superimposed on this average motion are more or less extended rotations around the average direction which in total lead to helical motions (see Fig. 4).

As ΔT−photophoresis should be related to the direction of illumination, the absolute velocities in that direction are of importance. The distribution of velocities can be seen in Fig. 5. The velocity component was measured as the length of each track in the y-direction, divided by the track time. The velocity distribution should be similar to the size distribution, as for otherwise identical particles the photophoretic drift velocity scales linearly with radius (Kelling & Wurm, 2013; Wurm & Krauss, 2006). However, there is a large fraction of small particles which move in the negative direction. This can be

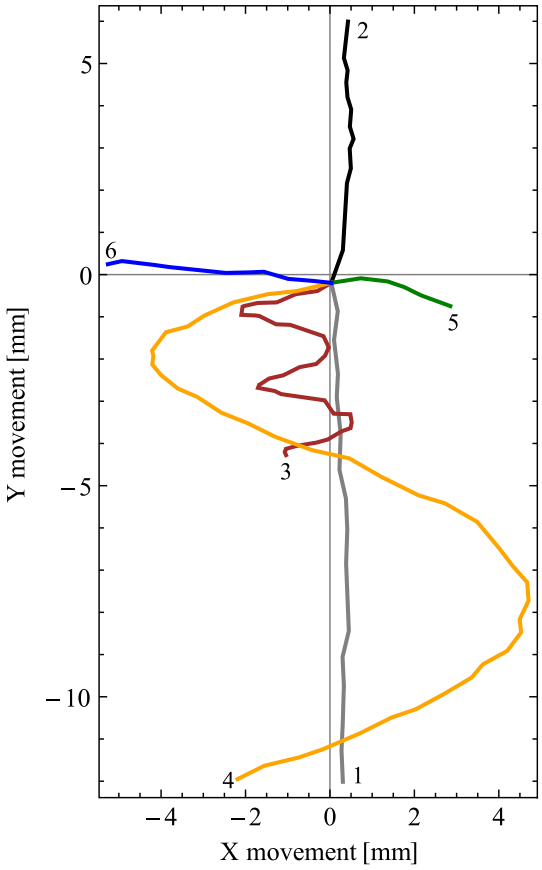

Fig. 4. A selection of the different typical particle movements, already corrected for the residual drift, (1 – grey) positive photophoresis, (2 – black) negative photophoresis, (3,4 – brown, orange) strong helical component, (5,6 – green, blue) with sideward component. (For interpretation of the references to colour in this figure legend, the reader is referred to the web version of this paper.)

Table 1
Movement characteristics of the tracked particles.

Movement	Number
Positive photophoresis (classes 1, 3, 4)	103
Negative photophoresis (class 2)	8
Perpendicular motion (classes 5, 6)	9
Total	120

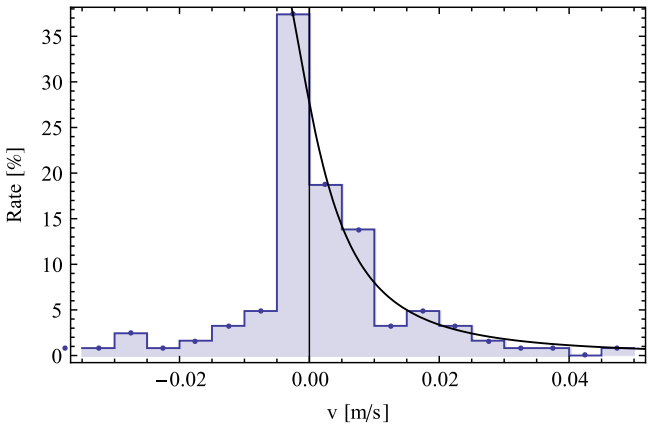

Fig. 5. Distribution of the observed particle speeds along the direction of illumination (photophoresis + gas motion); the solid line is a fit to the data (see text).

explained by a residual gas motion and an offset velocity probability has to be considered as

$$p_v = \frac{a}{b + \left(\frac{v - v_0}{c}\right)^2}. \tag{7}$$

As the values of a and b should be equal to those obtained from the dust size distribution, the scale factor between v and r is found to be $c = 1422(\pm 123)$ m/s and the offset drift velocity is $v_0 = 6.2(\pm 0.6)$ mm s^{-1}.

A rough comparison between the experimental data and the analytic solution essentially leaves only one free parameter, the thermal conductivity. The particle of mass m subject to a force F having a gas–grain coupling time τ has a terminal drift velocity of $v = \tau(F/m)$. The ratio of the terminal velocity due to the photophoretic force to the radius can be estimated as

$$\frac{v}{r} \approx \frac{33I}{v_g \lambda_p} \left[\frac{\mathrm{m}^2}{\mathrm{s}^2\mathrm{K}}\right], \tag{8}$$

where λ_p is the thermal conductivity in W/mK and I is the power density of incoming radiation in W/m^2. This estimate is based on the low pressure approximation of the photophoretic force in the free molecular flow regime

$$F_{ft_{free}} = \frac{\pi r^3 I p}{6 \lambda_p T_\infty} \tag{9}$$

and the gas–grain coupling time (Blum et al., 1996)

$$\tau = \frac{0.68 m_d}{\sigma \rho_g v_g} \tag{10}$$

where σ is the dust particle cross section, ρ_g is the gas density and m_d is the mass of the dust grain. The value of v/r is given from the size and velocity distributions as the scaling factor c/[m]. At $T = 300$ K and with the molar mass of air $\mu = 28$ g/cm^3, $v_g = \sqrt{8 R_g T/\pi\mu} = 480$ m/s. This leads to a value of $\lambda_p \approx 1$ W/(m K), which is on the order of the bulk value for silicates.

Earlier experiments showed that particles can decay into a large number of smaller particles after ejection from a dust bed. Particles up to mm in size were also observed, though the individual constituent grains are smaller. This implies that particles in our experiments are not just individual grains but also aggregates. For very large aggregates one might expect a strong increase in photophoresis as they might be treated by a lower thermal conductivity. However, the values of thermal conductivity estimated for these particles do not seem to support such a view.

The (new) result here is that the value of thermal conductivity is constant for all aggregate sizes as the velocity of the particles increases linearly with particle size.

In addition to the absolute strength of the photophoretic force, the experiments also allow a quantification of the direction of the photophoretic force. After correcting for the residual velocities there is still a fraction of particles moving in the negative direction. To visualize the distribution of particle trajectory directions, we determined the angular distribution of the photophoretic drift directions. As before, an average sideward drift of all tracks was subtracted to compensate for the residual gas motion. The distribution is shown in Fig. 6. About 93% of the particles fit the general idea of a positive ΔT−force. A distinctive fraction of 7% shows negative photophoresis. As we could not resolve the particles spatially, we do not know what makes these particles special or what separates these groups. It could be the size, morphology or special absorption sites located within the particle.

These findings are in perfect agreement with numerical calculations of photophoretic forces, to be treated in detail in a separate publication but outlined briefly in the next section below.

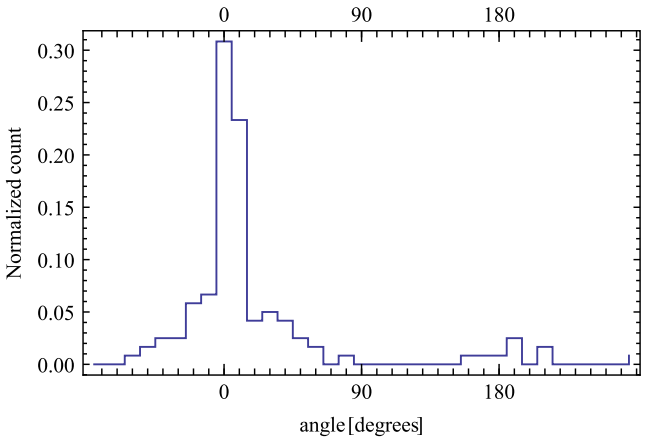

Fig. 6. Distribution of the trajectory angles with respect to the direction of illumination. 0° refers to the direction of the illumination.

3. Numerical model

A numerical model was used to compare the effect of the photophoretic force on irregular aggregates to that of spheres of the same mass. The aggregates in the model consisted of collections of spherical monomers, either of the same size (monodisperse) or of a range of sizes (polydisperse). In the model, the surface of an aggregate is defined by many patches which are used to determine the photon flux to each patch, the temperature gradient across the grain, the flux of gas molecules to the patch surface, and finally the net momentum transferred to the aggregate.

Assuming a light source along a given direction, the illumination flux is calculated at the centre of each patch taking into account the shadowing due to other monomers within the aggregate. The surface temperature was then defined by setting the average temperature of the aggregate to the mean gas temperature T, with the average temperature of a given monomer $\overline{T}_i$ determined by the fraction of its surface which is illuminated, such that shadowed monomers have a lower mean temperature than fully illuminated monomers. The temperature of each patch was then adjusted based on the illumination flux and the distance from the last illuminated point, as illustrated in Fig. 7.

3.1. Momentum transfer calculations

The incoming gas particles are assumed to move on straight-line paths which are not blocked by other monomers within the aggregate, i.e. along open lines of sight (LOS). The number of gas particles impacting a surface per unit area per unit time is given by the flux

$$I = n \iiint v \cos(\gamma) f(\boldsymbol{v})\, d\boldsymbol{v}, \tag{11}$$

where n is the particle number density, $v\cos(\gamma)$ is the component of the velocity normal to the surface, and $f(\boldsymbol{v})$ is the Maxwellian velocity distribution. The integral over the velocity may be separated into an integral over the magnitude of the velocity and an integral over the angles

$$I = n \int_0^\infty v^3 f(v)\, dv \iint \cos(\gamma)\, d\Omega. \tag{12}$$

The integral $\iint \cos(\gamma)\, d\Omega$, the LOS-factor, depends on the open lines of sight at the surface: points on an aggregate may have lines of sight which are blocked by other monomers within the aggregate, requiring the LOS-factor to be calculated numerically for each patch. Details of the method are given in Matthews et al. (2012).

Gas particles equilibrate to the local surface temperature before being re-emitted, assuming an accommodation coefficient $\alpha = 1$. Ejected particles may escape into space along an open LOS or collide with another monomer. If the rebound direction is blocked by another monomer in the aggregate, the gas is assumed to equilibrate with the new surface temperature, and the process repeats until an open rebound direction is selected. Rebounds continue until 99% of the gas has escaped; the remaining particles are assumed to rebound along the "average" open LOS for each patch.

The momentum transfer from an ejected gas particle is assumed to be cancelled if the gas particle collides with another monomer in the aggregate. Thus, the calculations consider only momentum transfer from the initial incoming gas particles and from gas particles rebounding along open paths. The magnitude of the change in momentum, and thus the force, at each patch is given by

$$F_p = \left(\frac{\Delta p_{out}}{\Delta t}\right)_p - \left(\frac{\Delta p_{in}}{\Delta t}\right)_p = mA_p\left(I'_p v_s - I_p v_g\right) \tag{13}$$

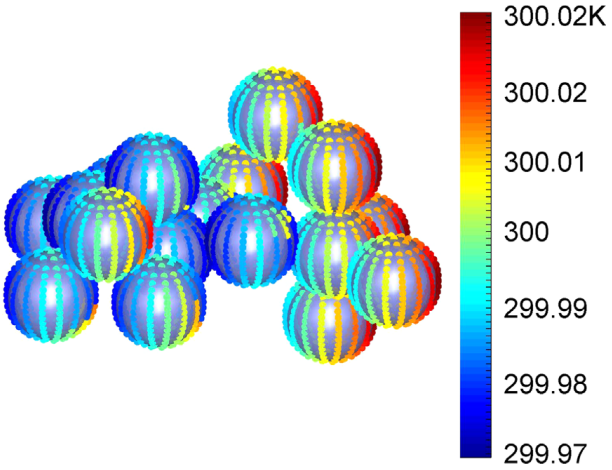

Fig. 7. Temperature gradient for an aggregate consisting of 17 monodisperse spheres, with the direction of illumination from the right. The monomers with the greatest illumination flux have the hottest temperatures.

where m is the mass of the gas particle, A_p is the area of the patch, I_p is the gas flux to patch p calculated by Eq. (12), I'_p is the flux adjusted for rebounding gas particles, v_s is the velocity determined by the surface temperature and v_g is the rms velocity of the gas. The direction of v_s is determined by the rebound direction, while the direction of v_g is along the average open LOS for a given patch. The average photophoretic force is determined by repeating the calculations numerous times and subtracting the force imparted by the gas when there is no temperature gradient present.

The components of the drift velocity of the aggregate are calculated by

$$v_{drift} = F_{ph}\tau/m_d \tag{14}$$

with τ being the gas–grain coupling time, given by Eq. (10). In this case, σ is the cross-sectional area of the aggregate projected in a plane perpendicular to the direction of the component of the force.

3.2. Numerical results

Simulations were run for two populations of aggregates, one built from monodisperse monomers ($r = 1.7$ μm) and the other built from polydisperse monomers ($0.5\ \mu m \le r \le 10\ \mu m; \langle r \rangle = 1.7\ \mu m$). The aggregates ranged in size from $N=2$ to $N=2000$ monomers, and a size distribution of the aggregates was chosen to match that given for the basalt powder shown in Fig. 3, where the radius of the an aggregate is defined by the equivalent radius, R_σ (Matthews et al., 2012). The material is assumed to be basalt with a material temperature gradient of 10^4 K/m, and the surrounding gas temperature is set to be $T=300$ K. The average force and drift velocity in the direction of illumination are normalized to that found for a single sphere with $r = 1.0$ μm ($m_0 = 1.3 \times 10^{-14}$ kg): $f_0 = 1.0 \times 10^{-14}$ N and $v_0 = 1.1$ mm/s, respectively. As shown in Fig. 8, the photophoretic force on the aggregates is similar to that acting on spheres of the same mass. The drift velocity of the aggregates tends to be smaller than that for the spheres, however, due to their open cross-sections (see Fig. 9), though the drift velocity of small aggregates, especially those consisting of monodisperse spheres, can be somewhat larger. Both types

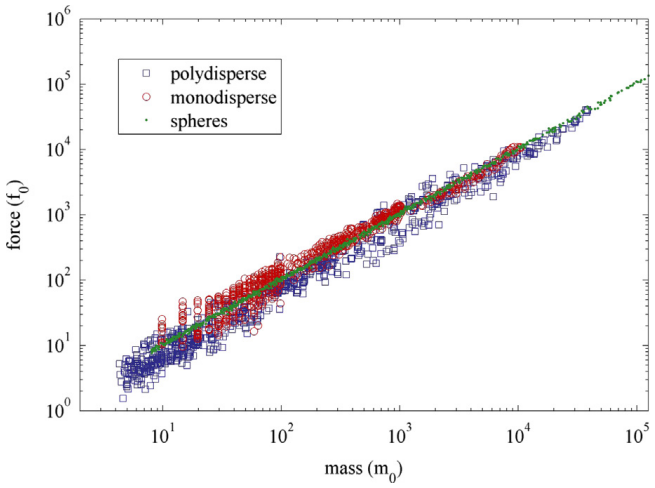

Fig. 8. Photophoretic force vs. mass, normalized to the force and mass of a sphere with $r = 1.0$ μm, $f_0 = 1.0 \times 10^{-14}$ N and $m_0 = 1.3 \times 10^{-14}$ kg.

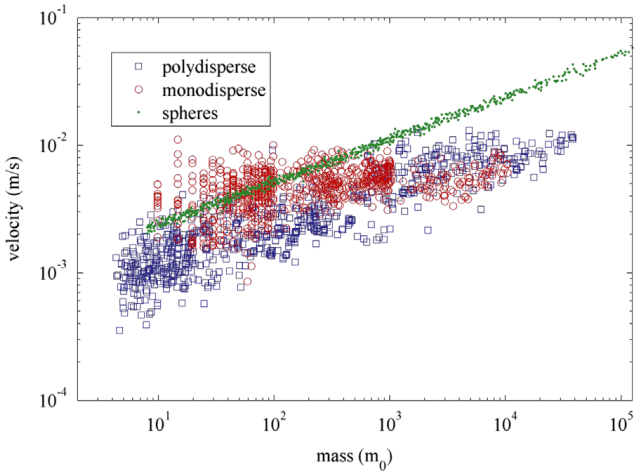

Fig. 9. Drift velocity vs. mass, normalized to the velocity and mass of a 1.0 μm–radius sphere, $v_0 = 1.1$ mm/s, $m_0 = 1.3 \times 10^{-14}$ kg. Both aggregate populations tend to have a smaller drift velocity than spheres of equivalent mass due to their larger cross-sectional areas.

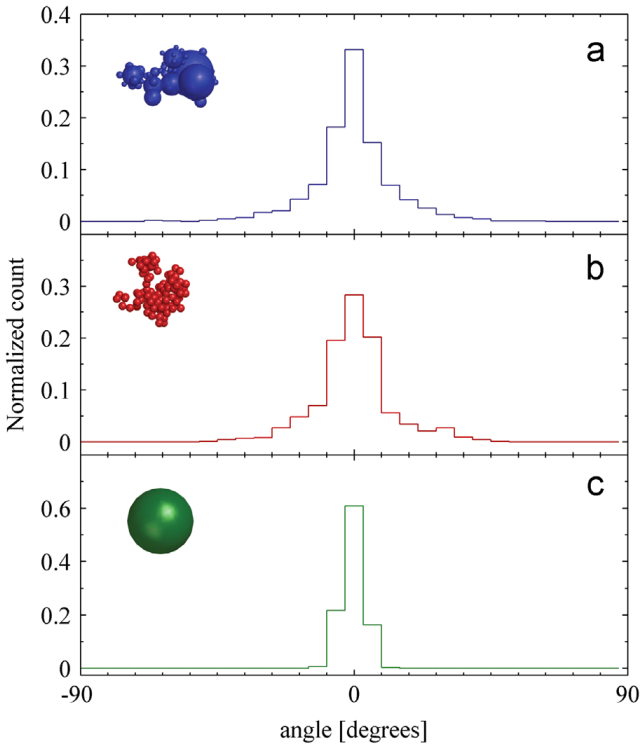

Fig. 10. Distribution in drift velocity with respect to the direction of illumination for (a) aggregates consisting of polydisperse spheres, (b) aggregates consisting of monodisperse spheres, and (c) single spheres.

of aggregates have a broad distribution of velocities about the direction of illumination (Fig. 10), whereas the distribution for the spheres is sharply peaked in the forward direction. The polydisperse aggregates, Fig. 10a, have a larger peak in the forward direction, probably due to the fact that the motion of the aggregate is dominated by the effective force on the largest monomer(s) in the aggregate, which behave more like spheres.

4. Discussion

Although the experiment and model were designed to be complementary, there are differences between the two cases. The experiments do not allow determination of the detailed morphology of the dust grains and aggregate structure, and particle sizes can only be assigned to velocities on average. The simulations, on the other hand, assume certain aggregate structures which consist of spherical monomers and assume a specified temperature gradient for an illuminated sphere. Keeping these caveats in mind, together they give the following picture.

Over the total size scale, the experimental photophoretic velocity is consistent with a linear size dependence as the probability distribution for particle size and velocity are proportional to each other. This would be expected for solid monolithic grains. Experimentally, the absolute values were fitted by adapting the thermal conductivity. Essentially all unknowns are embedded in this parameter.

The results of the simulation show the same trends. The temperature gradient over a sub-unit was fixed with illumination, which is equivalent to establishing a given thermal conductivity to each sphere. The simulations show that aggregation changes the absolute photophoretic force by a small factor of two to three at best compared to spheres of the same mass or volume, independent of the total mass. However, the drift velocity is reduced for the aggregates due to their porous structure: the mass of the aggregates scales as approximately $m \propto r^{2.5}$. This difference is reflected in slopes of the drift velocities (see Fig. 9). However, the studies also show a possible spread in the drift velocities by a factor of two to three for given mass or size.

The agreement in the absolute values of the measured drift velocities to the calculated drift velocities shows that the photophoretic forces are consistent with ΔT forces. This is also consistent with the fact that the photophoretic forces are strongly peaked in the forward direction. The deviations of several tens of degrees offset from the illumination direction are consistently seen in both experiment and simulation. Loesche et al. (2013) showed that almost spherical particles show photophoretic ΔT forces with directions deviating from the incident direction by several degrees. The basalt particles studied here are less spherical and thus have larger deviations, in agreement with this observation. As the motion of single grains (spheres) is essentially forward directed and the aggregates have a broad range of velocities (see Fig. 10), the somewhat broader peak observed in the experimental data (Fig. 6) might indicate a mix of individual grains and aggregates. Numerical and experimental data both also clearly show that sideways particle motion is possible, even in the absence of additional alignment forces.

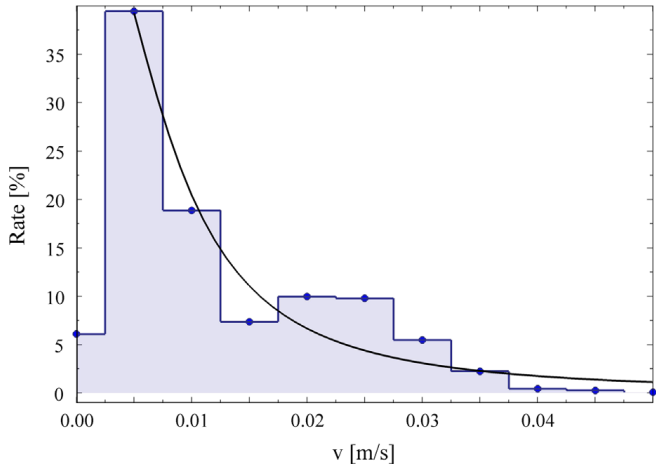

Fig. 11. Calculated distribution of particle speeds for a mix of spheres ($1 \leq r \leq 10$ μm) with polydisperse aggregates ($r \geq 1.5$ μm) matching the experimental results. The line is the fit that resulted from the experimental data.

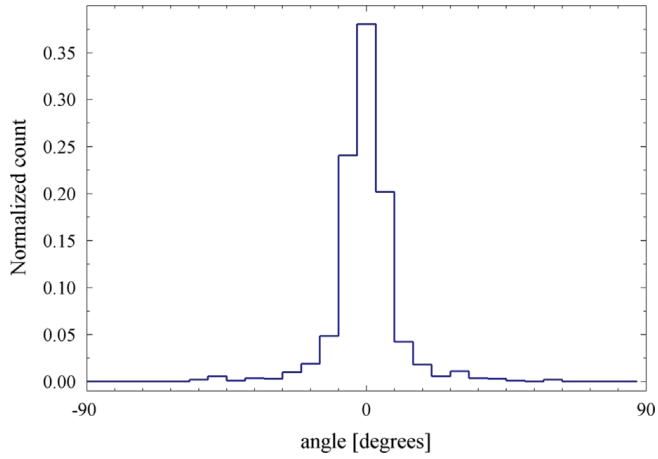

Fig. 12. Calculated distribution of velocities with respect to the direction of illumination (angles) for a mix of spheres ($1 \leq r \leq 10$ μm) with polydisperse aggregates ($r \geq 1.5$ μm) matching the experimental results.

Knowing the individual differences between spheres and aggregates it should be possible to match the experimental findings by a distribution of particles consisting of spheres and polydisperse aggregates. Figure 11 shows the results of a speed distribution calculated using a mix of aggregates and polydisperse spheres chosen to have a size distribution as shown in Fig. 3. The speeds are scaled by a factor 3 (accounting e.g. for the artificial temperature gradient chosen), but then match the observed experimental findings (Fig. 5) very well now as the superimposed fit from the experimental data indicates. The same mix of spheres and polydisperse aggregates also mirrors the experimental angular distribution now with the strong peak but wide wings (Fig. 12, cmp. Fig. 6).

The helical motion of particles can be understood as the particles align themselves to the illumination direction but maintain a residual torque around this direction (van Eymeren & Wurm, 2012). In this case, no net sideward motion will result in the long term as particles rotate around the direction of illumination. We note that the current measurements are related to the average observed drift directions which, due to the limited track length, can depend on the rotation frequency and initial position on a potential helix. In the case of $\Delta T-$forces we expect a continuous net sideward motion only if particles are aligned with a different direction different to the illumination. Future numerical simulations and experiments will address this behavior.

4.1. Magnetic alignment

While gravity plays no role in alignment under microgravity, magnetic fields might still act on particles with sufficient magnetization (Rohatschek & Horvath, 2010). Measurements of magnetic fields were not carried out in the experiment, though basalt can be magnetized. Values for the volume magnetization measured by eg. Cox & Doell (1962) are around $m = 4$ A/m. For a spherical 10 μm (radius) particle the total magnetization would be $M = 2 \times 10^{-14}$ A m^2. If we assume that the magnetic field within the experimental setup is on the order of the Earth's magnetic field of 50 μT, the maximum resulting torque is $D_m = 10^{-18}$ N m. This is enough to rotate magnetized particles in a few tens of ms which is short

compared to the experiment duration. Without other torques acting, we would therefore expect such particles to be aligned along the direction of the magnetic field.

In comparison, torques imposed by photophoresis on non-perfect inhomogeneous grains can be estimated as follows. The photophoretic forces measured for 10 μm grains are on the order of 10^{-11} N. If this acts on only one side of a grain, the maximum torque is $D_{Ph} = 10^{-16}$ N m, a factor of 100 larger than the magnetic torque. While this extreme is unrealistic, it is plausible that a 1% asymmetry in the alignment of the grain with the photophoretic force would be sufficient for the photophoretic torque to be comparable to the magnetic torque.

There is a difference in the motion of particles aligned along the direction of incident light or by a magnetic field pointing in a different direction. A particle self-aligned by ΔT photophoresis will afterwards only rotate around the direction of illumination. This is consistent with most of the helical motions observed in the experiment. If magnetic alignment dominates the particle motion, rotation induced by photophoresis or gas drag would be restricted to rotations around the direction of the magnetic field. This readjustment can change the magnitude and direction of the photophoretic force and might produce non-symmetric helical motions around the direction of the magnetic field. While this might be consistent with some of the sidewards trajectories, there are too few data on this to give a detailed analysis.

The direction of the Earth's magnetic field differs significantly different from the vertical, the direction of the laser light. If, however, any other remanent magnetic field within the experiment was present there is a small chance that it is aligned to the direction of illumination in which case we could not discriminate between the two types of alignment.

To conclude, we cannot rule out or confirm that particles are aligned by a remanent magnetic field within the experiment.

5. Conclusion

Micrometer-sized basalt particles entrained in a thin atmosphere will move preferentially along the direction of an illuminating light source due to ΔT forces. However, a significant fraction of a particle sample can move in directions other than the illumination direction depending on the particle orientation. To date, systematic motions in arbitrary directions not related to the illumination were often associated to $\Delta\alpha$ forces and aligning torques (gravitophotophoresis and magneto-photophoresis). This is only one possible option. We find that if particles are aligned by external forces, it is not necessarily a body fixed $\Delta\alpha$ engine; there is also a sideward movement associated with ΔT forces.

Unfortunately though, ΔT forces on basalt grains cannot be large enough to lift small basalt aggregates against Earth's gravity. The ratio between the photophoretic force at low pressure (Eq. (9)) and the gravity is

$$\frac{F_{ft_{free}}}{F_g} = \frac{Ip}{8\lambda_p T_\infty \rho_p g} \tag{15}$$

As an example, given the thermal conductivity and solar insolation on Earth (1000 W/m^2) at 2000 Pa pressure assuming a density of the particles of 3000 kg/m^3 and a temperature of $T_\infty = 250$ K, the resulting lift is only 3% of gravity. Applying photophoresis to particles in the Earth's stratosphere and mesosphere, or on the Martian surface, certain classes of particles might experience prolonged residence times (Pueschel et al., 2000), but these cannot be typical basalt particles. Either particles of lower thermal conductivity are needed or it has to be particles where $\Delta\alpha$ forces are active. The number of trajectories analyzed in our experiment was relatively small, yet there is a fraction of particles with negative photophoresis which require a more detailed analysis. Other experiments e.g. by Rohatschek (1983) on metal dust aggregates or by Kelling et al. (2011a) and van Eymeren & Wurm (2012) on micron sized ice aggregates suggest that lower thermal conductivities for certain classes of particles are feasible.

The results of this study lead to the conclusion that within the parameter range studied photophoresis on aggregates scales with their mass as for bulk particles. In this case the degree of aggregation does not change the effective thermal conductivity of a particle with respect to photophoresis.

Acknowledgements

This project is supported by DLR Space Management with funds provided by the Federal Ministry of Economics and Technology (BMWi) under Grant no. DLR 50 WM 1242, and in part by NSF Grant nos. 1002637 and 0847127. M. Kuepper is funded by the DFG. Adaptation of the experiment sketch (Fig. 1) has kindly been provided by T. Jankowski.

References

Beresnev, S.A., Kochneva, L.B., Suetin, P.E., Zakharov, V.I., & Gribanov, K.G. (2003). Photophoresis of atmospheric aerosols in the Earth's thermal radiation field. *Atmospheric and Oceanic Optics*, *16*, 431–438.

Blum, J., Wurm, G., Kempf, S., & Henning, T. (1996). The Brownian motion of dust particles in the solar nebula: an experimental approach to the problem of pre-planetary dust aggregation. *Icarus*, *124*(December), 441–451.

Cheremisin, A.A., Shnipov, I.S., Horvath, H., & Rohatschek, H. (2011). The global picture of aerosol layers formation in the stratosphere and in the mesosphere under the influence of gravito-photophoretic and magneto-photophoretic forces. *Journal of Geophysical Research (Atmospheres)*, *116* (October), 19204.

Cheremisin, A.A., Vassilyev, Y.V., & Horvath, H. (2005). Gravito-photophoresis and aerosol stratification in the atmosphere. *Journal of Aerosol Science*, *36*, 1277–1299.
Cox, A., & Doell, R.R. (1962). Magnetic properties of the basalt in hole EM 7, Mohole project. *Journal of Geophysical Research*, *67*(10), 3997–4004.
de Beule, C., Kelling, T., Wurm, G., Teiser, J., & Jankowski, T. (2013). From planetesimals to dust: Low-gravity experiments on recycling solids at the inner edges of protoplanetary disks. *Astrophysical Journal*, *763*(January), 11.
de Beule, C., Wurm, G., Kelling, T., Küpper, M., Jankowski, T., & Teiser, J. (2014). The martian soil as a planetary gas pump. *Nature Physics*, *10*, 17–20.
Haisch, C., Kykal, C., & Niessner, R. (2008). Photophoretic velocimetry for the characterization of aerosols. *Analytical Chemistry*, *80*(5), 1546–1551.
Hidy, G.M., & Brock, J.R. (1967). Photophoresis and the descent of particles into the lower stratosphere. *Journal of Geophysical Research*, *72*(January), 455.
Kelling, T., & Wurm, G. (2009). Self-sustained levitation of dust aggregate ensembles by temperature-gradient-induced overpressures. *Physical Review Letters*, *103*, 215502-1–215502-4.
Kelling, T., & Wurm, G. (2013). Accretion through the inner edges of protoplanetary disks by a giant solid state pump. *Astrophysical Journal Letters*, *774*(September), L1.
Kelling, T., Wurm, G., & Dürmann, C. (2011a). Ice particles trapped by temperature gradients at mbar pressure. *Review of Scientific Instruments*, *82*(November (11)), 115105.
Kelling, T., Wurm, G., Kocifaj, M., Klačka, J., & Reiss, D. (2011b). Dust ejection from planetary bodies by temperature gradients: Laboratory experiments. *Icarus*, *212*, 935–940.
Kocifaj, M., Klačka, J., Kelling, T., & Wurm, G. (2011). Radiative cooling within illuminated layers of dust on (pre)-planetary surfaces and its effect on dust ejection. *Icarus*, *211*(January), 832–838.
Loesche, C., Wurm, G., Teiser, J., Friedrich, J.M., & Bischoff, A. (2013). Photophoretic strength on chondrules. 1. Modeling. *Astrophysical Journal*, *778*(December (2)), 101.
Matthews, L.S., Land, V., & Hyde, T.W. (2012). Charging and coagulation of dust in protoplanetary plasma environments. *Astrophysical Journal*, *744*, 397–398.
Pueschel, R.F., Verma, S., Rohatschek, H., Ferry, G.V., Boiadjieva, N., Howard, S.D., & Strawa, A.W. (2000). Vertical transport of anthropogenic soot aerosol into the middle atmosphere. *Journal of Geophysical Research*, *105*, 3727–3736.
Rohatschek, H. (1956). Über die kräfte der reinen photophorese und der gravitophotophorese (on the forces of pure and gravito-photophoresis). *Acta Physica Austriaca*, *10*, 267–286.
Rohatschek, H. (1983). Photophoretic forces on stratospheric and mesospheric aerosols. In: *Aerosols in Science, Medicine and Technology*.
Rohatschek, H. (1995). Semi-empirical model of photophoretic forces for the entire range of pressures. *Journal of Aerosol Science*, *26*, 717–734.
Rohatschek, H. (1996). Levitation of stratospheric and mesospheric aerosols by gravito-photophoresis. *Journal of Aerosol Science*, *27*(3), 467–475 Atmospheric Aerosols.
Rohatschek, H., & Horvath, H. (2010). Magneto-photophoresis and mesospheric particles. *Journal of Geophysical Research (Atmospheres)*, *115*(December), 24208.
van Eymeren, J., & Wurm, G. (2012). The implications of particle rotation on the effect of photophoresis. *Monthly Notices of the Royal Astronomical Society*, *420*(February), 183–186.
von Borstel, I., & Blum, J. (2012). Photophoresis of dust aggregates in protoplanetary disks. *Astronomy and Astrophysics*, *548*(December), A96.
Watanabe, S.N., Iwaki, T., Kohira, M.I., Magome, N., & Yoshikawa, K. (2011). Negative photophoresis of smoke particles observed under microgravity. *Chemical Physics Letters*, *511*(August), 447–451.
Wurm, G., & Krauss, O. (2006). Concentration and sorting of chondrules and CAIs in the late Solar Nebula. *Icarus*, *180*(February), 487–495.
Wurm, G., & Krauss, O. (2008). Experiments on negative photophoresis and application to the atmosphere. *Atmospheric Environment*, *42*(11), 2682–2690.
Wurm, G., Teiser, J., Bischoff, A., Haack, H., & Roszjar, J. (2010). Experiments on the photophoretic motion of chondrules and dust aggregates: Indications for the transport of matter in protoplanetary disks. *Icarus*, *208*, 482–491.

Icarus 260 (2015) 23–28

Contents lists available at ScienceDirect

Icarus

journal homepage: www.elsevier.com/locate/icarus

An insolation activated dust layer on Mars

Caroline de Beule [a,*], Gerhard Wurm [a], Thorben Kelling [a], Marc Koester [a], Miroslav Kocifaj [b]

[a] Faculty of Physics, Universität Duisburg-Essen, Lotharstr. 1, D-47057 Duisburg, Germany
[b] Faculty of Mathematics, Physics and Informatics, Comenius University, Mlynská dolina, 842 48 Bratislava, Slovak Republic

ARTICLE INFO

Article history:
Received 16 January 2015
Revised 30 April 2015
Accepted 3 June 2015
Available online 8 July 2015

Keywords:
Mars, surface
Mars, atmosphere
Atmospheres, dynamics
Aeolian processes
Mars

ABSTRACT

The illuminated dusty surface of Mars acts like a gas pump. It is driven by thermal creep at low pressure within the soil. In the top soil layer this gas flow has to be sustained by a pressure gradient. This is equivalent to a lifting force on the dust grains. The top layer is therefore under tension which reduces the threshold wind speed for saltation. We carried out laboratory experiments to quantify the thickness of this activated layer. We use basalt with an average particle size of 67 μm. We find a depth of the active layer of 100–200 μm. Scaled to Mars the activation will reduce threshold wind speeds for saltation by about 10%.

1. Introduction

It is a long standing problem how to move particles on the martian surface. The most prominent mechanism is wind in analogy to transport of sand on Earth. Numerous work has been carried out on this in the past especially in wind tunnel experiments (Greeley et al., 1980, 1992; White et al., 1997).

Recent images of the HiRISE camera onboard the Mars Reconnaissance Orbiter show that martian sand transport is still active. They find dunes which travel several meters in a few years (Bridges et al., 2012). However, a problem encountered in the explanation of particle lift is that wind alone requires rather large speed to initiate saltation. The pressure on Mars on average is only 6 mbar in contrast to 1000 mbar on Earth. This reduces the dynamic pressure of a gas flow strongly. A speed of 30 m/s is supposed to be necessary to pick up the most susceptible particles of 100 μm in size (Greeley et al., 1980). High tangential wind speeds in vortices might also mobilize particles. Obviously, dust devils bear witness of dust lifting. Visible dust devils come in a variety of sizes (Lorenz, 2009). The largest ones might easily lift dust. However, Stanzel et al. (2008) and Reiss et al. (2014) find wind speeds (tangential and transversal) which are not always large enough. Also, Reiss et al. (2009) observed dust devil activity on Arsia Mons. This relates to an atmospheric pressure of only 2 mbar which requires still larger wind speeds.

There have been suggestions to support or ease particle lift one way or the other. The choice of particles to be picked up has been varied in wind tunnel experiments. As an example, the rolling of volcanic glass particles might reduce threshold speeds (de Vet et al., 2014). The pressure within dust devils is reduced compared to ambient conditions. It has been proposed that the traverse of such a pressure minimum might be sufficient to lift dust (Balme and Hagermann, 2006). Last not least and connecting to the work presented here, Wurm and Krauss (2006) found that illumination of a dust bed at low pressure provides a lift. This was applied to Mars by Wurm et al. (2008). Especially this latter effect is strongly depending on ambient pressure in a maybe non-intuitive way. Wind or gas drag and dynamic pressure decrease with decreasing pressure. The induced lifting force of an insolated surface can increase to lower pressure by orders of magnitude in strength. The force peaks around Knudsen numbers of $Kn \approx 1$, where Kn is the ratio between the mean free path of the gas molecules and the size of a particle or pore within the dust bed. Hence, for micrometer dust particles insolation supported lift is not important on Earth but maximized on Mars.

The model discussed for this lifting force so far included photophoretic forces, solid state greenhouse effects and gas compression by thermal creep (Kocifaj et al., 2011; Kelling et al., 2011; de Beule et al., 2013). These are important on long timescales (h) as current research is supporting (Koester et al., personal communication). However, here we consider gas flow through the dust bed and related pressure differences which was not included in the earlier models. This provides lift for a sample where illumination changes on short time scales of seconds or even fractions of seconds. The importance of this became obvious in microgravity experiments where de Beule et al. (2014) observed an efficient

* Corresponding author.
E-mail address: caroline.debeule@uni-due.de (C. de Beule).

http://dx.doi.org/10.1016/j.icarus.2015.06.002
0019-1035/

gas flow through an illuminated dust bed directed upwards. The effect is tied to the temperature profile within the illuminated dust bed.

The basic pumping is provided by thermal creep. For a constant temperature gradient pure thermal creep pumping does not require any pressure differences within the soil. However, the temperature profile along the top layer of an illuminated soil is rather flat as radiation is absorbed and thermally emitted. This layer cannot pump by thermal creep but has to keep up the thermal creep gas flow from below nevertheless. A pressure gradient is established close to the surface to do so. In accordance with Darcy's law the pressure increase below the surface transports the gas flow handed over by the Knudsen pump (thermal creep) below. Once set, this overpressure not only moves the gas but also acts on the dust particles. Particles within this top layer are under constant tension and can be ejected if cohesion and gravity can be overcome by any means. We call this an *insolation activated layer*.

We quantify the thickness of this layer here based on laboratory experiments. We illuminate a dust sample with sufficient light flux to compensate gravity. We then remove cohesion by short vibrations. This leads to a removal of the tension activated layer down to the pressure maximum and allows its thickness to be determined.

2. Sub-surface pumping

We detail the light induced sub-surface pumping in this section. The principle is shown in Fig. 1.

The light enters the dust bed and is absorbed. The heat is conducted further down into the dust bed. In addition, at the surface the dust bed can cool by thermal radiation. In consequence a temperature gradient is established starting a few particle layers within the dust bed (at depth x_1 in Fig. 1) and is directed to deeper layers. Temperature gradients always lead to a thermal creep gas flow in a porous medium, where gas is transported along the particles' surface from cold to warm. This was first introduced by Maxwell (1879) as thermal transpiration where two gas reservoirs

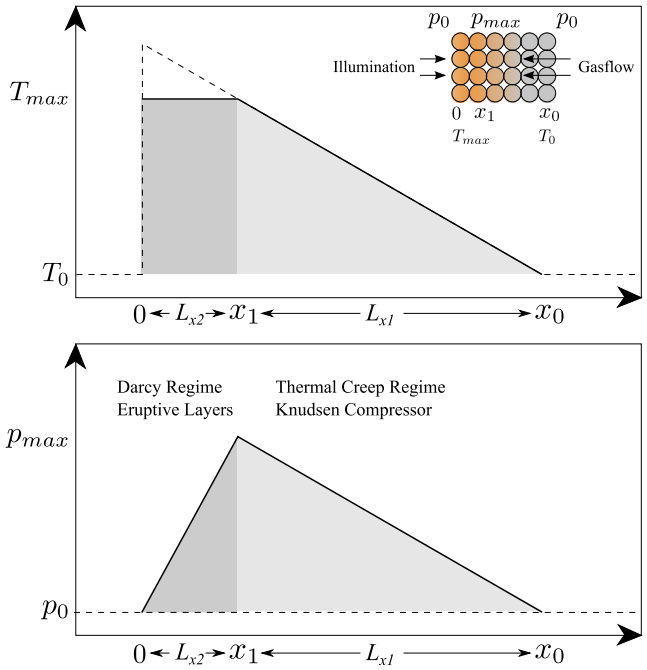

Fig. 1. Principle for pressure distribution for given temperature profile and open geometry (ambient pressure the same on both sides of the dust sample). L_{x2} marks the depth of the dust bed from 0 to x_1 with constant temperature and L_{x1} the part of the dust bed with a temperature gradient from x_1 to x_0.

with different temperatures are connected by a small channel in a low pressure environment. Gas molecules creep along the channel wall from cold to warm. If the diameter of the channel is comparable to the mean free path of the gas molecules the pressure driven back flow can be smaller than the thermal creep flow (Knudsen, 1909). In an illuminated dust bed the gas molecules creep from cool layers deep within the dust bed (x_0 in Fig. 1) upwards until the temperature levels off close to the surface at x_1.

If the temperature increase in Fig. 1 would be linear from x_0 to the surface there would be no pressure differences. Every sub-layer would just transport the same amount of gas by thermal creep. However, if there is a top layer of constant temperature the gas molecules do not creep along these particles all the way to the surface, but only to x_1. The thermal creep gas flow leads to a concentration of molecules and the pressure is locally increased.

The increase of pressure below the surface at x_1 leads to a pressure driven gas flow through the top layer. The pressure adjusts itself to a value where gas flow through the top layer matches the incoming thermal creep gas flow from below. Both aspects, the temperature gradient driven thermal creep gas flow (Knudsen compression) and the pressure driven gas flow (Darcy flow Darcy, 1856) are usually occuring in the same capillary. The mass flow of the gas through capillaries was described by Sone and Itakura (1990) and Muntz et al. (2002) as

$$\dot{M} = p_{avg} \frac{FA}{\sqrt{2\frac{k_B}{\mu}T_{avg}}} \times \left(\frac{L_r}{L_x}\frac{\Delta T}{T_{avg}} Q_T - \frac{L_r}{L_x}\frac{\Delta p}{p_{avg}} Q_p \right) \tag{1}$$

where p_{avg} and T_{avg} are the average pressure and temperature within the dust bed, F is a factor giving the amount of capillaries within the surface area A, k_B is the Boltzmann constant, μ the molecular mass of the gas, L_r and L_x are the radius and length of the capillaries and ΔT and Δp are the temperature and pressure differences within the dust bed, respectively. The coefficients Q_P and Q_T depend on the Knudsen number and describe the pressure driven (back) flow and the flow by thermal creep, respectively. It has to be noted that the length of the capillaries L_x is different in the thermal driven $(L_{x1}, |x_0 \rightarrow x_1|)$ and the pressure driven $(L_{x2}, |0 \rightarrow x_1|)$ part.

If the dust bed is heated two mass flows develop. The first one $\dot{M}_1$ is dominated by thermal creep (Knudsen pump) due to the temperature gradient

$$\dot{M}_1 = p_{avg} \frac{FA}{\sqrt{2\frac{k_B}{\mu}T_{avg}}} \times \left(\frac{L_r}{L_{x1}}\frac{\Delta T_{L_{x1}}}{T_{avg}} Q_T - \frac{L_r}{L_{x1}}\frac{\Delta p_{L_{x1}}}{p_{avg}} Q_p \right) \text{ with} \tag{2}$$

$$\frac{\Delta T_{L_{x1}}}{T_{avg}} Q_T > \frac{\Delta p_{L_{x1}}}{p_{avg}} Q_p \tag{3}$$

and the second one is driven by the pressure building up according to

$$\dot{M}_2 = p_{avg} \frac{FA}{\sqrt{2\frac{k_B}{\mu}T_{avg}}} \times \left(0 - \frac{L_r}{L_{x2}}\frac{\Delta p_{L_{x2}}}{p_{avg}} Q_p \right), \tag{4}$$

as the top layer temperature is flat or $\Delta T_{L_{x2}} = 0$. It might be noted that the latter is also equivalent to a description by Darcy's law. In total, the flow velocity is set by the Knudsen pump within the dust bed and the overpressure which maintains that flow also in the top layer activating it by putting tension on the dust particles. If the force caused by this pressure gradient overcomes gravity and cohesion, particles can be lifted from the dust bed's surface.

To quantify the temperature profile and the resulting flow velocities and pressure differences we modeled the insolation of a dust bed as described in earlier work by Kocifaj et al. (2011). Fig. 2 shows the numerical simulation of a temperature profile in a dust bed consisting of 25 μm (radius) spheres. The calculations

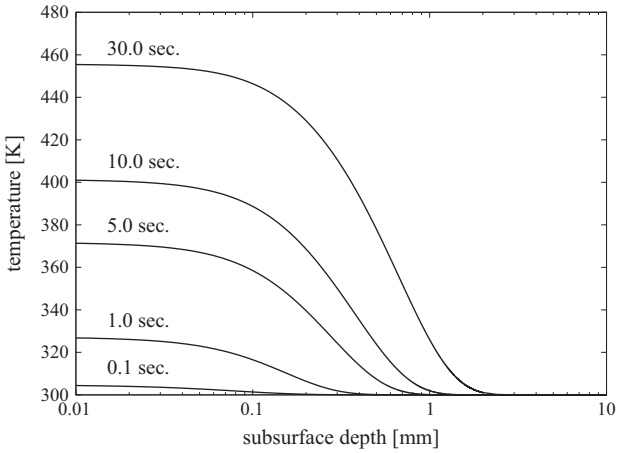

Fig. 2. Simulation of temperature profile within a dust bed consisting of 25 μm spheres. The dust bed has a thermal conductivity of 0.01 W K^{-1} m^{-1}. The light flux is 4 kW m^{-2} and illumination times are on the order of seconds.

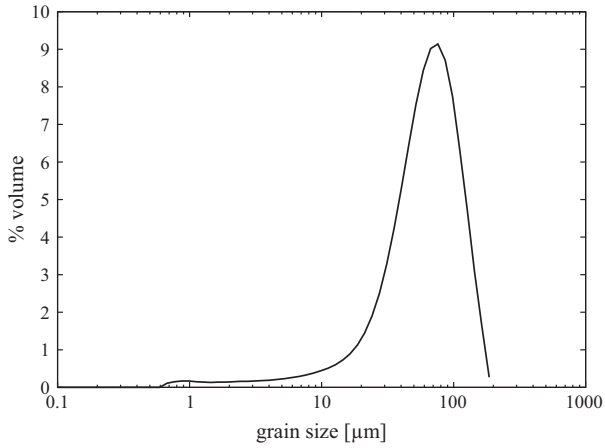

Fig. 4. Volume distribution of the used sample.

were chosen to closely match the experimental setting: a composition of 25 μm sized (radius) spheres in a dust bed with a thermal conductivity of 0.01 W K^{-1} m^{-1} (at $p = 10$ mbar Presley and Christensen, 1997) and illumination with 4 kW m^{-2} (see Kocifaj et al. (2011) for details). The temperature starts to decrease beyond 100 μm. Therefore, we expect that the activated layer would show a similar spatial scale.

3. Experiment

The setup of the experiment is shown in Fig. 3. Basaltic dust with grain sizes ranging from 0 to 125 μm (average size of 67 μm (diameter) in a volume distribution, see Fig. 4) is placed between two glass plates. It forms a thin dust bed with a width of 2 mm and 25 mm height.

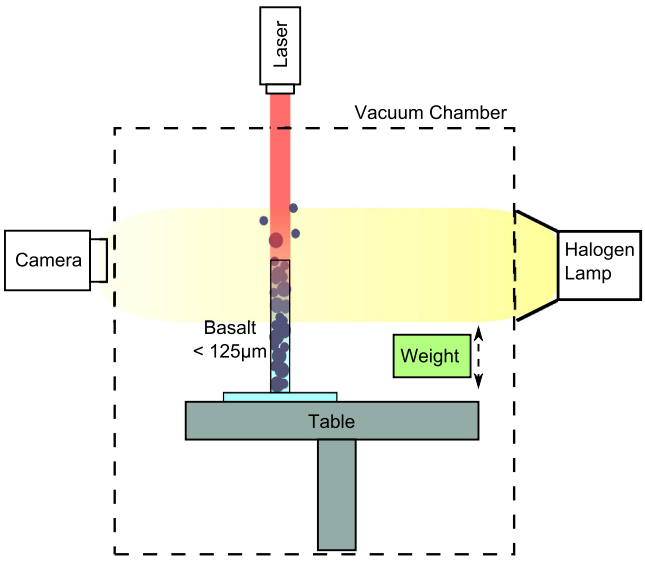

Fig. 3. Schematic setup of the experiment: A dust sample is placed between glass plates of 2 mm distance on a table inside of a vacuum chamber with ambient pressure of 0.1, 1 and 10 mbar. The dust is illuminated by a red laser (655 nm) from above. A weight inside the chamber can be dropped upon the table, leading to a tension release within the dust. In addition some particles move upon the impact without being illuminated. Images are taken before and after the impact within and outside the laser beam. For the images outside the laser beam an additional light source is used to observe the surface with the camera.

About 0.5 mm of dust emerges above the plates, forming a smooth surface which can be observed by a camera and microscope optics.

In a distance of 3 cm to the glass slides a weight of 30 g is locked 8 mm above the experimental table by an electromagnet. If the magnet is turned off, the weight drops. This results in a short vibration of the dust sample, removing cohesion between the dust particles and – if present – releasing the tension due to the overpressure. This installation is placed within a vacuum chamber and experiments have been carried out at an ambient pressure of 0.1 mbar, 1 mbar and 10 mbar. A red laser (655 nm) illuminates a spot of 8 mm width of the dust sample for ~20 s, providing a flux density of 4 kW m^{-2}. This flux is chosen to be close to the limit before a continuous particle ejection occurs. It provides the most tension to ensure that the whole activated layer is ejected on tension release.

Images of the dust surface before and after the impact are taken. After each measurement the laser spot is moved further over the surface. After 5 measurements new dust is added to the sample. The images within the laser beam show a light surface and a black background (Fig. 5(1a) and (1b)). In addition images outside the laser beam are taken before as well as after the impact to measure the particle loss without radiation. These are taken as bright field images with transmitted light to have a black surface on a bright background (Fig. 5(2a) and (2b)).

The surface lines before and after an ejection are traced. The particle loss is calculated by subtracting the lines of the surface before and after the impact. For each image an average of the thickness of the removed layer with and without illumination is determined. A total of 40–50 averaged measurements is taken for each pressure.

4. Model

The mass flow of gas through capillaries can be calculated by Eq. (1). We assume that two gas reservoirs are connected by a small capillary with a constant temperature gradient. For $Kn \approx 1$ the gas is driven by thermal creep and flows with a certain rate through the capillary until the rising pressure difference Δp balances the thermal creep flow as a pressure driven flow through the top layer. There is a maximum Δp at which no net gas flow is active ($\dot{M} = 0$, top layer as lid). From Eq. (2) we get (Muntz et al., 2002)

$$\Delta p_{max} = p_{avg} \frac{\Delta T}{T_{avg}} \frac{Q_T}{Q_P}. \quad (5)$$

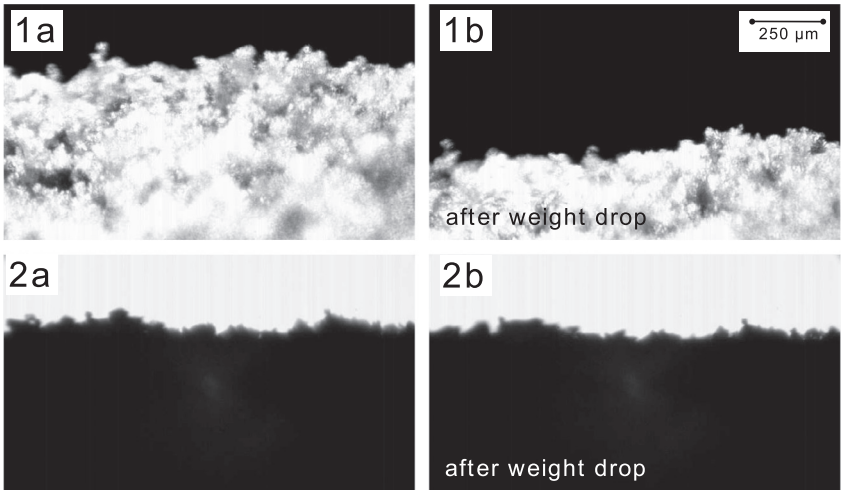

Fig. 5. Example of the dust bed within (1a) and outside (2a) the laser beam at 1 mbar ambient pressure. The images 1b and 2b show the results after tension release. The dust bed within the laser beam (1a and 1b) was illuminated by a red laser (680 nm) with a light intensity of 4 kW m^{-2}.

We model the dust bed as follows: The mean radius of the dust particles is $r = 25$ µm as used for the temperature profile in Fig. 2. We consider this a suitable approximation for the dust sample of 33.5 µm radius (Fig. 4). We further approximate the radius of the capillaries by a pore size $L_r = 0.2 \times r$ (Jankowski et al., 2012). The ambient pressure is $p = 10$ mbar (in one of the experimental sets). The illuminated area of the dust bed is $A = 2$ mm $\times$ 8 mm, the Boltzmann constant $k_B = 1.38 \times 10^{-23}$ J K^{-1}. We assume a temperature difference $\Delta T = 100$ K over a length $L_{x1} = 1$ mm (see Fig. 2) and an average temperature of $T_{avg} = 273\ \mathrm{K} + \Delta T/2$ K within the heated part of the dust bed. According to Sone and Itakura (1990), the coefficients are $Q_T = 0.22$ and $Q_P = 1.6$. This results in $\Delta p_{max} = 0.4$ mbar.

In more detail the overpressure $\Delta p_{L_{x2}}$ equals $\Delta p_{L_{x1}}$ in Eq. (2), and eventually, the gas velocity is the same in the temperature and the pressure driven part, as well as the mass flow. Solving the equation $\dot{M}_1 = -\dot{M}_2$ for the overpressure Δp, we get

$$\Delta p = \Delta p_{L_{x1}} = \Delta p_{L_{x2}} = \frac{L_{x2}}{L_{x1} + L_{x2}} p_{avg} \frac{\Delta T}{T_{avg}} \frac{Q_T}{Q_P}. \quad (6)$$

Calculating this overpressure we take $L_{x1} = 1$ mm for the length of the capillaries with a temperature gradient and $L_{x2} = 0.1$ mm for the length of constant temperature (see Fig. 2) we get an overpressure of $\Delta p = 0.05$ mbar. This is consistently lower that the estimate of the maximum pressure difference of $\Delta p = 0.4$ mbar. For an overpressure of about 0.05 mbar, the mass flow trough the pores is on the order of 10^{-8} kg s^{-1}. The velocity of the gas flow can be calculated by dividing the mass flow by the illuminated area and the density of the gas at the given pressure $\rho_{gas} = p\,\mu/(T_{avg} R_g)$ with the molar mass of air $\mu = 28.96$ AMU and the molar gas constant $R_g = 8.3$ J $(\mathrm{K\ mol})^{-1}$. At given parameters and $p = 10$ mbar, the gas flow is 11 cm s^{-1}. This is consistent with measurements of tracer particles in drop tower experiments by de Beule et al. (2014).

Further on, the force induced by the overpressure can be calculated for a particle column as

$$F_p = \Delta p\, \sigma. \quad (7)$$

With a particle cross section $\sigma = \pi r^2$ $(r = 25\ \mu\mathrm{m})$ we get $F = 6.7 \times 10^{-9}$ N.

The gravitational force which has to be overcome can be approximated by $F_G = m\, g\, L_{x2} (2r)^{-1}$ with $m = 4/3\pi r^3\, \rho$. With the density of basalt $\rho = 2890$ kg m^{-3} we get $F_G = 3.7 \times 10^{-9}$ N, which is lower than the force caused by the overpressure by a factor of about 2. This is consistent with the fact that we adjusted the light flux to a value where no constant particle ejections occured, i.e. where gravity is compensated but not yet cohesion. As the overpressure is sufficient to compensate gravity of the top layer, only cohesion needs to be overcome. As cohesion is removed by the impact the tension release leads to the ejection of the whole active particle layer.

5. Results

The measurements show a significant difference between the depth of particle loss within and outside the laser beam for each pressure value as seen in Figs. 6–8 and in Table 1. This proves that there is an activated dust layer. The green bins in the figures show the probability of the depth to which particle loss occurs without light. The blue bins show the probability to find a certain layer depth within the laser beam. The negative depths refer to the fact that the surface cannot be prepared perfectly smooth and therefore some aggregates can move during the tension loss, falling onto the measured spot and increasing the surface instead of decreasing it. Without light the measured values are strongly peaking around a depth within the dust bed of 50 µm. Within the illuminated area of the dust bed's surface the measured depth ranges from 50 up

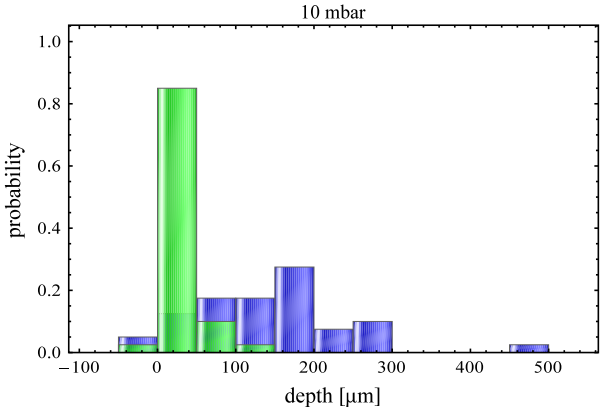

Fig. 6. Probability to find a certain depth of particle layer ejected at 10 mbar; blue bins are within the laser beam; green bins show the depth without radiation for comparison. (For interpretation of the references to color in this figure legend, the reader is referred to the web version of this article.)

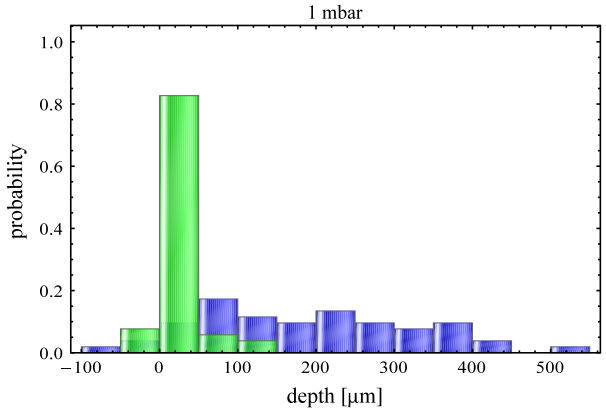

Fig. 7. Probability to find a certain depth of particle layer ejected at 1 mbar; blue bins are within the laser beam; green bins show the depth without radiation for comparison. (For interpretation of the references to color in this figure legend, the reader is referred to the web version of this article.)

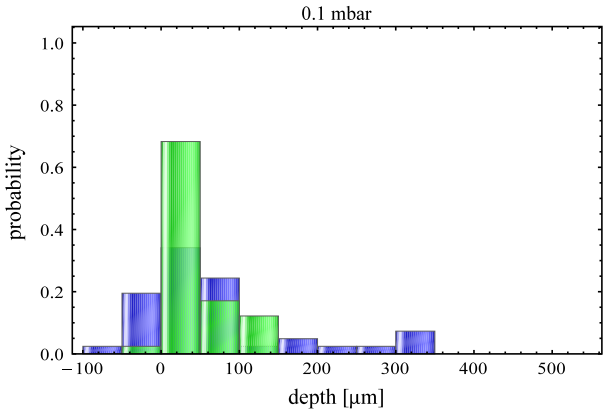

Fig. 8. Probability to find a certain depth of particle layer ejected at 0.1 mbar; blue bins are within the laser beam; green bins show the depth without radiation for comparison. (For interpretation of the references to color in this figure legend, the reader is referred to the web version of this article.)

to 500 μm for 1 and 10 mbar, where the variation of the values seems somewhat higher for 1 mbar. For 10 mbar the layer size shows less variation and is more centered around 100 μm. The values for 0.1 mbar show no significant loss attributed to illumination. This is due to the decrease in absolute pressure and pressure difference. While the temperature profile is similar as in the other two cases it is not imprinting itself enough on an overpressure to dominate over Earth gravity.

The temperature profile for the relevant time scales in our experiment shown in Fig. 2 is consistent with the experimental results. The flat temperature region has an extension of around 100 μm which is the same as the measured depths for 1 and 10 mbar. Average values are given in Table 1.

6. Application to Mars

The laboratory setting was chosen to quantify the active layer depth in a convenient way. On Mars the light flux is and the average temperature are lower and the durations of insolation are longer. We therefore adjusted our simulation to scale the experimental results to martian conditions. We choose 700 W m^{-2} for the solar insolation and illuminate the dust bed in our simulation for up to 12.5 h at an average temperature of T = 200 K. The temperature profiles are shown in Fig. 9. The maximum temperatures

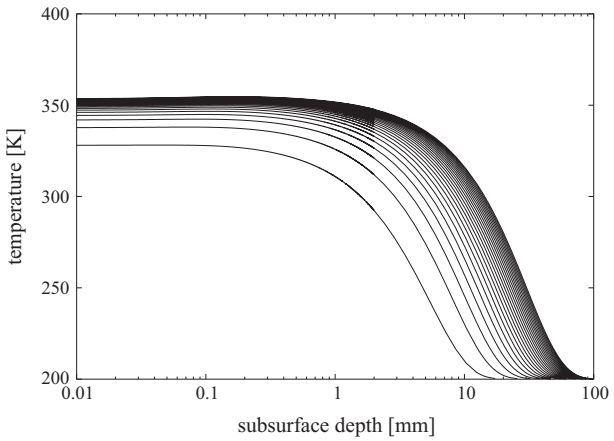

Fig. 9. S ame as Fig. 2 but for a light flux of 700 W m^{-2}, average temperature of 200 K. The illumination times are 0.5 h, 1 h, 1.5 h, …, 12.5 h from bottom to top.

Table 1
The mean thickness of the active dust layers for the different pressures. Each data point is based on about 40 measurements and the mean thickness was calculated after subtracting the mean offset.

Pressure (mbar)	Mean thickness (μm)	Mean deviation (μm)
0.1	33	±32
1	166	±57
10	109	±35

are somewhat larger than temperatures found on Mars. This is due to the simplifications of the model but we consider the results to capture the essential trend. Additionally we consider CO_2 instead of air with a molecular mass of $m_{CO_2} = 44$ AMU, a geometric radius of 4.63×10^{-10} m and a resulting cross section $\sigma = 1.6 \times 10^{-19}$ m^2. At p = 6 mbar with a particle density $n = pk_B^{-1}T^{-1}$ the mean free path of CO_2 is $\lambda = (\sqrt{2}n\sigma)^{-1} = 19$ μm. Hence, the ratio between Q_T and Q_P is 1.68 (Sone and Itakura (1990)). According to Fig. 9 we expect typical temperature differences of $\Delta T = 150$ K for a length $L_{x1} = 50$ mm (capillaries with a temperature gradient) and $L_{x2} = 1$ mm for the activated layer of constant temperature.

Eq. (6) gives a pressure difference of $\Delta p = 0.01$ mbar. This corresponds to a lifting force for a particle pile in the active layer of $F_P = 1.8 \times 10^{-9}$ N. Gravity on the same particles is $F_{G,Mars} = m\,0.38\,g\,L_{x2}(2r)^{-1} = 1.4 \times 10^{-8}$ N. That means that the activation accounts for 13% of gravity in a 1 mm thick layer of the soil. Variations in strength are expected for changing insolation and soil parameters.

7. Conclusion

Our laboratory experiments showed that the illumination of a dust bed at low ambient pressure leads to an overpressure below the surface. This pressure provides a lifting force on particles in insolated dust beds. The pressure and thickness of this activated layer can well be described by a thermal creep model. In the experiments we used 4 kW m^{-2} and illuminated dust beds for about 20 s. This results in an activated layer of about 100 μm thickness. In the laboratory the overpressure at 1 mbar and 10 mbar is large enough to compensate (Earth) gravity.

At martian conditions the activated layer is supposedly deeper up to 1 mm. The supporting force can be on the 10% level compared to gravity. We expect that this mechanism supports other lifting mechanisms significantly, e.g. by decreasing the threshold wind speed for saltation by 10%.

Acknowledgments

This project is supported by DLR Space Management with funds provided by the Federal Ministry of Economics and Technology (BMWi) under Grant No. DLR 50 WM 1242 and by the German Research Foundation (DFG) under grand number Ke 1897/1-1. We thank Ralph Lorenz and the anonymous referee for their thoughtful reviews.

References

Balme, M., Hagermann, A., 2006. Geophys. Res. Lett. 33, L19S01.
Bridges, N.T. et al., 2012. Nature 485, 339–342.
Darcy, H., 1856. Libraire des corps imperiaux des ponts et chaussees et des nines. Quat des Agustins, Paris.
de Beule, C. et al., 2013. Astrophys. J. 763, 11–18.
de Beule, C. et al., 2014. Nature Phys. 10, 17–20.
de Vet, S.J. et al., 2014. Planet. Space Sci. 103, 205–218.
Greeley, R. et al., 1980. Geophys. Res. Lett. 7, 121–124.
Greeley, R. et al., 1992. Mars 730.
Jankowski, T. et al., 2012. Astron. Astrophys. 542, 80–87.
Kelling, T. et al., 2011. Icarus 212, 935–940.
Knudsen, M., 1909. Ann. Phys. 336, 205–229.
Kocifaj, M. et al., 2011. Icarus 211, 832–838.
Lorenz, R.D., 2009. Icarus 203, 683–684.
Maxwell, J.C., 1879. Trans. Roy. Soc., 304–308
Muntz, E.P. et al., 2002. J. Vac. Sci. Technol. 20, 214–224.
Presley, M.A., Christensen, P.R., 1997. J. Geophys. Res. 102, 6535–6549.
Reiss, D. et al., 2009. LPI Contributions 1505, 15–16.
Reiss, D., Spiga, A., Erkeling, G., 2014. Icarus 227, 8–20.
Sone, Y., Itakura, E., 1990. J. Vac. Soc. Jpn. 33, 92–94.
Stanzel, C. et al., 2008. Icarus 197, 39–51.
White, B.R. et al., 1997. J. Geophys. Res. 102, 25629–25640.
Wurm, G., Krauss, O., 2006. Phys. Rev. Lett. 96, 1343011–1343014.
Wurm, G., Teiser, J., Reiss, D., 2008. Geophys. Res. Lett. 35, 102011–102015.